3D POWER PROFILE RECONSTRUCTION USING DISTRIBUTED SENSING FIBER OPTICS

A Dissertation

by

CHARLES DAVID STRATTON

Submitted to the Office of Graduate and Professional Studies of
Texas A&M University
in partial fulfillment of the requirements for the degree of

DOCTOR OF PHILOSOPHY

Chair of Committee,	Pavel Tsvetkov
Committee Members,	Philip Hemmer
	Ryan McClarren
	Lin Shao
Head of Department,	John Hurtado

May 2019

Major Subject: Nuclear Engineering

ABSTRACT

When it comes to reactor power monitoring, the old adage is the more information the better. An undetected hot spot or unexpected power shift could cause an early shutdown of the plant and have economic consequences. Distributed sensing fiber optics offer the unique ability to provide a real wealth of information due to having data points distributed all along the fiber. Considering that fiber optic lengths can stretch for kilometers, even crossing oceans, it is understandable that as intrinsic measurement, this device indeed can offer a lot of data. The question is then not only what data is available, but also how to use it.

The main objective of this dissertation was to develop the novel 3D power profile reconstruction method on the basis of distributed sensing fiber optics data acquisition technologies. The development and demonstration, both through computational simulations and experimentally, of such a method was the novel high impact contribution from this effort. To meet this objective, the work was divided into three tasks: (1) theoretical reactor power reconstruction method development and computational demonstration; (2) method demonstration via experimental heat source reconstruction, and (3) development of a correlation approach (response function) to radiation dose. Each of these individual research objectives had results that showed they could be implemented successfully.

ACKNOWLEDGEMENTS

I acknowledge being able to devote so much time to be within my studies and challenges is an opportunity few are afforded. Thank you, Dr. Tsvetkov for your patience and guidance as my advisor in this endeavor. I extend my thanks to my encouraging committee as well as all my professors and teachers I have had, from before grade 2 to beyond grade 22.

To my friends and family: your compassion and kindness amazes me when I look back and will keep me moving forward. I love you Mom, Dad, Chris, Carrie and Paola.

CONTRIBUTORS AND FUNDING SOURCES

Contributors

This work was supported by a dissertation committee consisting of Professor Tsvetkov as advisor and committee chair. Additional committee members from the Department of Nuclear Engineering were Professor Shao and Professor McClarren. The committee also included Professor Hemmer from the Department of Electrical and Computer Engineering and Professor Spitz from the University of Cincinnati, Nuclear & Radiological Engineering.

Irradiation of fiber optic materials was done with assistance from the Gamma Irradiation Facility at the High Flux Isotope Reactor, Oak Ridge National Laboratory.

All other work conducted for the thesis dissertation was completed by the student independently.

Funding Sources

Graduate study was supported in part by a fellowship from the US Department of Energy, Nuclear Energy University Program.

TABLE OF CONTENTS

Page

LIST OF FIGURES

1. INTRODUCTION

1.1 Power Monitoring Concerns

1.1.1 “Hotspot:” The Nuclear Engineered Limit

An engineered system is not limited by its performance under average conditions, but rather the need to accommodate the maximum values of its design parameters. As such, a nuclear reactor is limited in its power production by a single point in the core which has the maximum heat generation known as the “hotspot.” If the peaked heat generation exceeds a critical value, the reactor would be improperly cooled and fuel damage would occur. Reactor cores are designed to minimize the ratio of this peak to the average however this point still provides an operational limit.

1.1.2 Axial Power Profile

A major concern in the fuel design for hotspot mitigation is the axial power profile of the reactor core. The profile is strongly affected by a higher density moderator due to lower temperatures at the coolant intake portion for the bottom portion of the core. This is called an axial offset which dictates that the power production peaks below the centerline and causes the power profile to be nonsymmetrical. By lowering enrichment rates (fuel content) in the bottom portion of the core, the predicted power profile can minimize the axial offset and cause the fuel power profile to flatten near the peaked zone.

1.1.3 CIPS and AOA

Although core performance calculations aim to precisely model the power shape of the core, in practice, unpredicted power profiles can occur due to the phenomena of Crud Induced Power Shifts (CIPS) and has become a growing problem in recent years (Hawkes, 2004). This is seen in Pressurized Water Reactors due to the buildup of corrosion products which attach itself to the fuel rods and then has an uptake of the boric acid from the water chemistry. These are known by the acronym CRUD for Chalk River Unidentified Deposits. The boron in the crud reduces the reaction rate in these areas unevenly and thereby causes a shift in power production that is undesirable. When the axial power profile becomes too imbalanced, the plant may need to run at reduced power or even shut down early. This offset from the designed axial power profile is known as Axial Offset Anomaly (AOA).

1.1.4 Fuel Depletion

AOA / CIPS may not be severe enough to necessitate changes in operating power levels but the reactor still requires continuous power monitoring so that the fuel content depletion / burnup can be properly be accounted for. Only one of fourth of a core is sent to the spent fuel pool per fuel reload, so the future design of cycles are heavily dependent on knowledge of the cores operational history. Deviation from predicted power depletion take time to develop so rather than requiring instantaneous response of the monitoring device, it would be advantageous for an instrument to be monitoring the complete core with high resolution even if it has a slow response time.

1.2 Power Monitoring Technology

1.2.1 Current Power Monitoring Approaches

Current technology is more focused on fast response time and thus able to quickly monitor power changes caused by transients such as control rod movement. The older generation of technology uses a series of external core neutron detector to provide the axial power profile. From the detector count rates, pre-calculated radial hotspot factors are then used to determine the overall hotspot in the core. Newer methods use in-core monitoring with strings of self-powered neutron detectors at fixed locations within multiple fuel assemblies. A theoretical neutron calculation is then fit in real time to the detector count rates to determine the 3-D power distribution (Mourlevat). Both of these methods are limited by the accuracy of the core modeling software and by their capability to measure the flux at only a few fixed points. Therefore, a device that could capture the power profile from a distributed measurement would have a significant advantage over the current technology for hot spot detection.

1.2.2 Fiber Optic Technology Potential

Fiber optics are a proven technology for measuring temperature and strain in a distributed manner such that the entire length of the fiber can be used as separate sensing elements. The sensor functions by comparing the response of the fiber to a light source under reference temperature conditions to its response when the temperature is increased. This same principle can be used to make a distributed radiation sensor by evaluating the change of the fiber's response as it is irradiated. Research has shown the Rayleigh scattering of light increases almost linearly in the low dose range for an optical fiber (Wen et al. 2011). This material property of the fiber can be used as the basis for radiation sensing capability.

Utilizing a fiber with predictable performance at low doses would restrict the fiber to function as an external core sensor, however, this has the benefit of easy installation for retrofitting existing reactor instrumentation systems. Covering the reactor on all sides of the core of the external vessel then would provide a distributed measurement in all 3 dimensions. The axial power profile could be determined by simply comparing layers of the coil to each other. The radial profile would be more complicated but could be determined by comparing all the measurements of a single layer to each other. The overall result would be a complete 3-D measurement of the power production of the reactor core and a significant enhancement on hot spot detection from what is done today.

1.3 Research Objectives

1.3.1 Main Objective Introduction

The main objective of this dissertation is to develop the novel 3D power profile reconstruction method on the basis of distributed sensing fiber optics data acquisition technologies. The development and demonstration, both through computational simulations and experimentally, of such a method is the novel high impact contribution of this effort.

To meet this objective, the work is divided into three tasks: (1) theoretical reactor power reconstruction method development and computational demonstration; (2) method demonstration via experimental heat source reconstruction, and (3) development of a correlation approach (response function) to radiation dose.

1.3.2 Theoretical Reactor Power Reconstruction

An obstacle standing in the way of this technology is the need to take the large data set from the fiber optic radiation distributed response and reproduce the reactor power profile with its characteristic emission of radiation. This needs a method and its implementation as an algorithm to reconstruct the reactor power from the response of the fiber. Techniques for current technology do not have such a wealth of data points so the objective for reconstruction needs to test a new algorithm for its performance. In order to isolate variability and test only the algorithm, this should be done in a theoretical model of a nuclear reactor which assumes ideal detection of transported radiation particles. An appropriate modeling software for this type of problem is MCNP. The objective of developing a reactor power reconstruction algorithm with a theoretical model is clearly necessary for advancing this technology.

1.3.3 Experimental Heat Source Reconstruction

Measurement of temperature in a distributed fashion is a proven technology for fiber optics (Gifford D. , Soller, Wolfe, & Froggatt). Coinciding with the development of an algorithm for reactor power reconstruction with theoretical models, the algorithm can be further tested experimentally through temperature measurement rather than ionizing radiation. Additionally, an experiment to irradiate a fiber optic in the desired configuration for testing a power monitoring algorithm would be prohibitive technically and financially. Meanwhile, a similar arrangement can be constructed to test the algorithm experimentally using a powered system to induce a response to heat instead of a nuclear powered system inducing a radiation response. This provides for a research objective which is necessary to bolster the development of the reconstruction algorithm by using a heat source configuration in a real world experimental setup.

1.3.4 Correlation of Radiation Dose (Response Function)

Heat causes a measurable response by the heat flux integrated over time inducing a temperature increase in a fiber optic. Similarly, the radiation given off by a nuclear reactor can also be measured as a fluence measurement where the radiation particle flux is integrated over time. Fluence can thereby be converted to dose when considering the energy deposited by the radiation particles. As aforementioned, measuring temperature as a spatial distribution is a technology that is already developed. Contrarily, experiments have not yet attempted to measure dose response distributed spatially over fiber optic segments. Instead, experiments primarily evaluated dose response on the fiber as a whole rather than a designed test of the fiber's capability to respond to dose distributed along its length. This calls for a third and final objective to develop a correlation of radiation dose to fiber optics as a distributed measurement, or in other words, determine a radiation response function.

1.3.5 Overall Objective Discussion

Using fiber optics has the potential for a more detailed power monitoring technology as well a sensor that can withstand high temperatures. One of the missing puzzle pieces for feasible high temperature reactor designs is the development of power monitoring instrumentation that can withstand high temperatures. In this way, fiber optics can be an enabling technology for high temperature reactors.

Similarly, the research objectives outlined here are objectives that fit together to become enabling research for the enabling technology of fiber optics. The objective for theoretical modeling is needed to demonstrate the proof of concept for how the data from distributed measurement could be used to provide the reactor power reconstruction. The models are limited in their ability to evaluate the fine resolution in the distributed measurement. This lends itself to be supported by a second research objective as an experimental study. Heat source reconstruction fills this void since distributed measurement for radiation is not yet a proven technology like temperature sensing. Presenting a challenge for a third enabling objective, to provide for distributed radiation measurement dosing of fiber optics must be done in a study which examines the response distributed spatially. These objectives fit together to form an overall objective which is to enable the use of fiber optic distributed measurement to reconstruct power profiles in 3 dimensions.

2. THEORETICAL REACTOR POWER RECONSTRUCTION

2.1 Model Selection

2.1.1 Use of Models

Theoretical models are important for the development and testing of an algorithm which reconstructs reactor power from a distributed sensor. Models offer the ability for unique control that cannot be done in reality. For example, a radiation source in the reactor as an exact point in space. Additionally, real reactor testing is prohibitively expensive since producing radiation from a reactor requires consumption of nuclear fuel as well as dedicated time by highly trained operators. Furthermore, the algorithm development should be tailored to the intended reactor category needing such a sensor which are power production reactors rather than experimental reactors.

2.1.2 PWR versus BWR

Within the power reactor category, mainly the boiling water reactor type (BWR) and the pressured water reactor (PWR) are in operation. The PWR type were constructed in 3 fold greater number so development with models of this type has the widest application. In addition, with the detector being located external to the reactor vessel, the model for the BWR would have greater irregularities due to its design's inclusion of jet pumps between the core barrel and pressure vessel and the complication from large density changes due to boiling vertical flow. These complications in the model would also be complications for the sensor in practice. Therefore, just as the PWR model is simpler, it would also work better for the sensor's reconstruction algorithm by having less irregularities.

2.1.3 Selection of PWR Model

The algorithm should be developed with a sensor that is placed external to the core such that it accommodates a more sensitive fiber thus less radiation resistant. Perhaps it could then be possible to retrofit the sensor to the existing external structure of existing plants, and yet although this research objective is sought to account for widest possible application; it is for developing the reconstruction algorithm rather than precise sensor mounting and its inherent feasibility. New reactor designs such as small modular reactors could be designed with this technology in the future and consequently the smaller core may be better suited for the sensor since there would be less attenuation from the center to the periphery. However, the PWR has widest applicability currently and small modular designs as they may be built could vary widely while the PWR design is readily available (Westinghouse). For the above reasons, it was decided to base the reactor models on the PWR design.

2.1.4 Monte Carlo Methods

Monte Carlo methods are a statistical way of solving a complicated and seemingly unpredictable problem by simulating possible solutions one by one. The result is then a likelihood of a solution occurring and is calculated by tallying how often the result was simulated divided by all simulation trials. Since the number of trials is a statistical sample, the result must be considered a mean value with an associated standard deviation. For problems that have a normally distributed solution sample set, the standard deviation decreases as sample size increases. This dictates that the number of trials must be large to have high confidence in the calculated probability for an unlikely solution.

Although simulating with Monte Carlo methods is computationally intensive for problems requiring a large number of trials, it provides a suitable solution technique for transporting radiation particles. A random walk of a particle through a geometry matches well with the physics of how particles interact in reality. Much of their transport behavior of an individual particle is random. Examples include the direction of a particle emitted, how far it travels before interacting, and the results of an interaction.

2.1.5 MCNP Radiation Transport Simulation Tool

One such radiation transport simulation tool that uses Monte Carlo methods is MCNP (acronym for Monte Carlo N-Particle). It has a long history of use by national laboratories and academia giving it credibility as a reliable program. It has multiple solution techniques. A criticality source can be used to create a source distribution based on the reproduction of source particles by the materials in the problem geometry. This provides a solution for the criticality value known as “k” so MCNP uses a command called “kcode” to specify this type of model. Since a nuclear reactor reproduces neutrons in its fuel, it takes a criticality model to simulate the proper distribution of its source particles. Alternatively, a user can make a source definition model by defining its location and energy, either with discrete or distributed values.

Because the PWR model needs an initial source to investigate predicted radiation detection levels, criticality source modeling capability is needed. Source definition modeling capability is also needed so the initial source can be perturbed to assess the detection response for the algorithm development. MCNP has these capabilities and is a suitable computational tool for the modeling to complete this objective.

2.2 Algorithm Development

2.2.1 Radiation Transport for External Core Measurement

External core measurement is, in a way, an indirect measurement due to the radiation flux is being sampled at a location that is not where the radiation is produced and therein the location of interest. For this reason, a correlation by some factor must be determined to relate the magnitude of the radiation detected at the sensor to the strength of the emitting source. During transport from the source to the detector, the radiation strength can be greatly reduced due to the attenuation through materials and distance.

The distance reduces the radiation strength by the inverse square law as is true for physical phenomena that relate to the intensity of a flux of particles crossing a surface. The surface which encapsulates all particles can be thought of as a surrounding sphere. For a flux encountering a surface at a given distance, that flux can then be calculated by the number of particles emitted divided by the area of the surrounding sphere ($4\pi r^2$). Since the area takes the distance squared it then follows that the reduction caused by the distance takes the inverse of the distance squared.

The reduction by materials is dependent on material composition, its density, and the distance the radiation particles must take through the material. The material composition determines the probability that a radiation particle will interact with a given atom by either a scatter or an absorption event. Both will remove the particle from the path it was previously traveling, but while an absorption will remove the particle completely, through subsequent scattering events, a scattered particle can again travel on the path to reach the location of interest. Because of these multiple linked events, these scattered particles that are first removed from the path and yet reenter (referred to as inscattered radiation) are difficult to calculate.

A calculation without the inscattered radiation is more straightforward. The reduction can then be calculated as a first order differential equation where the rate of change is the interaction of the radiation intensity at a given distance traveled in the material and the material's probability of removal. While the probability is a constant, the intensity decreases as the distance through the material increases. Consequently, the solution is an exponential reduction of the intensity.

2.2.2 Pathways through Reactor Geometry

With the knowledge of how distance and materials affect radiation attenuation, it is understandable that the geometry in a reactor causes significant variability in external core measurement. Pathways from radiation sources to the detector location travel through several materials. All must traverse the reactor pressure vessel. Being made of thick, dense steel, its reduction is very large; and yet, being uniform in the radial direction, this reduction will be would lead to an even radiation intensity externally if it wasn't for other geometry construction. The reactor core itself is made up of fuel assemblies which are square. This dictates that the outermost assemblies must be arranged in a configuration that has an uneven number of assemblies per rows in order to configure a core to be as circular as possible. This still results in irregular geometry such that some outer fuel assemblies are closer to the periphery than others. The PWR reactor design selected for the model therefore has extra steel to shield radiation near the rows that are close to the periphery whereas the other rows have a larger water gap and distance, both reducing the radiation. The resulting radiation intensity measured externally then varies due to these different pathways.

2.2.3 4 X 4 PWR Reconstruction Algorithm

The current reconstruction algorithm uses data obtained from 4 banks of 4 axially spaced detectors, one bank at each quadrant external to the core. Since the detectors are spaced significantly apart, the pathways for radiation emitted in the same quadrant of a given detector are much shorter than for radiation emitted in a different quadrant. This allows the detectors to monitor power for increases within a single quadrant with minimal influence affect by the power level in other quadrants.

Conversely, the set of 4 detectors in each bank are close enough together that power in each axial level must be adequately appropriated in the response of a single detector. Solving for the power thereby requires a set of linear equations where each detector's response is the result of the summation of the radiation emitted within each axial level multiplied by the attenuation as the result of its pathway to that detector's location.

For a set of linear equations to be solved by a matrix inversion, there must be the same number of equations as variables to be solved. With only 4 detector responses, the axial power distribution can only be divided into 4 discrete levels. However, dividing the core in discrete levels is not consistent with how the core behaves in actuality because the neutrons that induce fission and produce power can come from neighboring levels. This suggests it is more informative to solve for the power as a continuous function rather than discrete levels.

In this aim, the modern reconstruction algorithm solves for the power as a function dependent on the height. Since the function must be bounded by zero power production at both the bottom and top height, it can be approximated by a Fourier series using only sine waves. In this way, the algorithm reconstructs the power by solving for the coefficients of the power function's Fourier series rather than the power itself (USA Patent No. 4,079,236, 1978).

2.2.4 Development of Source Point Method Algorithm

Unlike the reconstruction algorithm for current detectors, the distributed measurement of a fiber optic detector is not limited by the number of detection points. Each detector incremental response provides for another linear equation and thus another source location can be solved for. In this way, the multitude of detection locations along a fiber optic enables the reactor core to be divided into much smaller portions for reconstruction then the current technology. With enough divisions, the power can be discretely attributed to each portion rather than a power function in the current technology. This allows the power monitoring to capture sharper changes in the power distribution than a smooth curve.

The discrete core portions for which the reconstruction algorithm attributes power need to have a correlation from how much radiation emitted will travel to each fiber optic increment for detection. This correlation can be thought of as a factor for how much radiation emitted from its source location reaches the detector after being attenuated by its pathway hence providing for its nomenclature as an "attenuation factor." Since, the pathway is based solely on geometry, determining the attenuation factor provides a decoupling of source strength to geometry variability in problem. This assumes thermal changes due to power differences has minimum effect on overall geometry and its total attenuation. With the source strength being the only variable, the power in a core portion can be directly solved from combining each detector increment's response.

To calculate the attenuation factor for each core portion requires a simulation where all radiation is emitted from the source location. Using the MCNP simulation tool, the center point of that core portion's geometry becomes the discrete source location. This must be done because a source distributed over space can only be defined in the simulation as the function of one dimensional variable. Therefore, when the core portions are recombined to simulate a full core, it is not be possible to have specific source distribution for each core portion individually in the same way as specifying a source for each core portion's center point.

The reconstruction of the core power in this algorithm is then the reconstruction of a source point, each being at the geometric center of the portion of the core they represent. Each source point has an attenuation factor to provide an equation for contribution for each source to the total detector response for each increment. Solving the linear equation set offers a multitude of source points for the numerous detector increments. This necessitates the algorithm's development to require testing on how finely the core should be discretized for the core to be appropriately represented by source points. Yet also, it must be studied how finely the detector can be divided to account for finer discretization without the information provided by the detector response being redundant for solving the equation set.

2.3 Source Point Reconstruction Method, 4 Point Characterization

2.3.1 Introduction

This section details the models created with a source point characterization of the reactor core in which 4 points (1 per quadrant) were used. This was the bare minimum in resolution such that it could compare with current technology of 4 quadrant power tilt monitoring. The results herein demonstrate that the spatially distributed fiber optic measurement can be used to accurately calculate power shapes with the source point reconstruction technique that is being tested in such theoretical models.

2.3.2 From 3D to 2D Model Characterization

The 4 source point characterization of the core is utilized to reconstruct a power distribution within a cross section of the core. Although the goal being to reconstruct in 3 dimensions, it can be expected that the axial power distribution can be determined easily by the fiber optic measurement being spatially separated axially. Such use of a fiber optic can be envisioned as an external core measurement surrounding the entire reactor at the periphery of the reactor vessel. Figure 2.1 demonstrates such a use of such a distributed sensing fiber optic technology.

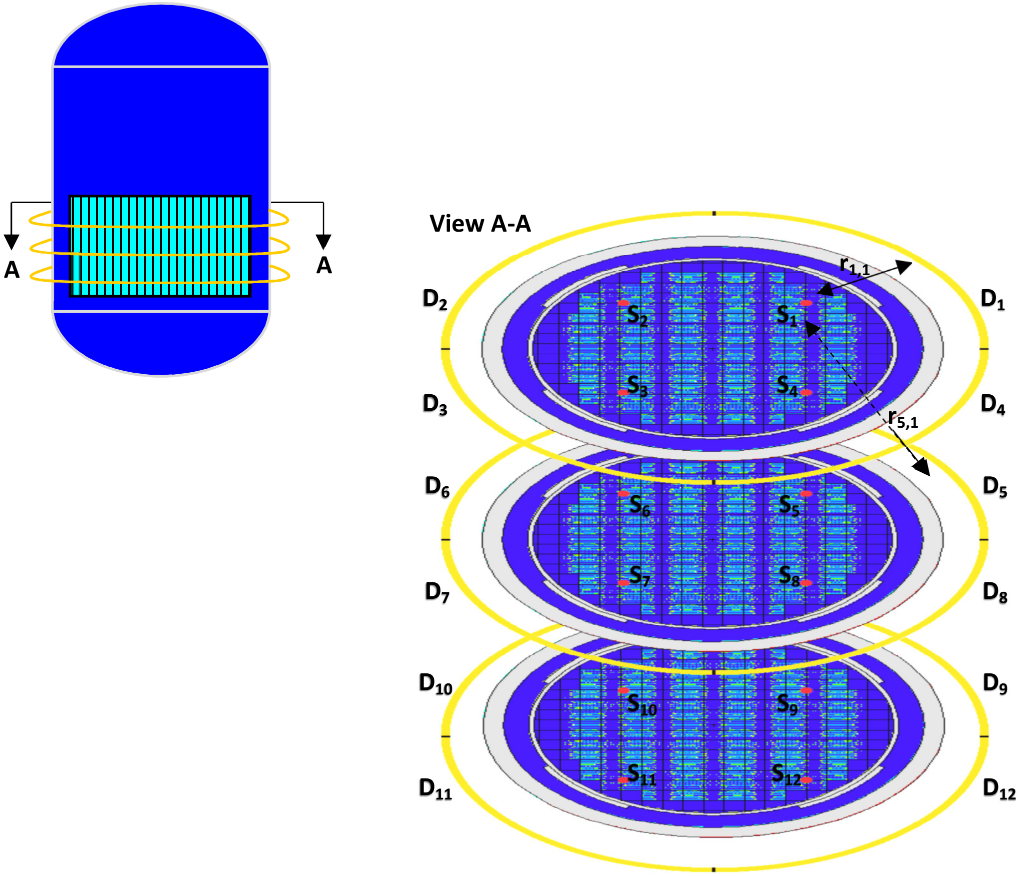

Figure 2.1: Diagram of External Core Distributed Sensing Fiber Optic

As can be seen in Figure 2.1, there are specific pathways from the located source points within the reactor to different axially levels. However, the radiation dose to the fiber at each respective axial level should be strongly correlated to the axial reactor power distribution. This lends itself to instead focus on a single cross section of the reactor core for the evaluation of reconstruction techniques. The model is then not concerned with calculating the radiation from one axial level to another (as specified by the pathway $r_{5,1}$ in the diagram) and rather only the calculation for a single axial level (pathway $r_{1,1}$).

Using reflective boundaries at the top and bottom, thereby representing the cross section as infinite in the axial direction, changes the modeling problem to 2 dimensional rather than 3 dimensions. Due to the nature of Monte Carlo simulations, this is much more desirable than modelling the fiber optic in 3 dimensions. As it exists in 3-dimensional reality, the miniscule diameter fiber optic cable can be expected to receive very few radiation particles per particle pathway simulated. Thus, a major drawback in Monte Carlo methods is invoked whereby a low number of hits on a tally creates a solution in which the sample mean has significant variability from poor statistics.

Utilizing a 2D model, the simulation can be such that all particles reaching the periphery as far as the fiber optic will be recorded in the fiber optic tally. This creates the opportunity for the fiber optic tally to have acceptable statistics. Furthermore, it enables the reconstruction algorithm to be tested for different types of core representations within the two-dimensional cross section. These dimensions provide for greater variability in discretization methods than envisioned for the axial dimension.

The distinct representations come from how the core is characterized as a collection of source points. For the simplest model, there are 4 source points (1 per quadrant). It is clear to see that multiple source points are needed each with unique paths from one source to different detector segments and accordingly unique paths to one detector from different sources. This dichotomy is seen in Figure 2.2 and Figure 2.3 as follows.

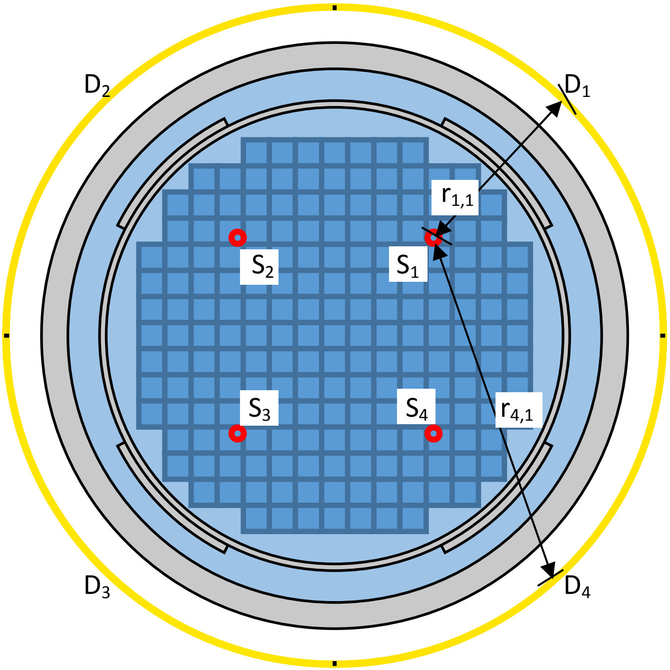

Figure 2.2: Diagram of Contribution to Different Detector Segments from a Single Source Point

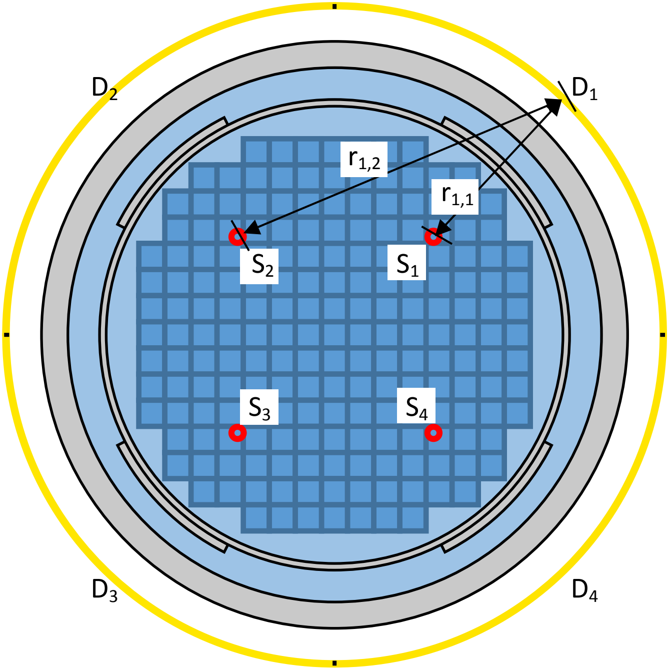

Figure 2.3: Diagram of Contribution from Different Source Points to a Single Detector Segment

2.3.3 Source Point Reconstruction Mathematical Methods for 4 Source Points

Assuming the detector response to dose is directly related to photon flux from the source treated mathematically as a point source, the following formula can be used for dose at a detector segment "D" from a source point "S" attenuated through a medium by a path of distance "r":

$$D = \frac{S}{4\pi r^2} e^{-\mu r}$$

With multiple source points to multiple detector segments, the variables take on indices as seen in the following equation:

$$D_{i,j} = \frac{S_j}{4\pi {r_{i,j}}^2} e^{-\mu_{i,j} r_{i,j}}$$

The total detector dose is therefore a summation of all source to detector doses for each detector segment:

$$D_i = \sum_{j=1}^{j=4} D_{i,j} = \sum_{j=1}^{j=4} \frac{S_j}{4\pi {r_{i,j}}^2} e^{-\mu_{i,j} r_{i,j}}$$

Examining this equation, it is useful to replace the right side of the equation into a product of two factors: a source and an "attenuation factor" which can be represented by a single letter variable chosen to be "K." This characterization is seen here:

$$D_{i,j} = K_{i,j} S_j$$

$$K_{i,j} = \frac{1}{4\pi {r_{i,j}}^2} e^{-\mu_{i,j} r_{i,j}}$$

This attenuation factor (term "K") is in itself the product of two factors. The first captures the reduction by the inverse square law which is typical for the physics of a flux from an isotropic source. The second part of “K” is an exponential reduction caused by the path through an attenuating medium. The medium must have a characteristic μ-value which is the rate of removal of the source per path length.

For a path in a reactor core, as is in the case of this analysis, the source traverses through several different materials which scatter the source as well as attenuate through absorption. For this reason, the μ-value is not a straightforward calculation thereby making the attenuation coefficient also difficult to calculate, in accordance with the formula. To solve this problem, simulations of the real radiation transport physics with Monte Carlo methods were used to solved the detector dose correlation for each source point. Although simulations were time-consuming, it was necessary to obtain correct attenuation factors for each unique pathway.

With attenuation factors known, the summation term of total dose for a detector segment creates a system on linear equations: one equation for each detector segment sum. For the analysis of a 4 detector – 4 source system, the following linear equation set applies:

$$D_1 = K_{1,1}S_1 + K_{1,2}S_2 + K_{1,3}S_3 + K_{1,4}S_4$$

$$D_2 = K_{2,1}S_1 + K_{2,2}S_2 + K_{2,3}S_3 + K_{2,4}S_4$$

$$D_3 = K_{3,1}S_1 + K_{3,2}S_2 + K_{3,3}S_3 + K_{3,4}S_4$$

$$D_4 = K_{4,1}S_1 + K_{4,2}S_2 + K_{4,3}S_3 + K_{4,4}S_4$$

This linear equation set can then be represented in matrix / vector notation:

$$\begin{bmatrix} D_1 \\ D_2 \\ D_3 \\ D_4 \end{bmatrix} = \begin{bmatrix} K_{1,1} & K_{1,2} & K_{1,3} & K_{1,4} \\ K_{2,1} & K_{2,2} & K_{2,3} & K_{2,4} \\ K_{3,1} & K_{3,2} & K_{3,3} & K_{3,4} \\ K_{4,1} & K_{4,2} & K_{4,3} & K_{4,4} \end{bmatrix} * \begin{bmatrix} S_1 \\ S_2 \\ S_3 \\ S_4 \end{bmatrix}$$

Or

$$D_{4\times1} = K_{4\times4}S_{4\times1}$$

Using Monte Carlo simulation of a reactor core criticality (known by MCNP, the simulation software, as a "kcode"), both the detector and the source distribution can be calculated (tallied) in the same model. The product of calculated source by the attenuation factor matrix, if produced correctly, should provide the same detector dose distribution as the model. This enables an evaluation of whether the combination of the attenuation factor matrix and the source point characterization is an adequate representation of the reactor core. Therefore, the "product" formula, seen as follows, is the first of the two derived formulas important to this research objective:

$$D_{i_{max}\times1} = K_{i_{max}\times j_{max}} * S_{j_{max}\times1}$$

While still beneficial to use the source distribution calculated in the criticality model for comparison, the real world application is to determine this distribution from the known detector response such that the source information is otherwise unavailable. In this way, the true aim of evaluating the source point method is to see if it can provide a reconstruction of reactor power. The research object is then to calculate the reverse (or more accurately, the inverse) of the previous "product" formula equation.

Solving for the source from an inversion of the attenuation coefficient matrix is possible if the matrix is square, meaning the row and column size are the same ($i_{max}=j_{max}$). This is true for the 4 source point / 4 detector segment characterization. In this way, the detector response should provide for the reactor power distribution as a reconstruction method by inverting the matrix, therefore, the second important equation, referred to as the "inverse" formula, can be seen as follows:

$$S_{j_{max}\times 1} = K_{i_{max}\times j_{max}}{}^{-1} * D_{i_{max}\times 1}$$

2.3.4 Illustration of the Source Point Reconstruction Method for the Full Core Case

To model the core with a 4 Source Point Characterization, the core becomes divided into 4 equal portions which coincidentally are each of the 4 quadrants. The detector segments are divided accordingly. These two representations can be seen in the following figures:

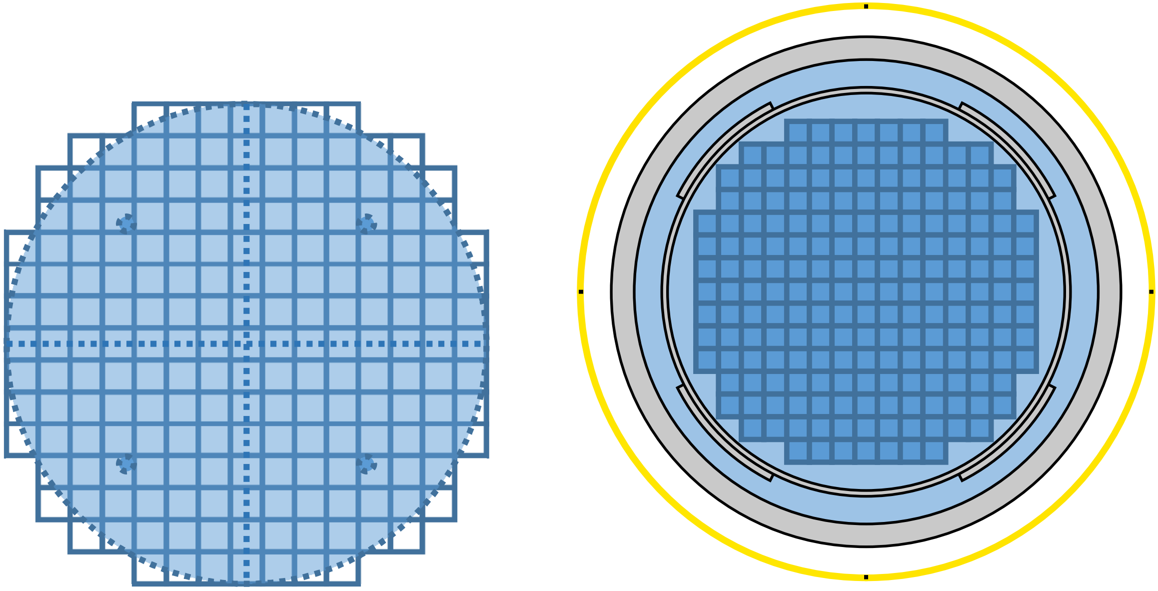

Figure 2.4: The 4 Source Point Characterization (Full Core Case)

This case is referred to as the "full" core representation reactor because the square fuel assemblies throughout the core are all considered fully enriched at 5% Uranium-235 by weight. This makes the core power distribution symmetrical for all quadrants. It can be expected that with a single detector segment and single source point per quadrant, the symmetry would then cause both to be uniform throughout. This is shown in the figure above by the detector being uniformly color-coded. In the following plot, the uniformity of this case's core power (source distribution) and the detector dose can be seen numerically for each respectively.

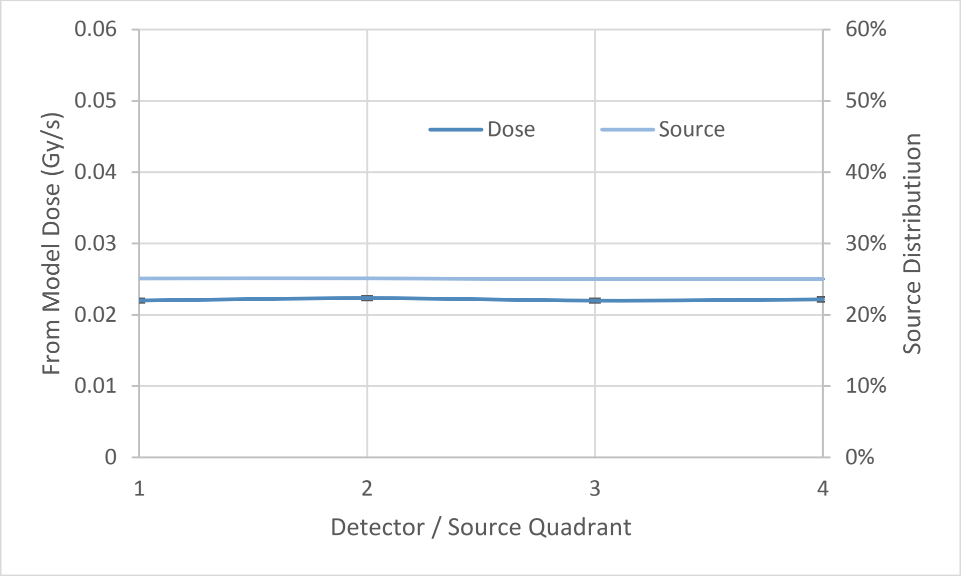

Figure 2.5: Dose and Source Distribution for Full Core Case

Applying the "product" formula with the known source distribution and a calculated matrix of attenuation factors, provides a predicted dose calculation which is also uniform, thus matching the model's dose distribution. Using the product formula in this way provides an alternative to the calculation of the dose from a criticality model. These two different methods of "from model" and "from calc." carry this nomenclature whereas the "from calc." is the product formula application while "from model" is the criticality model. Figure 2.6 shows this comparison for the full core case.

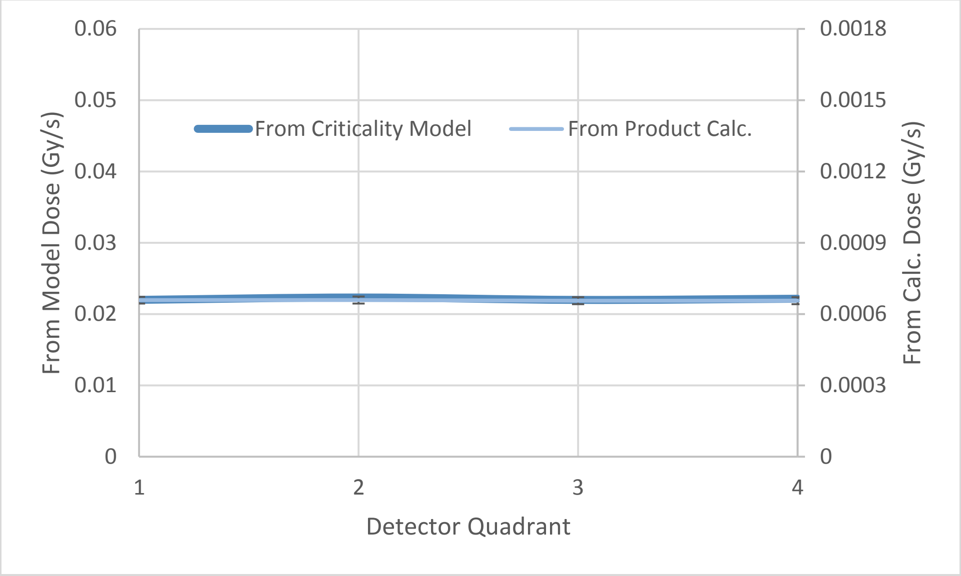

Figure 2.6: Dose Distribution Comparison for Full Core Case

Figure 2.6 demonstrates that although the distributions are very much in agreement, by examining the scales of each, however, it can be seen that the magnitude of each is very different. Accordingly, the calculated dose is only 3% of the dose from the model (scale of 0.0018 compared to 0.06).

Since the distribution matches but not the magnitude, it could be expected that the use of the inverse formula would produce similar results. A difference here occurs though because in calculating the source distributions as a percentage of total core power the results becomes normalized. This allows both the distribution and the magnitude to be closely aligned. With one source point per quadrant and a uniform core, the power distribution should be uniform with each source having 1/4th of the total or 25%. This expectation is shown in the results of both from the criticality model and from the reconstruction by calculating with the inverse formula, Figure 2.7.

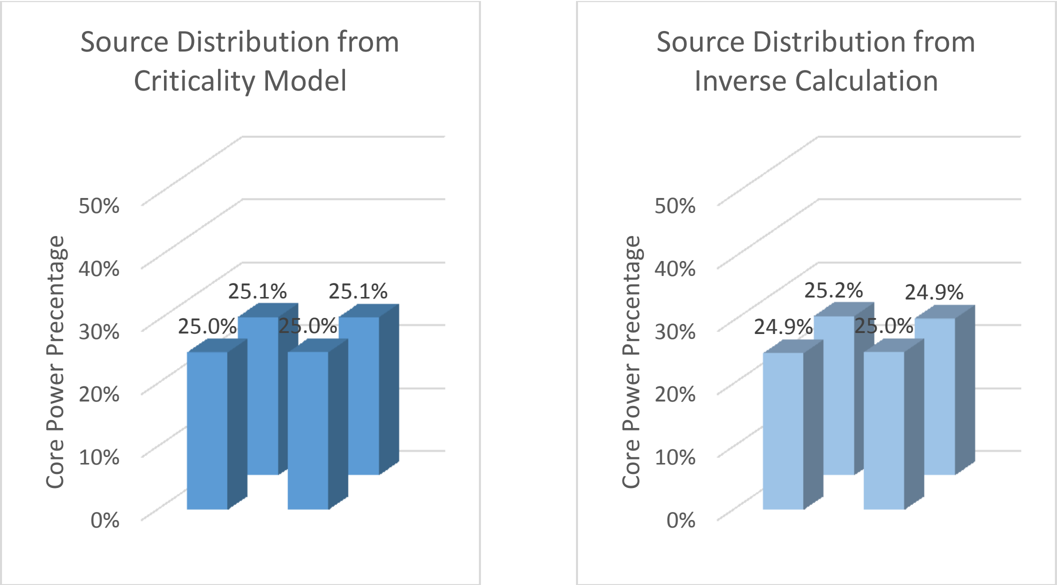

Figure 2.7: Comparison of Reconstructed Source Distribution for Full Core Case

2.3.5 4 Characterization Point Reconstruction for Cases with Depleted Core Regions

Further important analysis on the reconstruction method was performed by applying the same methods for the full core case to various other power distributions. The difference was created by modifying the full core case to have different regions of “depleted” fuel. For those regions, the enrichment of U-235 was changed from 5% to 1%. This provided quite large changes in power distribution but this was desirable for testing unique power distributions.

The first alternative power distribution had the most extreme power tilt due to an entire quadrant being changed to the depleted enrichment. The results for this case can be seen as follows:

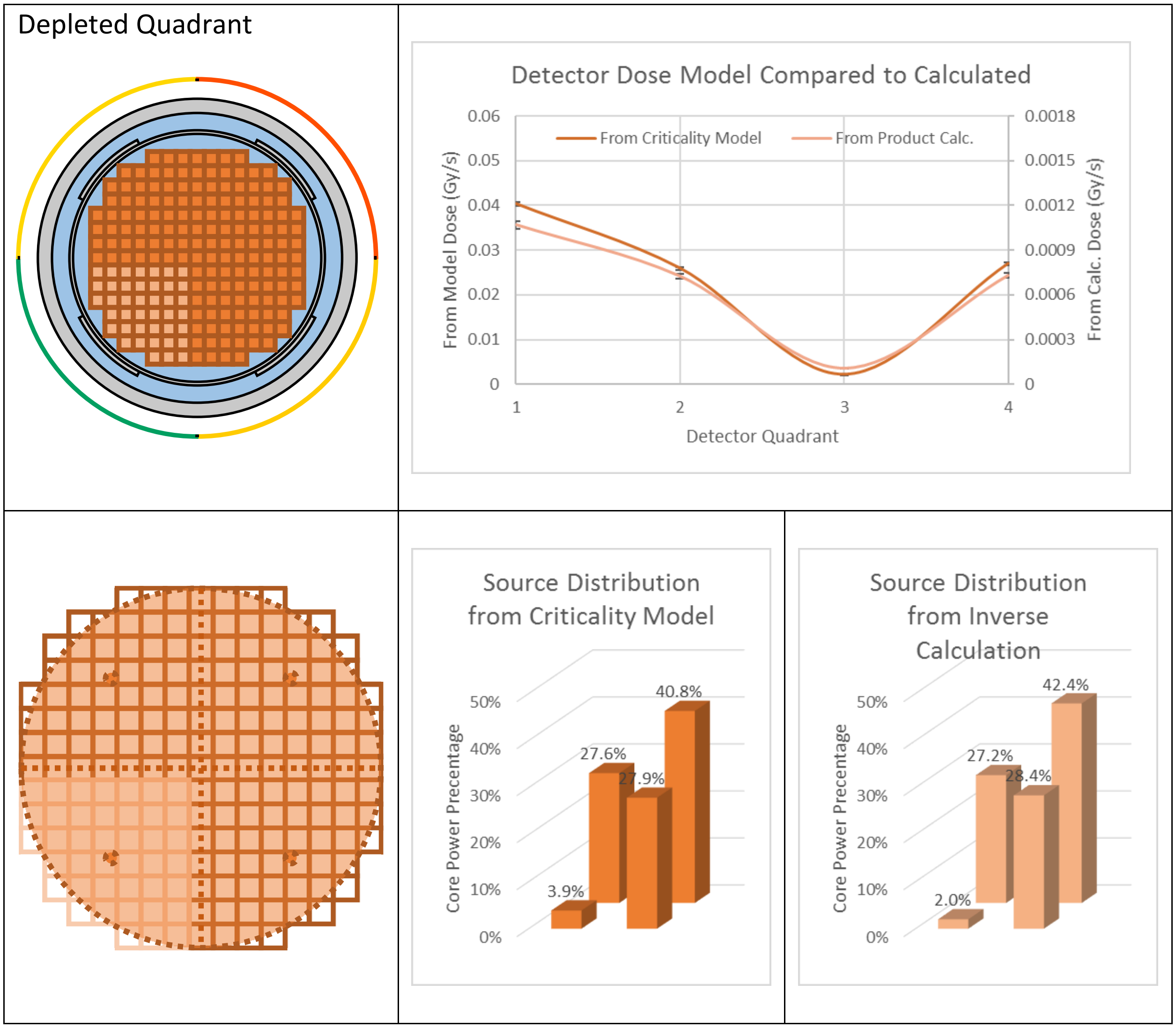

Figure 2.8: Depleted Quadrant Results

Like the full core case, the source distributions in the bar graphs are in good agreement even for such a drastic reduction in the core's third quadrant. Yet, the method still works because the detector dose for that quadrant was reduced accordingly. This is seen in the color code of the detector in the first quadrant with a "hotter" red while the third quadrant was reduced to a "colder" dark green. The application of the product formula also worked well as shown in the top graph, presenting numerically a good comparison for the model and calculated detector dose distributions.

Another variation in power tilt was evaluated whereby a center region of 9 fuel assemblies was changed to the lower enrichment. These results were as follows:

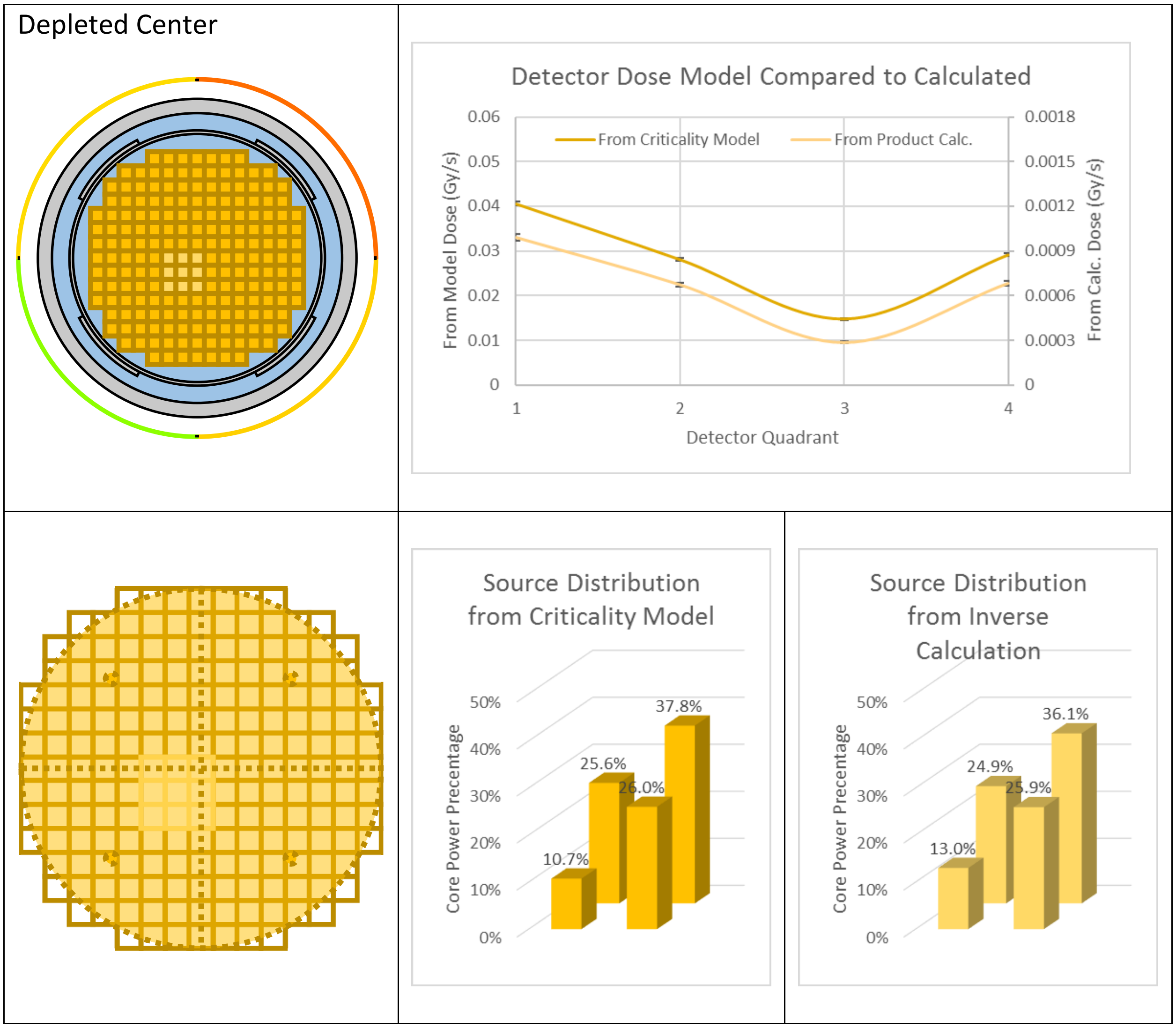

Figure 2.9: Depleted Center Results

Comparing to the depleted quadrant, the third quadrant had a reduction that, although significant, was not as pronounced as its predecessor. The color-coded detector once again displayed green for the third quadrant but not as dark, while the first quadrant had an orange-tinted red. Such colors demonstrated qualitatively that there was less disparity of the minimum to maximum detector values than the depleted quadrant case. Once again, the results had good agreement of the model and the product formula calculation for the distribution of dose as well as the power distribution calculated with the inverse formula.

The third variation of depleting a region was the case of 9 depleted assemblies being located on the periphery of the core rather than the center. The results can be seen as follows:

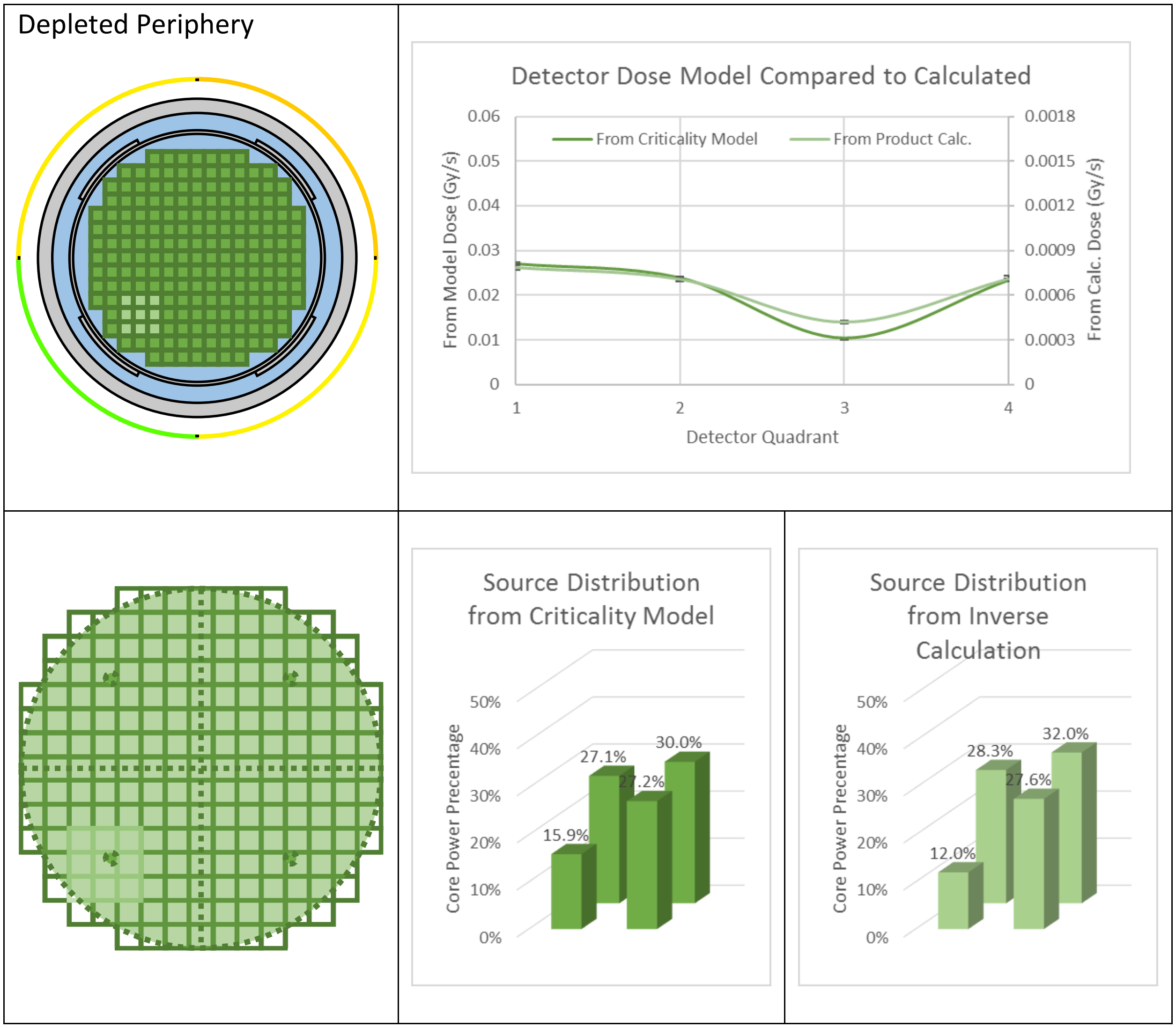

Figure 2.10: Depleted Periphery Results

The depleted periphery case showed the least variation in source distribution among the three cases. The depleted region was very far from the opposite core quadrant which caused its detector and source to have a very similar values compared to the adjacent quadrants. The application of the product formula for the detector dose matches the distribution well for these quadrants while the depleted third quadrant had a significant discrepancy. Consequently, the inverse formula calculated source distribution does not match as well as for the third quadrant as the other three quadrants.

In summary, the three variations of the full core case, each with uniquely depleted regions, demonstrate the use of the source point method for reactor power reconstruction when 4 source points are used. Although the method could produce very similar distributions in each case, it must be noted that it could not capture the magnitude correctly. Perhaps not surprisingly that with only 4 points, or 1 per quadrant, this was not adequate resolution to represent a reactor core that emits radiation completely and non-discretely throughout. Subsequent models were developed to build on these results in order to further test the algorithm and enhance its ability to capture the distribution as well as its magnitude.

2.4 Source Point Reconstruction Method, 12 Point Characterization

2.4.1 Introduction

The next set of models created to evaluate the source point reconstruction method was the 12 Source Point Characterization which used three points per reactor core quadrant corresponding to 3 detector segments per quadrant (30°segments each). The following figure demonstrates the use of this characterization. Similar to the 4 Source Point method, this method utilizes attenuation factors from each source to each detector. This is shown in the Figures 2.11 and 2.12.

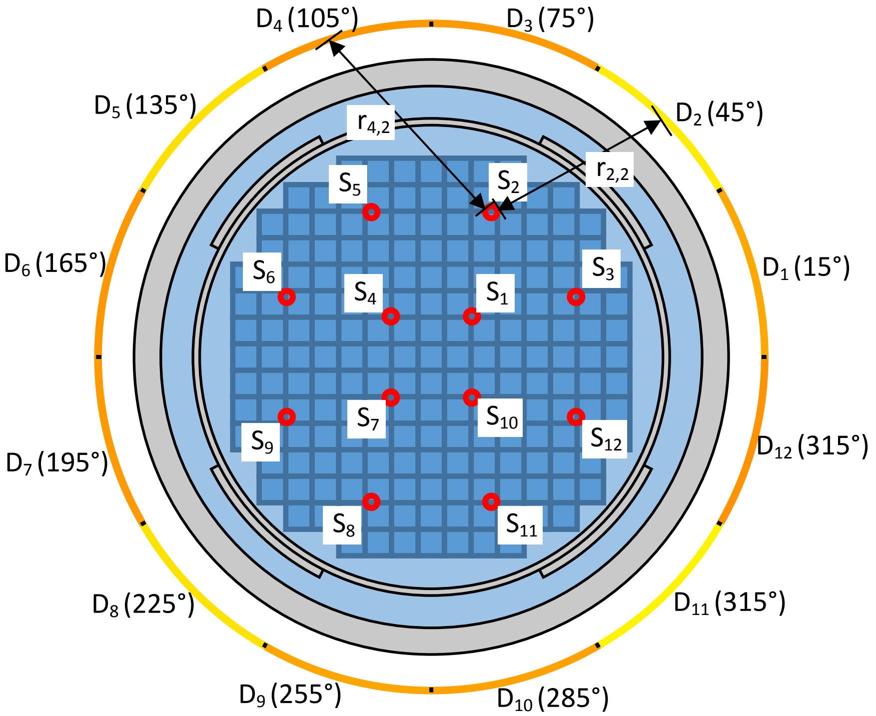

Figure 2.11: Diagram of Contribution to Different 30° Detector Segments from Single Source Point

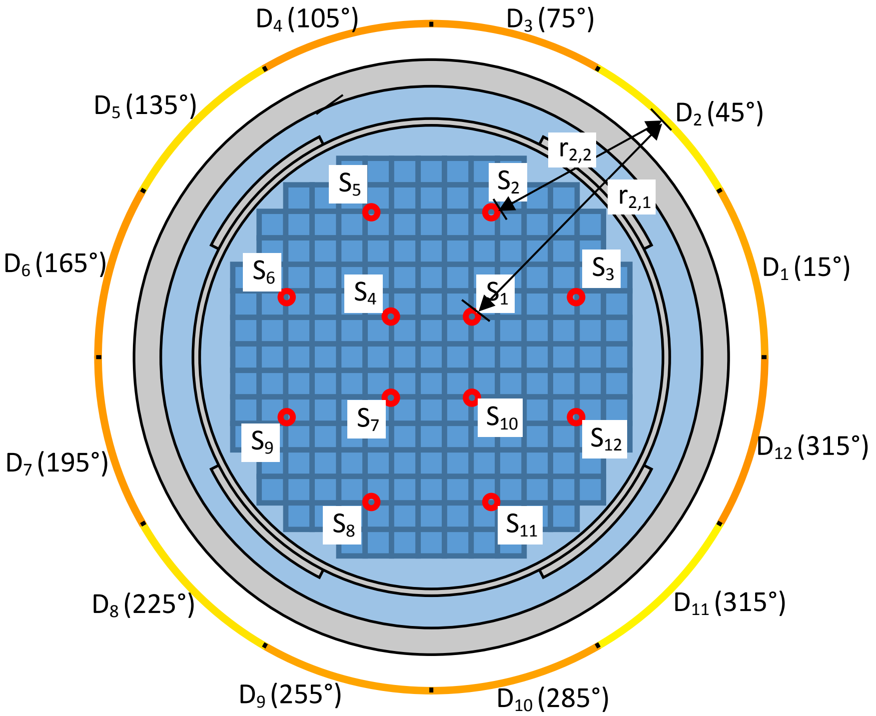

Figure 2.12: Diagram of Contribution to a Single 30° Detector Segment from Different Source Points

2.4.2 Unique Attenuation Factors by Radius

What is unique about the source points in the 12 point characterization is that there are two different radii for the set of points, compared to all points being on the same radius from the center of the core in the 4 point characterization. The set of points on the inner radius have a much longer distance through the core to any of the detector segments than the set of points on the outer radius. This can be seen in Figure 2.12 for the path length to Detector Segment 2 from Source 1 compared to Source 2.

As can be expected, the set of attenuation factors for each point differ significantly depending on which radius the point lies. Plotting the attenuation factors for the three points can be seen in the following figure table (Figure 2.13). Although the plot for Source Point 1 and Point 3 look very similar, the scale is over 3 orders of magnitude different. The color scale for the color mapped detector is 3 orders of magnitude different, accordingly. Plotting the average attenuation factor by radius reflects this difference clearly (Figure 2.14).

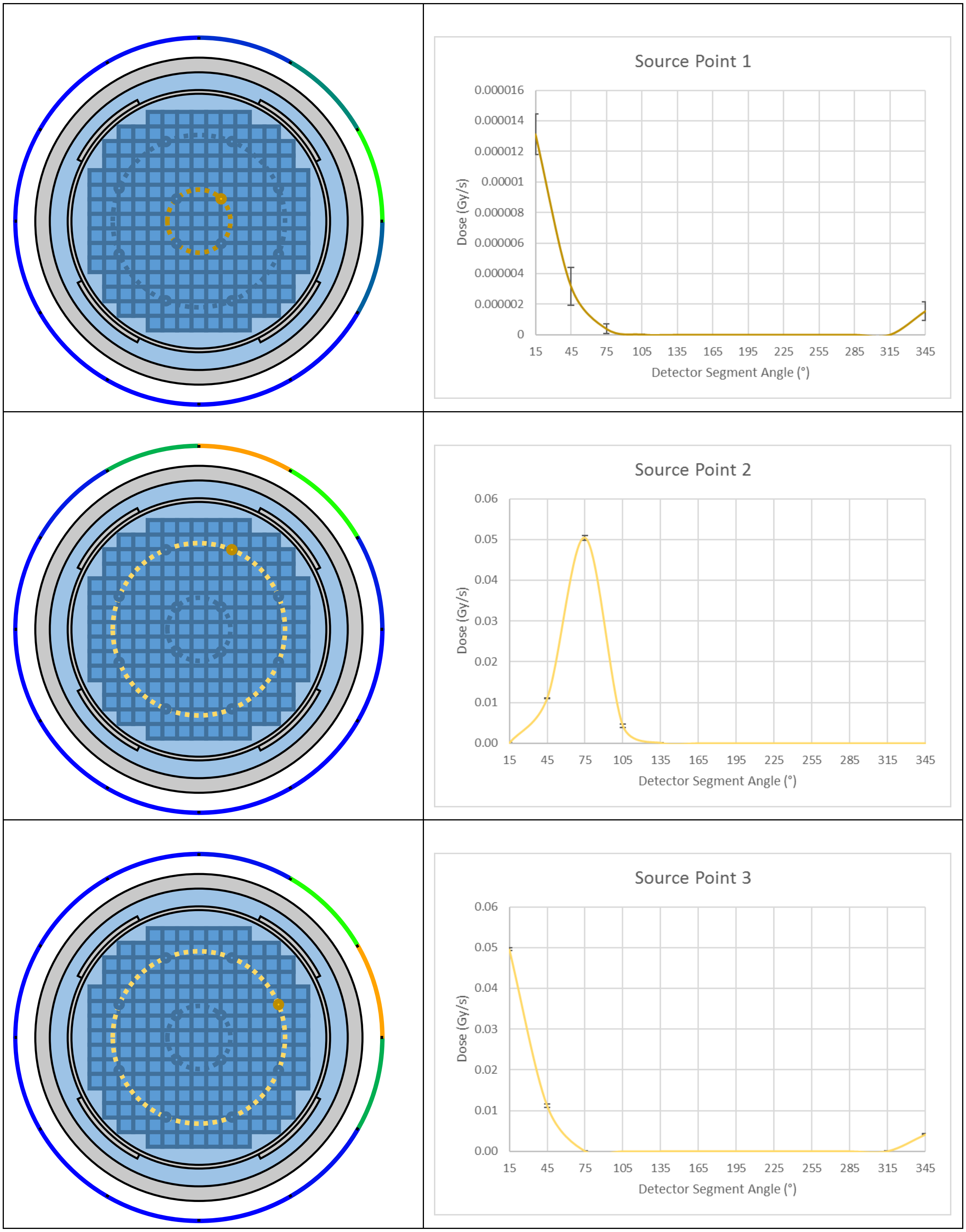

Figure 2.13: Table of Figures for Attenuation Factor Distribution from each Unique Source Point

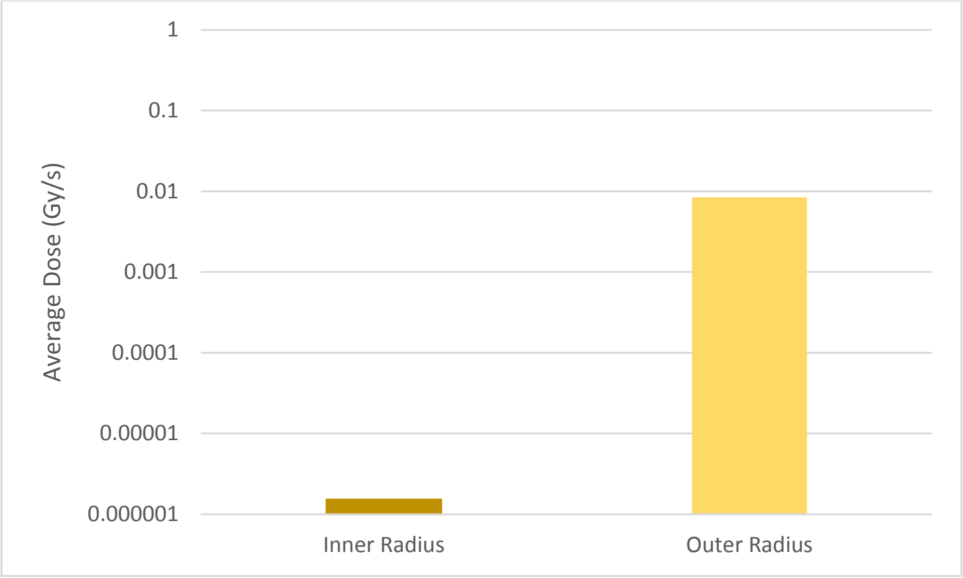

Figure 2.14: Comparison of Attenuation Factors Averaged by Radius, 12 Source Points

These attenuation factors are used in the same way they were applied in the 4 Source Point Characterization. The larger number of source points and detector segments necessitate a modification of the indices but otherwise the same formulas apply:

Product Formula:

$$D_{12\times1} = K_{12\times12} * S_{12\times1}$$

Inverse Formula:

$$S_{12\times1} = {K^{-1}}_{12\times12} * D_{12\times1}$$

2.4.3 Unique Features of Application of 12 Source Points Characterization

Locating the source points for the 12 point characterization follows similar logic to the 4 source point. The change being that with a 12 source point characterization, the core is instead divided into 12 equal portions. Instead of one source point representative of the entire quadrant, there are 3 sources representing 3 regions per quadrant in each of the 4 quadrants. This application to the full core case is seen in Figure 2.15.

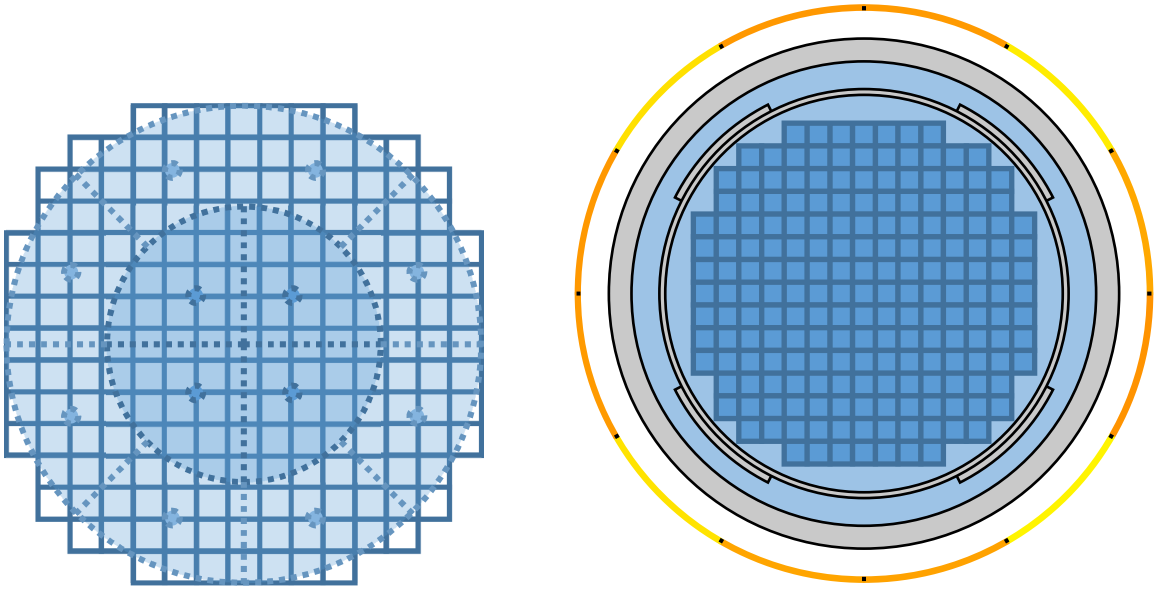

Figure 2.15: The 12 Source Point Characterization (Full Core Case)

Unlike the full core case for the 4 point characterization, the detector dose fluctuates when divided into 12 segments as can be seen by the varied colors of the detector representation in Figure 2.15. An interesting feature of this variation is that it does not match the power distribution when the core is divided in the same 30°increments as the corresponding detector segments. In fact, they are exactly out of phase when compared to each other. Figure 2.16 displays this feature.

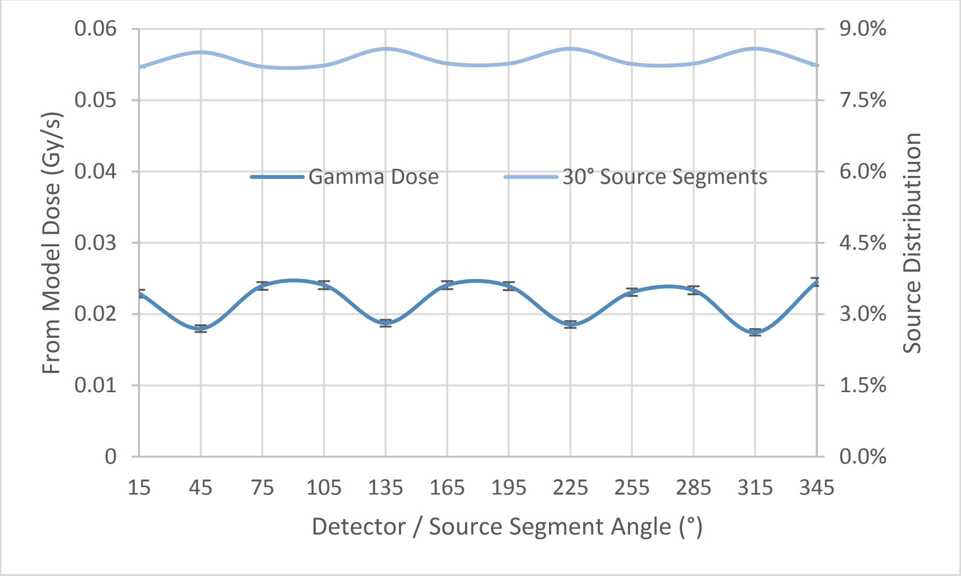

Figure 2.16: Gamma Dose and Source Distribution for Full Core Case

Figure 2.17 is a graphic of the core divided into 30° source segments as it is represented in this analysis.

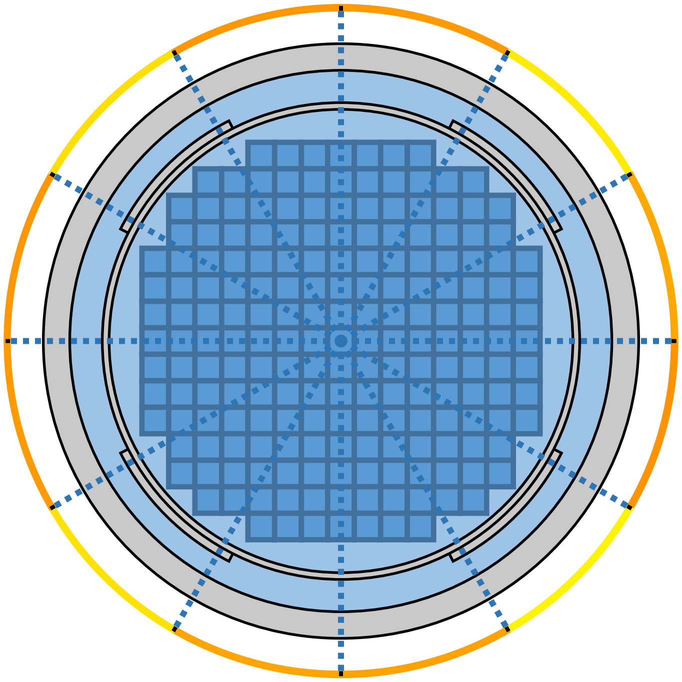

Figure 2.17: Full Core Case Divided into 30 Degree Source Segments

The 30° source segments corresponding with the 4 power peaks (at 45 degrees for example), are the segments with the greater number of fuel assemblies (represented by the blue squares in Figure 2.18). On either side of the peaked segment are segments of reduced power and exactly equal to each other due to symmetry. In this way, the core model exhibits Eighth Core Symmetry which is key to further analysis within the Theoretical Model research objective.

Because the peak power has a greater quantity of fuel assemblies, the outer ones are closer to the steel of the reactor pressure vessel. For this reason, the PWR reactor design consists of an extra region of steel to act as a vessel shield from the damaging radiation that is peaked at these areas. In turn, this causes a reduction in the gamma dose significant enough to make the dose distribution lower for that corresponding detector segment, despite contradicting the actual power distribution. This characteristic pattern of an oscillating detector dose even for a uniform core can thus be seen in the dose distributions of the other cases with depleted core regions as well (Figure 2.18).

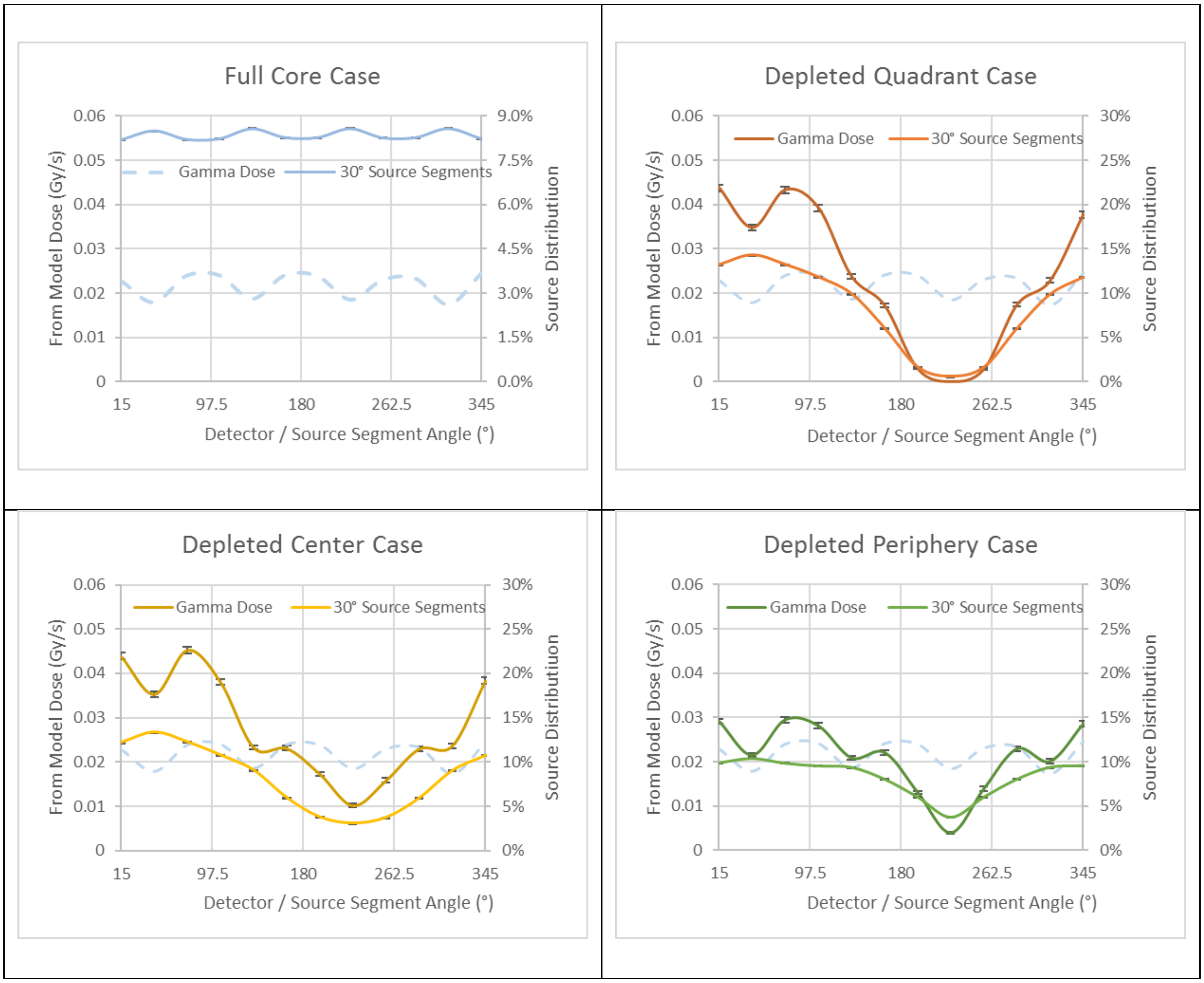

Figure 2.18: Gamma Dose Comparison Depleted Cases with Full Core Case

Compared across the different cases, the dose distributions reflect that it is a combination of the gamma reduction by the reactor geometry and the distinct power distribution. For this reason, the reconstruction algorithm cannot simply attribute the hottest detector segment as being the hottest core segment. The use of the attenuation factors is instead an improvement in capturing the unique reactor geometry as shown when the product formula is applied to calculate the detector dose distribution, demonstrated for the full core case in Figure 2.19.

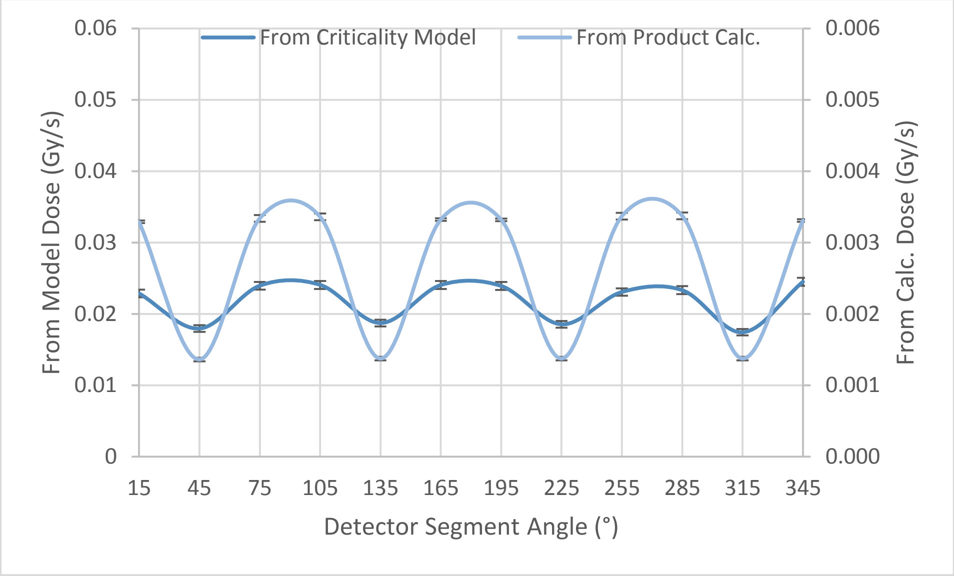

Figure 2.19: Dose Distribution Comparison for Full Core Case

The full core case best demonstrates that the geometry features which cause a non-uniform attenuation of the source are captured by the source point method. Despite the core being uniform, the product formula calculates an oscillating dose distribution and it is indeed in phase with the dose obtained from the criticality model simulating the reactor core behavior.

2.4.4 Source Point Reconstruction Applied to the Full Core Case

Applying the inverse formula from the gamma dose detector distribution to calculate the source term provides the comparison in Figure 2.20.

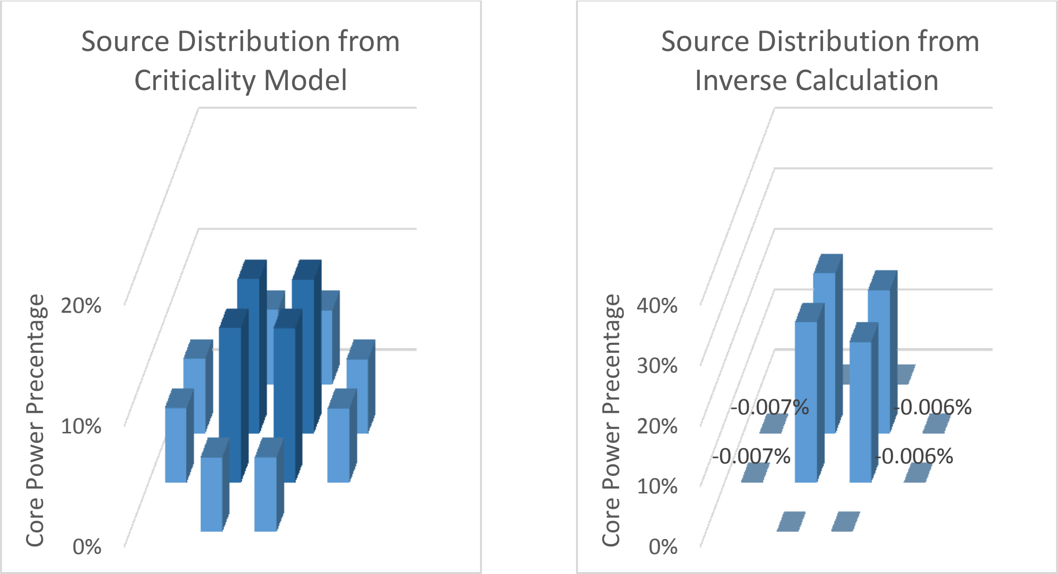

Figure 2.20: Source Comparison for Full Core Case

Although the calculated negative values seem insignificant (less than 1/100th of a percent), the attenuation factors are so much larger for the outer radius than the inner radius (Figure 2.14). Therefore, when a source point from the outer radius is calculated as a negative value, it corresponds to a solution from a highly negative dose. This is revealed when the product formula is applied to the source solution from the inverse and diving the result into both positive and negative components.

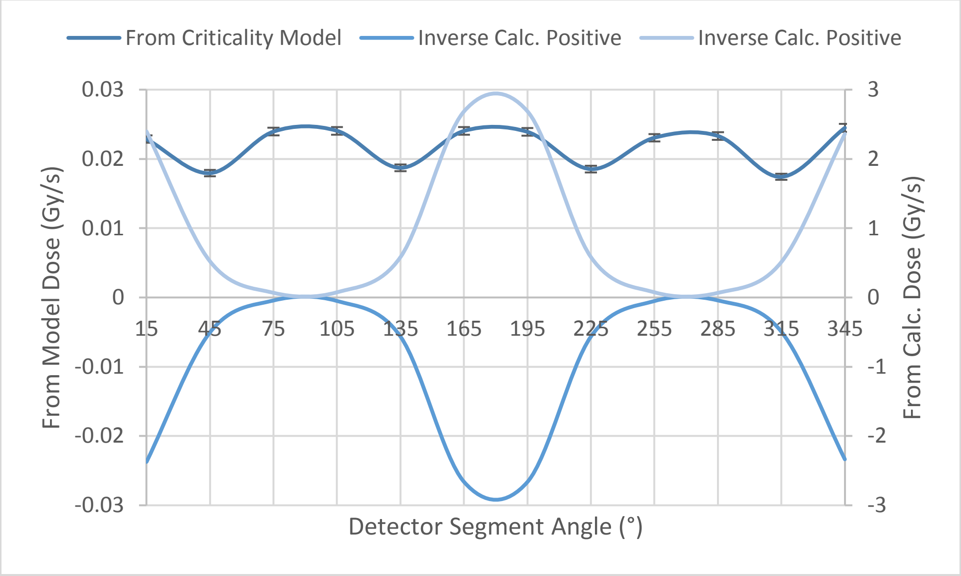

Figure 2.21: Comparison of Dose Distribution from Different Source Distributions

The sum of both components is then the dose distribution from the criticality model but this is not obvious since both negative and positive components of the solution are a factor of 100 higher. The highly positive values are offset by the negative dose calculated from the negative source for the outer radius points. Neither negative source nor negative dose make physical sense because these values can only be positive in reality. Though the source comparison graphic (Figure 2.20) shows the source calculated from the inverse formula on the same scale as the model, this is because it has been normalized for a total of 100%.

The inverse formula is shown here to be an inadequate solution technique for the 12 source point characterization, demonstrating the need for an alternative algorithm which calculates a solution with positive values only. This is possible using a regression analysis method known as Non Negative Least Squares (NNLS). This technique is discussed in detail including its specific application as programmed code in the appendix chapter *A5 Programming Methods.*

An additional benefit of using the NNLS algorithm instead of the regular matrix inverse is that the number of variables in the solution (source points) does not have to match the number of equations (detector dose distribution). Contrarily, with equal detector segments and source points, the distribution was the only the result from gamma ray dose. However, with NNLS, the neutron dose distribution can also be used such that there are more detector doses than source points. Unlike the gamma dose (plotted in Figures 2.16 and 2.18) which contrasts with the source distribution by angle, the neutron dose, specifically from fast neutrons, is instead in phase with the source as seen in Figure 2.22.

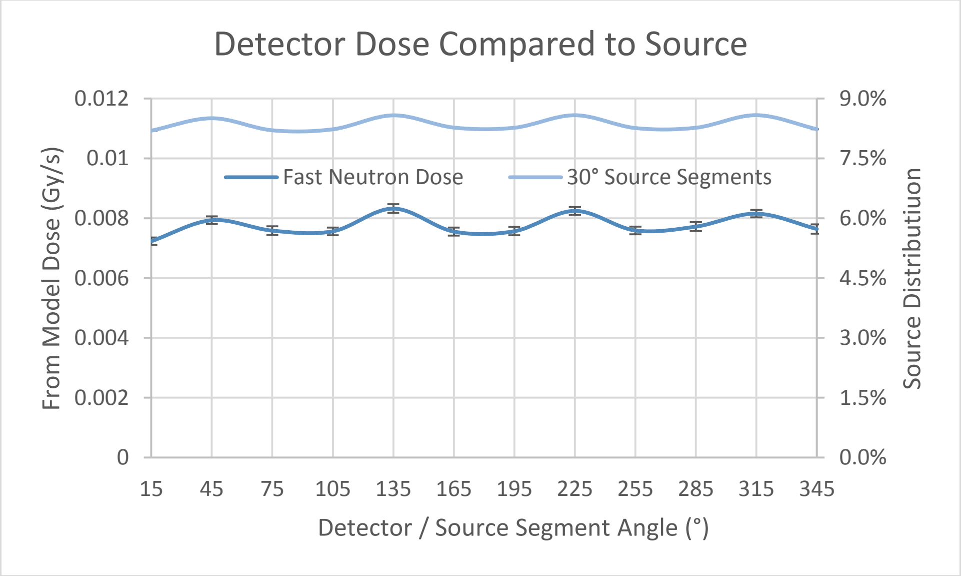

Figure 2.22: Fast Neutron Dose and Source Distribution for Full Core Case

Because there is a difference between the gamma dose distribution and the neutron dose distribution, the neutron dose provides new information which can improve the results when applied to the NNLS algorithm. The results for the full core case are compared in Figure 2.23.

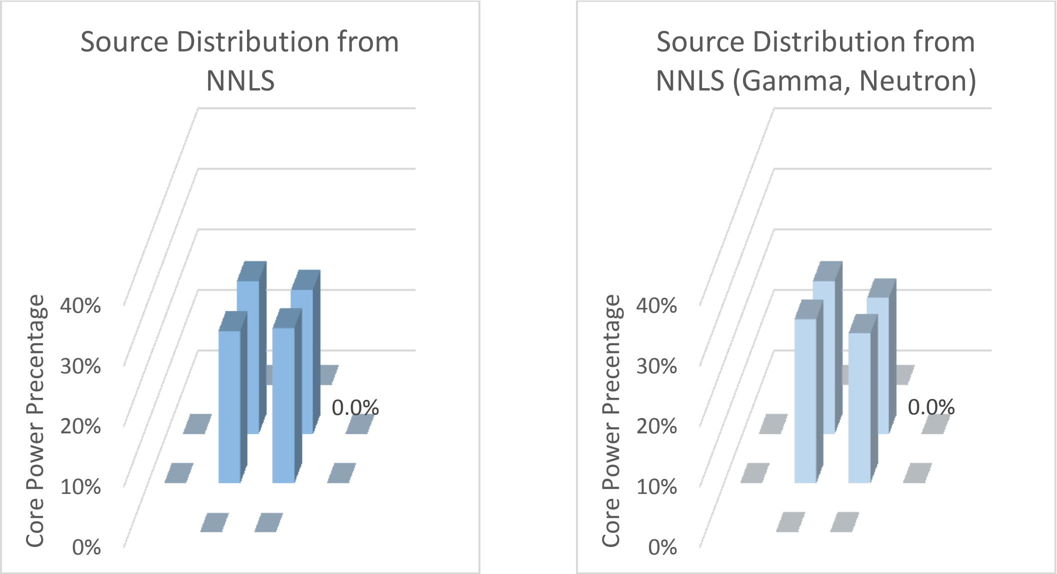

Figure 2.23: Source Distributions for Different NNLS Solution Techniques, Full Core Case

These results appear very similar to the inverse solution, with the key difference being that the outer radius results are exactly 0, being the purpose of utilizing the non-negative algorithm. A comparison of results averaged by quadrant is in the next graphic, Figure 2.24.

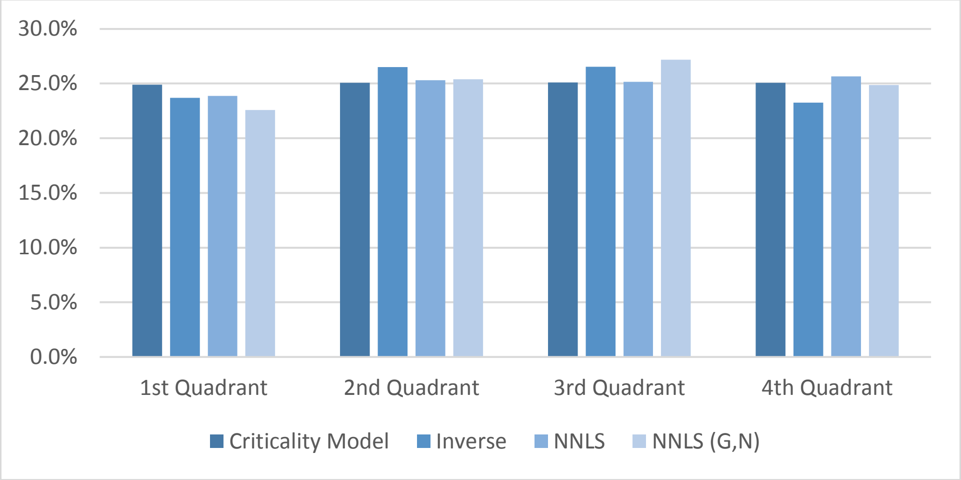

Figure 2.24: Source Averaged by Quadrant for All Solution Techniques, Full Core Case

The average by quadrant is very comparable for all solution techniques. However (aforementioned), the solutions are all normalized to be a percentage of the total value. Only the result from the criticality model is correct without need to be normalized. By comparing their true magnitudes, the differences between each solution technique demonstrates the NNLS with multiple solution bins (gamma and neutron) is the closest to matching the model, yet 3 orders of magnitude off.

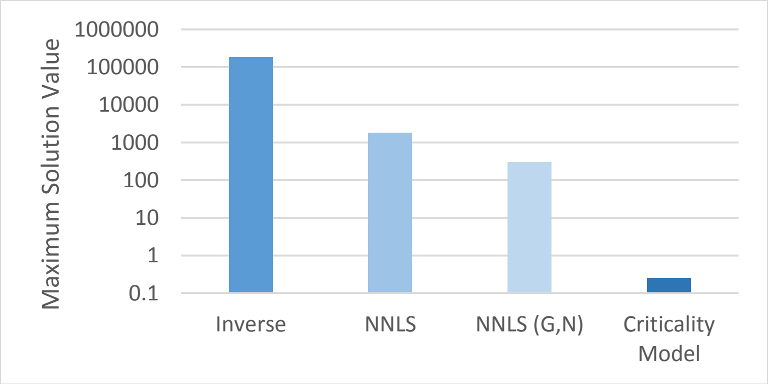

Figure 2.25: Maximum Solution Value for All Solution Techniques, Full Core Case

2.4.5 Depleted Core Cases Results and Discussion

To test the reconstruction algorithms for alternative source distributions, the same cases were evaluated for the 12 source point characterization as the 4 source point, namely the depleted quadrant, depleted center, and depleted periphery. The results for detector dose distribution from the criticality model of each of these cases were already presented in Figure 2.18, but in the following figures, this dose is compared to its alternative calculation using the product formula. Once again, the results can be presented with this dose distribution comparison as well as the source reconstruction compared to the source from the criticality model. These results are displayed in the following figures (Figure 2.26 through Figure 2.28).

Each of the depletion case have significant power tilts, yet their results have their similarities to the full core case. For all source reconstruction results calculated from the inverse, it can be seen that that the inner radius source points obtain all the positive source distribution, while the outer radius points have very small values but negative, not to be underestimated however. As demonstrated earlier, these outer radius negative values cause the inverse result to be of a very high and unrealistic magnitude.

On the topic of magnitude, it should be noted that the detector dose comparison is closer in magnitude than the 4 source point characterization results. For 12 points, the scales are a factor of 10 different, or in other words, the calculated dose is 10% of the dose distribution obtained from the criticality model. The 4 point characterization was 3% so this is an improvement. The dose distribution otherwise appears to amplify the fluctuations caused by the core model geometry while demonstrating the effect of the depleted source in the appropriate quadrant. Results are shown as follows.

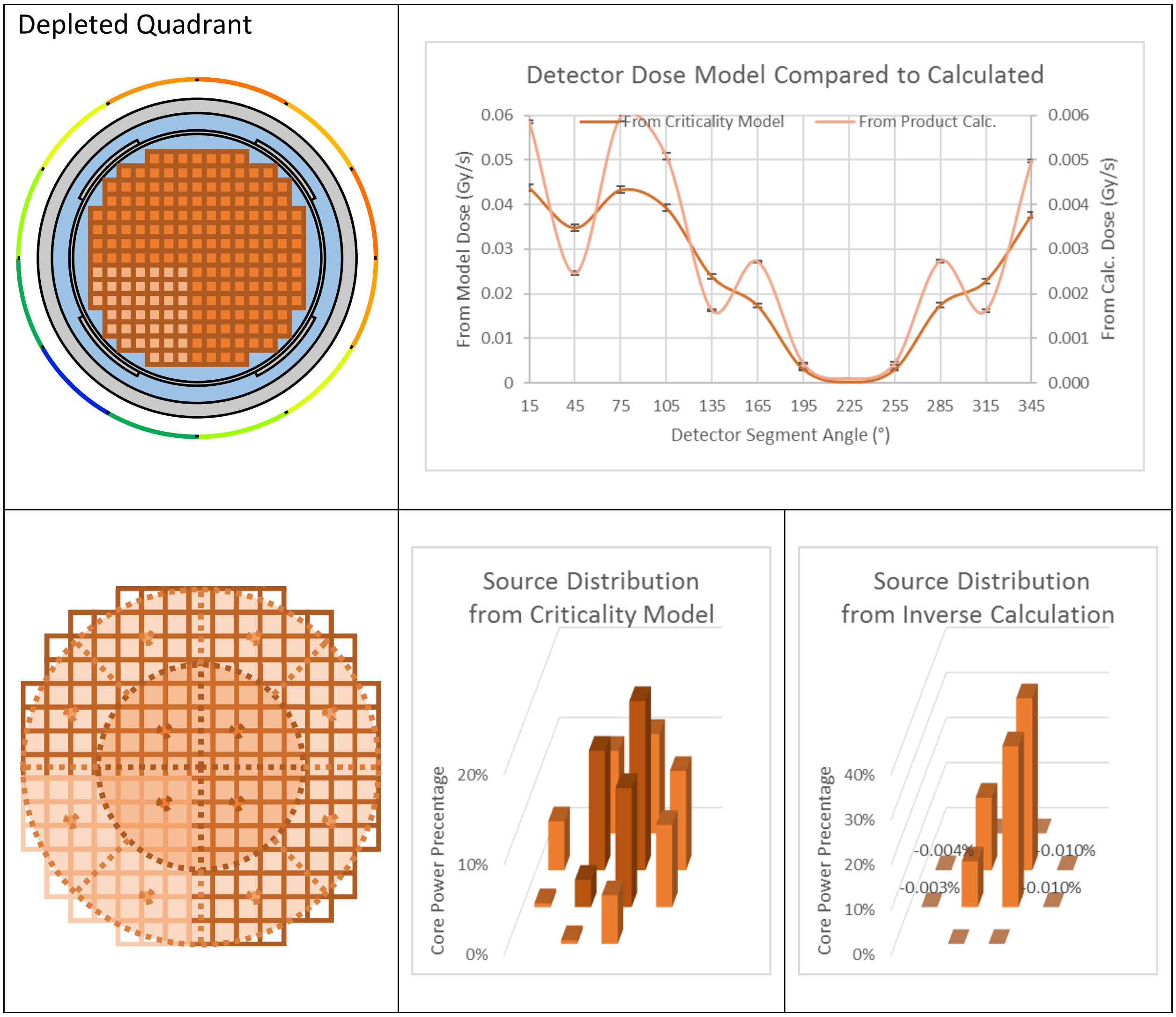

Figure 2.26: Depleted Quadrant Case, 12 Source Point Characterization

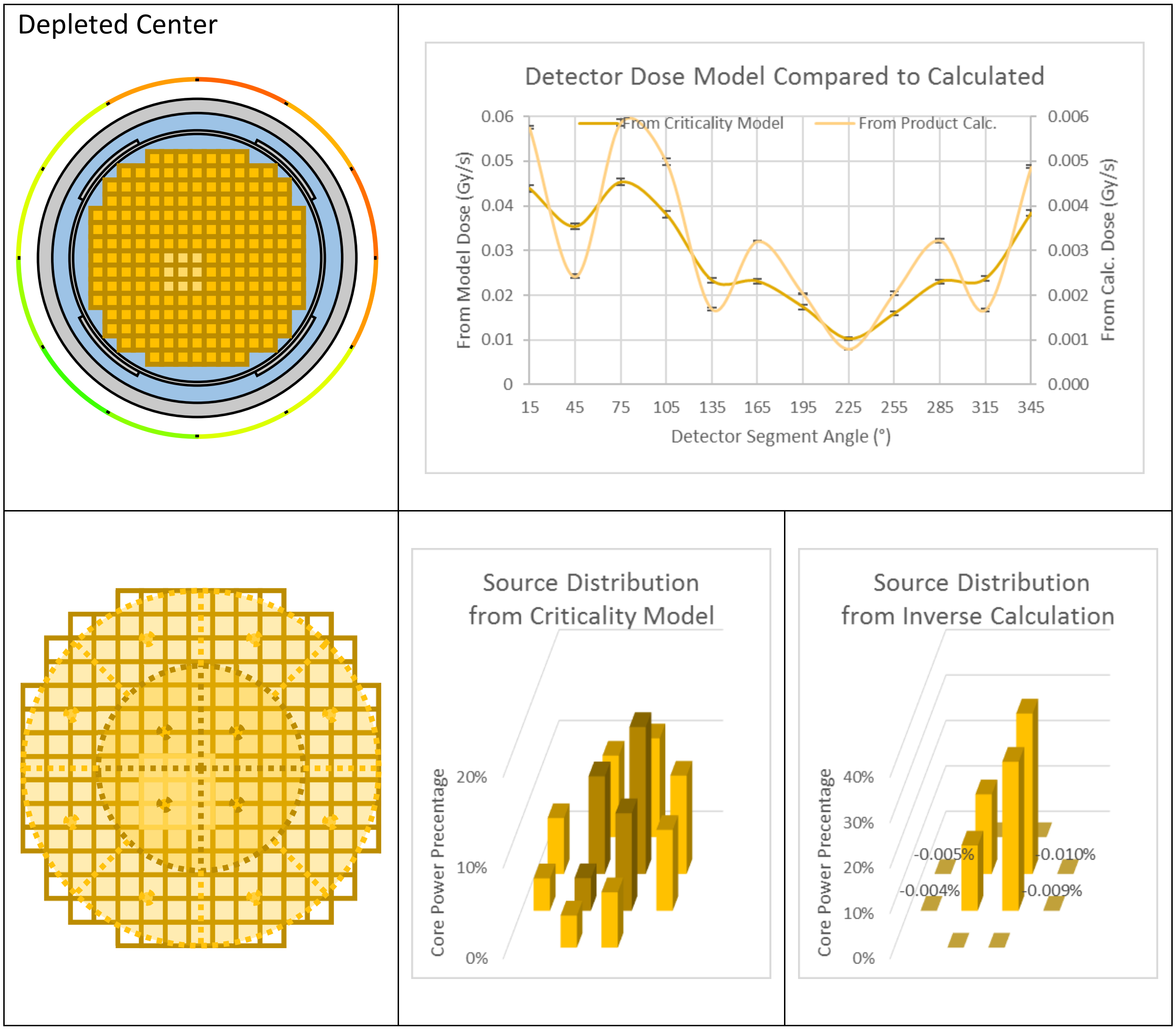

Figure 2.27: Depleted Center Case, 12 Source Point Characterization

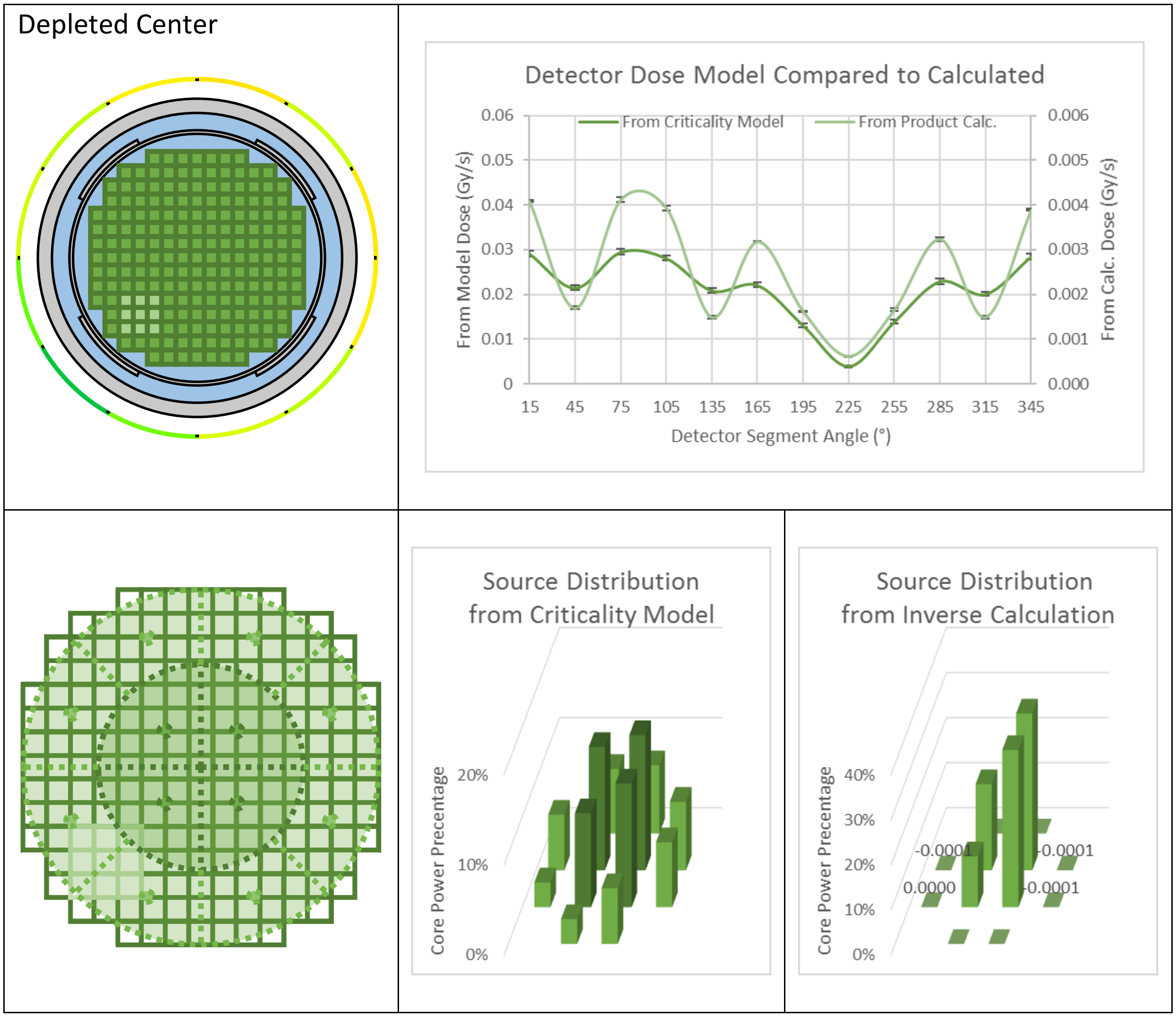

Figure 2.28: Depleted Periphery Case, 12 Source Point Characterization

Although with 12 characterization points the magnitude comparison of dose distribution improves, it does not offer improvement over the 4 point models for source reconstruction. Averaged over the entire quadrant, the solution from the inverse formula recognizes which quadrant has the depleted zone, but is not able to accurately attribute dose between the two different radii. The outer radii often even are calculated to be a negative source according to the inverse formula. Negative results for either dose or source are not possible physically so this shows how the inverse formula algorithm can fail, suggesting the need for an alternative algorithm going forward that solves only for a positive solution set. This ability is offered by the regression technique, Non-Negative Least Squares.

In conclusion, the 12 source point characterization demonstrates the necessity of the attenuation factors to account for the core geometry. It shows improvement in capturing the core geometry, acknowledging that the highest detector dose for a 30° detector segments does not correspond to the hottest core region. Yet the reconstruction technique is not able to correctly account for the source magnitude and the inverse application creates nonsensical negative solutions. Closing the gap between the dose distribution of the model compared to calculated from the attenuation factor matrix is essential to provide appropriate reconstruction. For this purpose, a better point characterization is needed. It should then make sense that there is a need for further models with more points. The expectation being that a higher resolution representation of the core offers a better implementation of the source point reconstruction method.

2.5 Reconstruction with 8th Core Models

2.5.1 Introduction

For the goal of higher resolution characterization of the core, it made sense to take advantage of the symmetry of the core. The modelling software (MNCP) is capable of using what is called a "reflective" boundary. This essentially mirrors the boundary of the model so that the simulation would yield the same results on either side of the boundary. Since the reactor core model has 8th core symmetry, a reflective boundary at 0° and 45° creates in principle a full core. The advantage of reducing the model size is that it increases the probability of a score in the detector tally compared to if a full core geometry was used. For an 8th core model, one can expect 8 times as many detector "hits" / tally scores of a particle. Figure 2.29 shows the model as an 8th core compared to the full core.

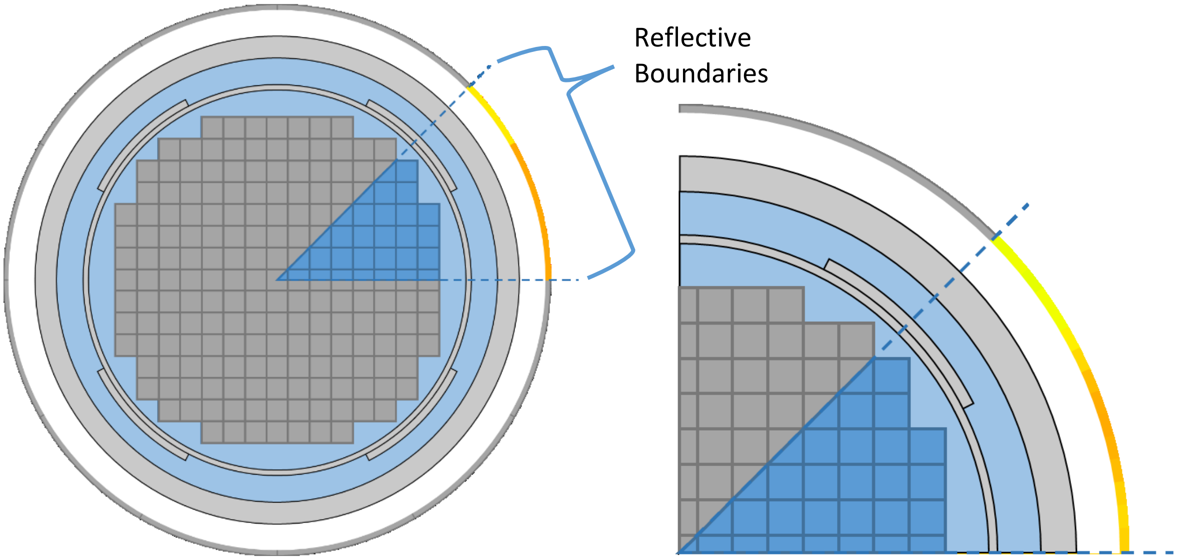

Figure 2.29: Reflective Boundary at 0° and 45°

2.5.2 15 Source Point Characterization Description

The next highest resolution and first model making use of 8th core symmetry was the 15 source point characterization. Similar to the previous 4 source point and 12 point characterizations, each point location was selected such that it could be considered representing an equal amount of core area. The innermost radius had 1 source point, while each additional radius had an additional point. Figure 2.30 shows this characterization.

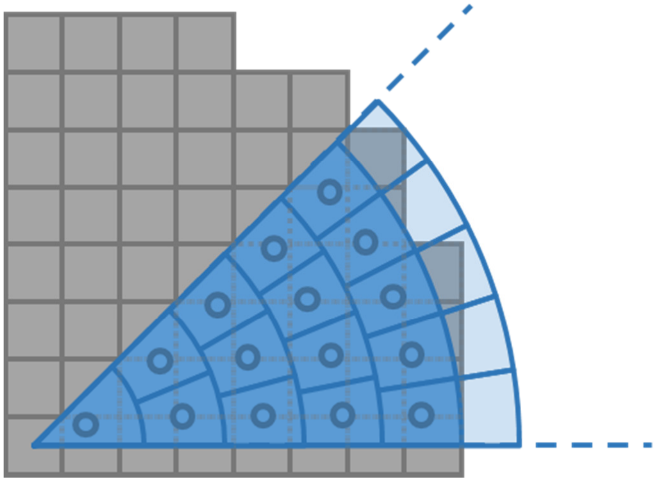

Figure 2.30: 15 Source Point Characterization

Because of the 8th core symmetry, this characterization is indeed a very significant increase in resolution than the previous full core 12 point version. The equivalent full core model of the 15 source point would instead be an 120 point characterization, a factor of 10 higher resolution. This depiction is shown as follows:

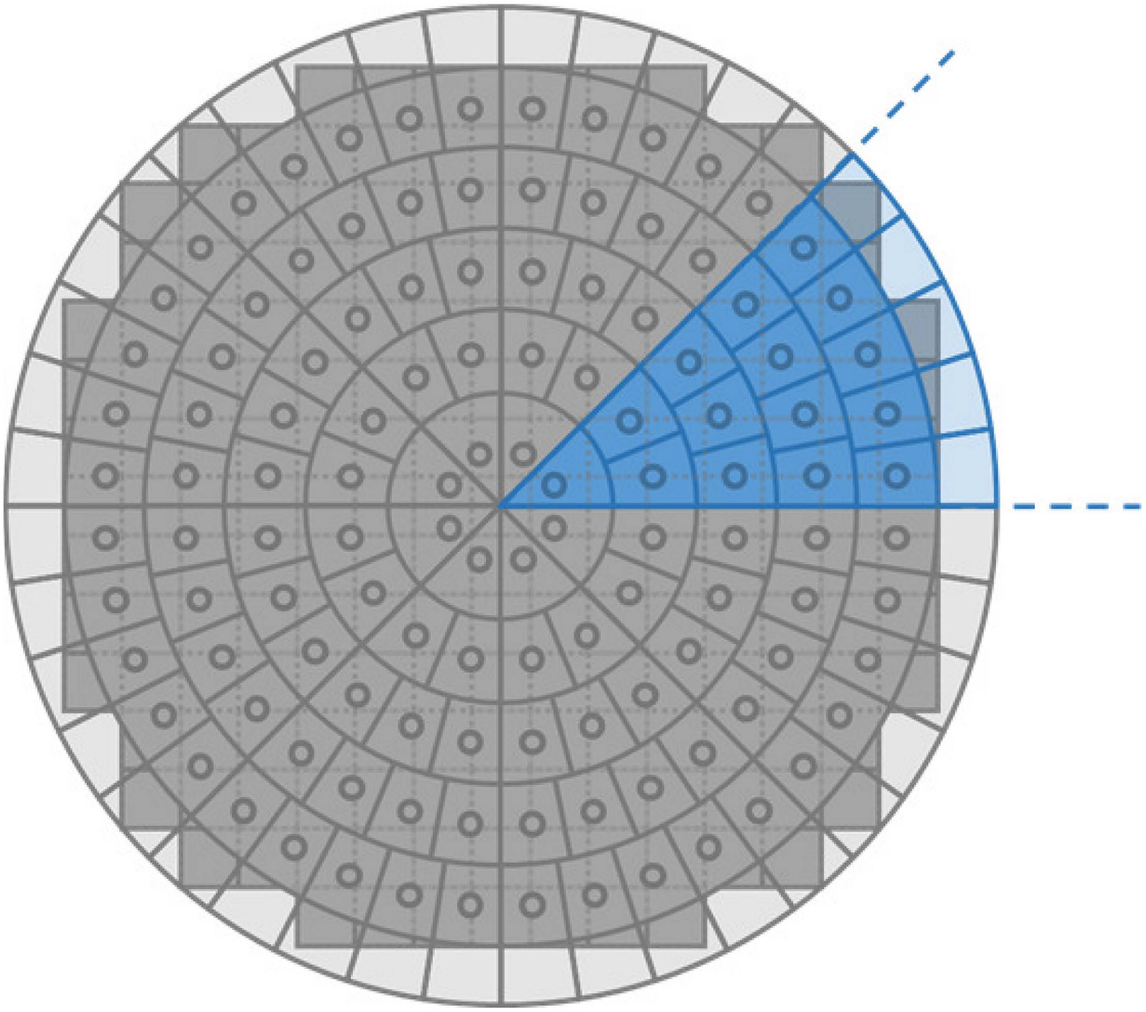

Figure 2.31: Full Core Depiction of Repeated 8th Core Symmetry with 15 Source Points

The decision was made to have the outermost radius be the same dimension as the core width. Because the core assemblies are square, there is no radius that has a uniform fuel geometry at the outer most periphery. At the radius equal to the core width, the outermost point is 7 ½ fuel assembly pitches from the center. Conversely, the outermost point of the whole core is 6 ½ assembly pitches from the center horizontally and 5 ½ pitches from the vertical center. This outermost radius as shown in Figures 2.30 and 2.31 is drawn with sections that are transparent while the core width radius (5th radius from center) has sections that are colored solid.

This 5th radius group of sections is the outermost radius that contains source points but it does not cover the core in its entirety. To account for the additional power generated by the core portion outside the source point radius group, these points were shifted off center according to their combined power needed to be represented. In this first set of formulas, it is defined the amount of power represented by the displacement of the source point to a given radius.

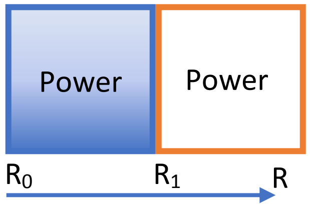

$$Power = \int P_R \, dR$$

$$Power_1 = \int_{R_0}^{R_1} P_{1_R} dR$$

$$Power_1 = P_{1_R}[R_1 - R_0]$$

$$P_{1_R} = \frac{Power_1}{[R_1 - R_0]} = \frac{Power_1}{\Delta R_1}$$

Figure 2.32: Power Represented by Source Point Displacement per Radius

In the case that the adjacent sections power has a zero value, it can be derived that the proper source point displacement to represent the middle of the geometry section should be the middle of the power producing section. This is shown in the following set of formulas.

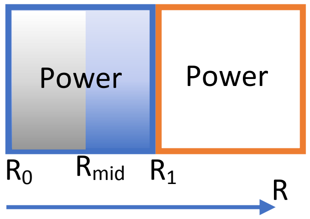

$$Power_{Mid} = \int_{R_0}^{R_{mid}} \frac{Power_1}{\Delta R_1} dR$$

$$Power_{Mid} = \frac{Power_1}{\Delta R_1}[R_{mid} - R_0]$$

$$Power_{Mid} = \frac{Power_1}{\Delta R_1}[R_{mid} - R_0] = \frac{Power_1}{2}$$

$$\frac{1}{\Delta R_1}[R_{mid} - R_0] = \frac{1}{2}$$

$$R_{mid} = \frac{\Delta R_1}{2} + R_0$$

Figure 2.33: Source Point Radius at Middle of Power Producing Region

For the source point radius location to account for an adjacent power producing region, the formula must then be modified accordingly to represent both regions. This modification is calculated by the following formula.

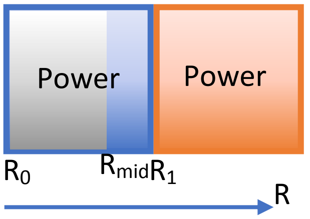

$$Power_{Mid} = \frac{Power_1 + Power_2}{2}$$

$$\frac{Power_1}{\Delta R_1}[R_{mid} - R_0] = \frac{Power_1 + Power_2}{2}$$

$$[R_{mid} - R_0] = \frac{\frac{Power_1 + Power_2}{2}}{\frac{Power_1}{\Delta R_1}}$$

$$R_{mid} = \frac{\frac{Power_1 + Power_2}{2}}{\frac{Power_1}{\Delta R_1}} + R_0$$

Figure 2.34: Modification of Source Point Radius for Adjacent Power Producing Region

Using this calculation, the 5th radius of source points was modified to be offset from the middle of the sections to instead account for the adjacent power producing outer assemblies.

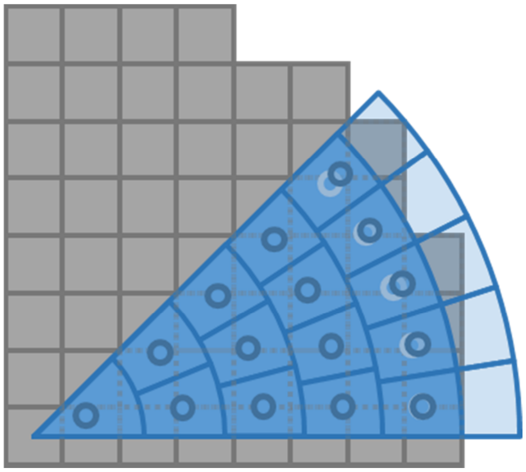

Figure 2.35: 15 Source Point Characterization with Modified 5th Radius Source Points

2.5.3 Attenuation Factors Grouped by Each Radius of 15 Source Points

The 15 source points could be grouped by which radius the points are located on. In Figure 2.36 it can be seen that there were a total of five radii, each with progressively one more point. Therefore, the first radius had only one point and the fifth radius had five points.

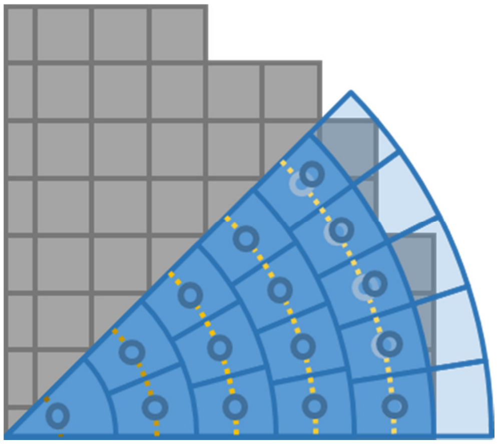

Figure 2.36: Grouped by 5 Radii for 15 Source Point Characterization

These attenuation factors were calculated in the same was the previous source point characterizations. A difference here being that although for the 8th core model a score in the detector tally was 8 times more likely than with the full core, the higher resolution models included points that are very far into the interior of the core. These simulations became difficult when scores became a rare event. To get reliable statistics in this instance, models must be run with a very large number of particles. For the central source points, even 1 billion particles would not be nearly enough.

However, using variance reduction technique known as “Weight Windows” it was possible to obtain statistically reliable results for even the first and most central radius. This involved running iterations of the same simulation with each new iteration using the results of the previous one to optimize particle weights and favor tracks that will lead to a tally score. Significantly better tally statistics could be achieved in this way by increasing the number of scores thereby decreasing the calculated variance. Although using multiple iterations of lengthy simulations is very time consuming, it did provide for results with optimal statistics which would not be possible if the model was run with no variance reduction. An example of the improved results can be seen in Figure 2.37 for one of the interior points (point 2 of radius 2).

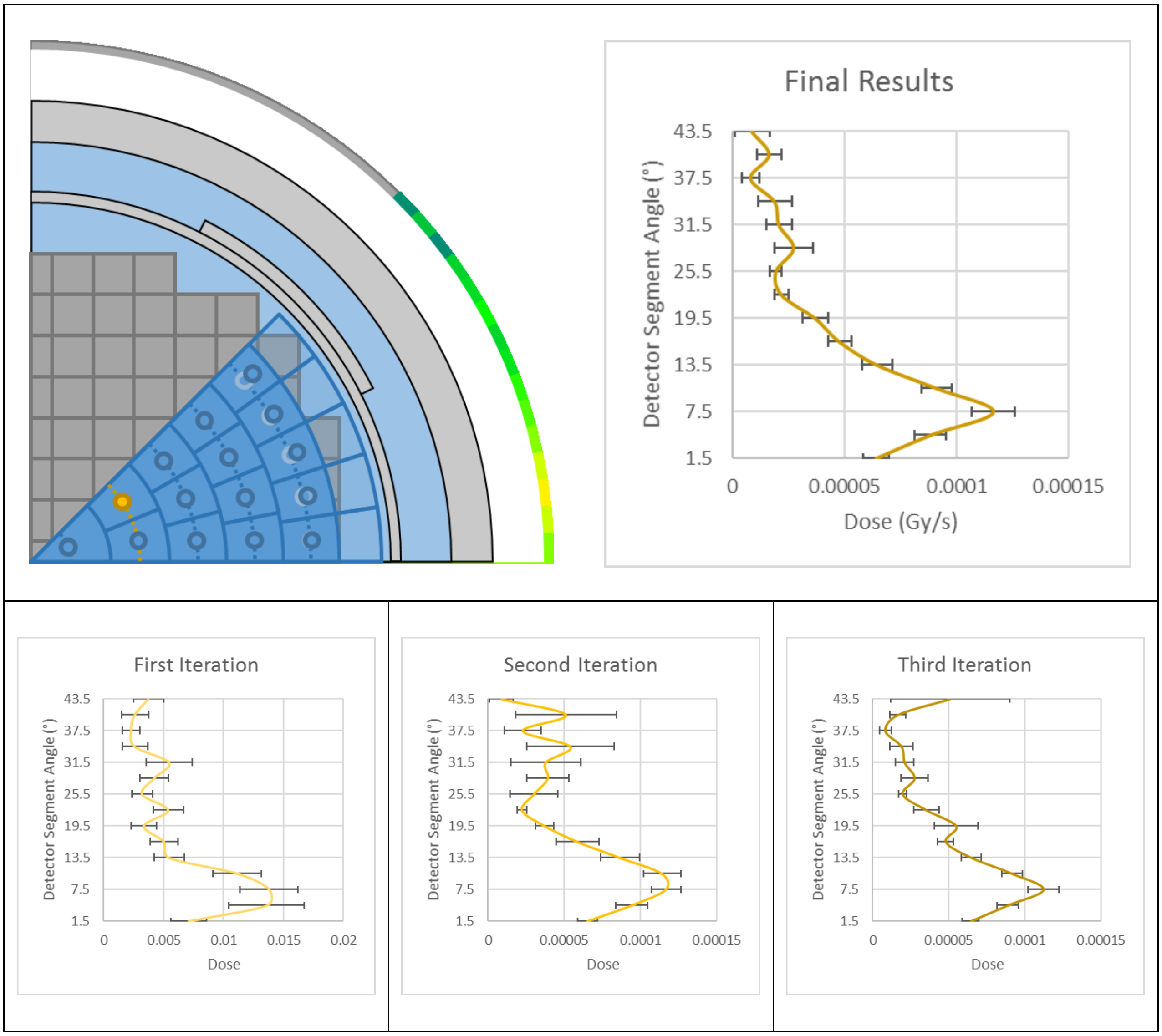

Figure 2.37: Results from Iterations on Variance Reduction Models for Source Point 2 of Radius 2

In the example of Figure 2.37, it should be noted that the dose obtained was much larger (by around a factor of 100) for the first iteration than the subsequent 2 iterations and the final result. This was due to modifying the density of the reactor pressure vessel (RPV) material such that it was decreased by a factor of 10. The RPV is essentially a steel wall nearly 8 inches thick so decreasing the material's density to less than the density of water provided for a much greater number of particles to penetrate the wall and reach the detector. Although the tally results were then completely inaccurate, it provided a first iteration of the geometry-based weight window variance reduction technique which would lead to useable results in subsequent runs having the RPV at its actual density.

Results were deemed acceptable when the dose distribution had continuity, i.e. without large fluctuations or high frequency oscillations caused by statistical noise. This required each point's result to be plotted and reviewed individually as can be seen in appendix chapter *A2.1.2 15 Source Point Characterization*. In general, results were obtained with the same level of difficulty when grouped by the same radius. This is as could be expected because each successive radius group had shorter and shorter paths through the reactor core geometry than the radius group before it. The shorter paths belonging to outer the radius groups would then need either less iterations or less simulated particles or both. Figure 2.38 displays this comparison for the number particles needed for the different radius groups.

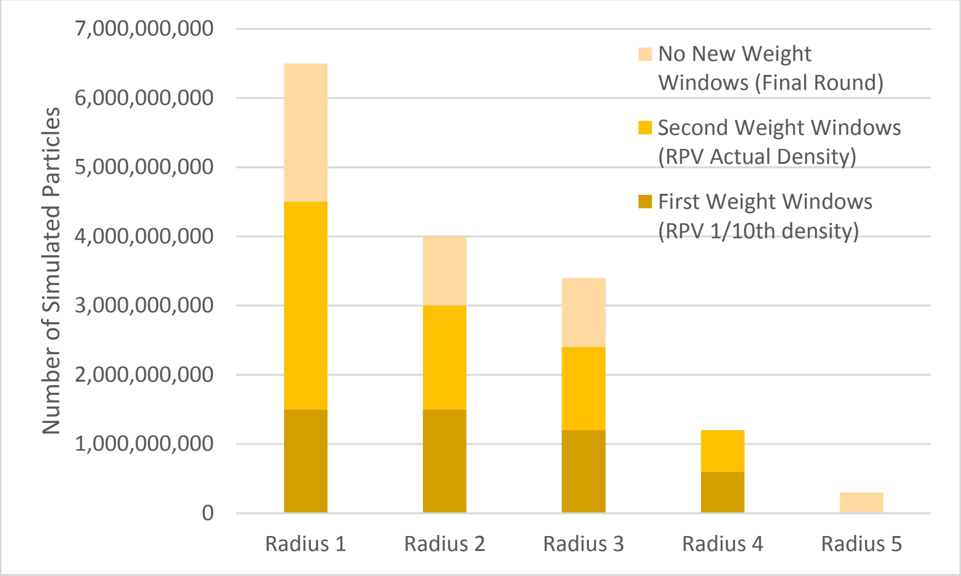

Figure 2.38: Number of Simulated Particles for Each Radius Group

Radius 1 was clearly the most difficult results to obtain, as can be expected since it has the farthest path through the reactor core. Similarly, the dose for radius 1 was at the lowest level of all models. To compare dose overall, the dose distribution for each source point and all the points in each radius group can be averaged together which is plotted in Figure 2.39. This figure shows the average dose for each radius group differs by around 1 order of magnitude respectively.

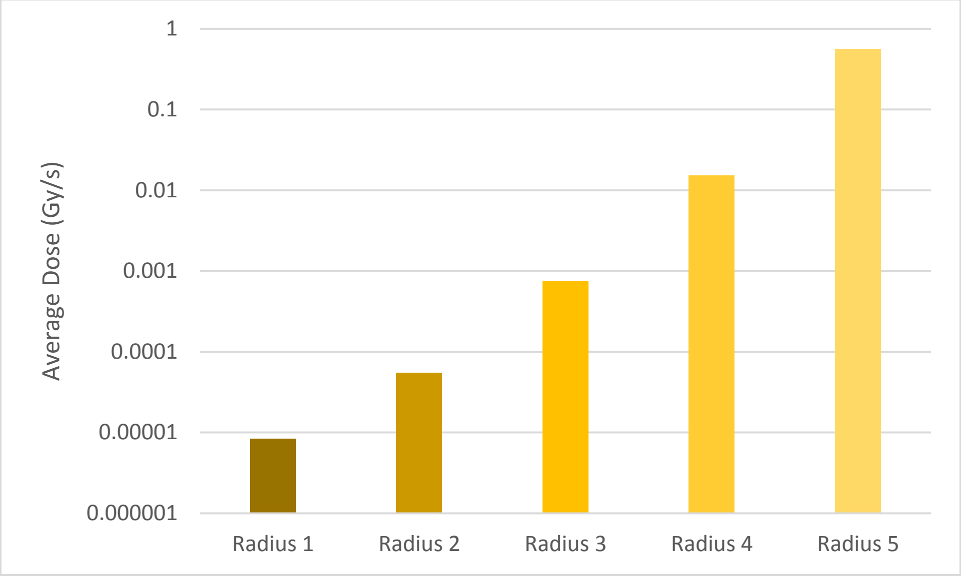

Figure 2.39: Average Dose Grouped by Radius for 15 Source Point Characterization

2.5.4 Results for 15 Source Point Characterization

Similar to the full core 4 point and 12 point source characterizations, the same equations apply for source reconstruction but just take larger indices:

Product Formula:

$$D_{15} = K_{15 \times 15} * S_{15}$$

Inverse Formula:

$$S_{15} = K^{-1}{}_{15\times 15} * D_{15}$$

In addition to the source reconstruction with the inverse formula, the non-negative least squares (NNLS) was used as well as its counterpart which includes the epi-thermal and fast neutron bins in addition to the gamma results (NNLS (G,N)). The results of the product formula can be compared to the criticality model results for detector dose distribution to investigate if the 15 source point characterization is an adequate representation of the model. This result for the full core case is displayed in Figure 2.40.

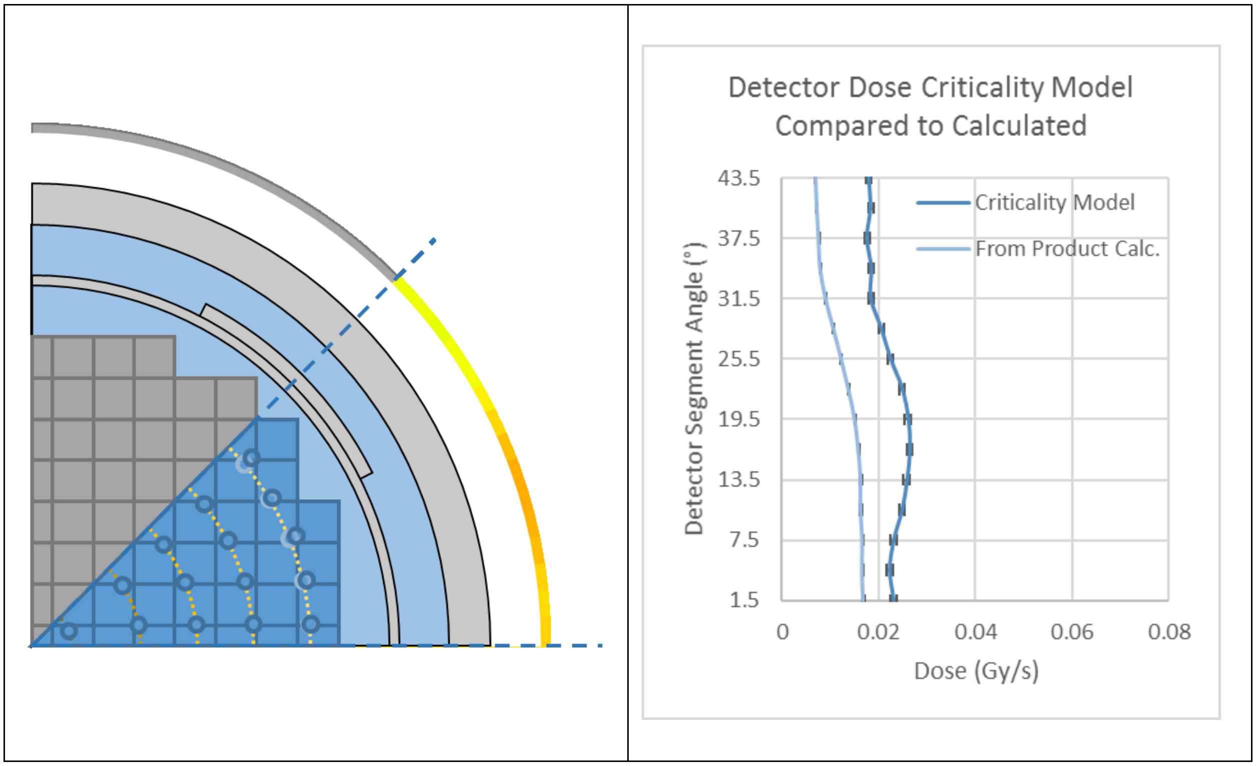

Figure 2.40: Detector Dose Distribution Calculated by Product Formula Compared to Criticality Model for Full Core Case, 15 Source Point Characterization

Although the distribution calculated by the product formula did not match the criticality model, they are for the first time on the same order of magnitude to each other. This was not true for the full core characterizations of 12 point and 4 point characterizations which were calculated as 1/10th and 1/30th respectively. The source distribution from the criticality model is displayed in Figure 2.41.

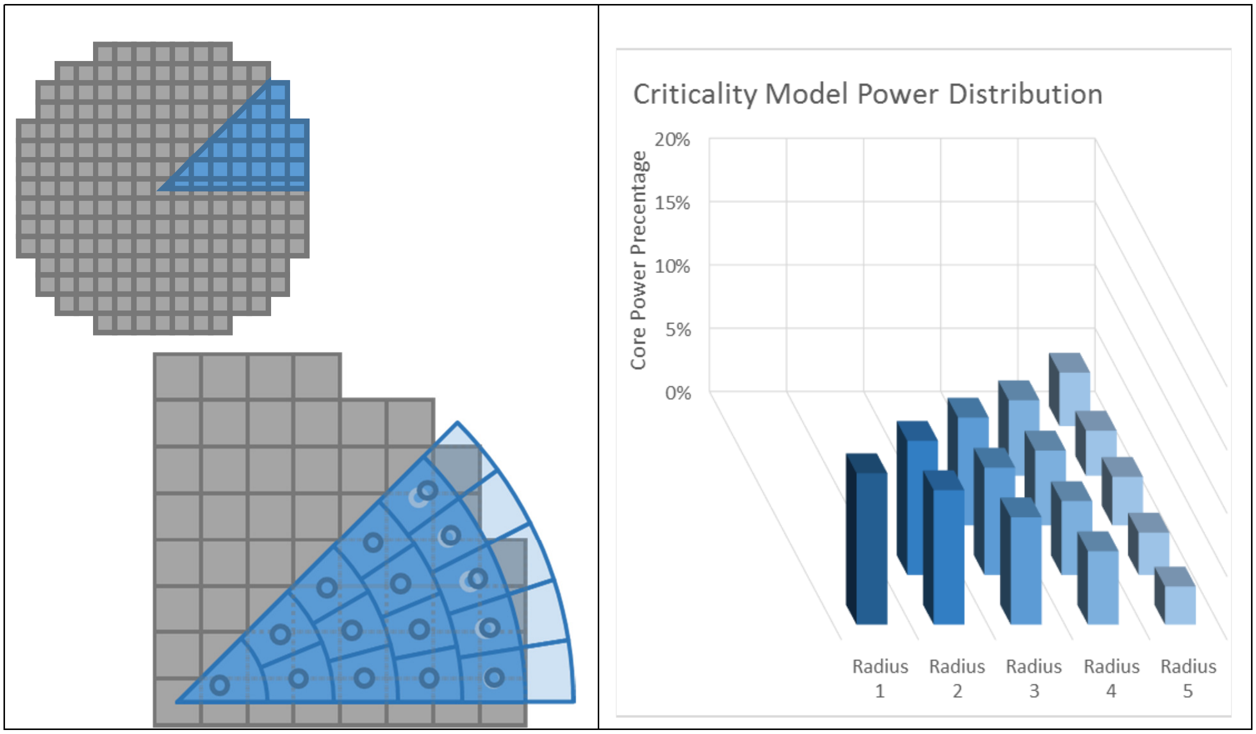

Figure 2.41: Source Distribution from Criticality Model for Full Core Case, 15 Source Point

Because the product formula calculation of the dose distribution did not match the criticality model, it could not be expected for the reconstruction of the source to be accurate. This was indeed true with the results to be seemingly random source distributions for all solution techniques (inverse formula, NNLS, and NNLS (G,N)). The results were averaged by radius group for easier comparison, yet still there was seemingly no discernable pattern. These results are displayed in Figure 2.42.

The results for the other cases are similar, being that the product formula calculates a detector dose distribution on the same order of magnitude but does not match well enough to provide for an accurate source reconstruction. These results are displayed in Figure 2.43 thru 2.48.

Figure 2.42: Source Reconstruction Results for Full Core Case, 15 Source Points / 5 Radii

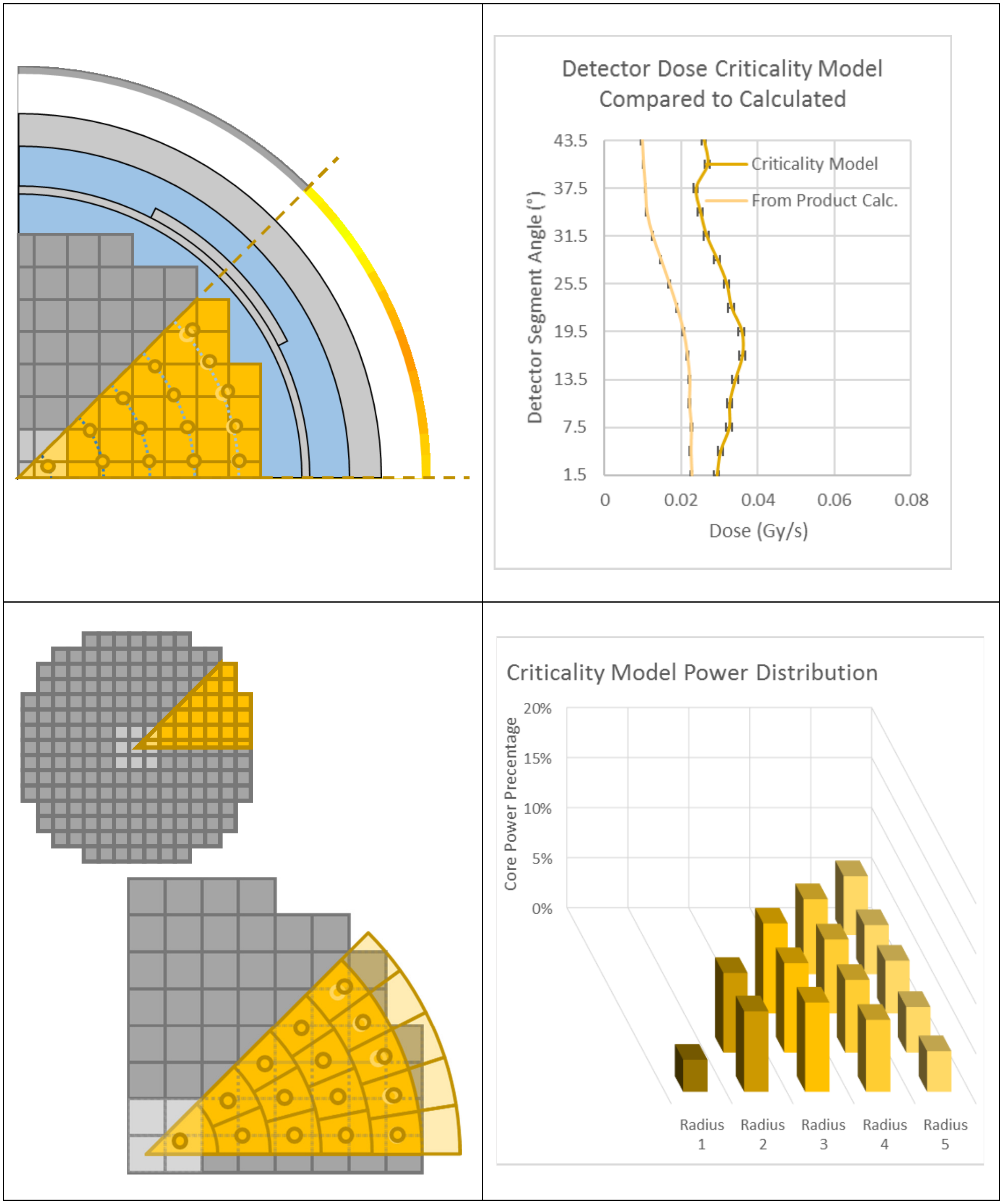

Figure 2.43: Criticality Model Results for Depleted Center Case and Product Formula Calculation Comparison, 15 Source Point Characterization

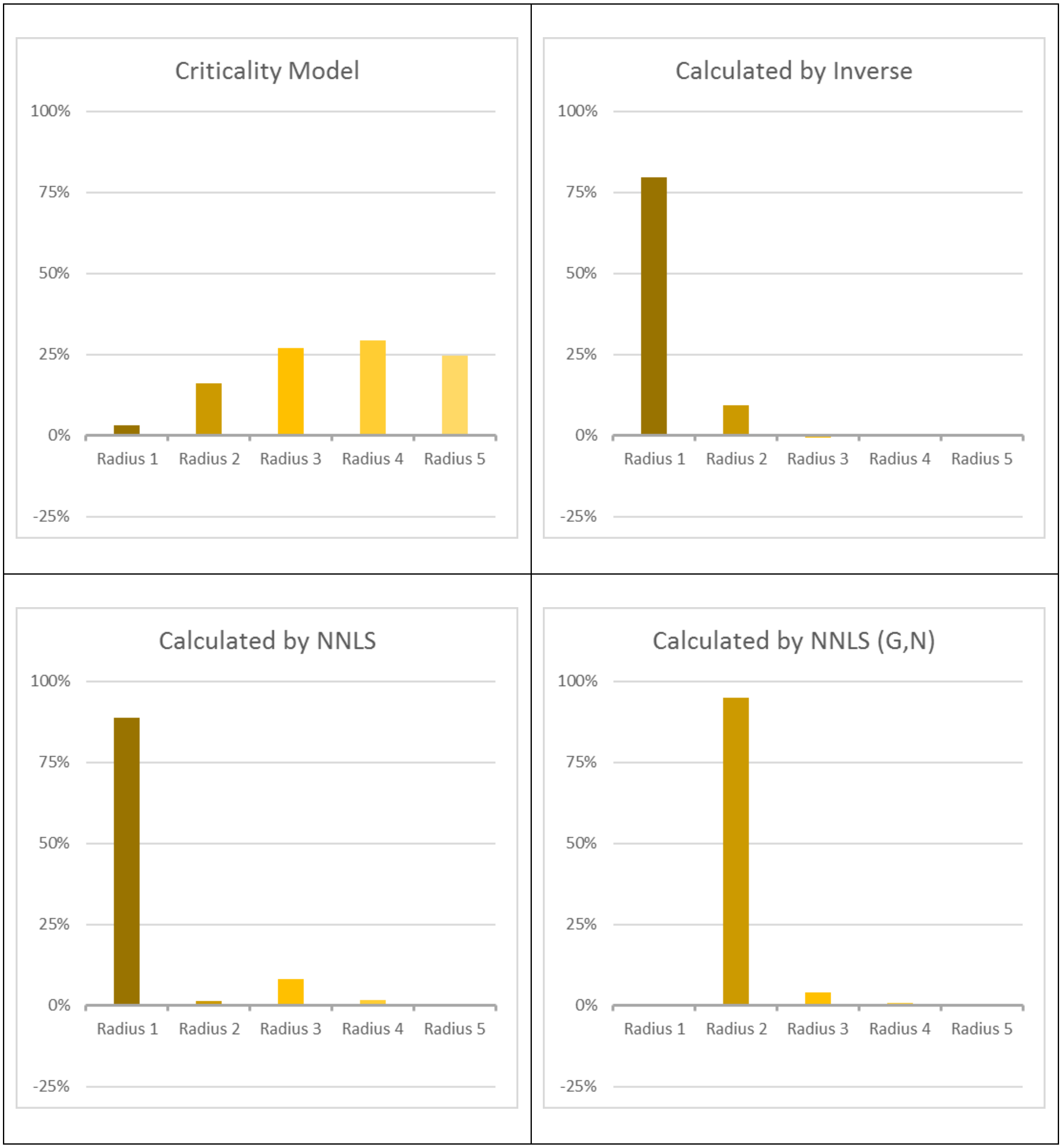

Figure 2.44: Source Reconstruction Results for Depleted Center Case, 15 Source Points / 5 Radii

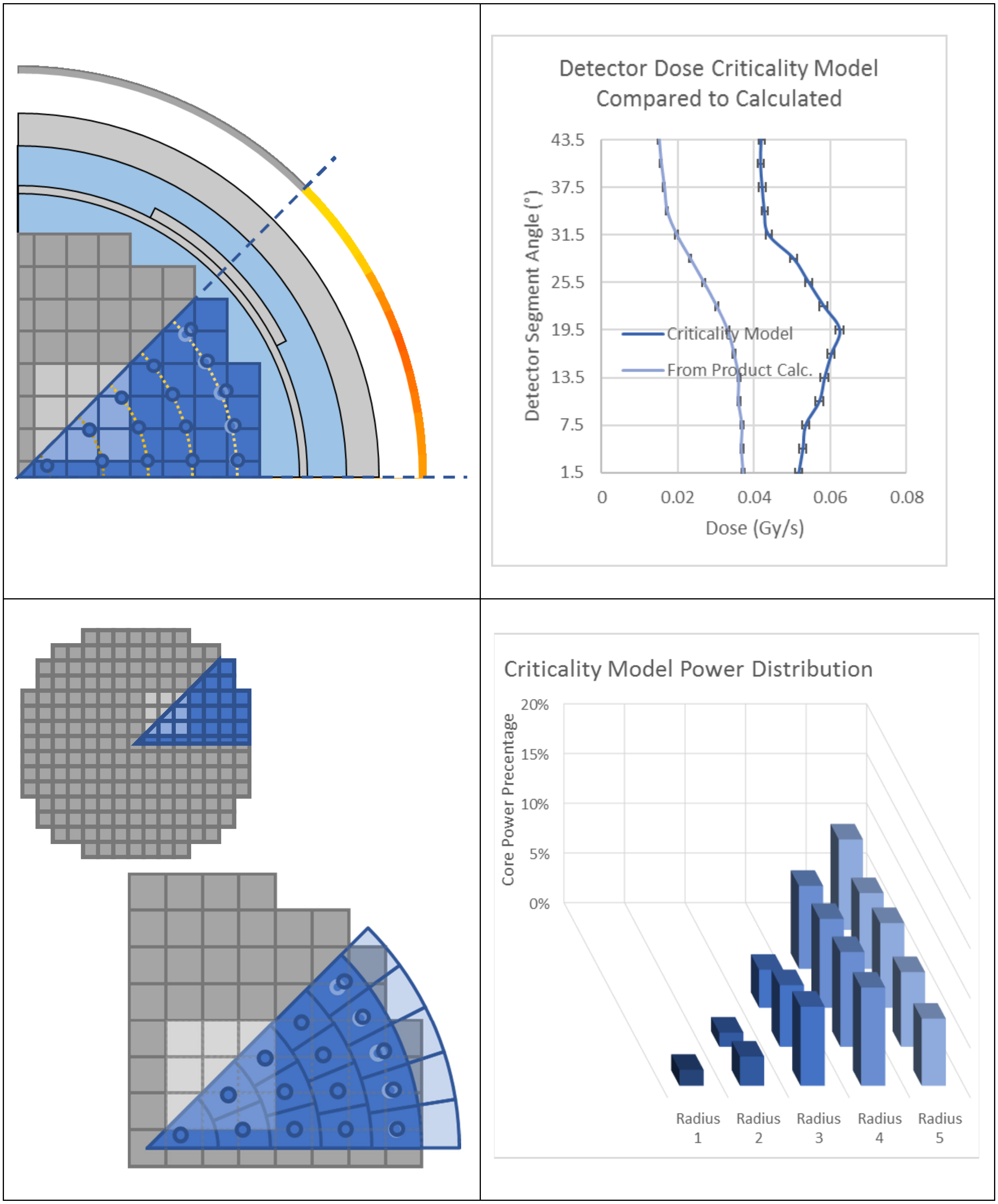

Figure 2.45: Criticality Model Results for Depleted Interior Case and Product Formula Calculation Comparison, 15 Source Point Characterization

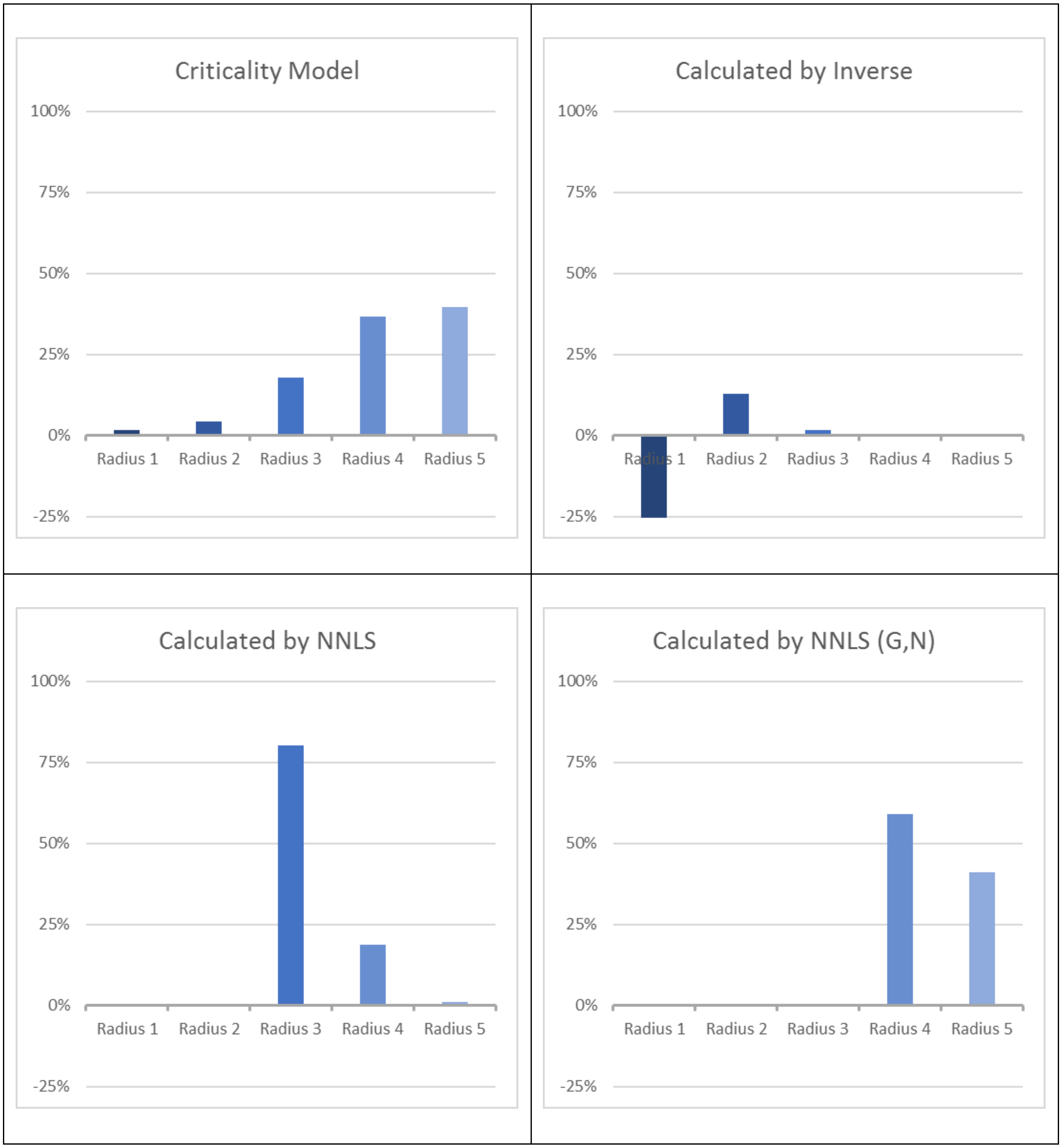

Figure 2.46: Source Reconstruction Results for Depleted Interior Case, 15 Source Points / 5 Radii

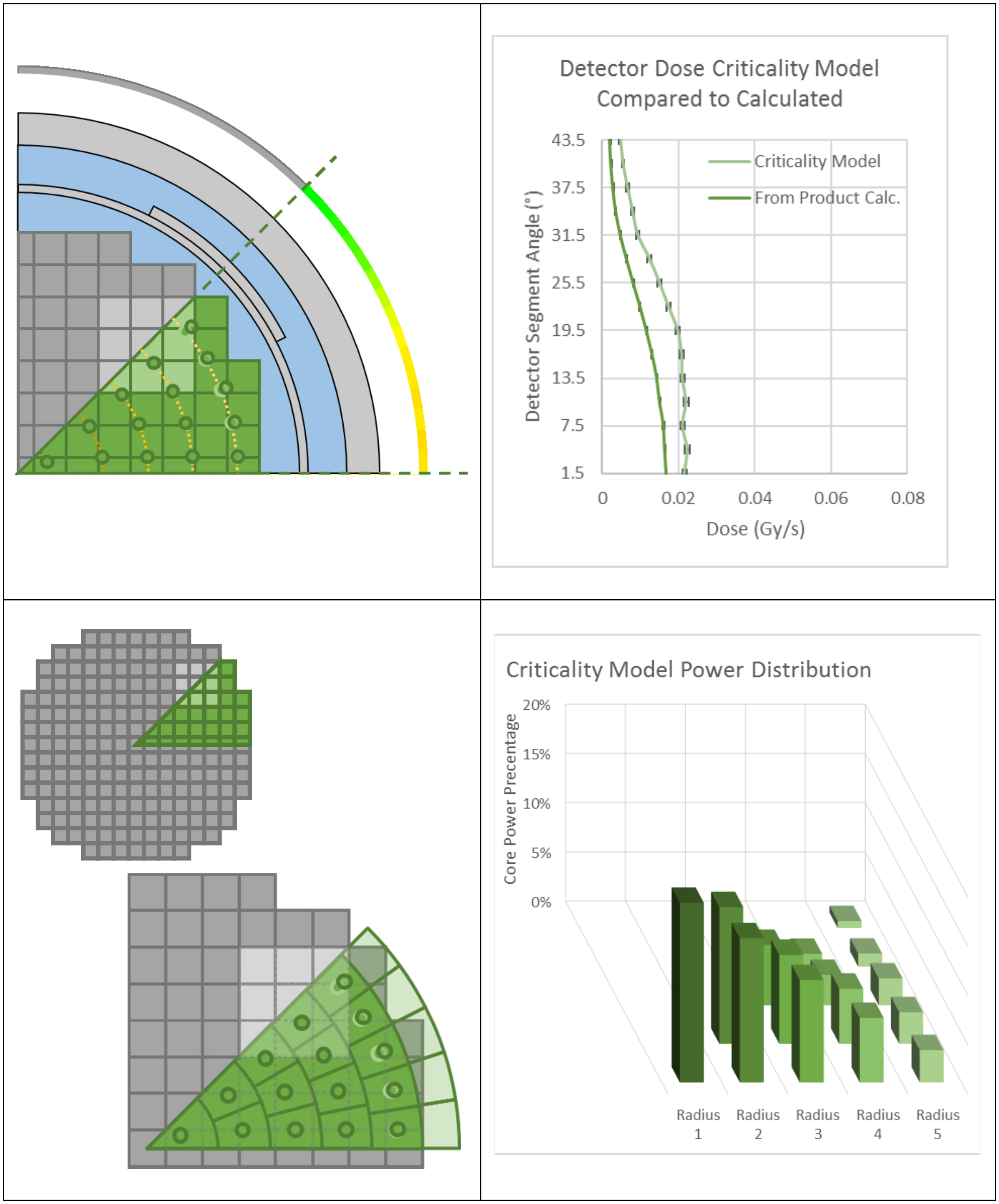

Figure 2.47: Criticality Model Results for Depleted Periphery Case and Product Formula Calculation Comparison, 15 Source Point Characterization

Figure 2.48: Source Reconstruction Results for Depleted Periphery Case, 15 Source Points / 5 Radii

2.5.5 Source Point Characterization Description

The next source point characterization had a significant increase in resolution, from 15 points to 45 points. Similarly, each successive radius group contained one more source point such that there were a total of 9 radius groups for a total of 45 points. The outermost group was adjusted according to the formula of Figure 2.34 as was done for the 5th radius group of the 15 source point characterization. A depiction of the 45 source point characterization with 9 radius groups can be seen in Figure 2.49.

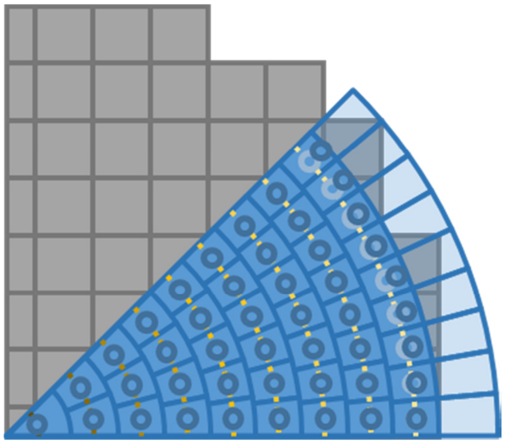

Figure 2.49: 45 Source Point Characterization with 9 Radius Groups

Attenuation factors for each source point had to be calculated by simulations. As was the case for the central source points in the 15 point characterization, the attenuation factors for the central source points of the 45 point characterization were difficult to obtain, requiring long simulations of large numbers of particles and successive iterations of the weight window variance reduction technique. Appendix chapter *A2.1.3 45 Source Point Characterization* displays each and every source point's attenuation factor result, all of which were checked for an acceptable level of continuity. In order to view the results as a whole, averaging the results of each radius group provides for comparison as displayed in Figure 2.50 that follows. Here it can be seen that each successive radius group has between one and one-half orders of magnitude difference.

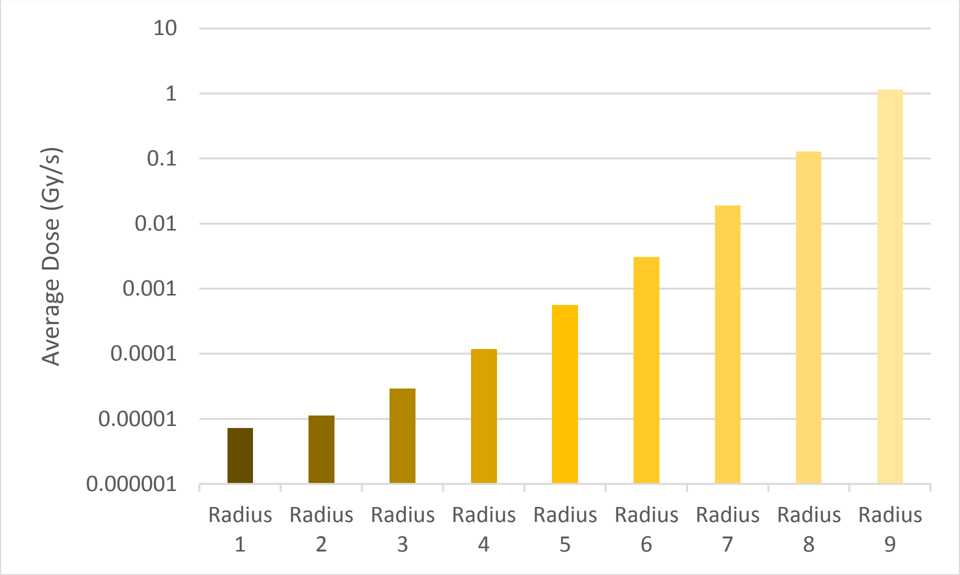

Figure 2.50: Average Dose Grouped by Radius for 45 Source Point Characterization

2.5.6 Results for 45 Source Point Characterization

The detector dose distribution was kept to 15 individual segments just as for the 15 source point characterization. This was useable for the product formula as follows:

$$D_{15} = K_{15 \times 45} * S_{45}$$

This formula can be solved just as the previous characterizations; however it was not possible to solve the inverse formula as before because the attenuation factor matrix (K term matrix) was not square (as in the row indices count does not match the column indices). A square matrix could be achieved by adding the epithermal and fast neutron bins instead of the gamma dose only as was done for the previous matrix inversion implementations. This provides the following set of formulas:

$$D_{Gamma_{15}} = K_{Gamma_{15\times 45}} * S_{45}$$

$$D_{Epithermal_{15}} = K_{Thermal_{15\times 45}} * S_{45}$$

$$D_{Fast_{15}} = K_{Fast_{15\times 45}} * S_{45}$$

Combining these 3 formulas provides for a K term matrix that is square (45 rows by 45 columns) and a detector distribution vector that is 45 rows matching the length of the source term vector. This allows the inverse formula to be calculated as follows:

Inverse Formula:

$$S_{45} = K^{-1}{}_{45\times 45} * D_{45}$$

Applying the product formula to the 45 source point characterization yielded similar results to the 15 point. The calculated dose distribution was again on the same magnitude yet was slightly closer to the results of the criticality model. This is seen for the full core case in Figure 2.51 together with the source distribution for 45 source points.

Since the detector dose distributions didn't match, as was the case for the 15 source point characterization, it could be expected that the source reconstruction would not work well. Indeed, once again, the solved source distributions were inaccurate and seemed to be a random set of results. The full core case results are seen in Figure 2.52. The results for the rest of the cases are seen in Figure 2.52 to Figure 2.58.

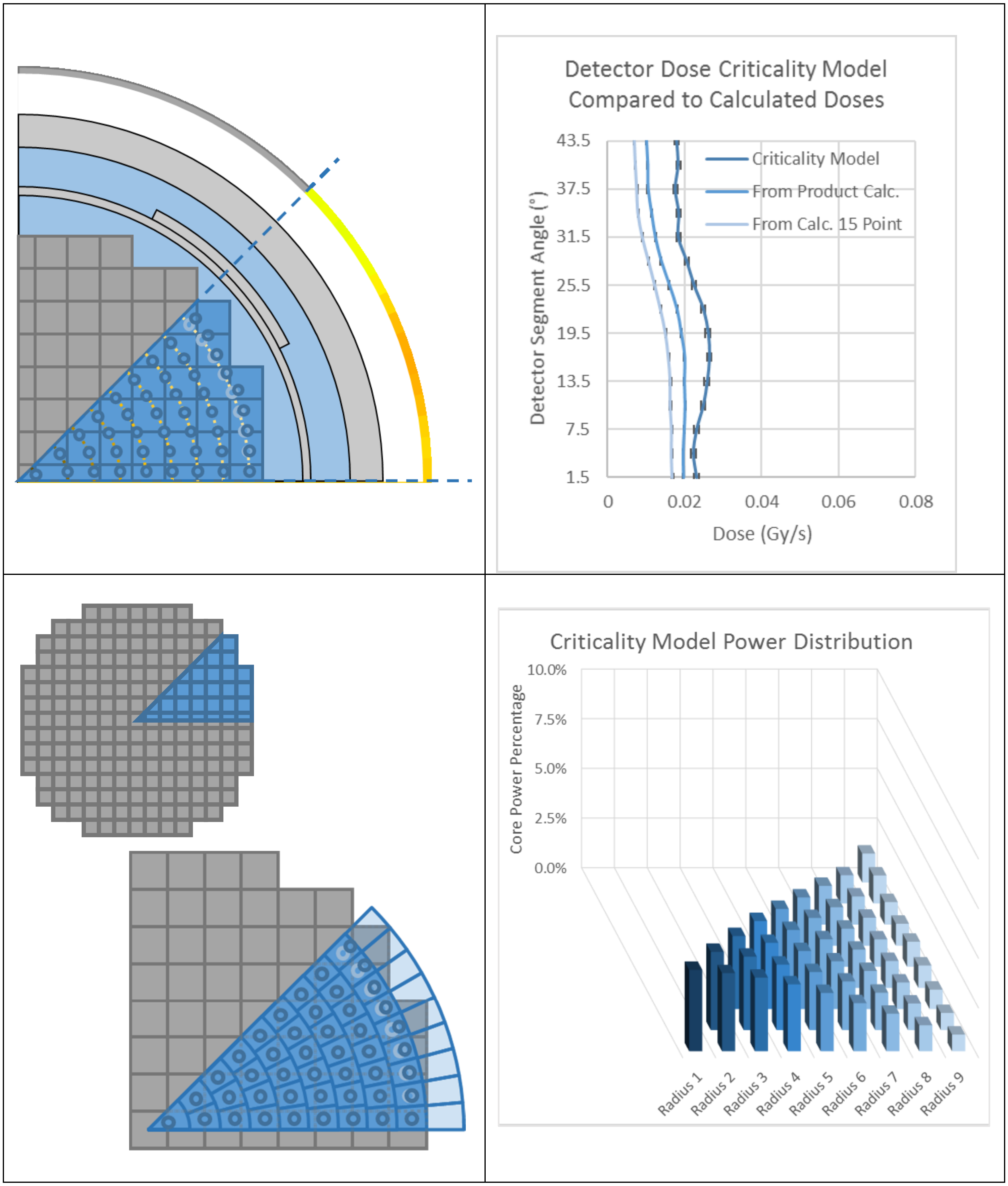

Figure 2.51: Criticality Model Results for Depleted Periphery Case and Product Formula Calculation Comparison, 45 Source Point Characterization

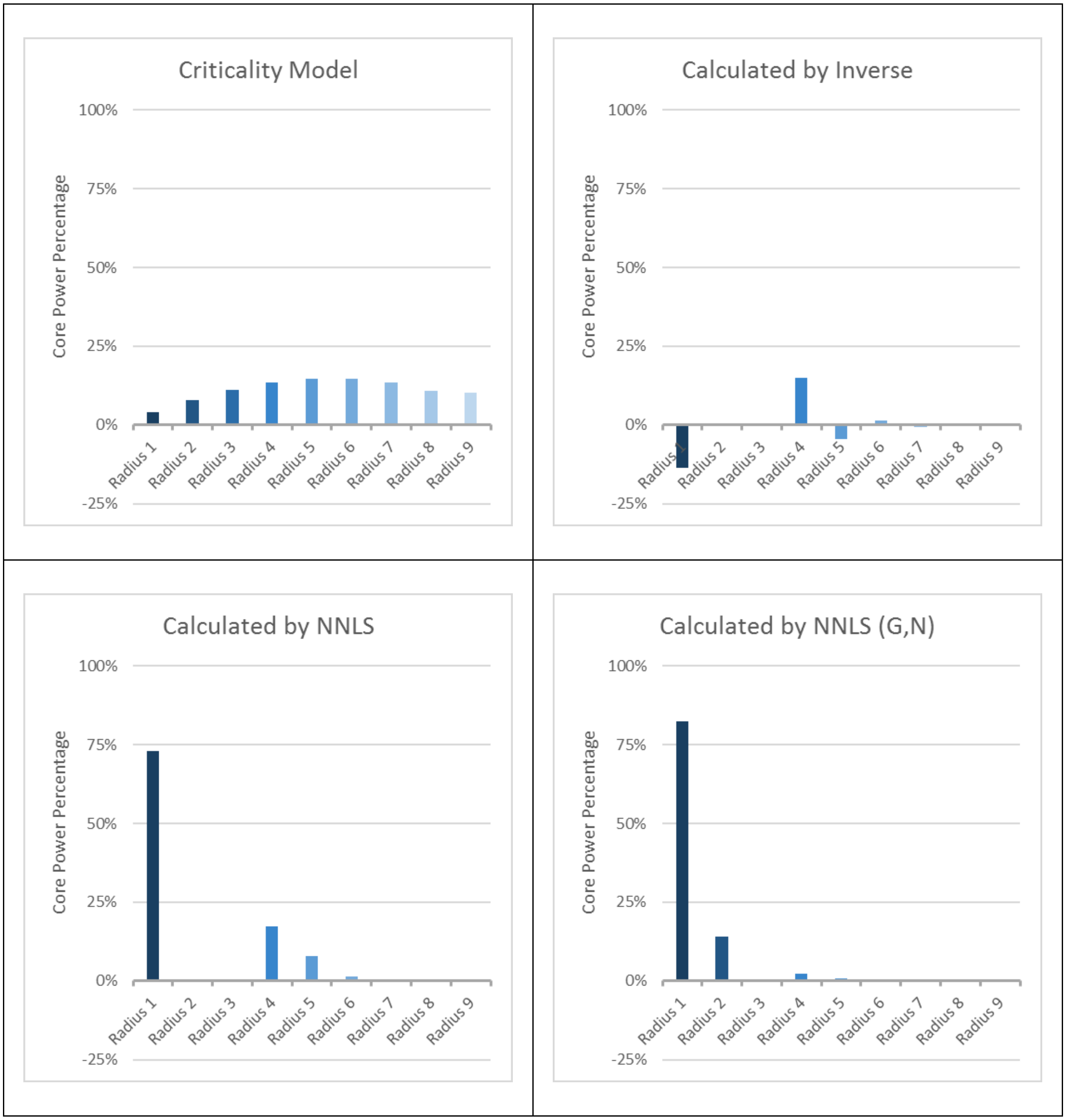

Figure 2.52: Source Reconstruction Results for Full Core Case, 45 Source Points / 9 Radii

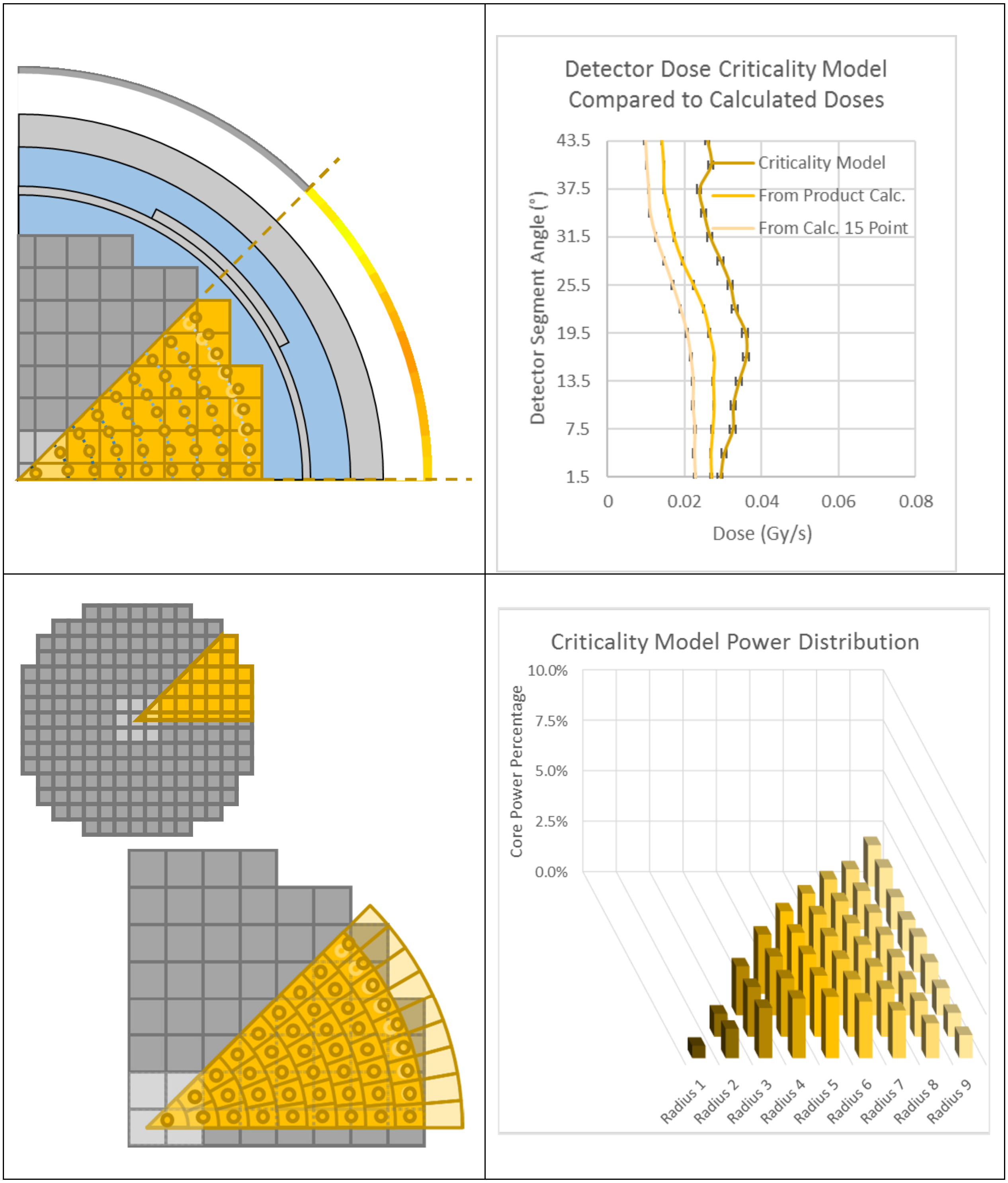

Figure 2.53: Criticality Model Results for Depleted Center Case and Product Formula Calculation Comparison, 45 Source Point Characterization

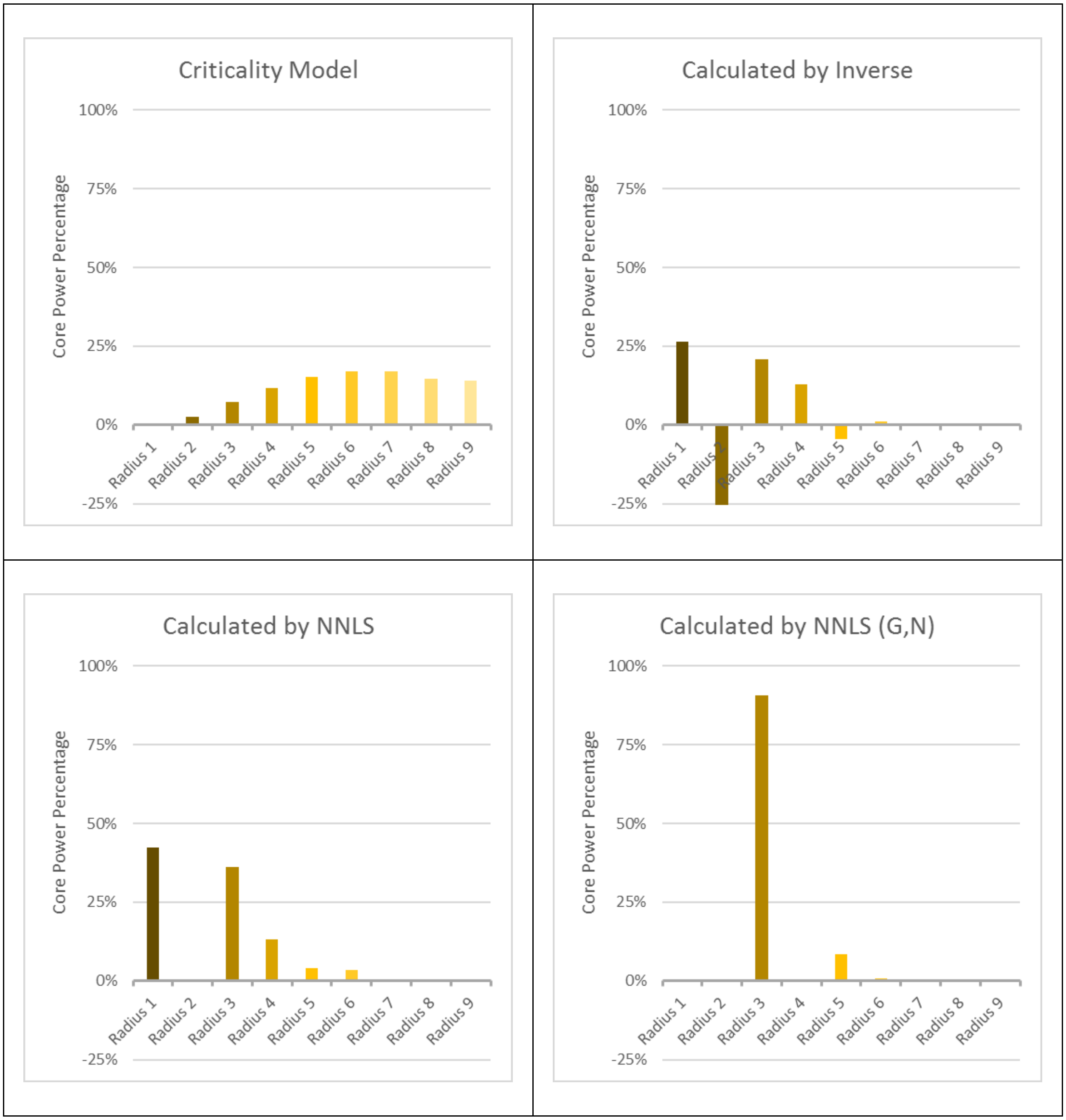

Figure 2.54: Source Reconstruction Results for Depleted Center Case, 45 Source Points / 9 Radii

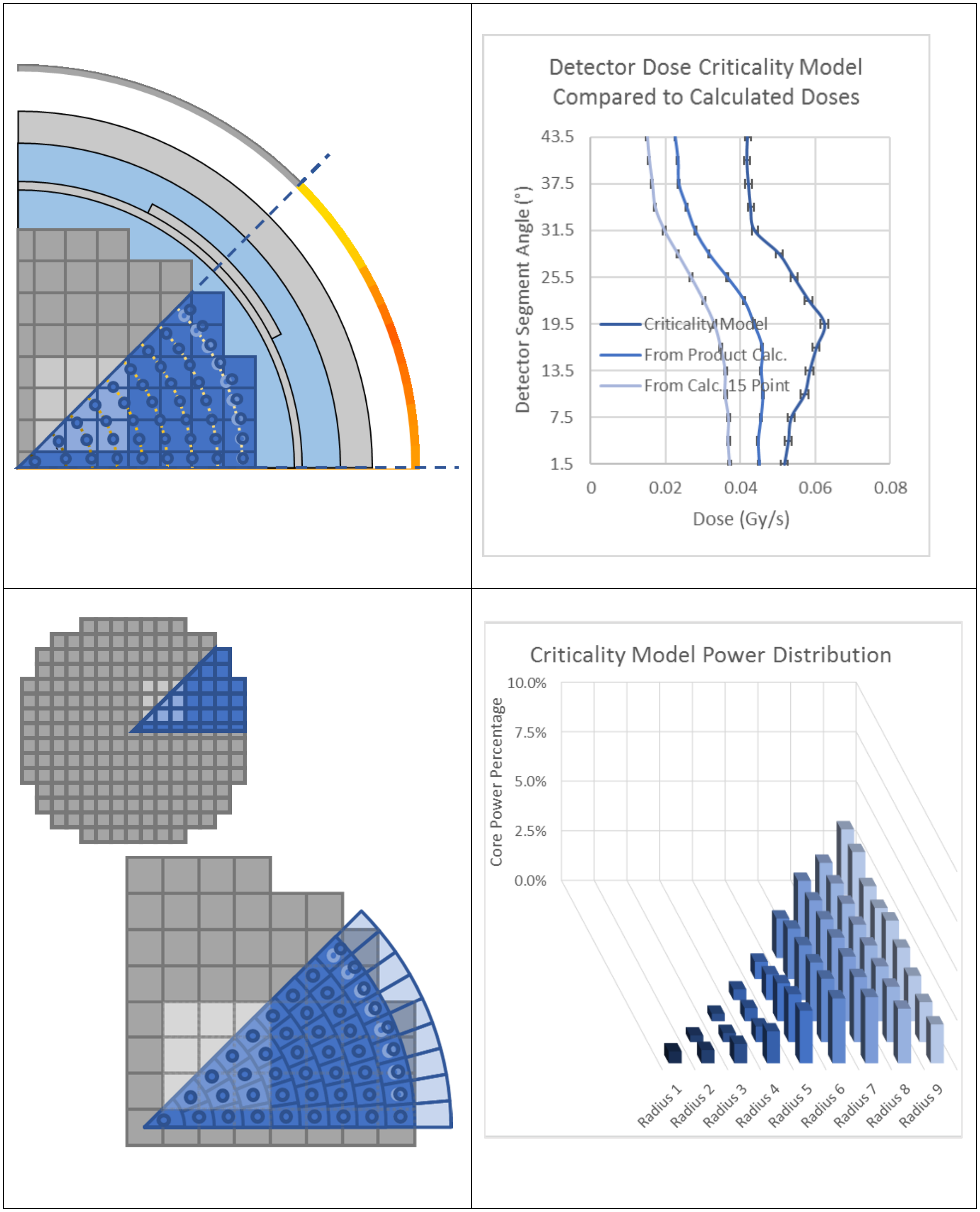

Figure 2.55: Criticality Model Results for Depleted Interior Case and Product Formula Calculation Comparison, 45 Source Point Characterization

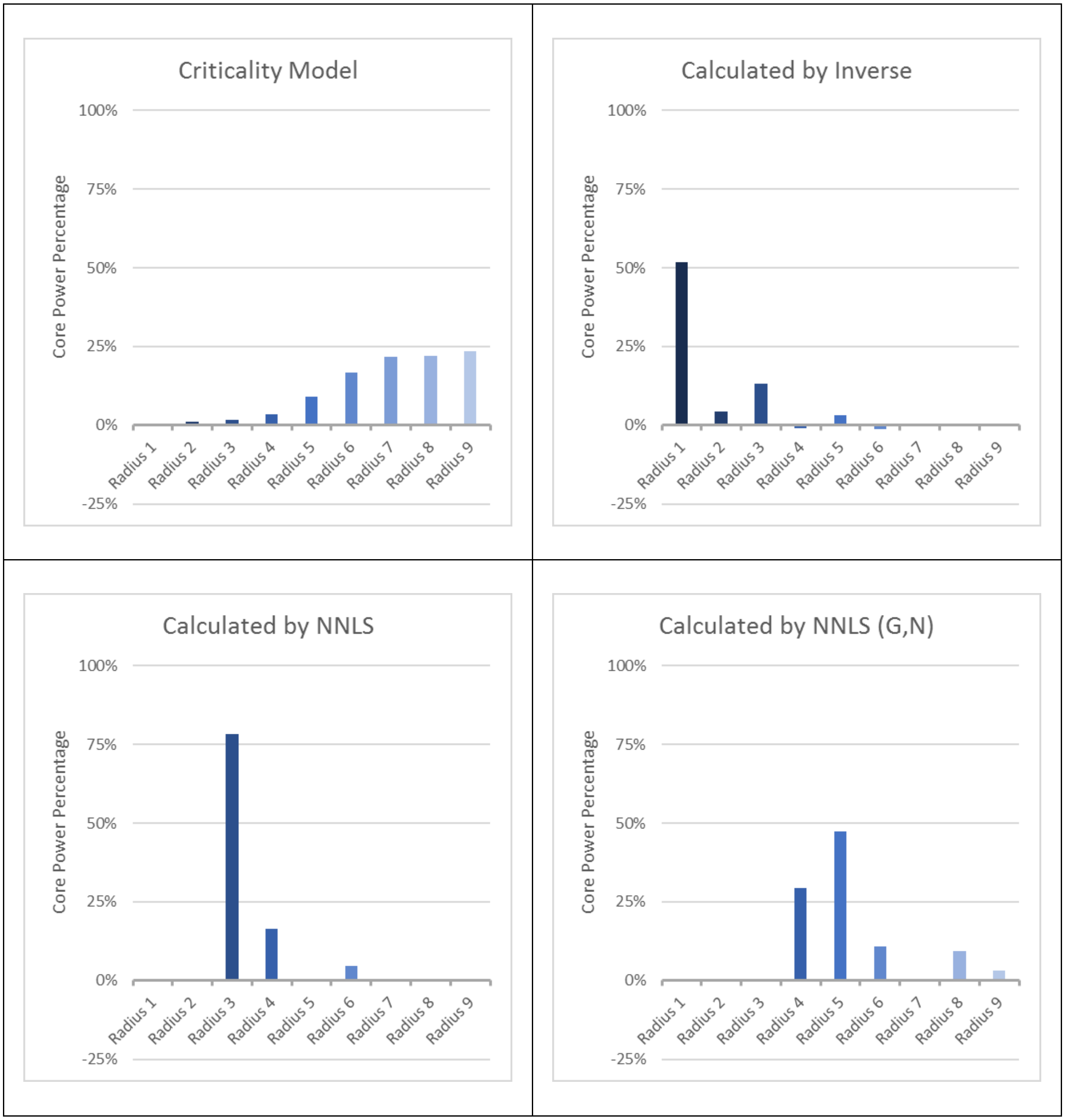

Criticality Model

Calculated by Inverse

Calculated by NNLS

Calculated by NNLS (G,N)

Figure 2.56: Source Reconstruction Results for Depleted Interior Case, 45 Source Points / 9 Radii

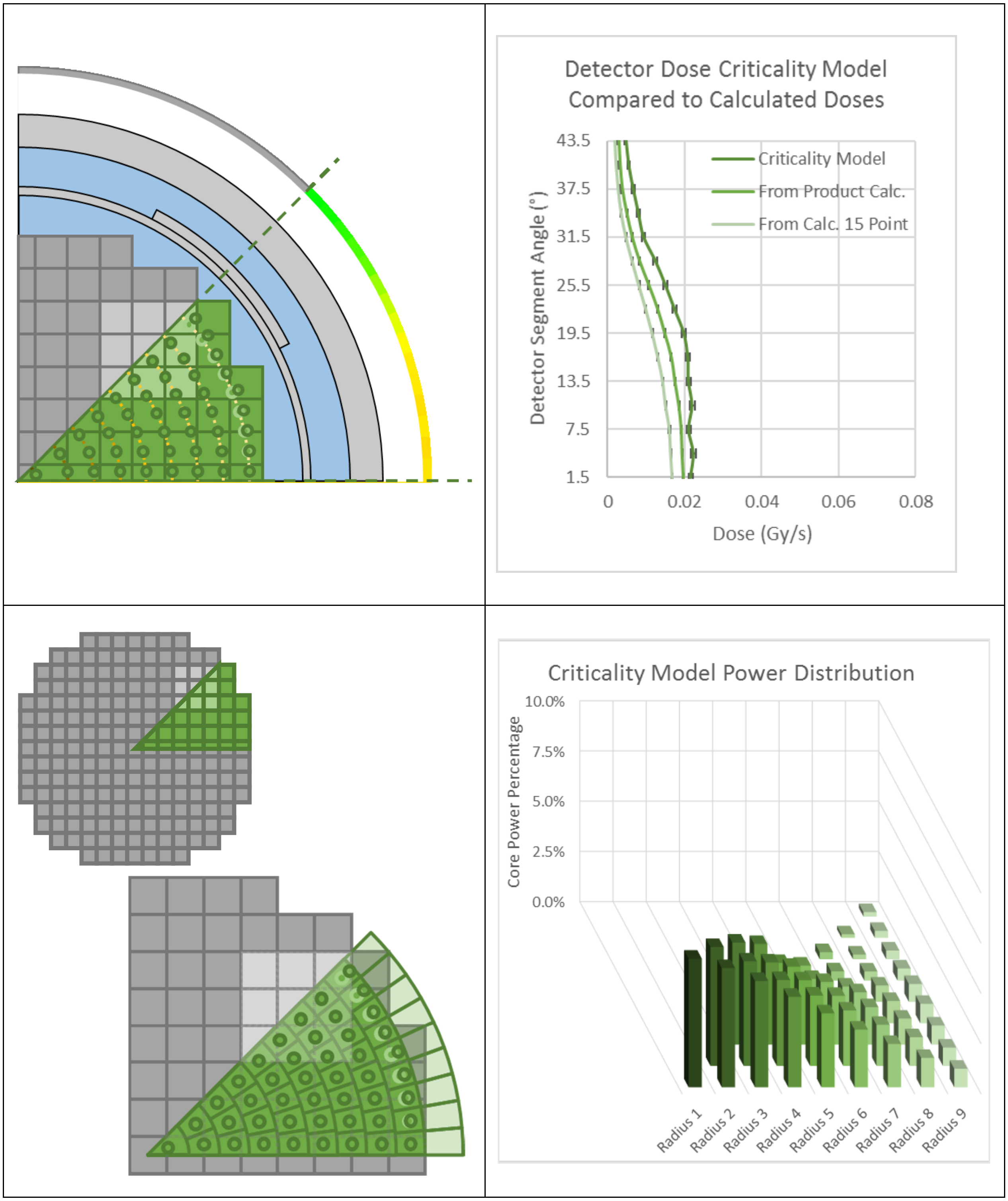

Figure 2.57: Criticality Model Results for Depleted Periphery Case and Product Formula Calculation Comparison, 45 Source Point Characterization

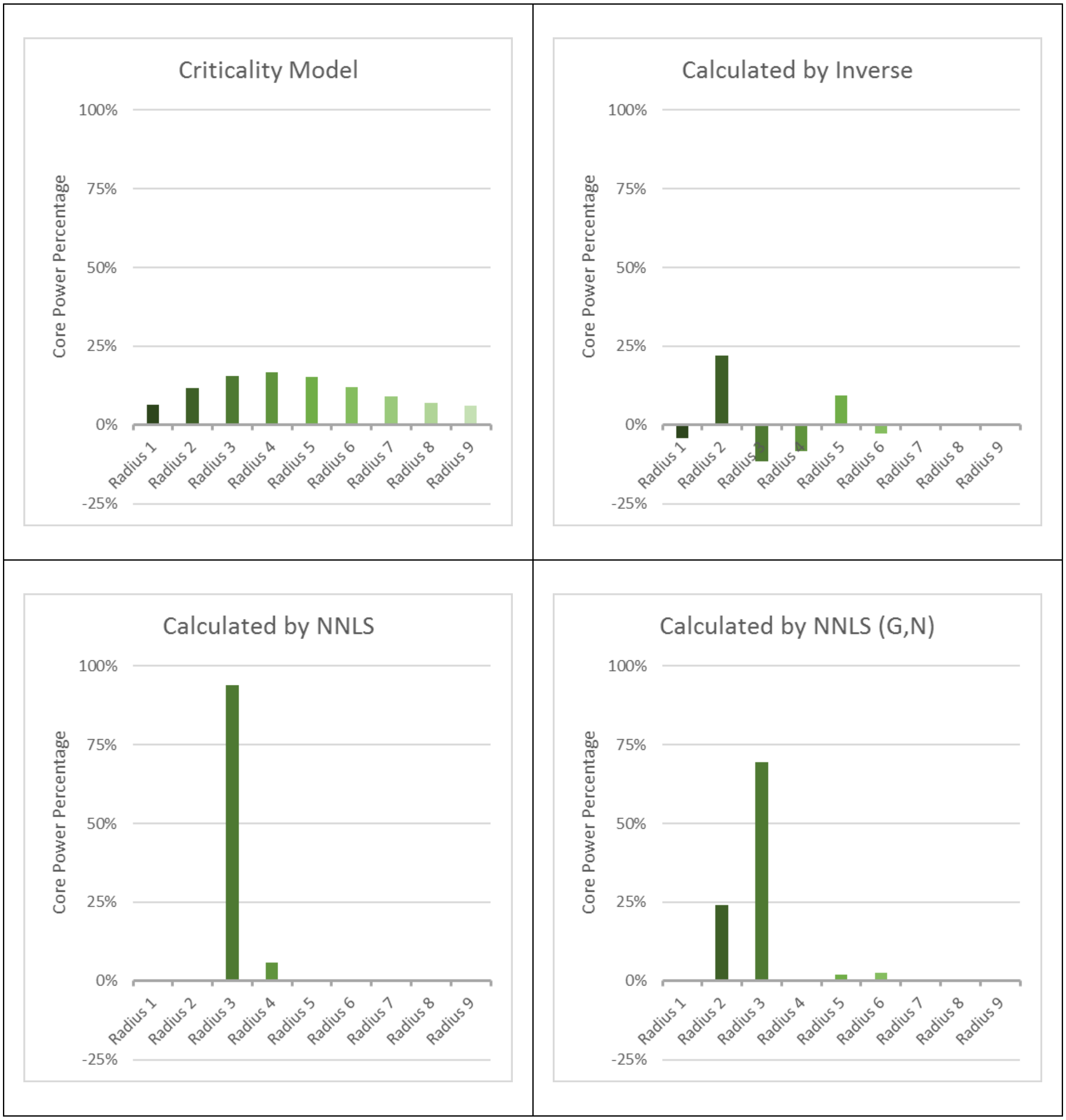

Figure 2.58: Source Reconstruction Results for Depleted Periphery Case, 45 Source Points / 9 Radii

2.5.7 55 Source Point Characterization Description

Even with the high resolution of 45 source points and all of the points' attenuation factors well determined using long and multiple iteration simulations, the calculated detector dose distribution could not match the criticality model. This suggested a different method of characterizing the core was needed. The attenuation factor dose distribution averaged by radius (Figure 2.39 and Figure 2.50) displayed that the inner radial groups had very low attenuation factors, many orders of magnitude less than the outer groups. This meant their effect on the total dose distribution was minimal, suggesting that the outer radius groups needed to be modified. Adding another radial group (radius 10) created a new characterization with 55 source points.

The 55 source point / 10 radius groups characterization was thereby designed to have equal area radius sections as before but was changed such that the outermost radius was dimensioned to completely cover the very farthest fuel assembly from the center of the core. Because of the irregularity caused by having square assemblies in a circular configuration, some of the source points for radius 10 had no fuel assembly portions to represent at all. This was the significant difference between the 55 source point compared to the 45 source point and 15 point characterizations. The other characterizations did not have empty sections for any of the source points but instead modified their outer radius points according to the radius shifting formula of Figure 2.34. This was not needed in the 55 source point characterization, therefore all radius sections were of equal area and all source points were exactly centered. This characterization is depicted in Figure 2.59.

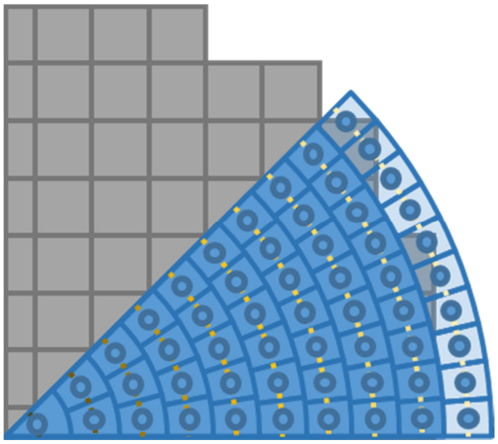

Figure 2.59: 55 Source Point Characterization with 10 Radius Groups

In the 55 source point characterization, only the outer 3 radius groups (radius 8, 9, and 10) were considered important for the calculation of attenuations factors. All source points were simulated, but from radius 7 and inward to radius 1, the long and iterative simulations were not done with as much effort as was undertaken obtaining the results for the 15 source point and 45 point characterizations. Appendix chapter *A2.1.4 55 Source Point Characterization* displays these outer radius group source points and demonstrates that, beginning with radius 7, the inner radius groups' results were not as important. Averaging the results of each radius group was done again and plotted in Figure 2.60.

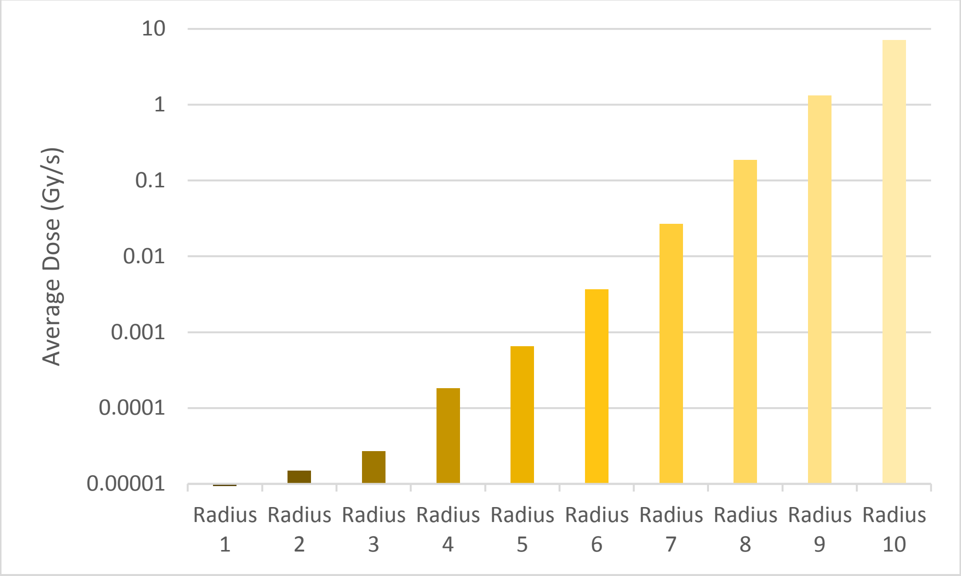

Figure 2.60: Average Dose Grouped by Radius for 55 Source Point Characterization

As seen in the bar chart, the radius groups' averages differed by about one order of magnitude for every one to two groups. For the outer radius groups of 8,9, 10, the difference was about an order of magnitude for each. That means for radius group 7 there was a difference by a factor of 1,000 from radius group 10. This was clear evidence that group 7 and inward had a minimal effect on the detector dose distribution.

2.5.8 Results for 55 Source Point Characterization

If the source points from radius group 7 inward were indeed to be ignored, the reconstruction formulas had to be adjusted accordingly. Radius groups 8, 9, 10 provided a total of 27 points such that the solution would be as follows:

$$D_{15} = K_{15 \times 27} * S_{27}$$

And for the technique of gamma, epithermal neutron, and fast neutron dose binned accordingly, the following equation applied:

$$D_{45} = K_{45 \times 27} * S_{27}$$

Neither equation had a square matrix so this 55 source point (27 points resolved) reconstruction cannot be done with an inverse formula. However, in all analysis except for the 4 point source characterization, the solution from inverse formula was not useable anyway because it solved for negative (non-real) values.

With this last studied characterization, the detector dose distributions were finally obtained where the product formula calculation using attenuation factor matrix is closely aligned with the result from the criticality model. Figure 2.61 displays these results for the full core case.

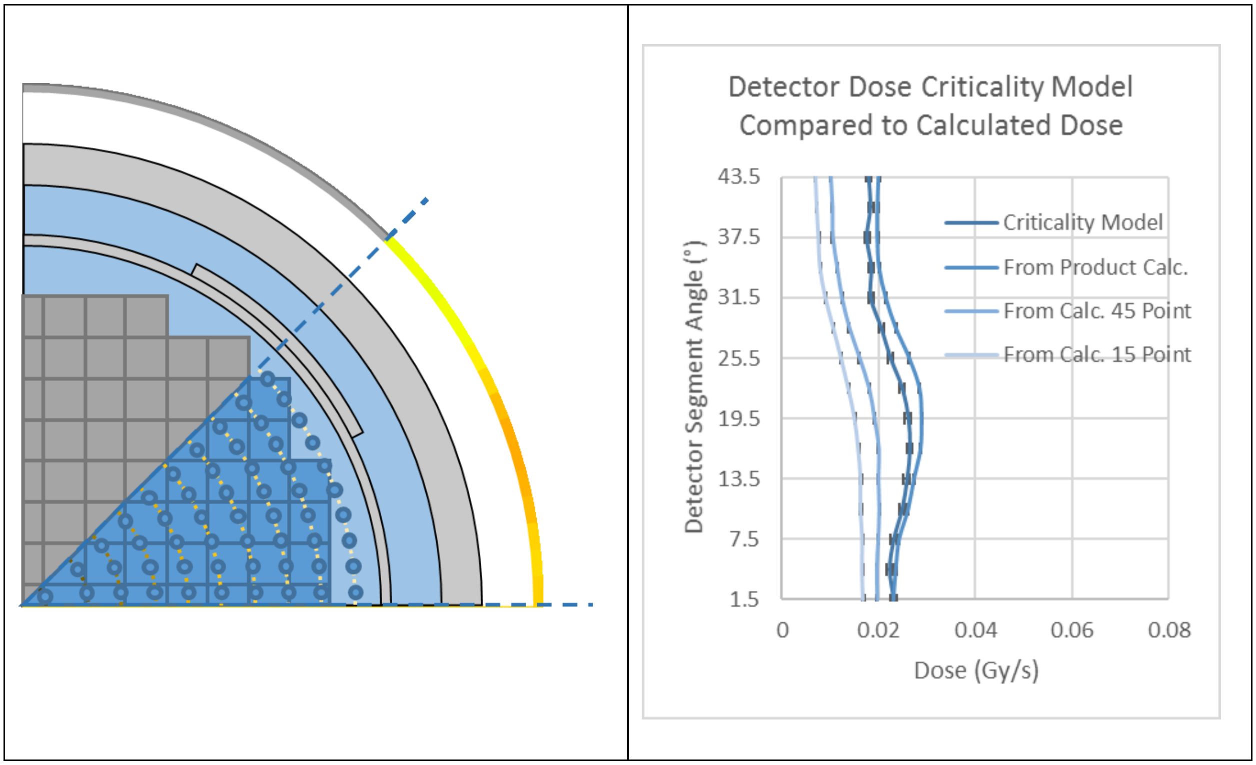

Figure 2.61: Detector Dose Distribution Calculated by Product Formula Compared to Criticality Model for Full Core Case, 55 Source Point Characterization against other Characterizations

Since the product formula calculation of detector dose was considered accurate, the composition of this dose distribution could be examined. This demonstrated that for radius group 7 and all other groups inwards (groups 7 to 1) had a minimal effect on the dose distribution as was postulated. Only 2% of the total dose came from these radial groups while 98% came from the radius groups 8, 9, 10 respectively. These results are displayed in Figure 2.62.

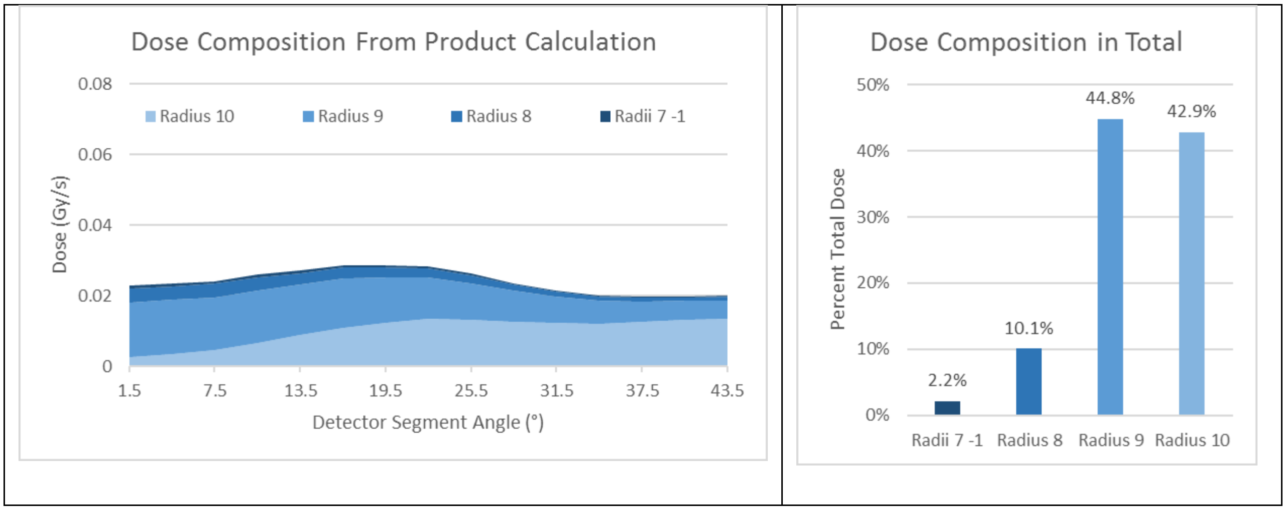

Figure 2.62: Detector Dose Composition of Distribution Full Core Case

Without using the source points of radius groups 7 inward to group 1, the outer 3 radius groups (8, 9, 10) can be solved accordingly. This is seen for the full core case in Figure 2.63. From Figure 2.63, it can be seen that this solution technique no longer solves for seemingly random source distributions. For example, the outermost radius group (radius 10) is the smallest for both solution techniques as it was the case for the criticality model. Here is also demonstrated that using the neutron energy bins of epithermal and fast provides an improved reconstruction than the gamma by itself (NNLS G,N) solution technique). These results are repeatable for the other core design cases with depleted regions (Figures 2.64 through 2.69).

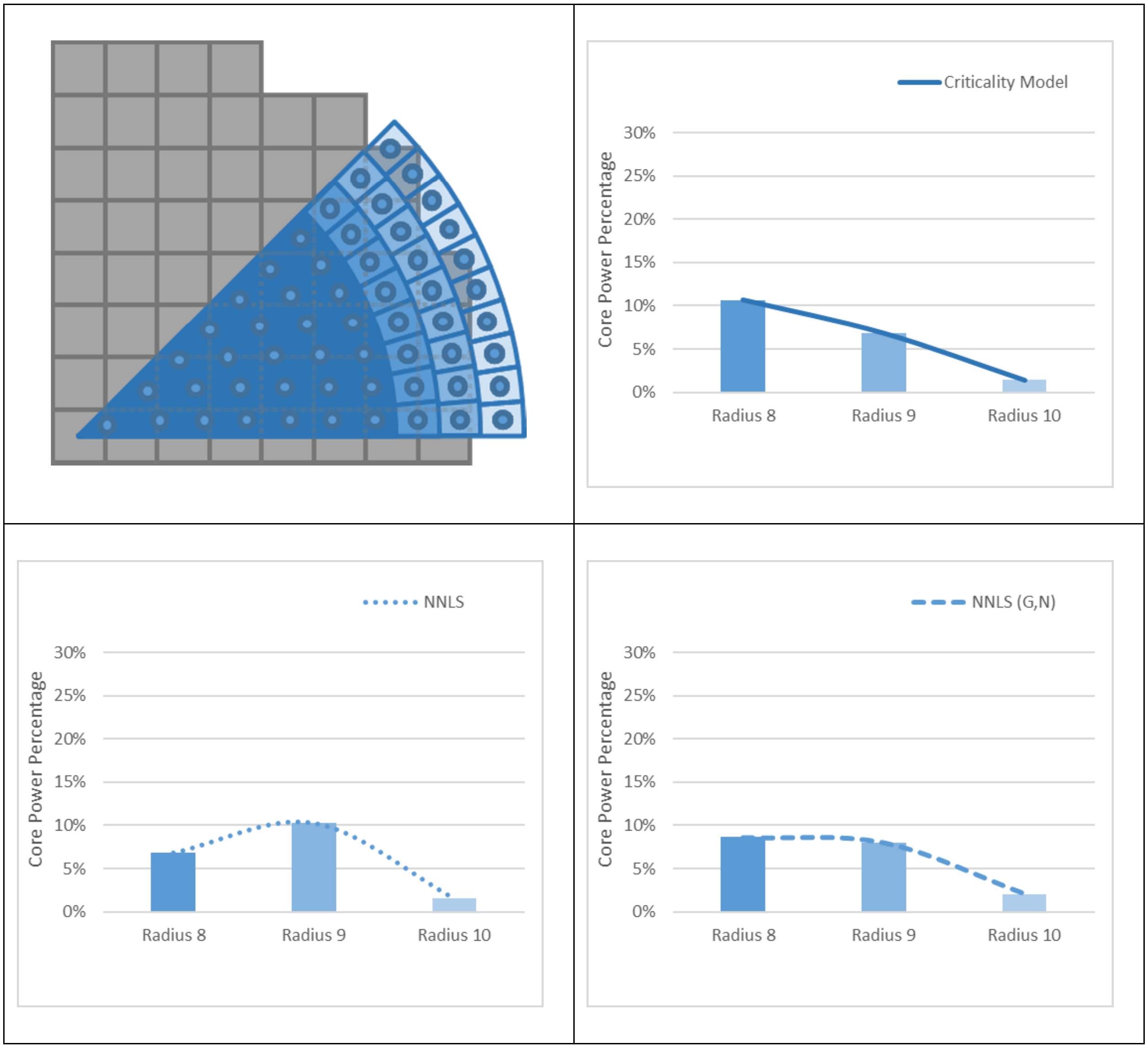

Figure 2.63: Results for Outer Radius Groups 8,9,10, Full Core Case

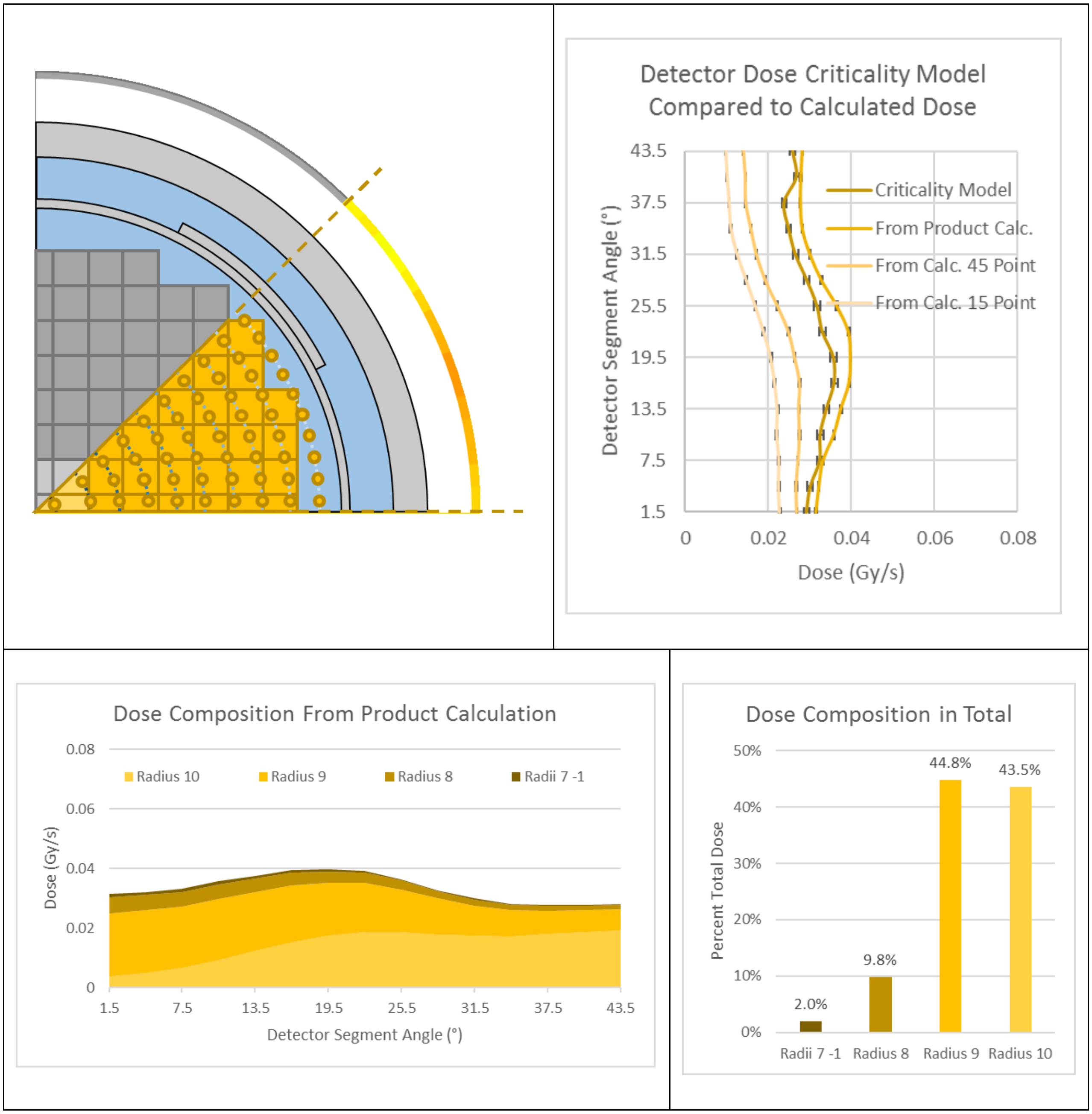

Figure 2.64: Detector Dose Distribution and Composition Calculated by Product Formula Compared to Criticality Model for Depleted Center Case, 55 Source Point Characterization

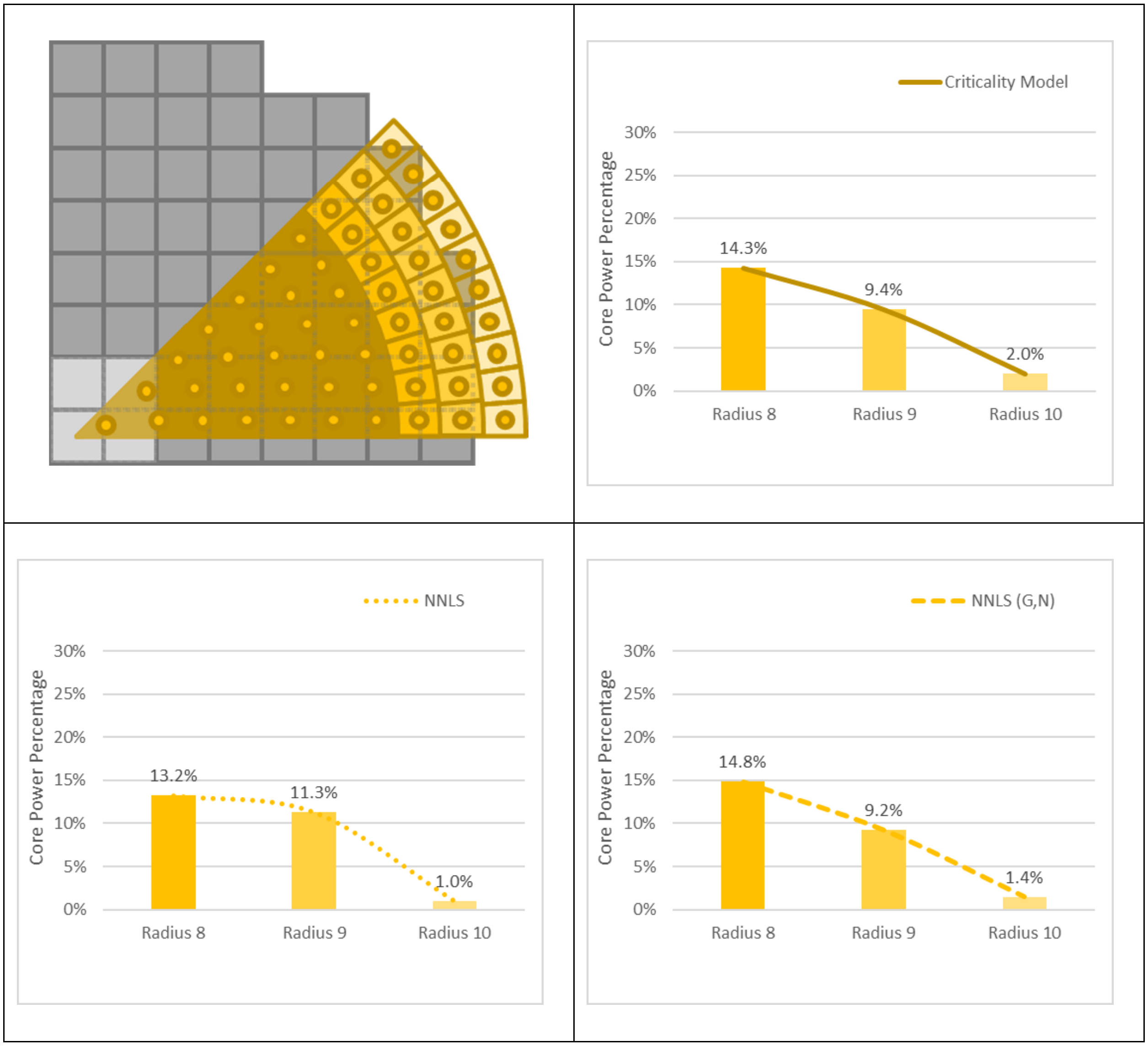

Figure 2.65: Results for Outer Radius Groups 8,9,10, Depleted Center Case

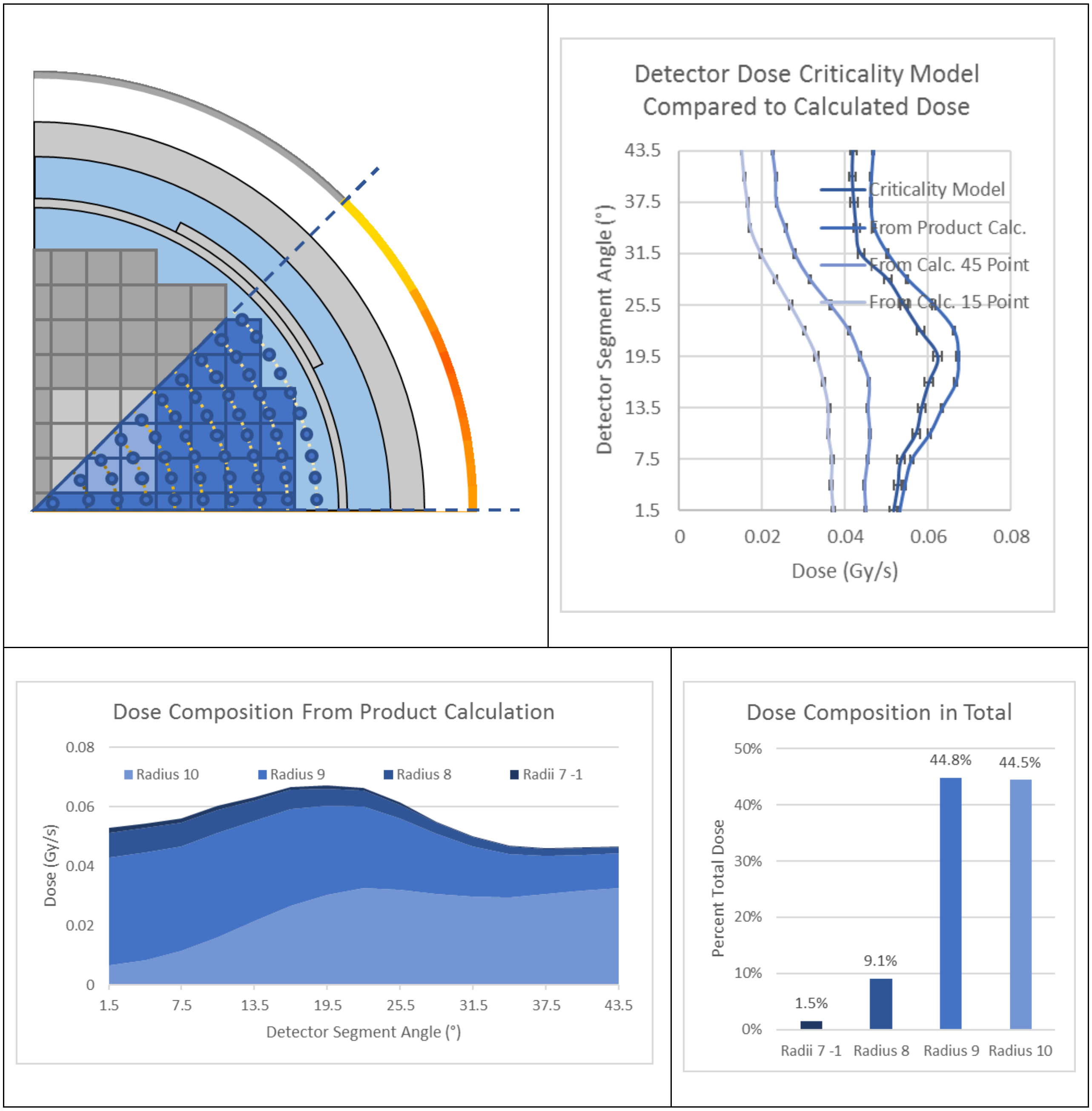

Figure 2.66: Detector Dose Distribution and Composition Calculated by Product Formula Compared to Criticality Model for Depleted Interior Case, 55 Source Point Characterization

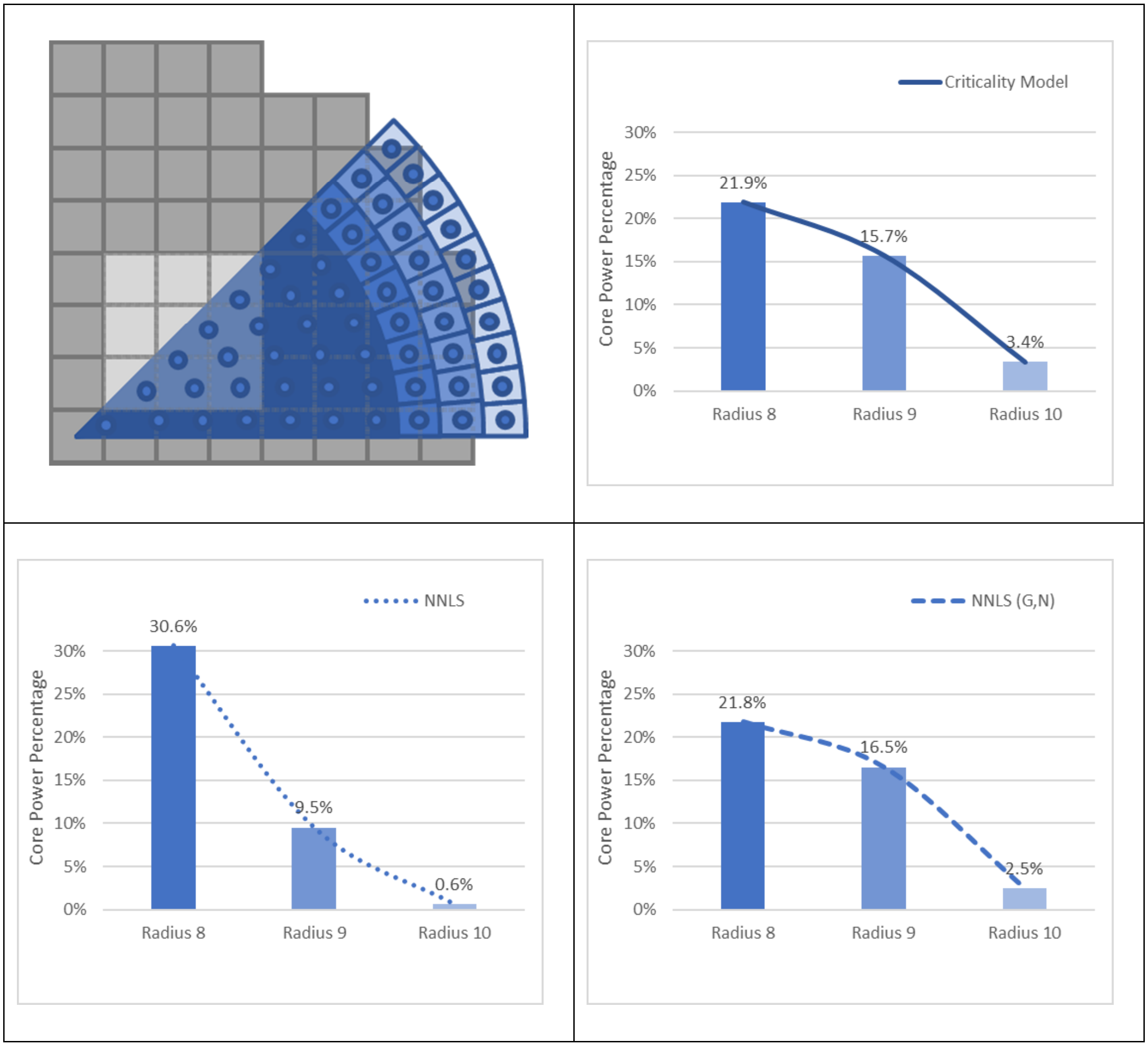

Figure 2.67: Results for Outer Radius Groups 8,9,10, Depleted Interior Case

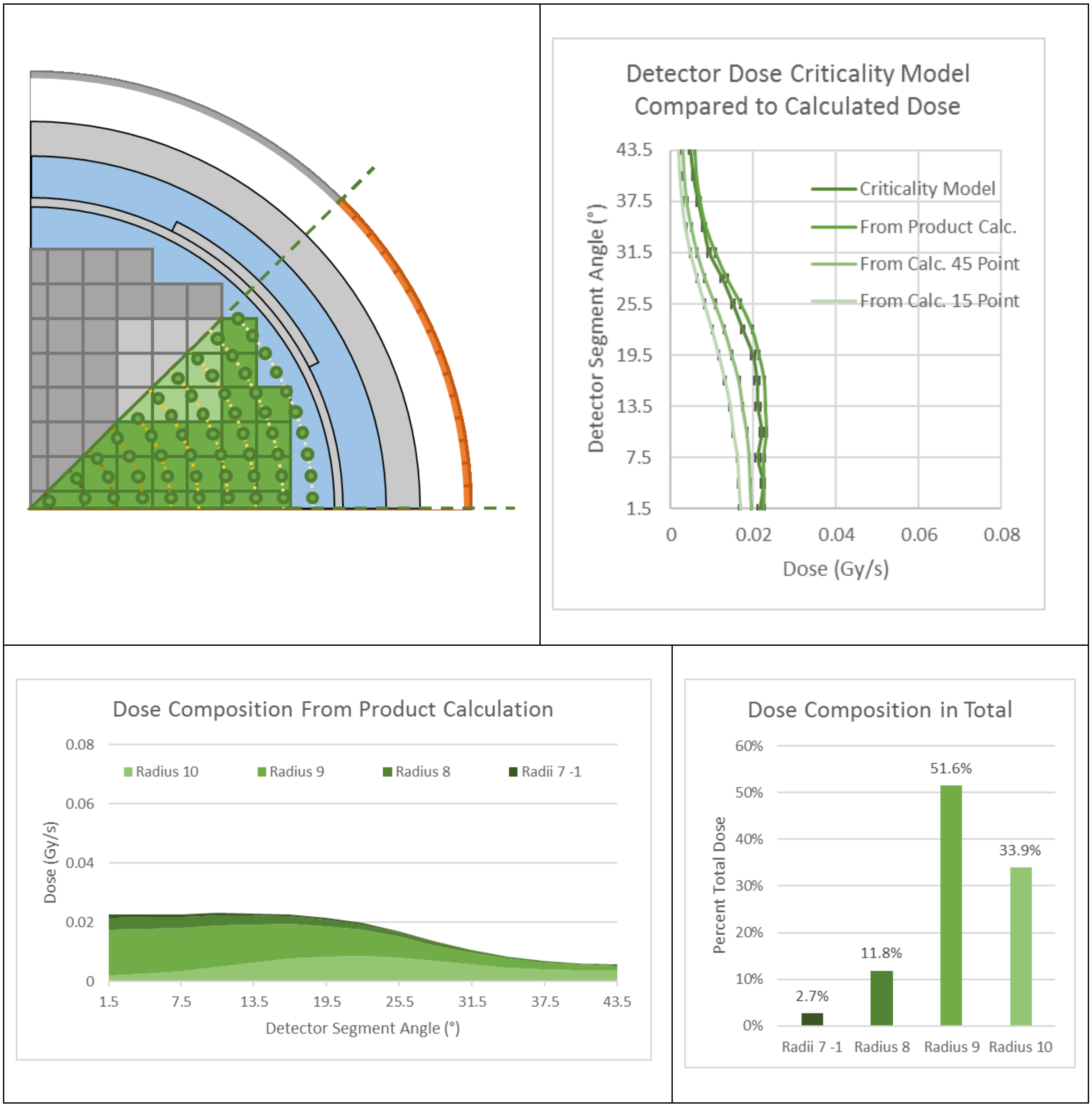

Figure 2.68: Detector Dose Distribution and Composition Calculated by Product Formula Compared to Criticality Model for Periphery Case, 55 Source Point Characterization

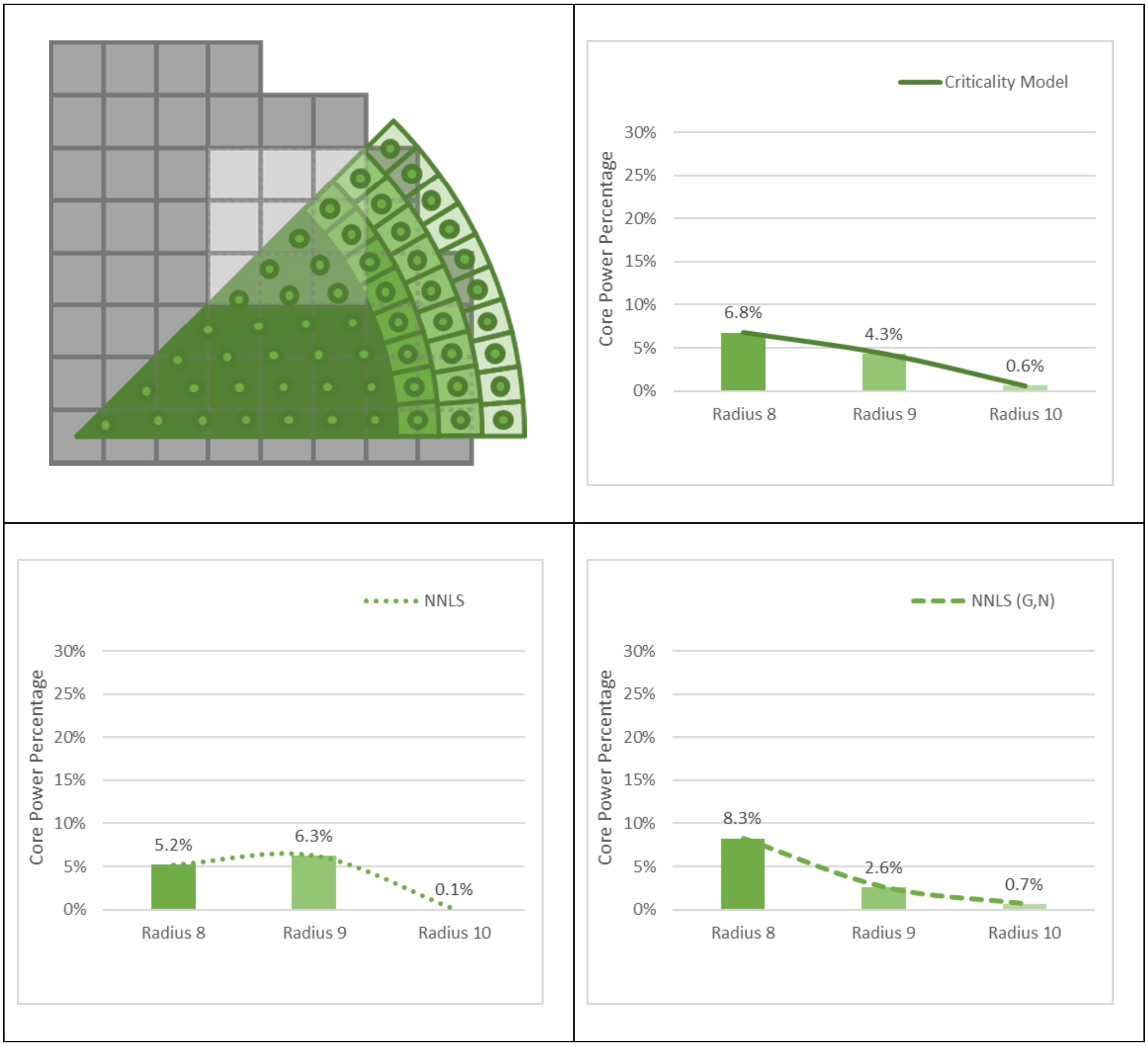

Figure 2.69: Results for Outer Radius Groups 8,9,10, Depleted Interior Case

For concluding the results of this analysis, a comparison of all 4 cases against each other was able to provide an evaluation of the 2 different solution techniques against each other (gamma dose only (NNLS) and gamma plus epithermal / fast neutron doses (NNLS (G,N)) seen in Figure 2.70 and 2.71.

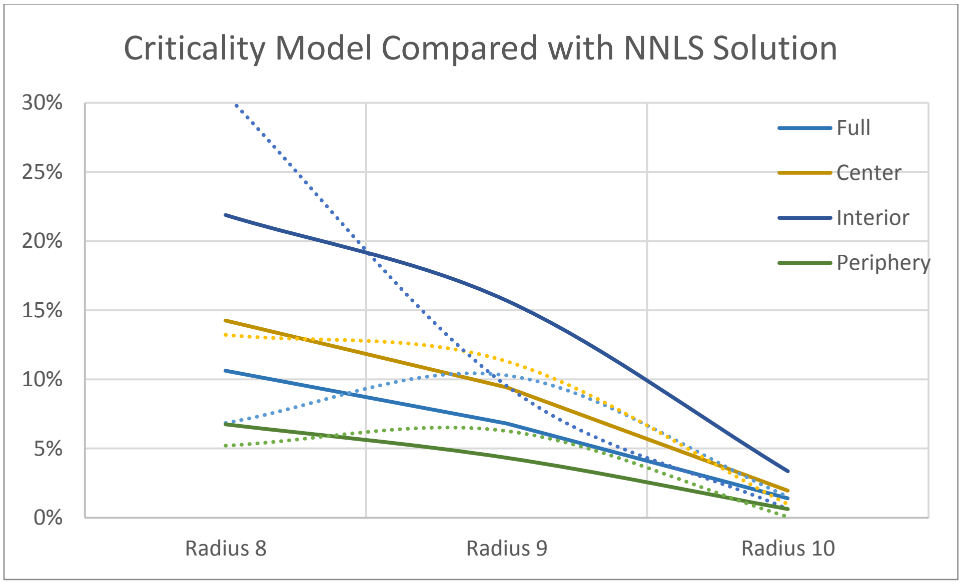

Figure 2.70: Comparison for NNLS Solution Technique across All 4 Cases

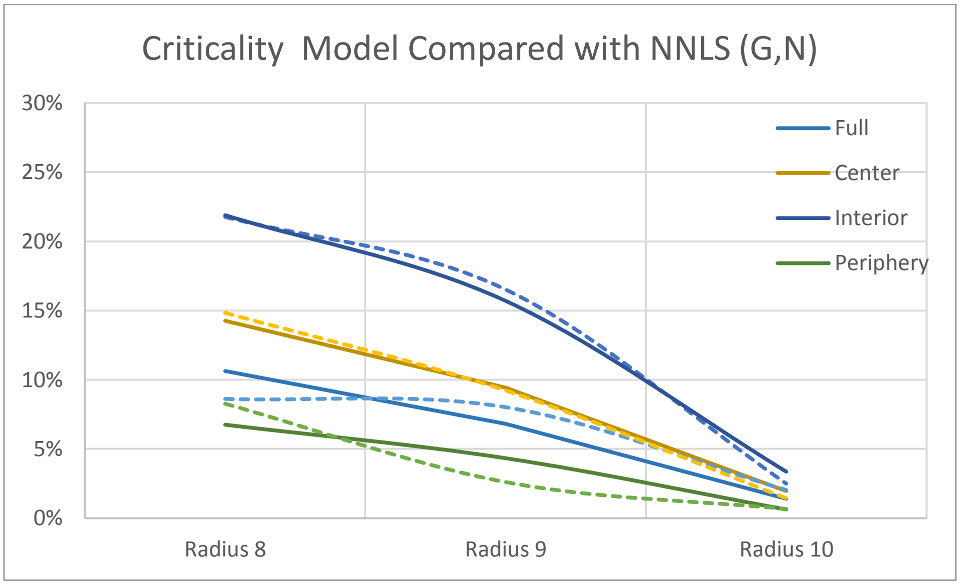

Figure 2.71: Comparison for NNLS (G,N) Solution Technique across All 4 Cases

The NNLS (G,N) is clearly a better solution technique for matching the criticality model. To explain this improvement, it is helpful to understand the dose distribution for the neutron epithermal and fast energy bins compared to the gamma distribution which was the only distribution displayed normally. For each case, these complete dose distributions are displayed in Figures 2.72 through 2.75.

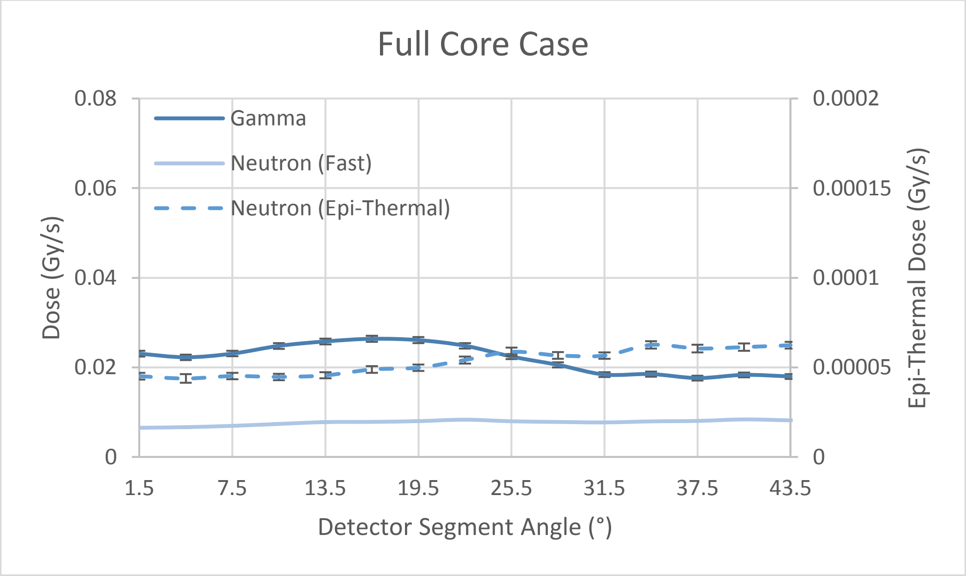

Figure 2.72: Comparison of Dose Distributions for Different Radiation Types, Full Core Case

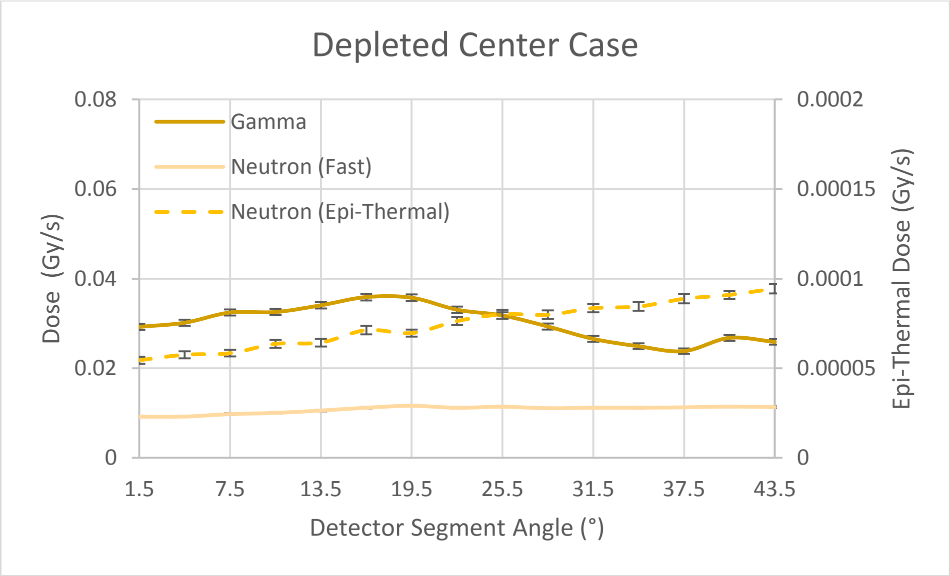

Figure 2.73: Comparison of Dose Distributions for Different Radiation Types, Depleted Center Case

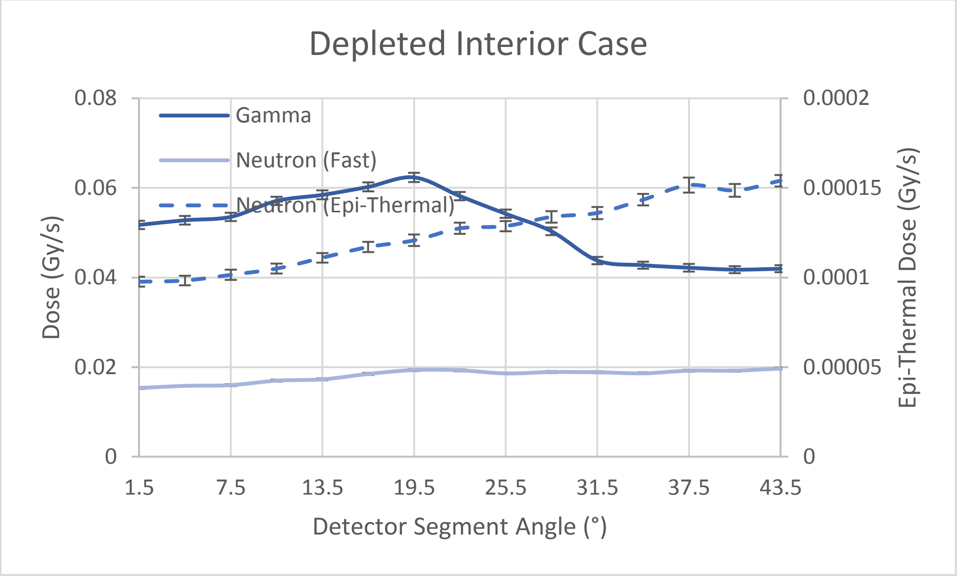

Figure 2.74: Comparison of Dose Distributions for Different Radiation Types, Depleted Interior Case

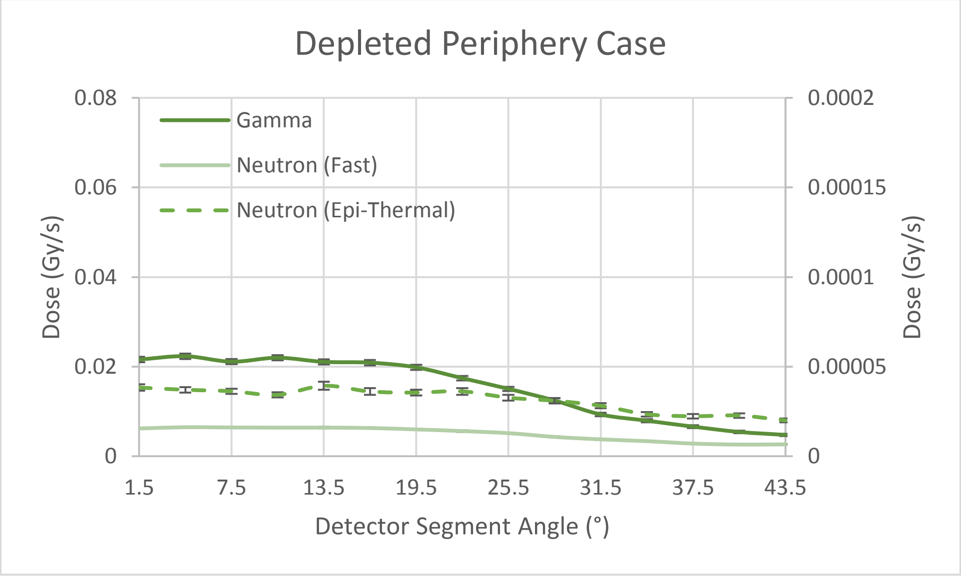

Figure 2.75: Comparison of Dose Distributions for Different Radiation Types, Depleted Periphery Case

What is noticeable when these distributions are plotted is that each radiation type has a unique profile compared to each other. This is important because if they matched closely then the addition of the other radiation dose types would not add new information to the solution technique. It was very evident that the solution technique of NNLS with the gamma and neutron radiation types was an improvement on the NNLS with gamma radiation evaluated only. Furthermore, it was not just an improvement but indeed was accurate in comparison to the criticality model for reconstructing the source distribution grouped by radius. This is something none of the other source point characterizations could do. Although they could predict the distribution determined by angled segments of the core (such as each quadrant for the 4 source point), knowledge within the section by different radius depths seemed undiscernible.

With the correct distribution by radius, even if only the outermost portion of that radius, is useful for reconstructing the entire core including the center region. This is because the known distribution serves as an outer boundary condition from which the center can be extrapolated. This was evident in the way that the depleted center case had a unique power distribution for the outer radius groups compared to the other depleted cases, even though the depleted center was far from these outer radii. Perhaps a pattern recognition algorithm would be able to determine which interior core power distribution matches with a reconstructed outer boundary condition. Otherwise, an algorithm with known core physics such as diffusion theory could determine interior core power. The demonstration that an outer core power distribution can be reconstructed opens the door to various other analysis techniques and algorithms to be explored.

3. HEAT SOURCE RECONSTRUCTION

3.1 Heat Source Experimental Need

3.1.1 Distributed Temperature Sensing Technology

Distributed sensing of temperature using fiber optics is a proven technology. Optical Frequency Domain Reflectometry uses a tunable laser to record the response of a fiber optic as a function of frequency. When this signal is transformed into the time domain using a Fourier transform, the result is a spatial resolved scan of the reflected light as fine as 10 micrometer resolution. The reflected light is a profile unique to the fiber such that temperature changes causing the fiber to expand or contract can be detected when a previous scan of the fiber is used for comparison. The measurement is continuous and therefore provides temperature data distributed along the fiber.

Using the proven temperature sensing technology in an experimental setup allows for a real world experimentation on the reconstruction algorithm for reactor power. Testing on a heat source rather than an ionizing radiation source allows for versatility in the source distribution and does not need expensive reactor time. Also, the correlation is well defined for temperature effects on the fiber so the distributed measurement of temperature is reliable.

3.1.2 Heat and Radiation Source Similarities

The real world experiment on the effects of a heat source has similarities to the simulations of ionizing radiation. The heat source in the experimental setup primarily induces a temperature change in the distributed fiber optic measurement by radiative heat transfer. The medium between the heat source and fiber optic cables is an enclosed air cavity so the conductive and convective heat transfer is minimized. This dictates that the heat source has the same attenuation with distance (inverse square law) as the radiation emitted in the reactor monitoring simulations. Also, materials blocking the fiber optic from receiving the heat produce a unique pattern from each heat source similar to each reactor source point has a unique path to the detector segment.

Secondly, the heat source experiment is a time integrated measurement in a similar manner to the postulated reactor reconstruction methods. The longer the fiber optics are exposed to the heat source, the more their temperature is going to be affected. Similarly, the fiber optics irradiated as reactor sensors, will have a radiation induced change which coincides with time of radiation exposure. In this way, the radiation is monitored as a fluence measurement rather than flux which is an instantaneous measurement. Moreover, dividing the induced change by the time increment does provide the instantaneous power being monitored or heat source intensity.

3.1.3 Advantage of Experimental Results

There is a need to test the reconstruction algorithm experimentally because the simulation of radiation detection is limited to a coarse resolution of the distributed measurement since each segment must be large enough to capture a statistically reliable number of radiation particles. The real world reactor produces many magnitudes larger particles per second than what can be simulated so to test the reconstruction algorithm in fine resolution, a real world experiment is needed. Also, a correlation for radiation affects is not well defined hence a third and final research objective in this dissertation proposal.

The heat source experiment cannot however simulate a volume source as is the case for a real reactor. The setup is instead a collection of point heat sources which lends itself to work well with the point source algorithm being used for source reconstruction. In a real world experiment there is a demonstration of how noise in the measurement can reduce the reconstruction accuracy similar to the statistical uncertainty affect in the simulation. Using the same algorithm in both cases provides the same optimization goal.

3.2 Experiment Development

3.2.1 Design of Test Setup

The test setup for the experiment consisted of a 3x3 array of lightbulbs. The lightbulbs were each 150 Watts of electrical power which equates to the same wattage as a rate of heat production. The bulbs could be turned on or off individually and each column could be dimmed incrementally to 6 discrete power levels. A wire diagram of an individual column can be seen below:

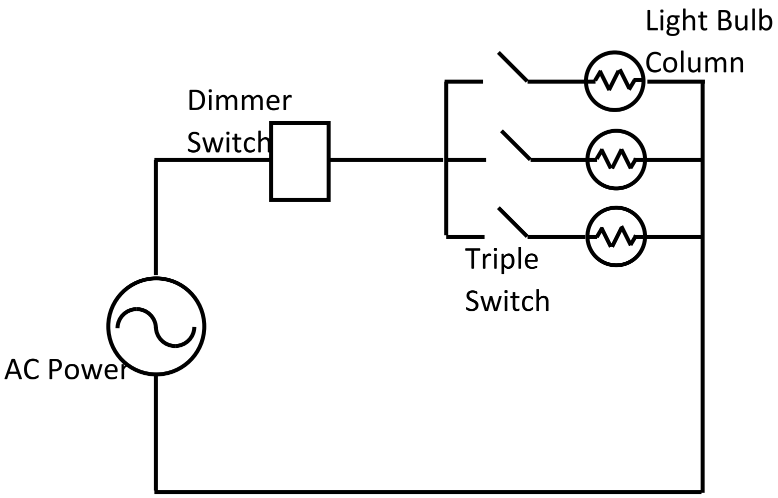

Figure 3.1: Wire diagram of Heat Reconstruction Experiment

Therefore, the three columns had a 3 gang junction box for all 3 dimmer switches and a 3 gang box of triple switches, corresponding to the 3x3 light bulb array. The bulbs were mounted on threaded rods so that they can be moved axially. The experimental setup and the junction boxes are detailed in the following figure:

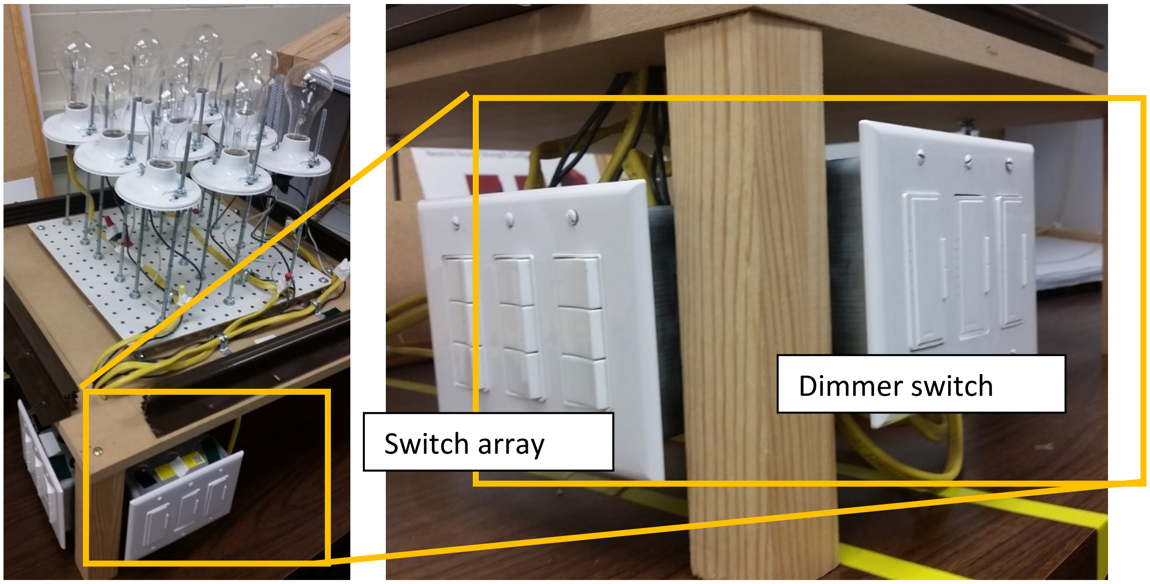

Figure 3.2: Mounting of Switches

Surrounding the light bulb array was an insulated rectangular box. On the inside are clips holding fiber optics in a spiral design so that the measurement of the heat source could be captured at the periphery in 3 dimensions. The fiber optics were connected at an outlet of the box to an external jumper fiber optic that is to be connected to the OFDR. This setup can be seen in the following figure with the junctions highlighted:

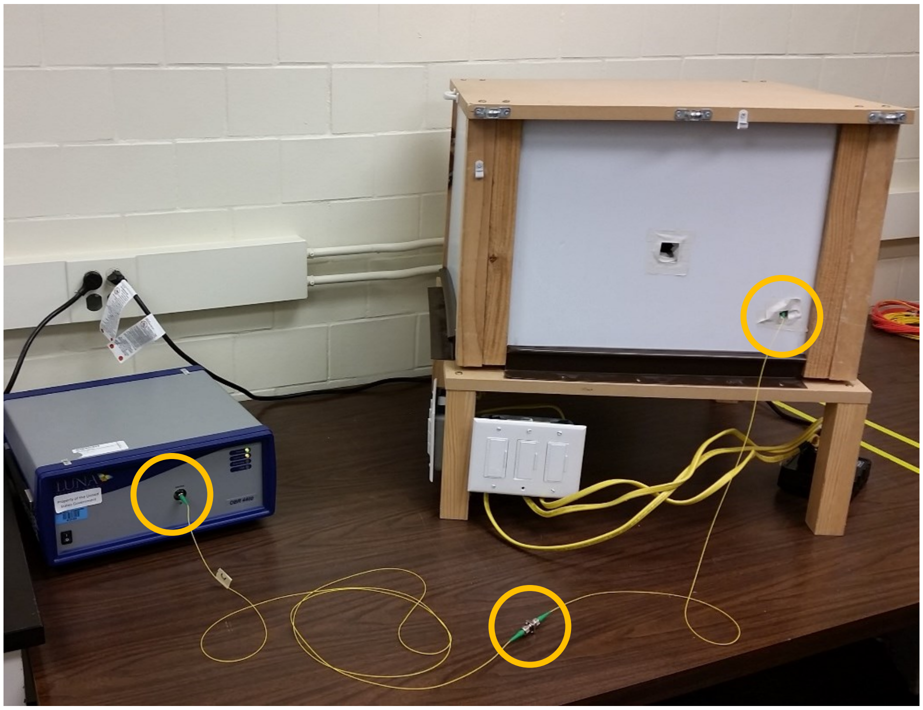

Figure 3.3: Fiber Optic Setup with Junctions Highlighted

A full description detailing the materials and methods used to construct the experimental setup can be found in the appendix chapter *A3.1 Heat Source Experiment Setup*.

3.2.2 Graphical Capability Development

A graphing tool created within Microsoft Excel was utilized which enabled 3-D plotting in accordance with specified viewing angles (Doka, 2012). This can be seen in the following overlay graph such that the viewing angle matches the perspective captured by the picture.

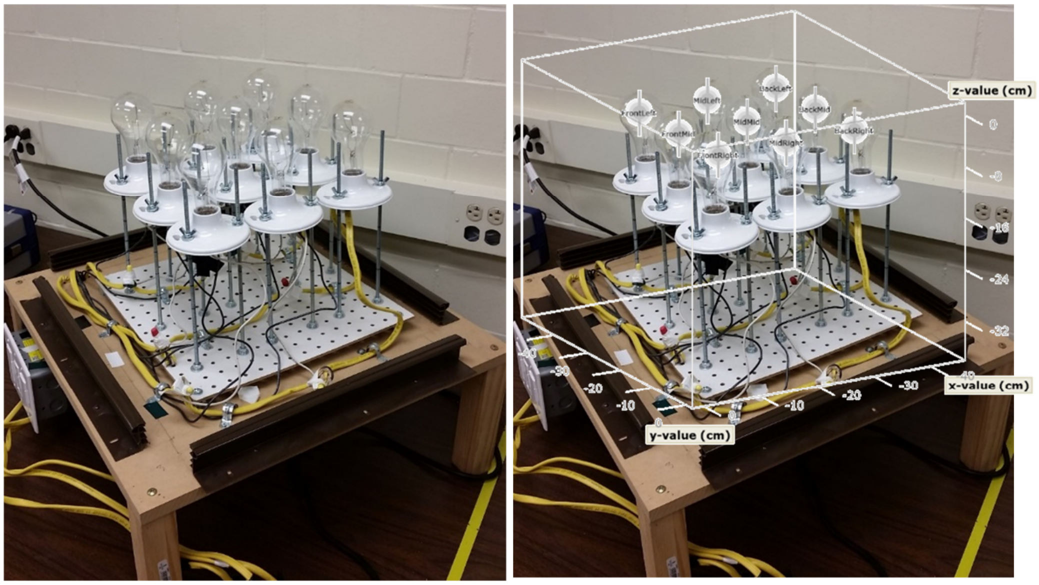

Figure 3.4: Graph Overlay of Light Bulb Heat Sources

A picture is not capable of capturing the view of the complete experiment setup. This is due to the setup being covered by a top box to provide structure for the fiber optic while insulating the heat sources. A graph of the experiment internal view combining the heat source placement and fiber optic spiral can be recreated using the 3D plotter. This can be in the following figure.

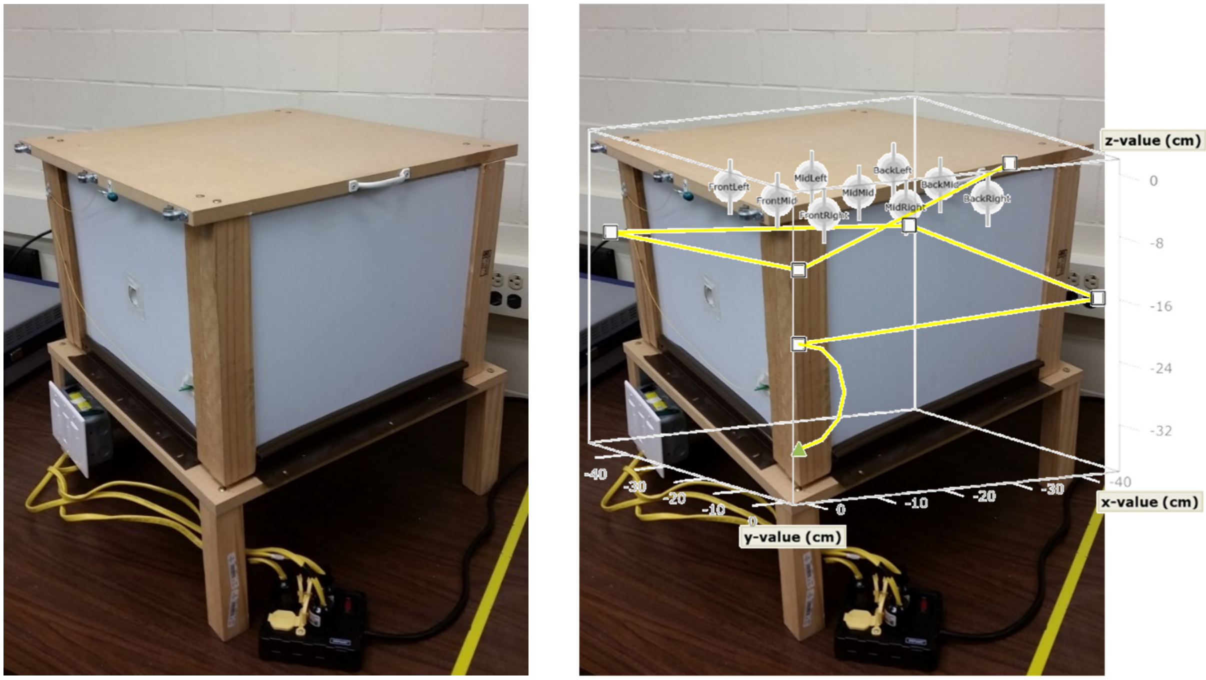

Figure 3.5: Combined Graph of Setup as 3D Overlay

An additional feature to this graphing tool was added such that the temperature change induced in the fiber can be plotted in accordance with the graphical representation of the fiber's location by color coding the magnitude of the temperature change. In this way, the maximum temperature change would be plotted a vibrant shade of red while the minimum temperature change would be a greenish yellow. Although plotting in this way does not provide quantitative data numerically, it is an appropriate representation for comparing the different temperature distributions due to different heat source configurations. A complete color coded plot combined with a picture for the respective heat distribution of a corner light bulb at half power can be seen as follows:

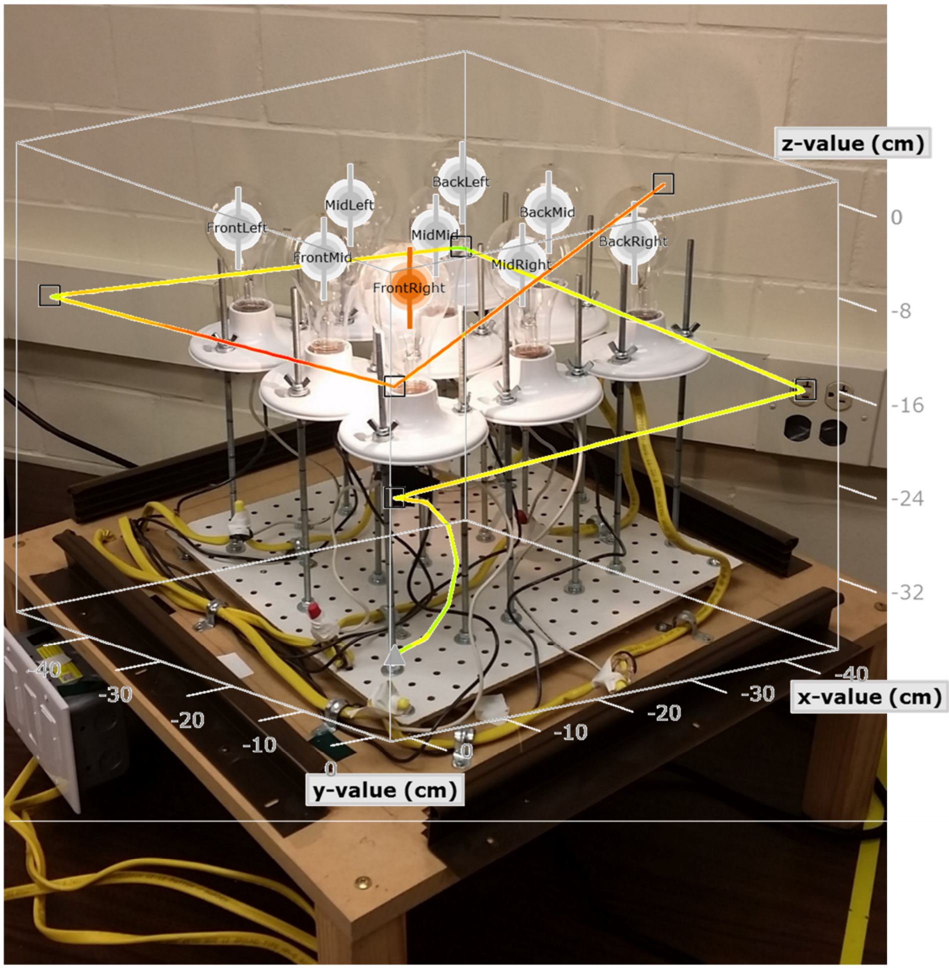

Figure 3.6: Full Size Temperature Distribution Graph

3.2.3 Conducting Experiment

The experiment was conducted such that each bulb will be tested individually to capture its heating effect on the distributed temperature fiber optic. As seen in the previous figure, the heating distribution for each light bulb yields a unique effect on the fiber optic measurement device. The geometry of the test setup such as the shielding from the heat of a bulb by the other bulbs and the threaded rod structure materials created this unique pattern of temperature change induced by the heat of each bulb. This can be seen graphically for the captured point source data from a single column in the following figure.

Single Bub Full Power at 10 Minutes (Color Range 0° C to 50° C), Left Column

Back Left

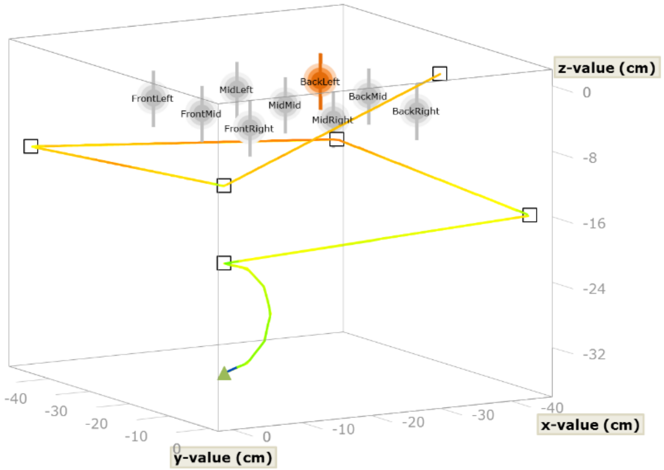

Middle Left

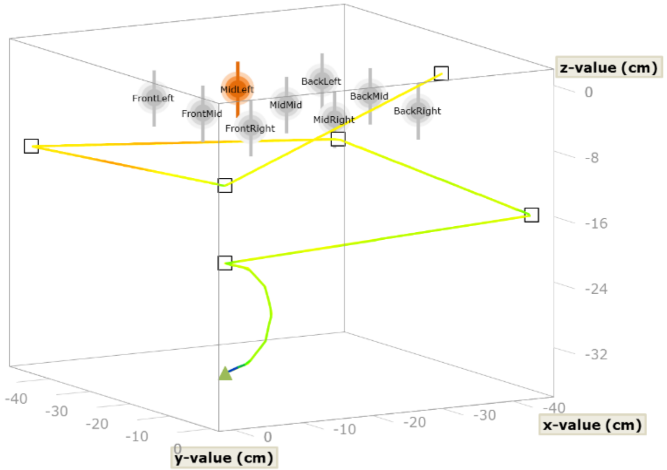

Front Left

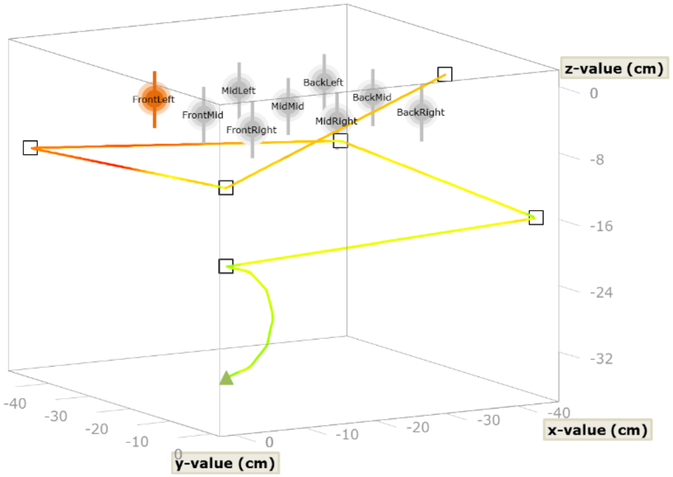

Figure 3.7: Display of Left Column

This test was done for each bulb at 2.5 minute intervals up to 10 minutes. Once each bulb’s heating affect is captured, each segment of the fiber optic would then have a known correlation for temperature rise from each bulb in each position. From here, a combination of different heat sources powered on and at different power levels were captured to test the performance of the point source reconstruction when used for heat source reconstruction.

3.3 Results

3.3.1 Power Distribution Descriptions

There were a total of 6 power distributions tested. These tests were chosen to test how the reconstruction algorithm would be able to discern contrasting power distributions. Therefore, a left power tilt (left column full power, middle column half-powered, right column off) was contrasted with a right power tilt and full power versus half power was tested for powering of the 4 corner bulbs and for all 9 bulbs. The results at the 10 minute mark of the test can be seen in the following figure:

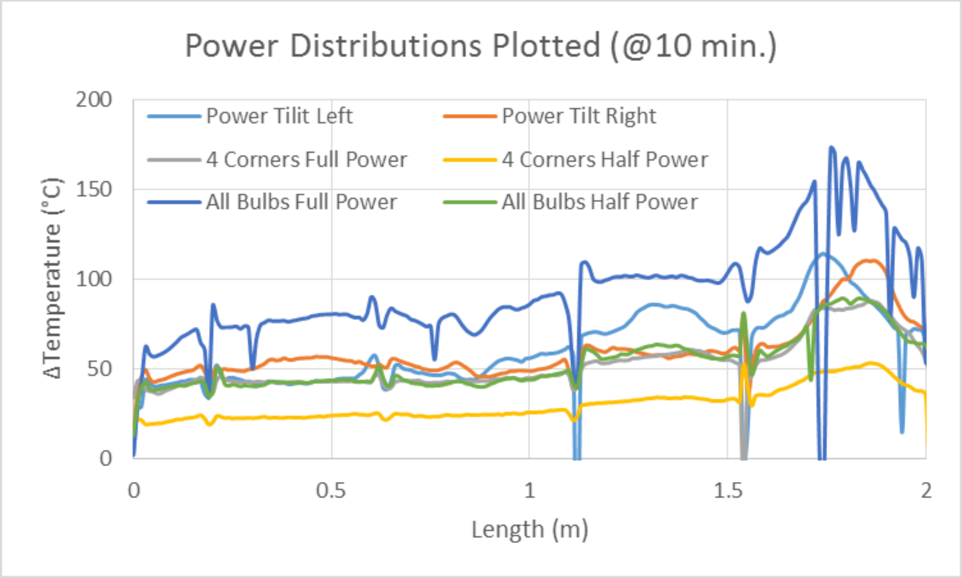

Figure 3.8: Data Graphed of All 6 Temperature Distributions

One thing that should be noted from this figure is the all bulbs full power has large temperature fluctuations which is due to the algorithm used to calculate temperature change has limitations when the change is large. This is discussed in more detail in appendix chapter *A3.2 Experiment Results*.

3.3.2 Left / Right Power Tilt

Although it is difficult to discern the contrasting distributions in the plot of all 6, when 2 distributions are compared the differences are very clear. The left power tilt versus right can be seen in the figure below:

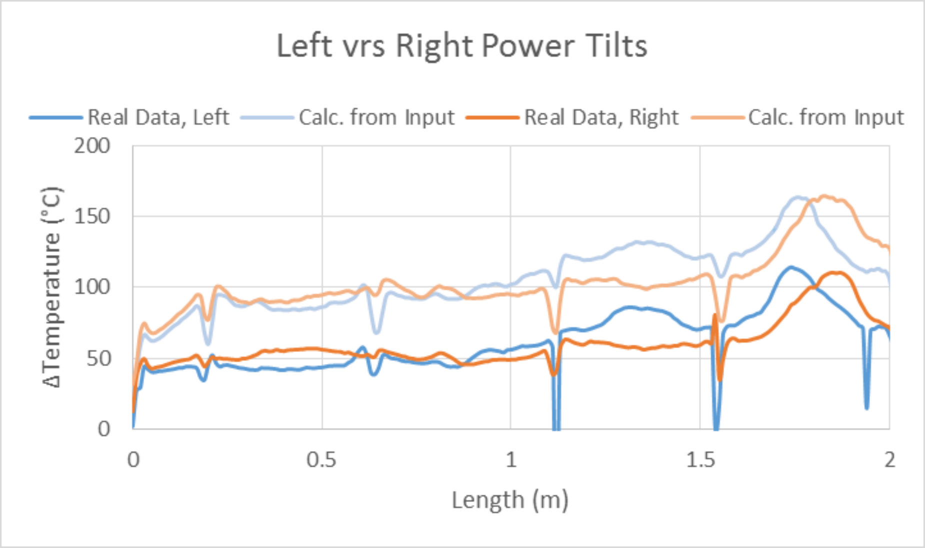

Figure 3.9: Graph of Both Left and Right Power Tilts, Data and Calculated

The “Calculated from Input” is the result of computing what the data would look like if it was the result of the linear combination of the individual bulbs temperature distribution data multiplied by the input power configuration. What is interesting from these plots is that although the “Calculated by Input” is not accurate to magnitude, it does represent the shape and plot features of its respective “Real Data” counterpart. It is these features, perhaps, what enables the reconstruction non-negative least squares (NNLS) algorithm to discern one power distribution from the other. The algorithm is explained in detail in appendix chapter *A5: Programming Methods*.

The results of the reconstruction using the NNLS algorithm can be seen as follows:

Figure 3.10: Solver Comparison for Left and Right Power Tilts

3.3.3 Full and Half Power Configurations

In the analysis of the other 4 power distributions, the half power results were used in comparison to full power results. Although the contrast in the results and reconstruction was not as clear as in the left versus right power comparison, it was a demonstration how the algorithm could predict the lower versus higher power comparison even if it could not attribute the power to the correct bulbs. The results are seen in the following figures:

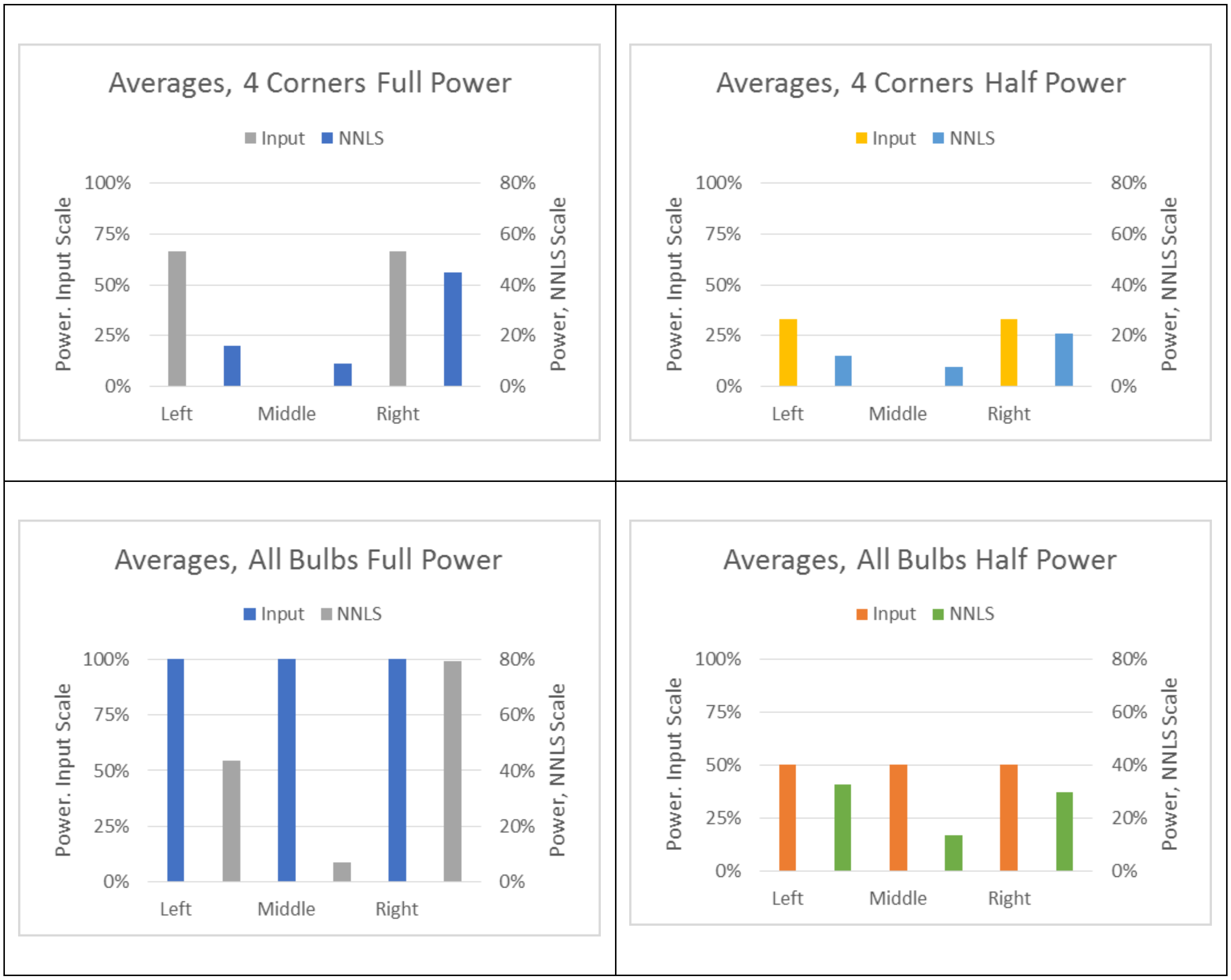

Figure 3.11: Solver comparison for Full versus Half Power Distributions

3.3.4 Summary

Although non-linear combination of the heating attenuation factors from each bulb prevented the solver from reconstruction of the power distribution with complete accuracy, the experiment did demonstrate the ability of the reconstruction algorithm to discern one power distribution contrasted with another. This was most prominent in the left versus right power tilts. Having a real world experiment to test the algorithm was proved useful. Experimenting with heat from a power distribution rather than ionizing radiation from a reactor power source was a successful implementation of the reconstruction algorithm.

4. CORRELATION OF RADIATION DOSE (RESPONSE FUNCTION)

4.1 Use of Fiber Optics for Dosimetry

Fiber optic response to ionizing radiation is known to increase the Rayleigh scattering of light guided within the fiber core (Wen 2011). Where this increase in scattering can be directly correlated to increase in dose, the fiber becomes a useable dosimeter. What becomes remarkably unique as a dosimeter is the geometry of the fiber itself. Although it's diameter across is very small (on the order of 100 μm), the center axis can be kilometers in length. For all intents and purposes, it has the geometry of an infinite cylinder. Furthermore, as a dosimeter based on the property of Rayleigh scattering, the fiber takes on the ability to detect radiation as a spatial distribution along its near infinite length when coupled with a tool that can measure Rayleigh scattering as a spatial distribution. Tools of proven technology that have this functionality are the Optical Time Domain Reflectometer (OTDR) with course spatial resolution and also the Optical Frequency Domain Reflectometer (OFDR) which has very fine spatial resolution (Gifford D. , Soller, Wolfe, & Froggatt).

The lifespan of fiber optics in a radiation environment has been shown to withstand doses of 10 gigagray as pure silica fibers while Germanium doped fibers experienced a large signal loss at just 5 kilogray (Cheymmol, Long, Villard, & Brichard, 2008) (Wen, et al., 2011). Therefore, to use a fiber optic as a distributed dosimeter, the sensitivity to radiation must be known for the fiber's composition and a material selected that is sensitive enough to show the dose over a respective time increment while being resilient enough to survive the power cycle.

4.2 Test Rig for Oak Ridge National Lab Gamma Facility

To evaluate the dose range applicable for 3 fiber materials manufactured by Luna Technologies (P. Tsvetkov, 2013), the same company which provides the OFDR, test rigs were built to be irradiated at Gamma Irradiation Facility at Oak Ridge National Laboratory. The test rigs were built to fit the dimensions of the irradiation container. By wrapping the fibers around a central axis, the compact test rig could contain over 7 meters (23 feet) of each of 4 different fibers from 3 different materials. The test rig design was able to maximize the length of fiber to be irradiated by coiling the fiber within the rig as seen in the following figure:

Figure 4.1: Assembly of Fiber Optic Coil on Central PVC Pipe

Although the fiber materials were provided by Luna Technologies, it was significantly cheaper to obtain just the bare fibers than have Luna provide them pre-fabricated. Fabrication was done in-house by attaching onto the bare fibers a fiber pigtail, which is a short length of fiber terminated by a pre-installed connector. The attachment procedure involved using a fusion splicer to align the fiber and fiber pigtail and then melt the fibers together at that point with an electric arc. This type of connection is known as a “splice.” For further details on the assembly procedures, a complete description of the construction materials and methods can be seen in appendix chapter *A4.1 Construction of Test Rig*.

Once the splice connection was made, it was possible to measure the scattering within the fiber. In the following graphs for the lowest irradiated test rig (color coded as yellow), the scattering pattern post-splice is displayed:

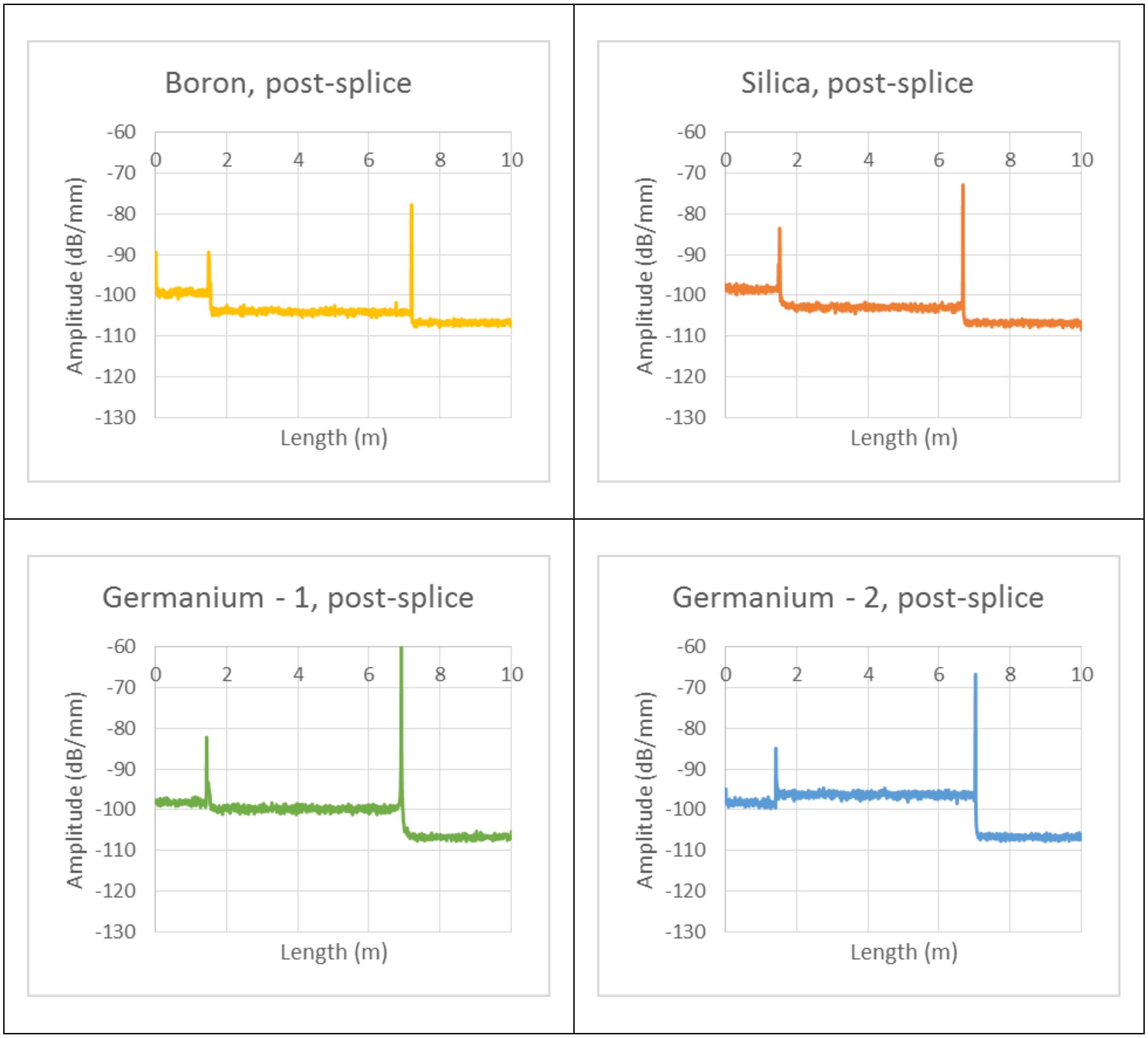

Figure 4.2: Fiber Scans of Scattering Pattern Post-Splice

After assembly it was then possible to take the scans of the fiber optic test rigs to provide for the 0 gray dose scattering pattern. Unfortunately, during assembly it was common for the splice connection to break. This was easily apparent in the 0 gray scans by a large reflection at the break point followed by the scattering pattern which matches the noise floor rather than a small reflection and continued scattering data until a large reflection at the fiber end. The following graph for the boron fiber displays a broken splice (note the scattering before the break point matches the post-splice scan except with addition of 2.5m jumper cable to connect from the test rig to the measurement device):

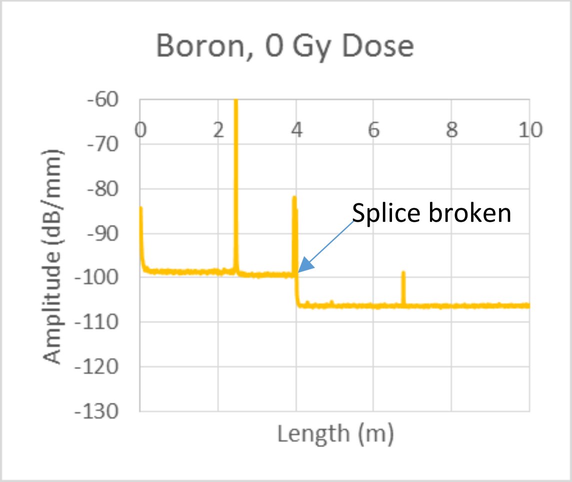

Figure 4.3: Fiber Scans of Scattering Pattern Post-Splice

Complete description of scans of all fibers in all test rigs can be seen in appendix chapter *A4.2 Measurement Data*. The following table shows a summary of which fibers from which rigs had splices broken during assembly:

Rig Color Code	Boron	Silica	Germanium – 1	Germanium – 2
Yellow	Broken	Intact	Intact	Intact
White*	Broken	Broken	Broken	Broken
Green	Broken	Broken	Broken	Broken
Black	Broken	Broken	Broken	Broken
Blue	Broken	Broken	Intact	Broken

*White fibers all Boron

Figure 4.4: List of Fiber Splices Broken / Intact

4.3 Irradiations

The assembled test rigs were to be irradiated at the Oak Ridge National Laboratory Gamma Radiation Facility (ORNL GIF) for 3 different orders of magnitude: 10 kilogray, 100 kilogray, and 1 Megagray. For each irradiation order of magnitude, it was suspected the fibers would show an increase in Rayleigh scattered light in accordance with the radiation dose as suggested by literature. With doses being on different orders of magnitude, an appropriate dose range could be obtained for the establishment of a response function. The data on these particular fibers and data as a distributed measurement did not previously exist.

Additional low dose irradiations were conducted at the University of Cincinnati Cobalt – 60 facility. This provided for doses of 100 Gy and 1 kGy. The test rig coincidently was the correct size for the facility's air tight container. This was lowered into the shielding pool as can be seen in the following figure:

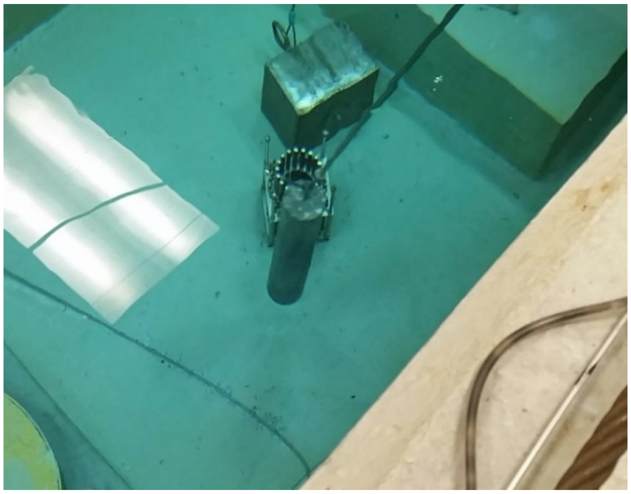

Figure 4.5: Cobalt-60 Pool Source Irradiation

The higher doses were achieved using the ORNL GIF. This facility uses an intense radiation field created by spent fuel from the High Flux Isotope Reactor. The test rigs exhibited a distinct color change in their structural materials corresponding to their respective dose range as can be seen in the following figure.

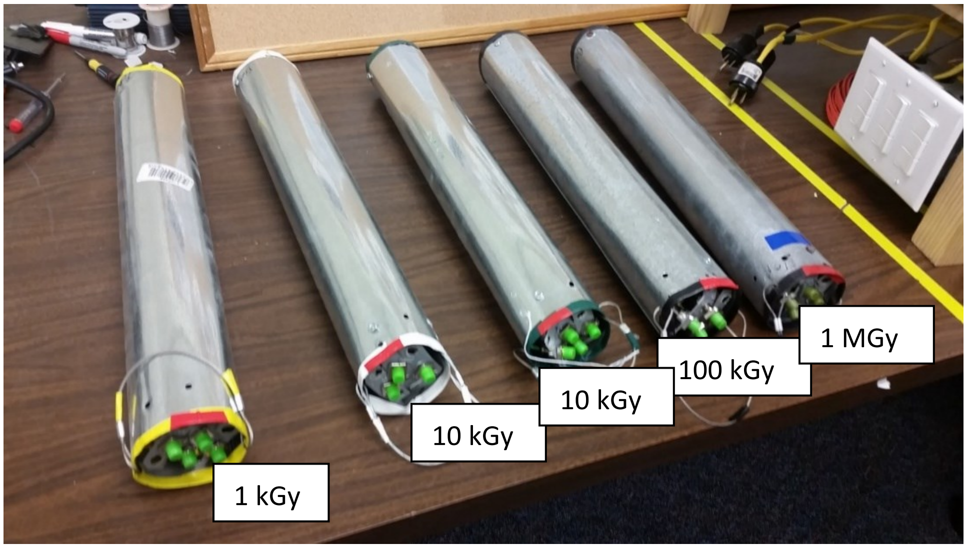

Figure 4.6: Color Comparison for Test Rig Dose Ranges

The 1 MGy color change was most significant. The PVC structural center tube changed from white to a charred black. This is due to gamma radiation only therefore there is no residual activity from neutron activation. The color comparison is clear in the figure below:

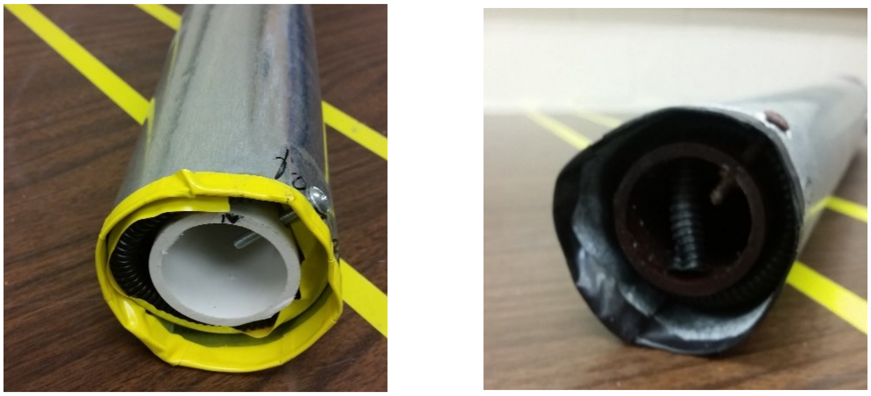

Figure 4.7: Charred black of 1 MGy compared to white for 1 kGy

4.4 Results

The fibers with intact splices could be easily compared from post-irradiation to pre-irradiation. For the 1 MGy test rig, the Germanium – 1 fiber had an intact splice. Analyzing the results of this fiber showed a significant change post irradiation. Normally the scattering within the fiber is too low to attenuate the signal. Conversely, the irradiated fiber exhibited a significant negative slope due to signal attenuation. This is seen in the analysis of the graph below:

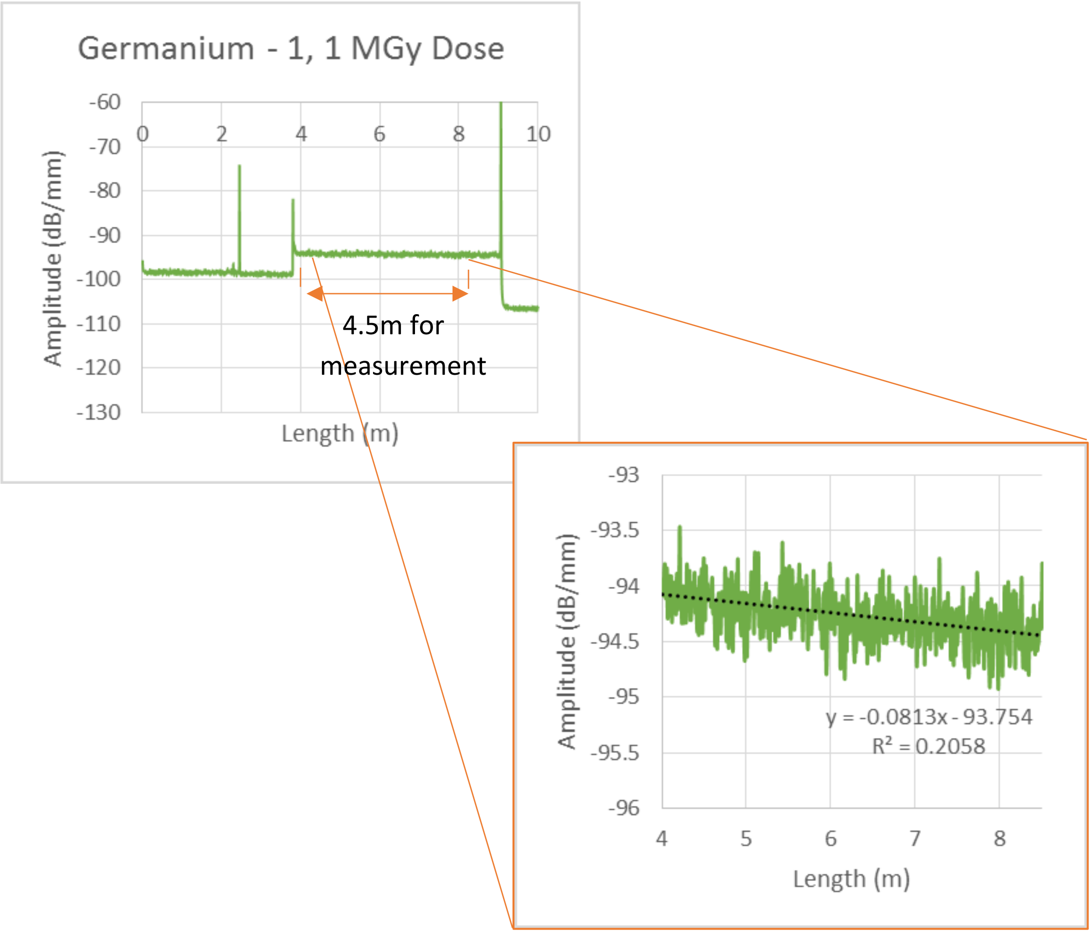

Figure 4.8: Negative Slope within Signal from 1 MGy Dosed Germanium Fiber

The scattering exhibits high frequency fluctuations around the negative trendline, therefore averaging techniques were used to better graph the signal. Complete detail on these techniques are explained in appendix chapter *A4.2 Measurement Data*. Taking the average of sequential segments of the signal before and after the irradiation shows the fluctuations as a scattering pattern unique to the fiber and consistent in both signals. This further supports the conclusion that the radiation response of the fiber is a clearly evident negative-sloped trendline. The trendline has a coefficient of determination (R^2 value) very close to 1 demonstrating how good of fit this trendline is to the difference in the signals.

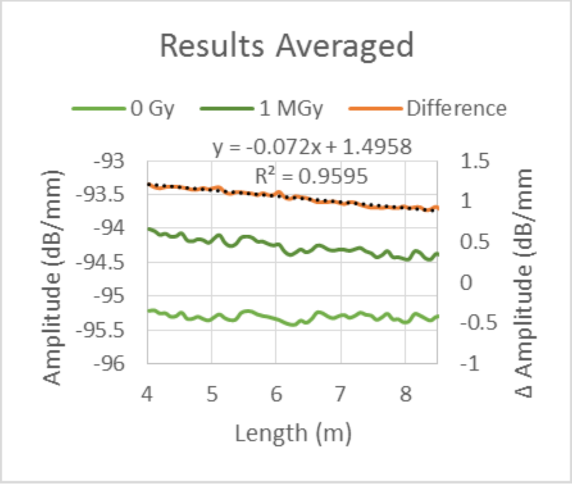

Figure 4.9: Comparison of Difference Before and After Irradiation by Averaging Results

Furthermore, within the negative-sloped trendline, it can be found that the slope calculated from shorter segments of the differential data have a varying slope. This can be seen for 1.5m segments and 0.9m segments in the following graphs:

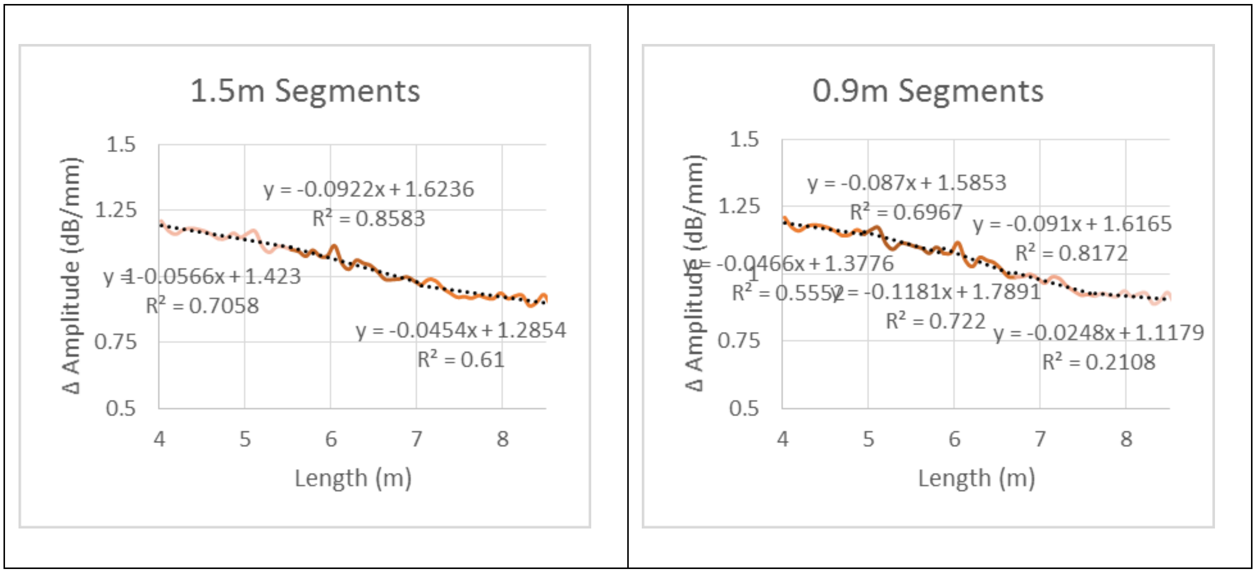

Figure 4.10: Trendlines Calculated from Difference Data in 1.5m and 0.9m Segments

Using 1.5m segments provided for 3 data points. This corresponds to 3 data points provided by Oak Ridge on the dose rate of their gamma irradiation facility. The 0.9m segments provided 5 data points. This can be mapped alongside the measured dose rate with the first and last points extrapolated. Mapping the trendline and radiation dose data sets next to each other provides for a significant new finding: the trendline data (either as 3 or 5 data points) appears to follow the radiation dose distribution. Although it is not a perfect match, it is difficult to dictate exactly where the dosimetry data was taken so the fact that it matches as well as it does is noteworthy. This can be seen graphically as follows:

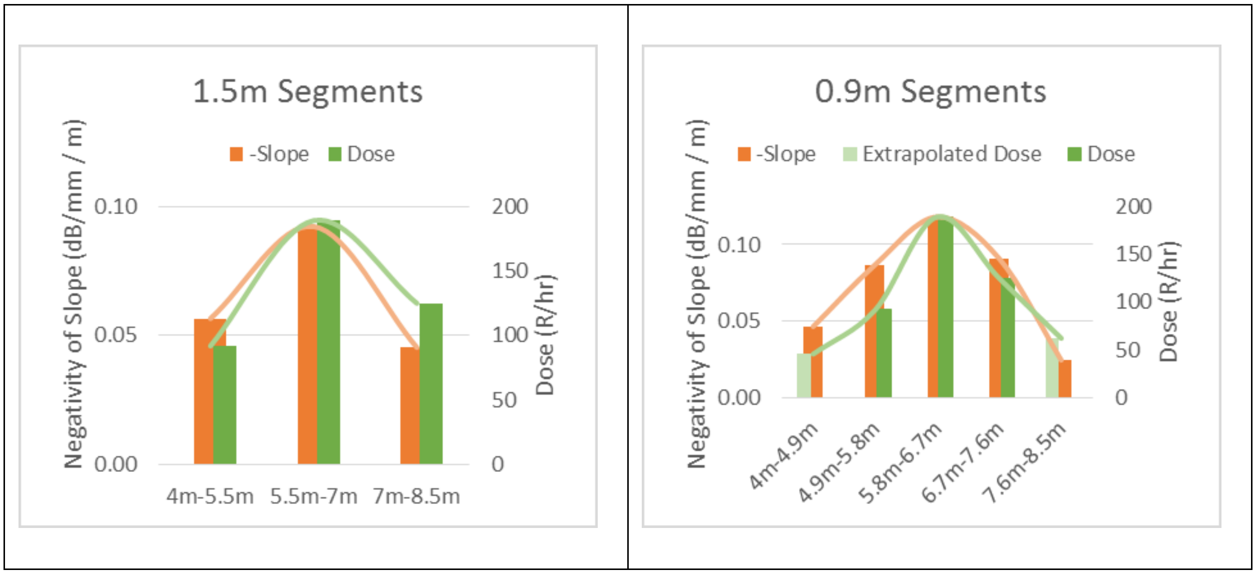

Figure 4.11: Trendline Data Compared to Radiation Dosimetry Data

Because the distributions of this data is so similar, the evidence is supported that the response to radiation of the fiber for the 1 MGy dose range correlates to the irradiation received and can be demonstrated as a spatially distributed measurement. For a projection of the lower magnitude doses, it is likely not evident that such a correlation can be obtained. For an order of magnitude less irradiation, it can be anticipated that the results would exhibit a negative slope one order of magnitude less significant which is within the noise range of the measurement. This is demonstrated by conducting the same analysis techniques for the lowest dose ranges, 100 Gy and 1 kGy. These doses exhibited a signal difference with a slope close to an order of magnitude less significant however in the positive rather than negative direction. It should be expected that the response to radiation should be an induced negative slope. However, as the positive slope demonstrates, the comparison of scattering profiles for these dose ranges does not exhibit a discernable radiation response. These results can be seen in the figure as follows:

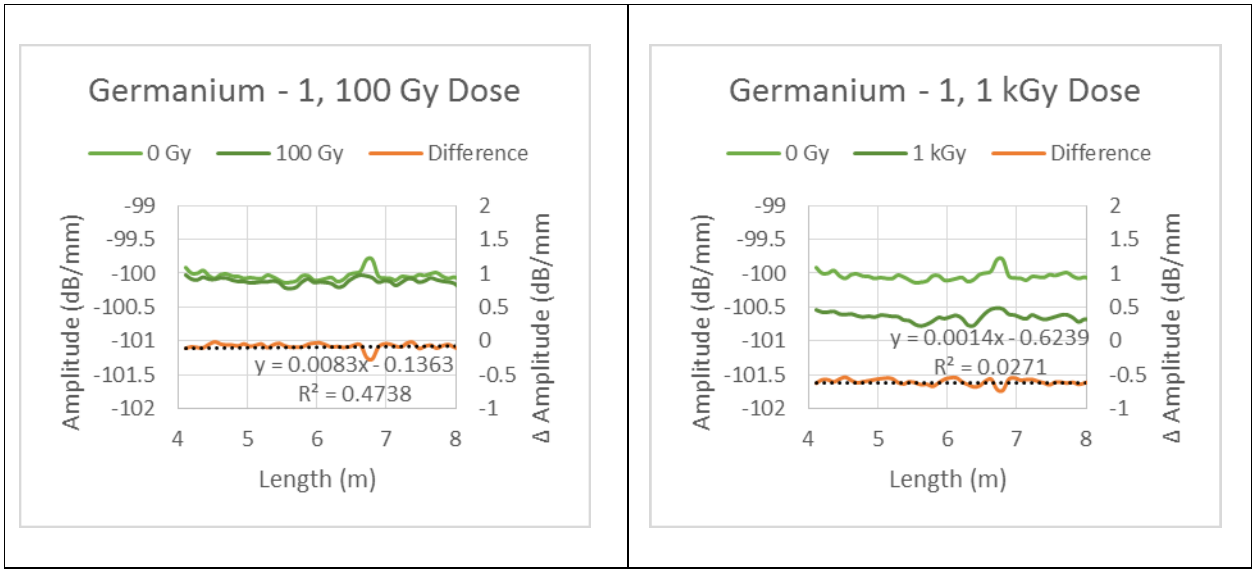

Figure 4.12: Response Analysis for Germanium (1) Fiber at Low Dose Ranges (100 Gy and 1 kGy)

5. FINAL SUMMARY

The 3 research objectives theoretical reactor power reconstruction, experimental heat source reconstruction, and correlation of radiation dose establish the overall objective as the use fiber optics for reactor power monitoring. This is unique from past research on fiber optics for survivability as a material. Instead, this research is for the application of fiber optics for power monitoring by their use as a measurement device distributed along a continuous spatial domain. Each of these individual research objectives had results that showed they could be implemented successfully. With the combination of 3 separate and distinctive dissertation objectives, the feasibility of using fiber optics for reactor power monitoring can be supported towards further development. There may be a day that this research can be applied to enable fiber optics to provide key measurements for reconstruction of power in high temperature reactors where current technology cannot be used. Furthermore, the application of fiber optics might be of use right now in support of existing light water reactor designs to alleviate concerns from the limits in power profile detection by current technology.

REFERENCES

Chapra, S. C. (2008). *Applied Numerical Methods with MATLAB.* New York: McGraw Hill.

Cheymmol, G., Long, H., Villard, J. F., & Brichard, B. (2008). High Level Gamma and Neutron Irradiation of Silica Optical Fibers in CEA OSIRIS Nuclear Reactor. *IEEE Transactions on Nuclear Science*, 2252-2258.

Doka, G. (2012). *Excel 3D Scatter Plot*.

Gifford, D., Soller, B., Wolfe, M., & Froggatt, M. (n.d.). *Distributed Fiber-Optic Temperature Sensing using Rayleigh Backscatter.* Blacksburg, VA: Luna Technologies.

Gifford, D., Soller, B., Wolfe, M., & Froggatt, M. (n.d.). *Distributed Fiber-Optic Temperature Sensing using Rayleigh Backscatter.* LUNA Technologies.

Graham, K., & Gopal, R. (1978). *USA Patent No. 4,079,236.*

Hawkes, J. M. (2004). *The Simulation and Study of Conditions Leading to Axial Offset Anomaly in Pressurized Water Reactors.* Georgia Insitute of Technology.

Luna Technologies. (2009). *Optical Backscatter Reflectometer Model 4400, User Guide.* Blacksburg, VA.

Mourlevat, J. L. (n.d.). *A fixed incore based system for an on line core margin monitoring.* Paris, France: Framatone-ANP.

Newman, C. (2015, June 22). *Format VBA Code Inside A Microsoft Word Document*. Retrieved from TheSpreadsheetGuru: https://www.thespreadsheetguru.com/the-code-vault/format-vba-code-inside-microsoft-word-document

P. Tsvetkov, e. a. (2013). "A Distributed Fiber Optic Sensor Network for Online 3-D Temperature and Neutron Fluence Mapping in a VHTR". *NEUP Final Report, Project No. 09-808*.

The MathWorks, Inc. (2012). LSQNONNEG Linear least squares with nonnegativity constraints. *MATLAB*.

Wen, J., Peng, G.-D., Luo, W., Xiao, Z., Chen, Z., & Wang, T. (2011). Gamma irradiation effect on Rayleigh scattering in low water peak single-mode optical fibers. *OPTICS EXPRESS*.

Westinghouse. (n.d.). *Westinghouse Tecnology Systems Manual, Section 3.1, Reactor Vessel and Internals.*

Wikipedia. (2018, February). Retrieved from Non-negative least squares: https://en.wikipedia.org/wiki/Non-negative_least_squares

Yokogawa. (2014). *AQ7277 REMOTE OPTICAL TIME DOMAIN REFLECTOMETER*. Retrieved May 29, 2014, from http://tmi.yokogawa.com/us/products/optical-measuring-instruments/optical-time-domain-reflectometer/aq7277-remote-optical-time-domain-reflectometer/

APPENDIX 2: THEORETICAL REACTOR POWER RECONSTRUCTION

A2.1 8th Core Models Source Point Attenuation Factors

A2.1.1 Appendix Introduction

This appendix chapter documents the attenuation factors obtained for the theoretical models research objective with 8th core models. These models had high resolution for their source point characterizations required numerous simulations which took a very long time to obtain consistent data, specifically for the internal core points. Each source point's attenuation factor for each characterization (15 point, 45 point, 55 point) are displayed here.

A2.1.2 15 Source Point Characterization

The 15 source point attenuation factors are displayed here as follows.

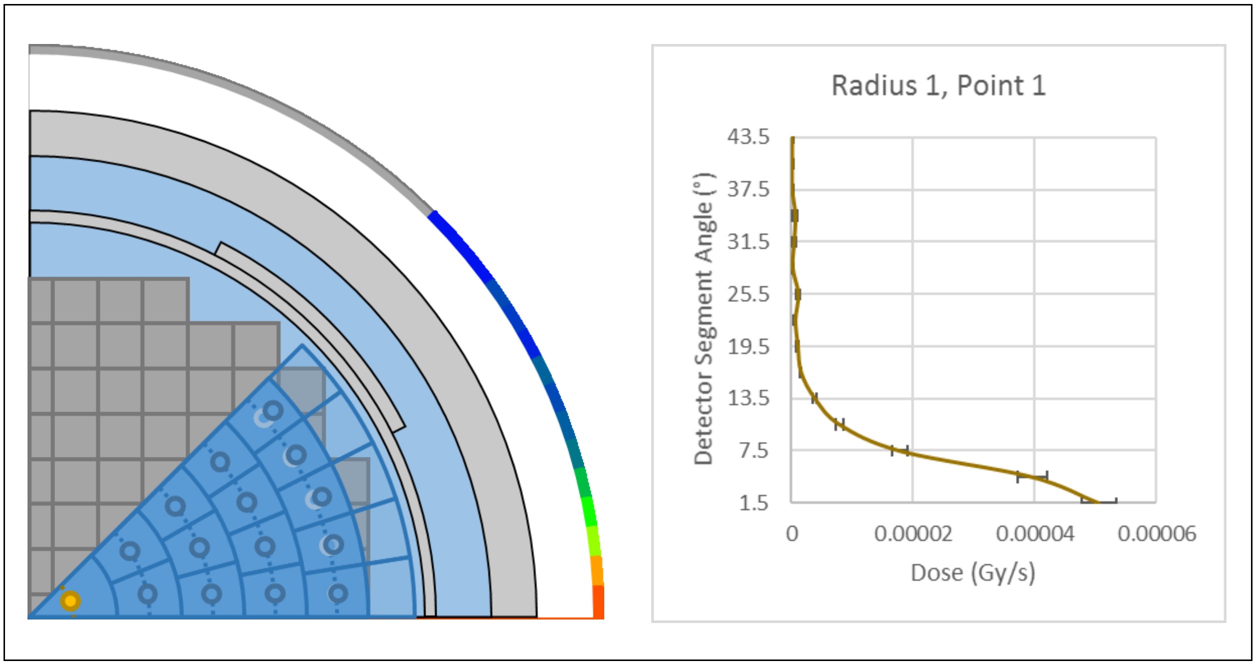

Figure A2.1: 15 Point Attenuation Factors Plotted, Radius 1

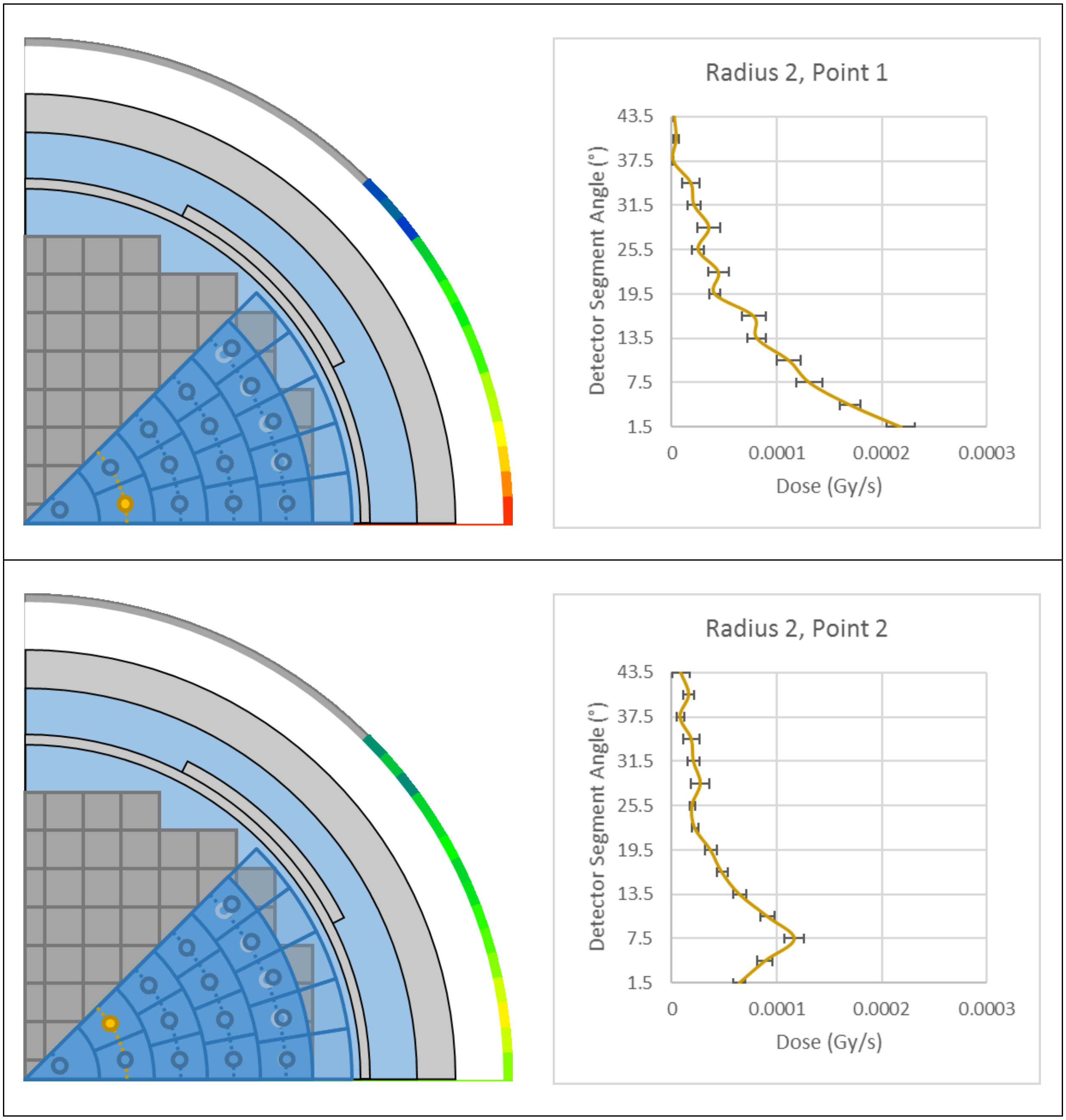

Figure A2.2: 15 Point Attenuation Factors Plotted, Radius 2

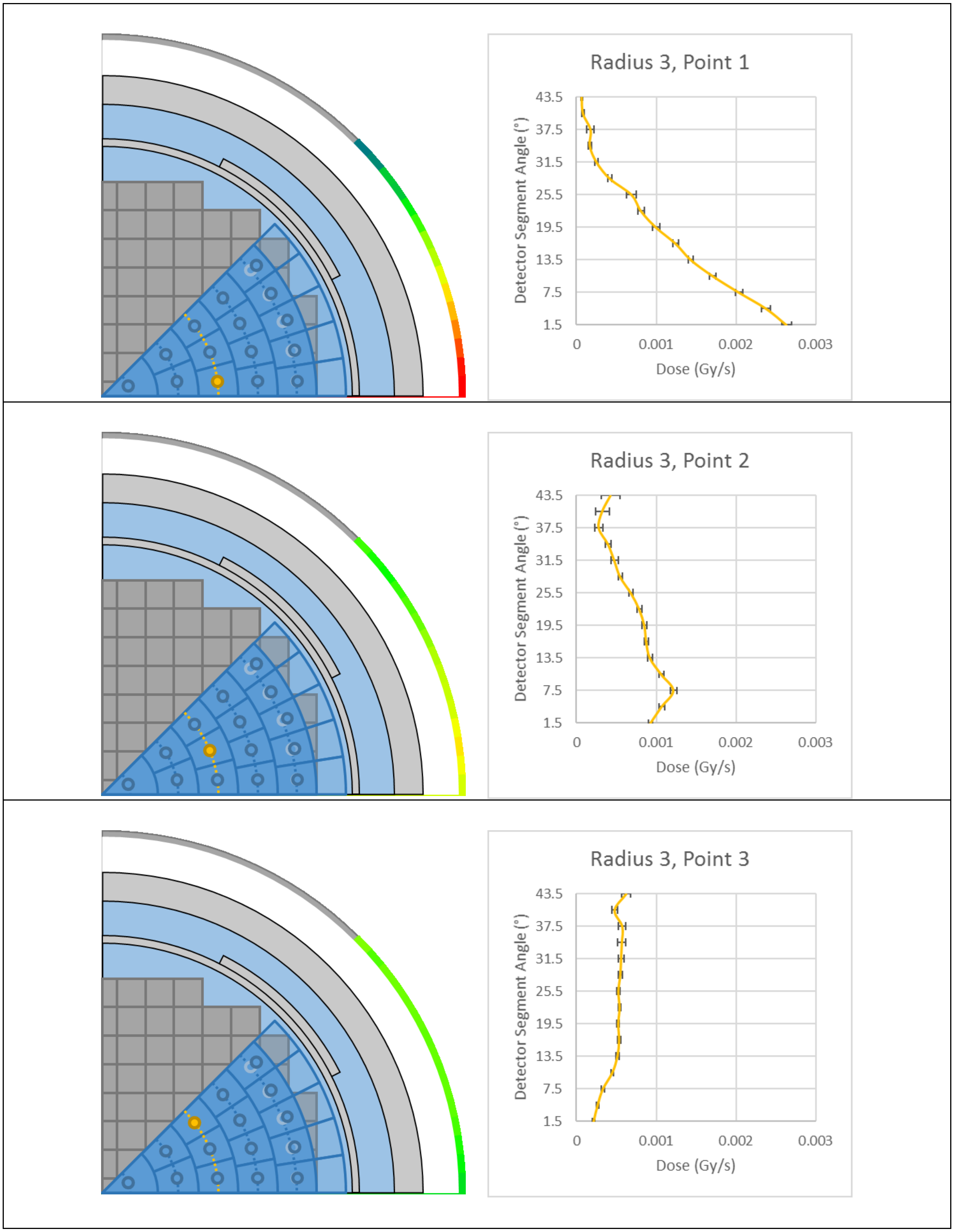

Figure A2.3: 15 Point Attenuation Factors Plotted, Radius 3

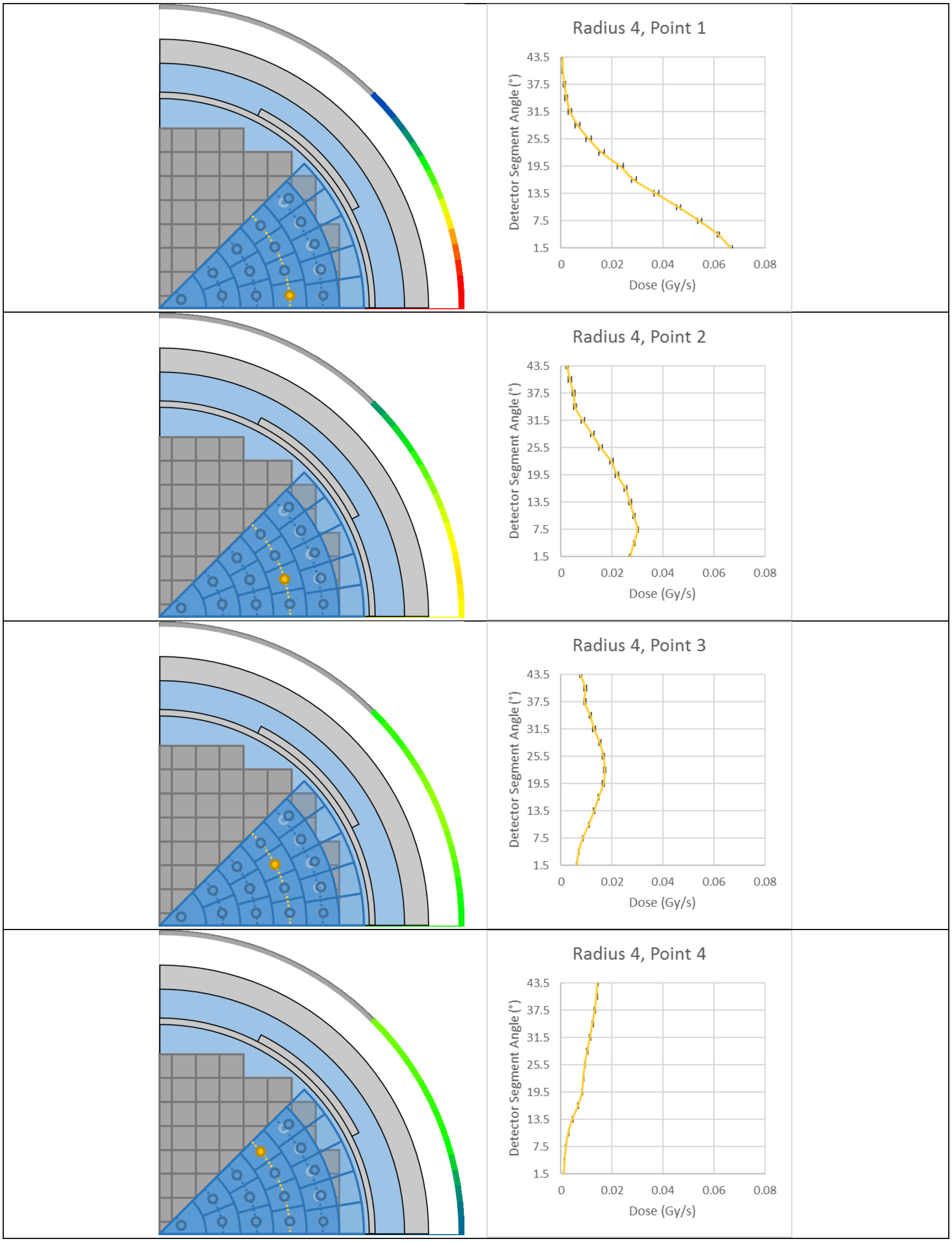

Figure A2.4: 15 Point Attenuation Factors Plotted, Radius 4

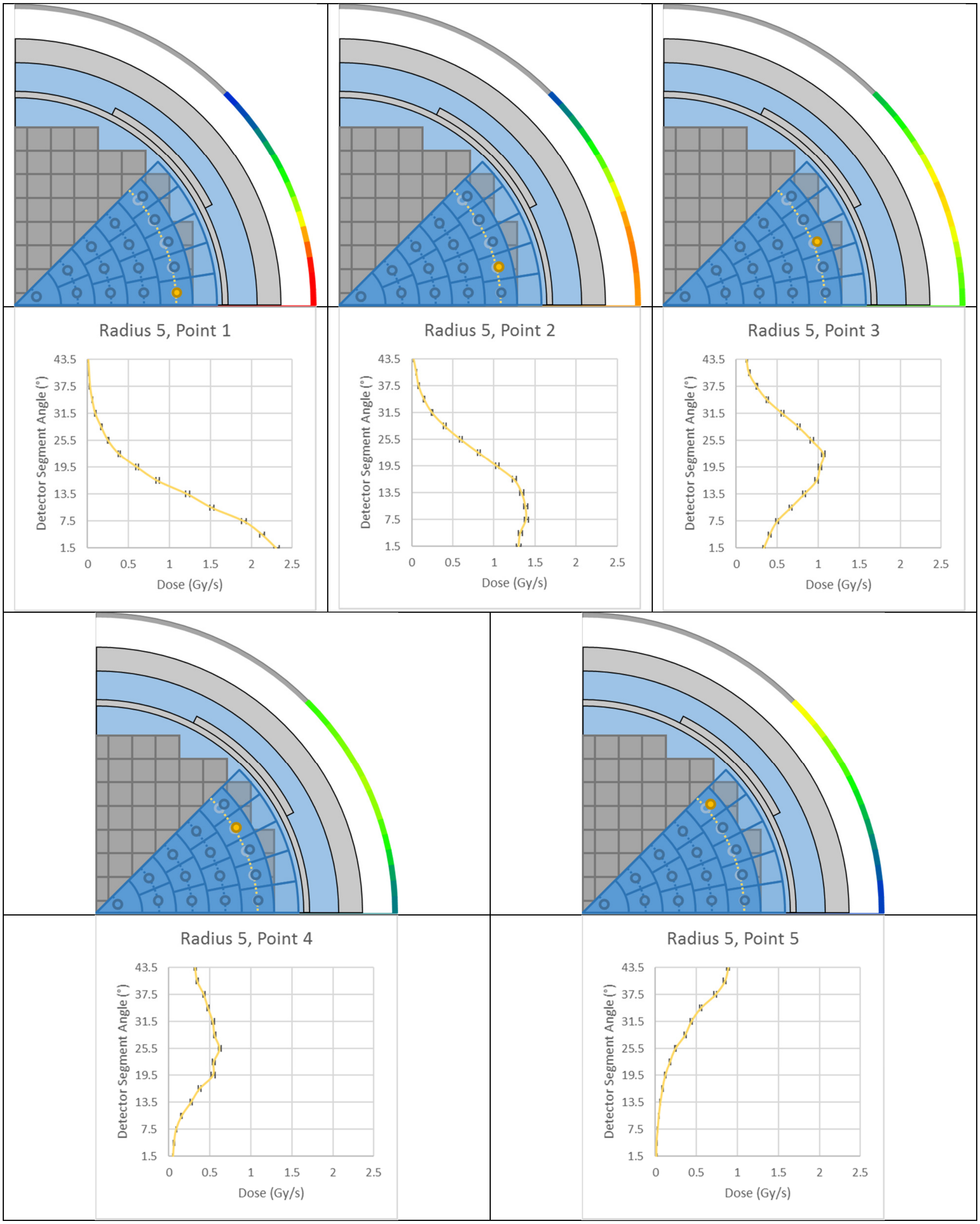

Figure A2.5: 15 Point Attenuation Factors Plotted, Radius 5

Something interesting to note is that the reflected boundary at 0° has an affect on what is being simulated. This best demonstrated by the outermost radius for the comparison of the first two points when the bottom reflective boundary is taken into account.

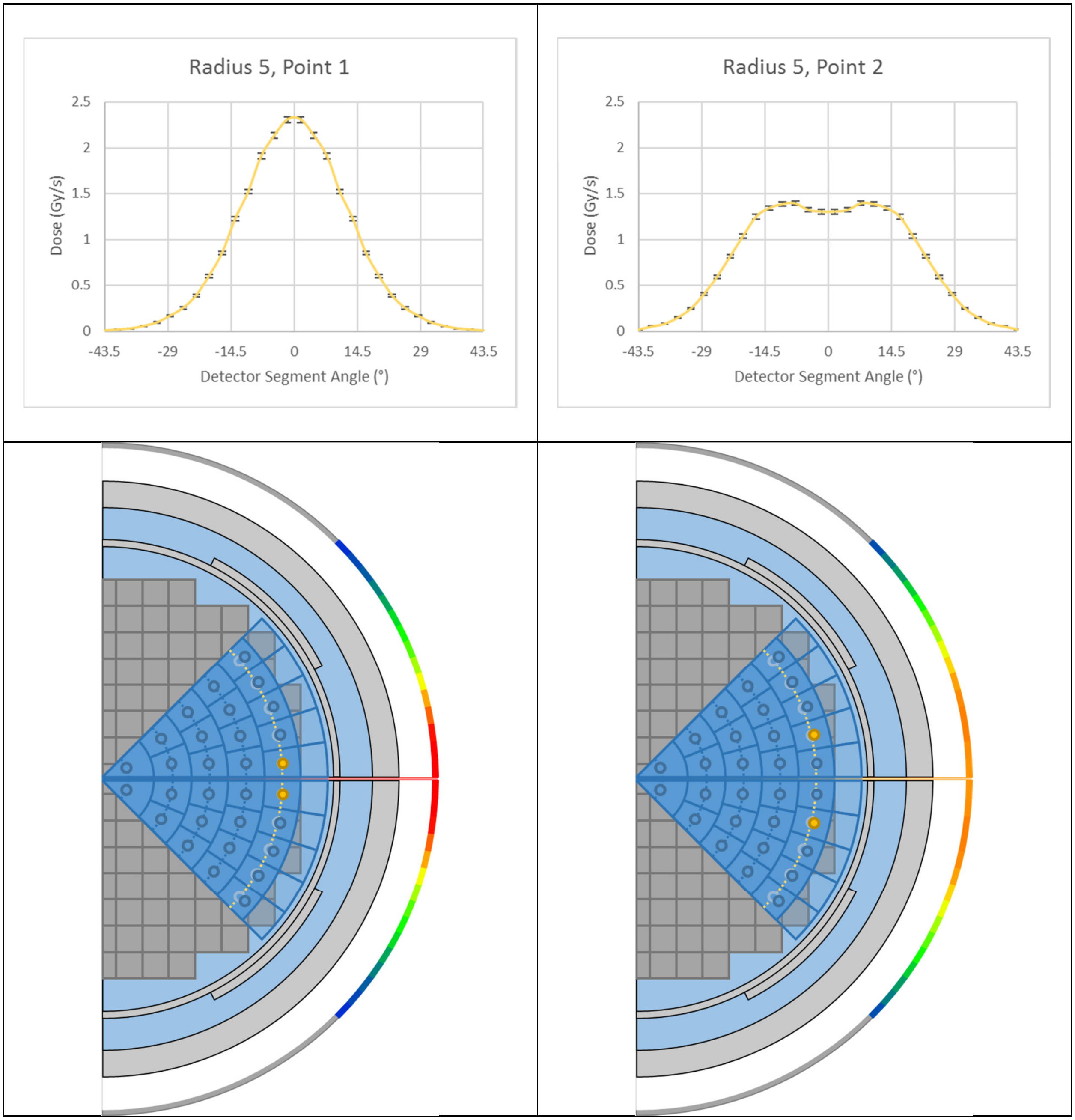

Figure A2.6: Attenuation Factors Plotted Across Reflective Boundary

A2.1.3 45 Source Point Characterization

This appendix section displays the 45 source point attenuation factors as follows.

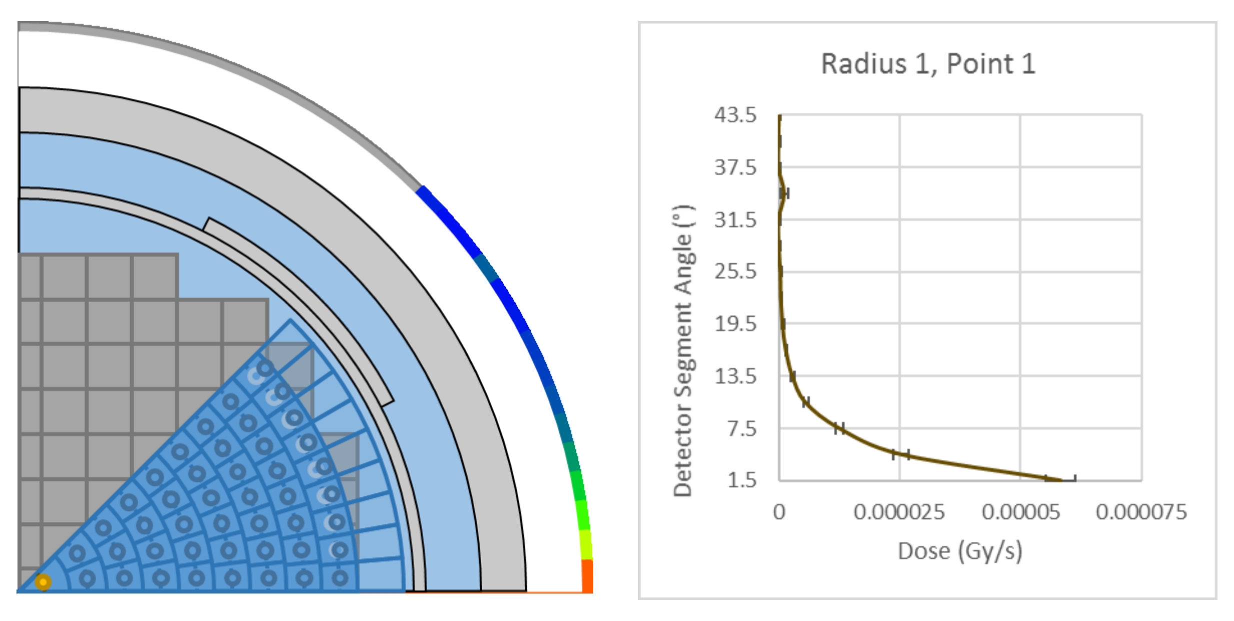

Figure A2.7: 45 Point Attenuation Factors Plotted, Radius 1

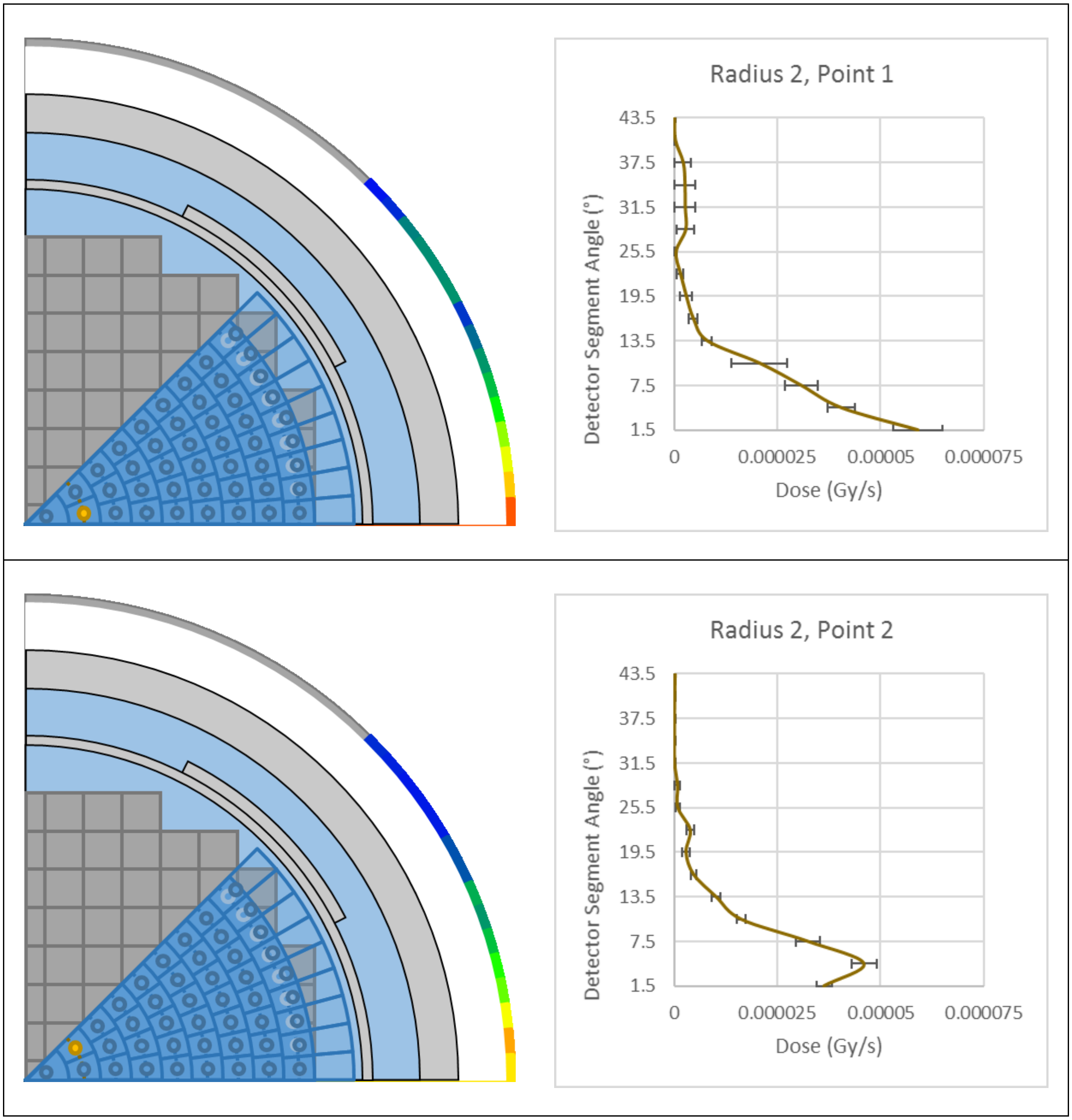

Figure A2.8: 45 Point Attenuation Factors Plotted, Radius 2

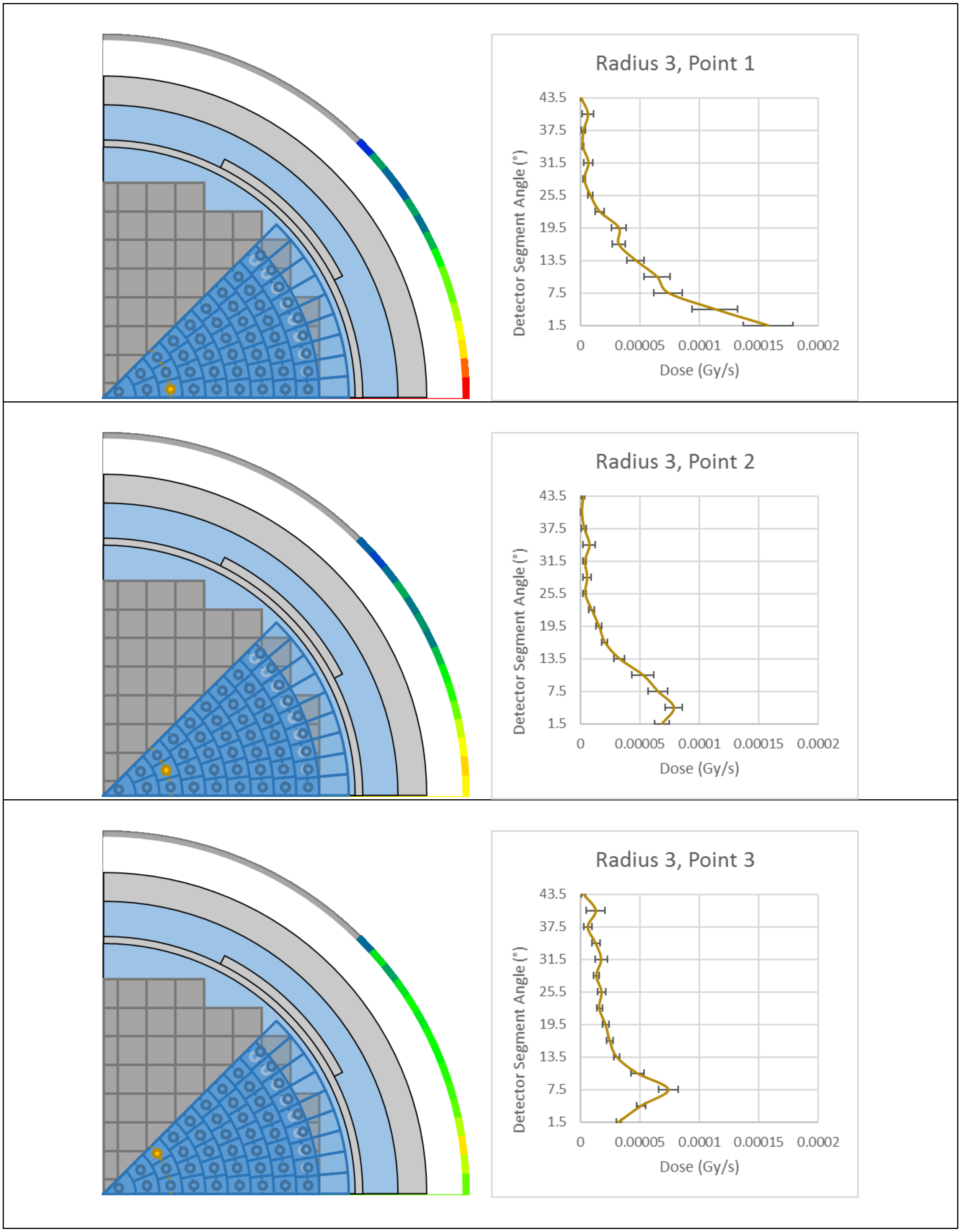

Figure A2.9: 45 Point Attenuation Factors Plotted, Radius 3

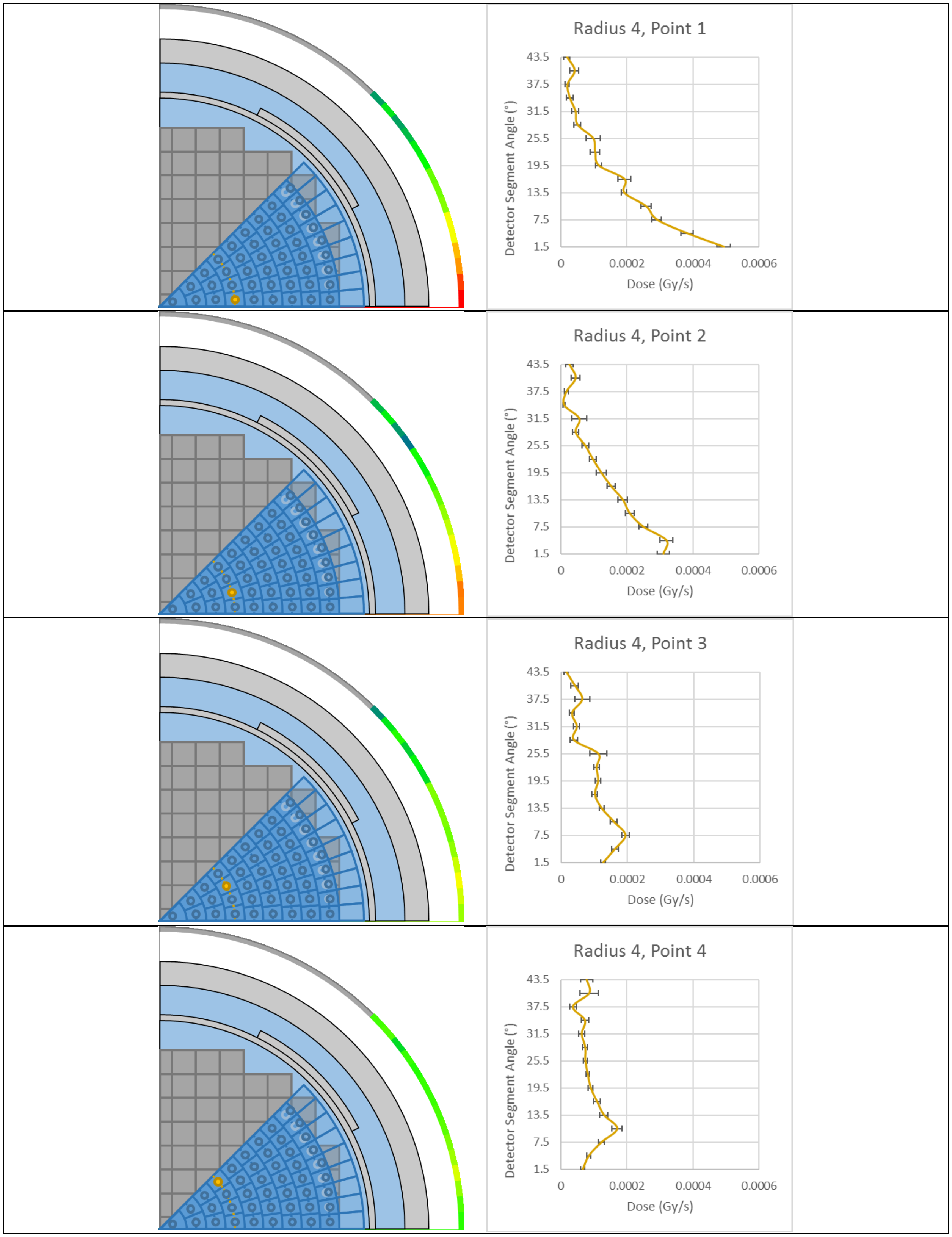

Figure A2.10: 45 Point Attenuation Factors Plotted, Radius 4

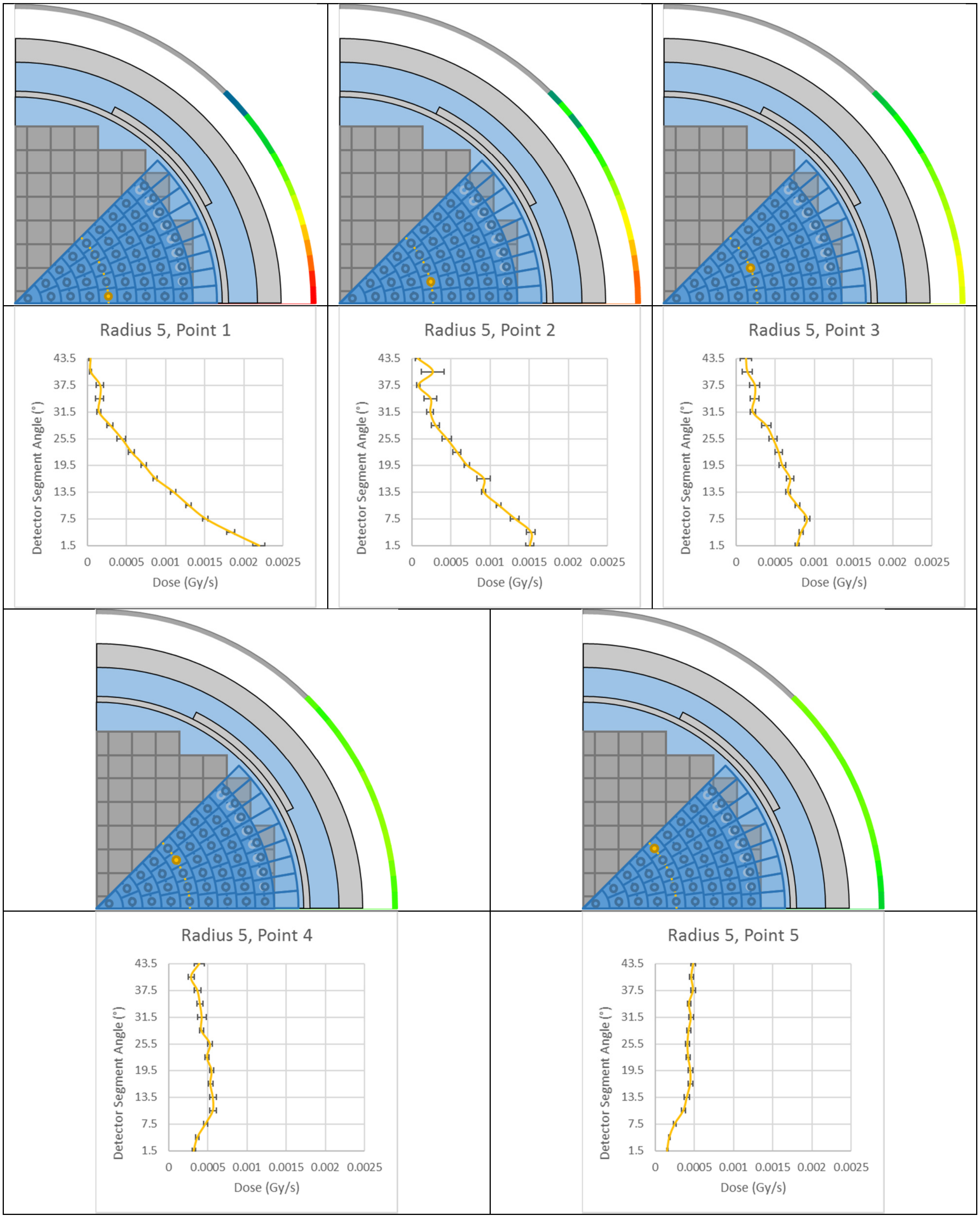

Figure A2.11: 45 Point Attenuation Factors Plotted, Radius 5

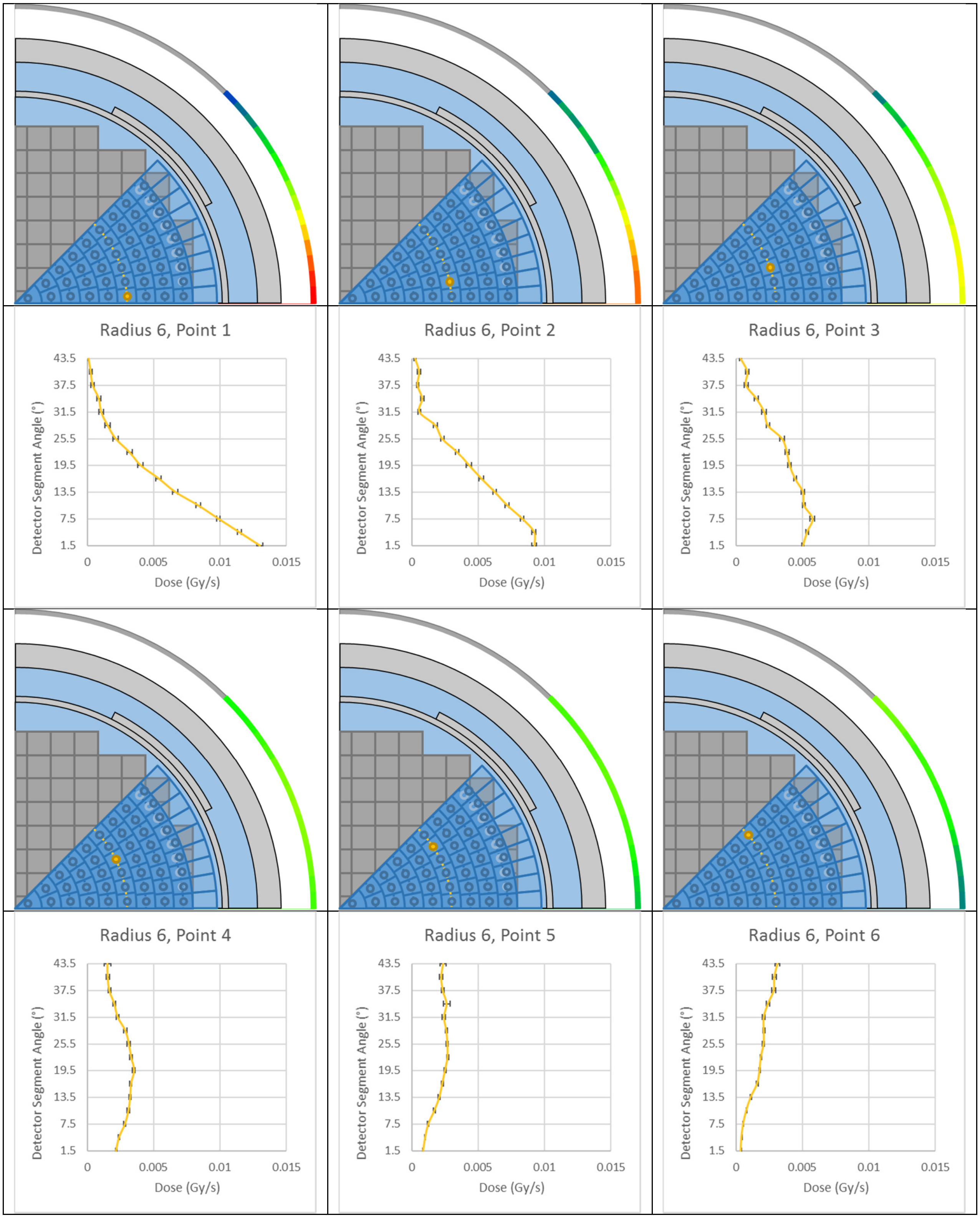

Figure A2.12: 45 Point Attenuation Factors Plotted, Radius 6

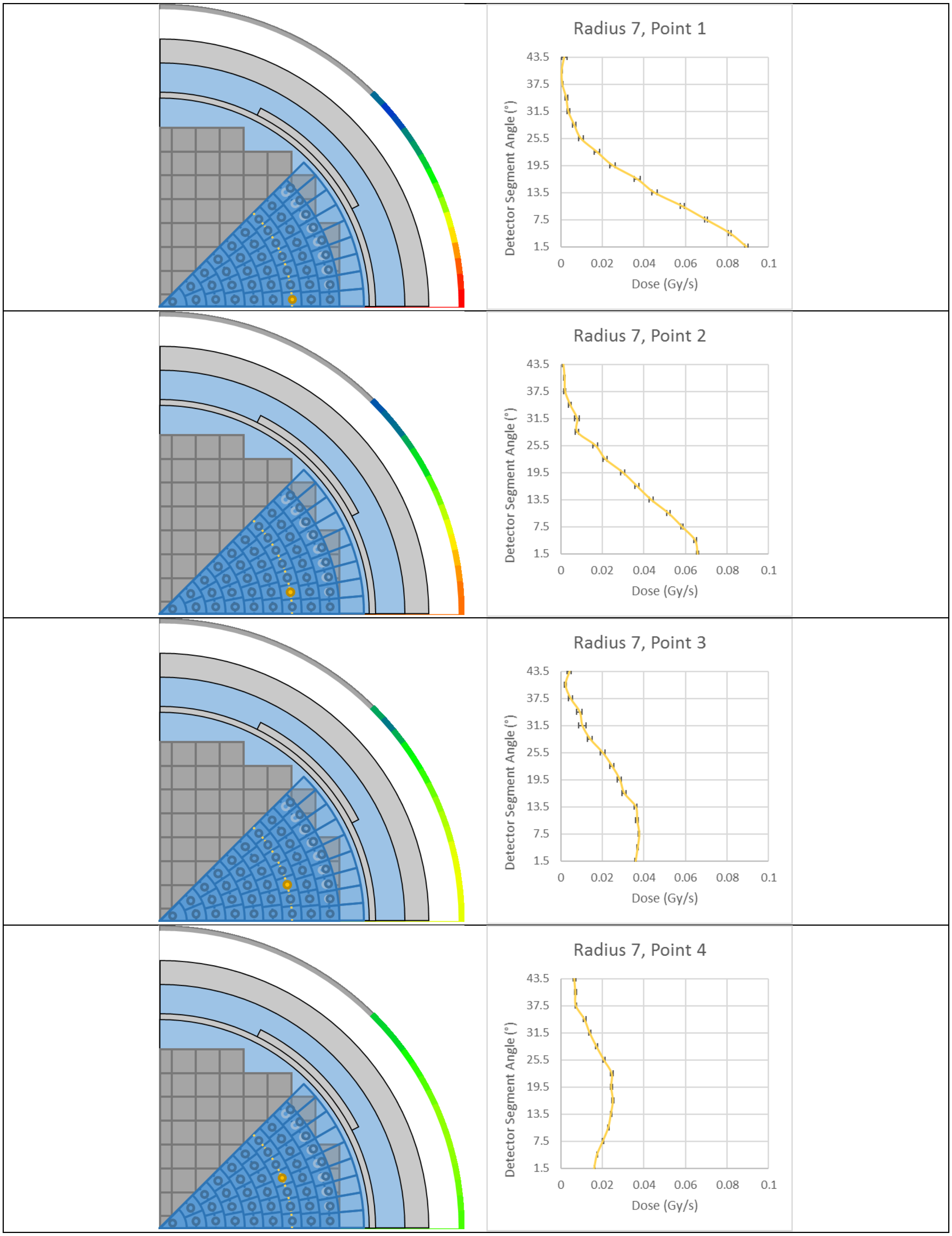

Figure A2.13: 45 Point Attenuation Factors Plotted, Radius 7

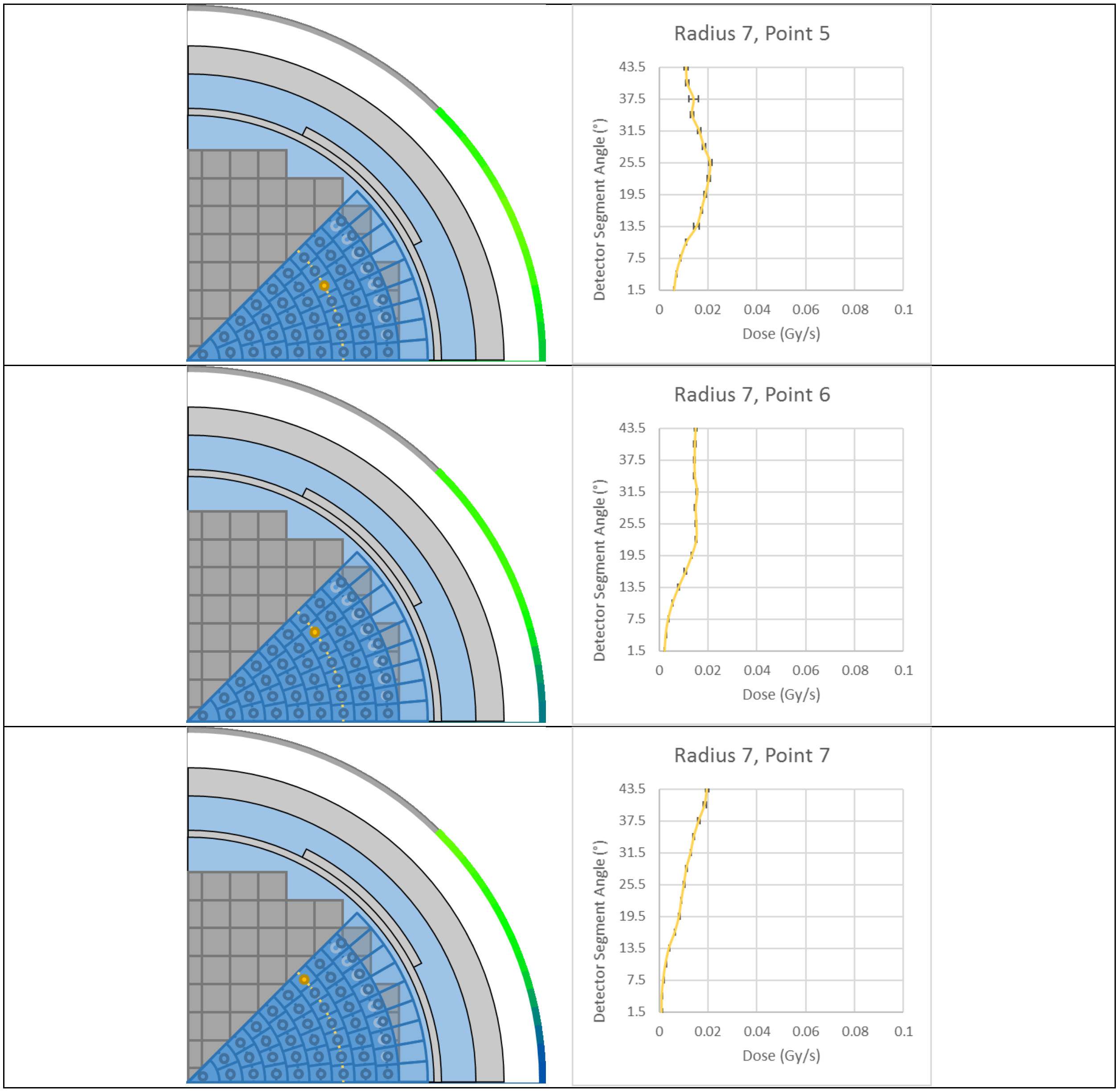

Figure A2.14: 45 Point Attenuation Factors Plotted, Radius 7 Continued

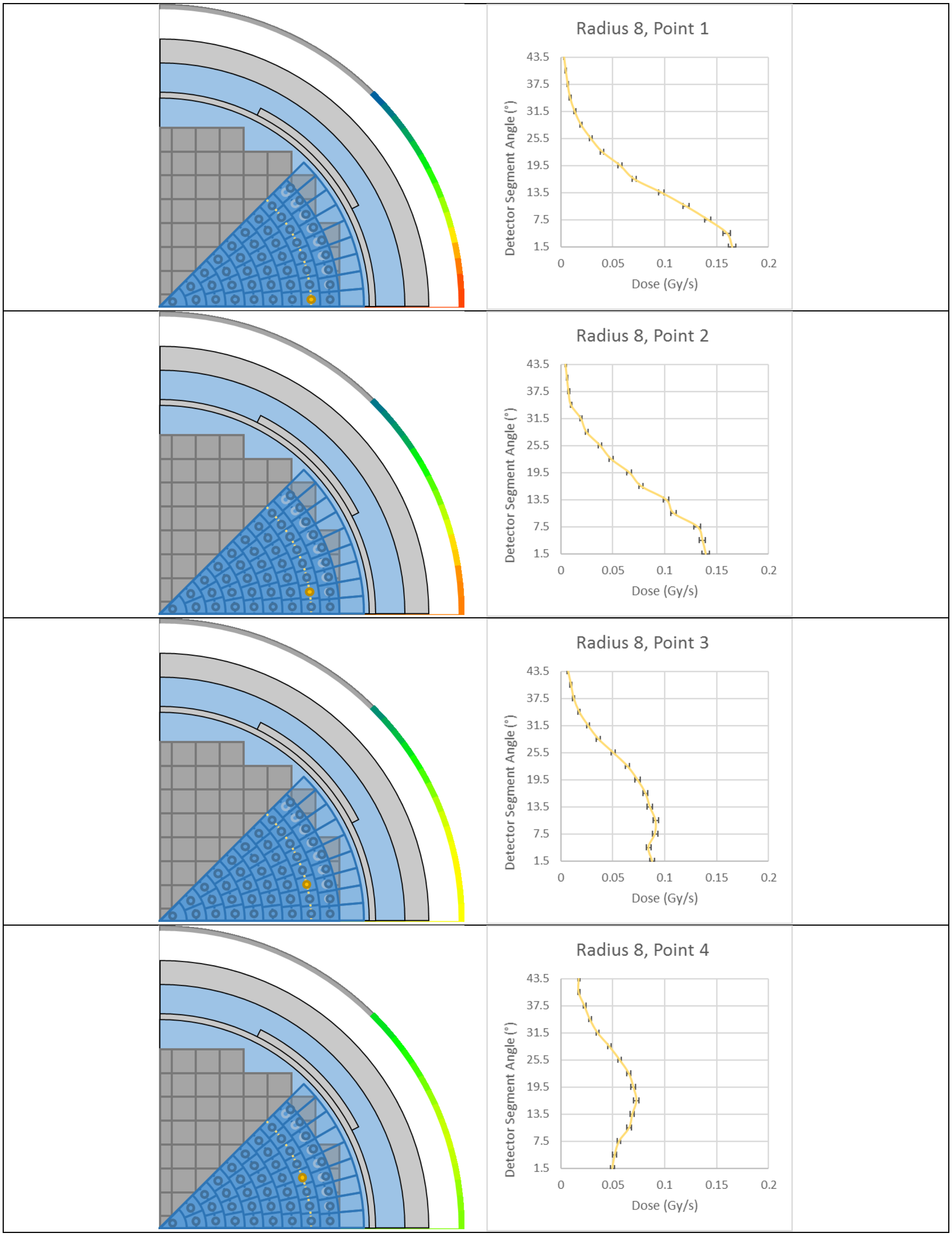

Figure A2.15: 45 Point Attenuation Factors Plotted, Radius 8

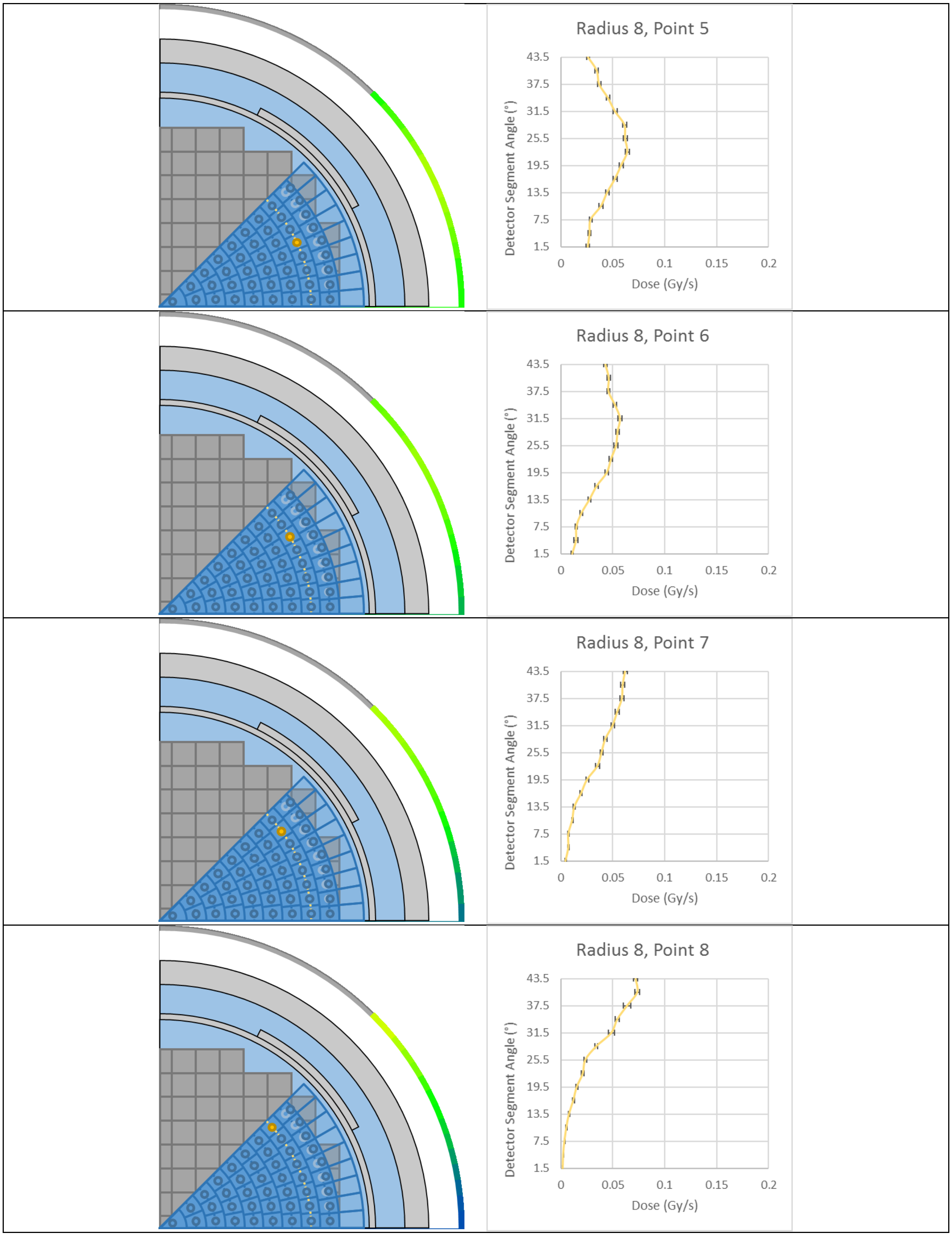

Figure A2.16: 45 Point Attenuation Factors Plotted, Radius 8 Continued

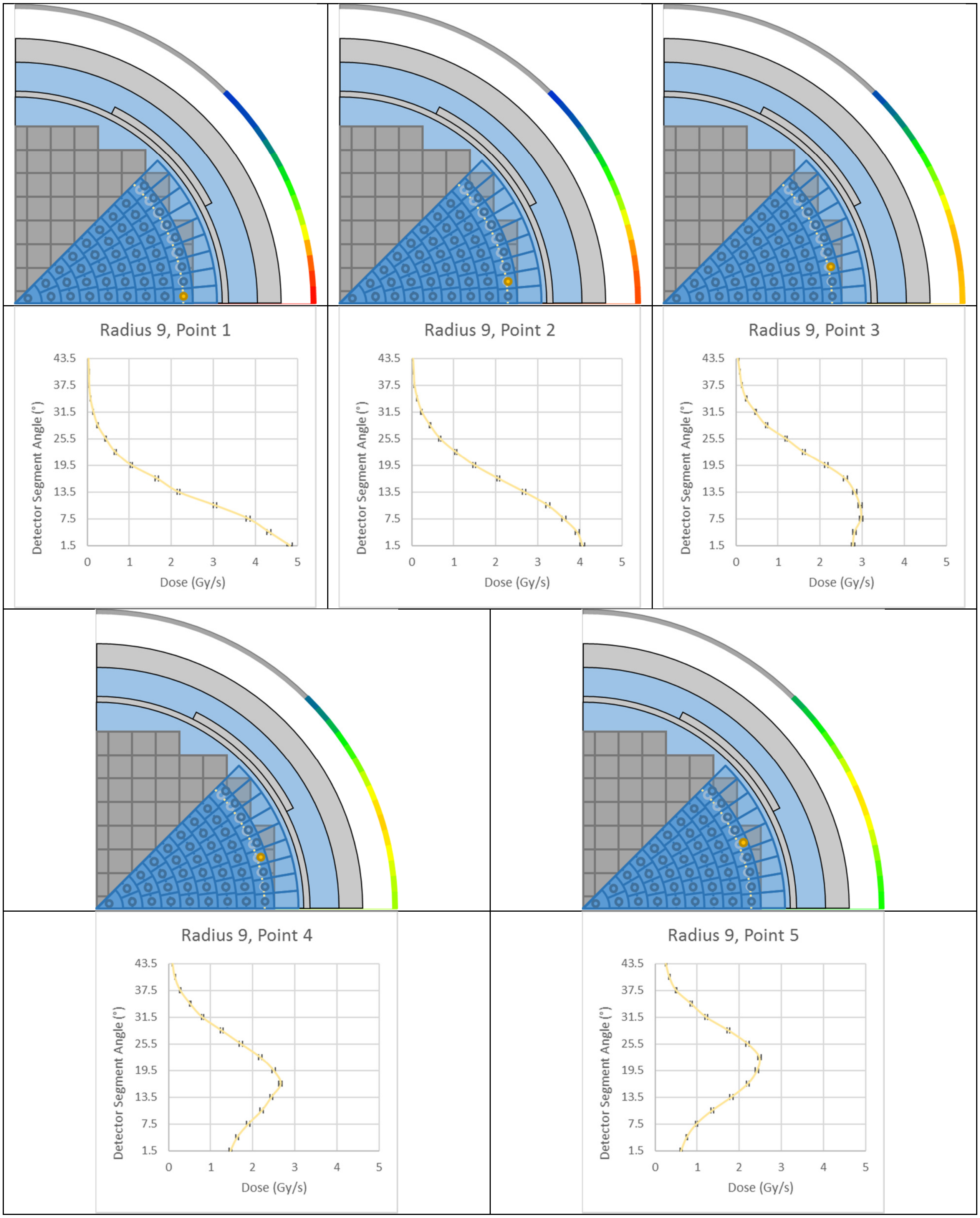

Figure A2.17: 45 Point Attenuation Factors Plotted, Radius 9

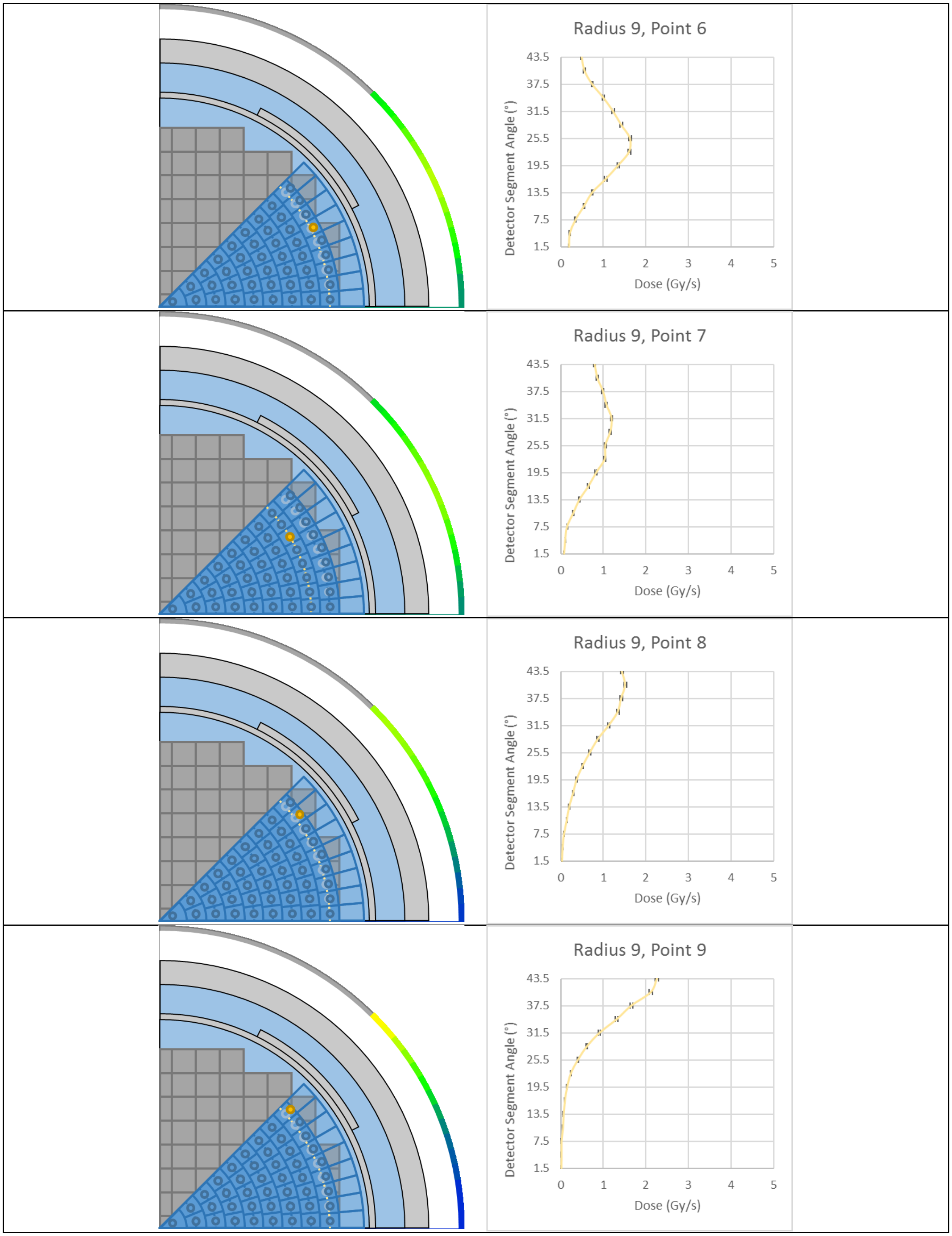

Figure A2.18: 45 Point Attenuation Factors Plotted, Radius 9 Continued

A2.1.4 55 Source Point Characterization

The 55 source point characterization has its attenuation factors plotted in reverse order. This is to better demonstrate their features. First of all, it should be noted that the outermost radius is very high, on a scale close to 10 times higher than the other models' outermost radii. This can be attributed to some of the points are outside the core so do not have any attenuation through the fuel assemblies. Figure A2.19 and Figure A2.20 display this data.

For the other radius groups, a consistent maximum value for both the colored detector plot and the scale on the line graph. This was different for the other characterizations (15 and 45 source points) which had a consistency within a radius group and not between. This different scale provides a better representation how the inward radius groups have a very diminished influence on the detector. After demonstrating this for select points of radius group 7 (Figure A2.25), it was deemed not necessary to continue plotting the other radius groups.

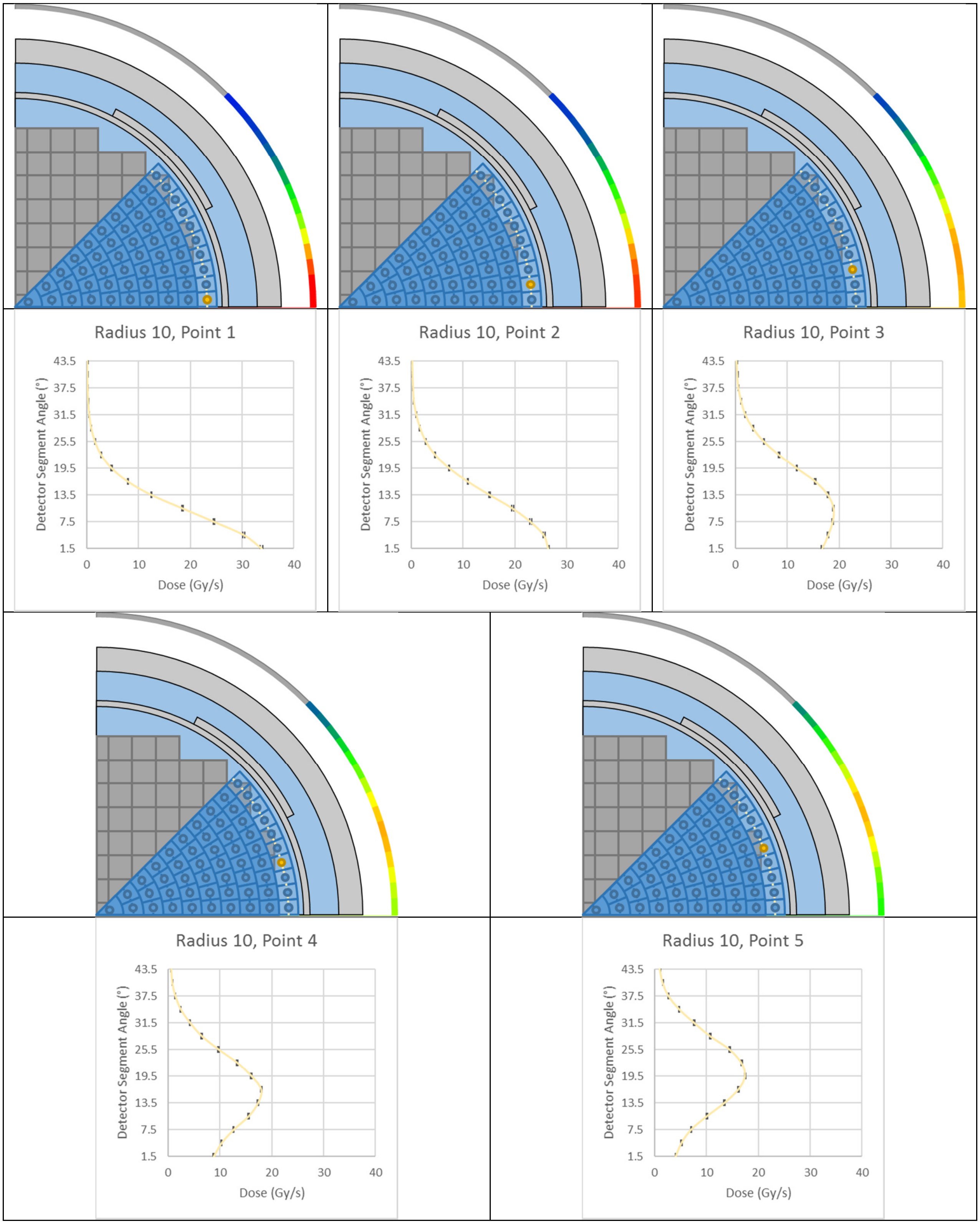

Figure A2.19: 55 Point Attenuation Factors Plotted, Radius 10

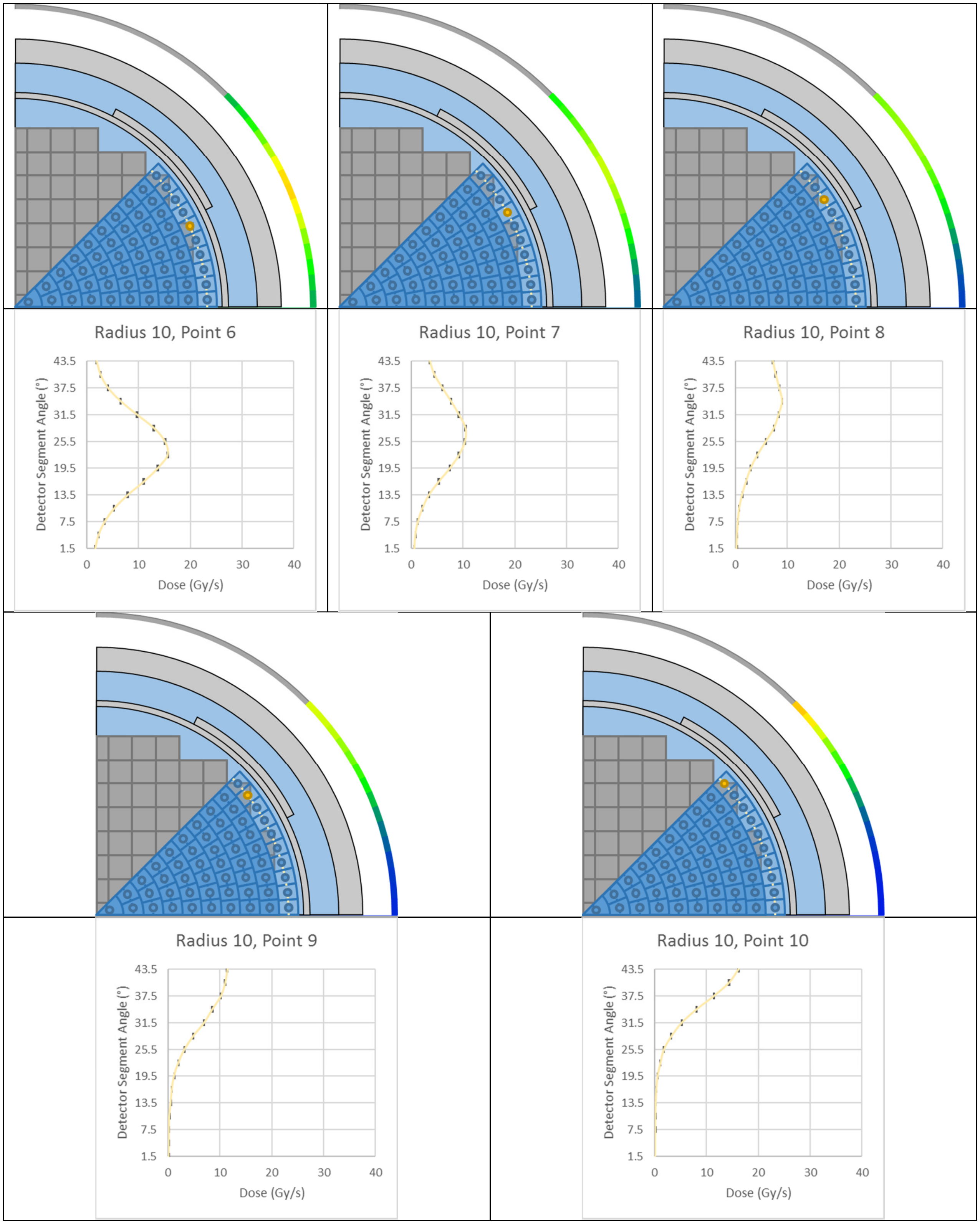

Figure A2.20: 55 Point Attenuation Factors Plotted, Radius 10 Continued

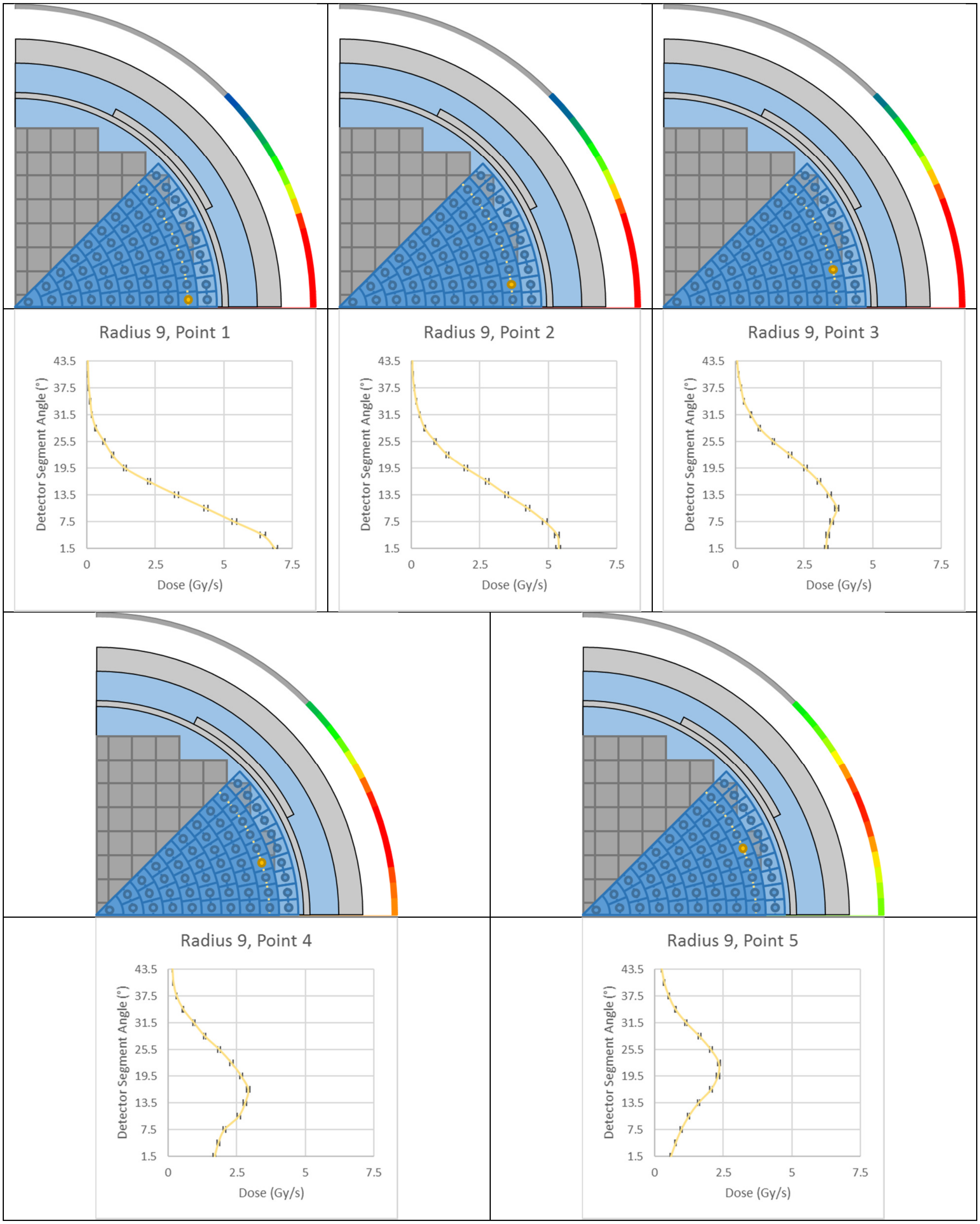

Figure A2.21: 55 Point Attenuation Factors Plotted, Radius 9

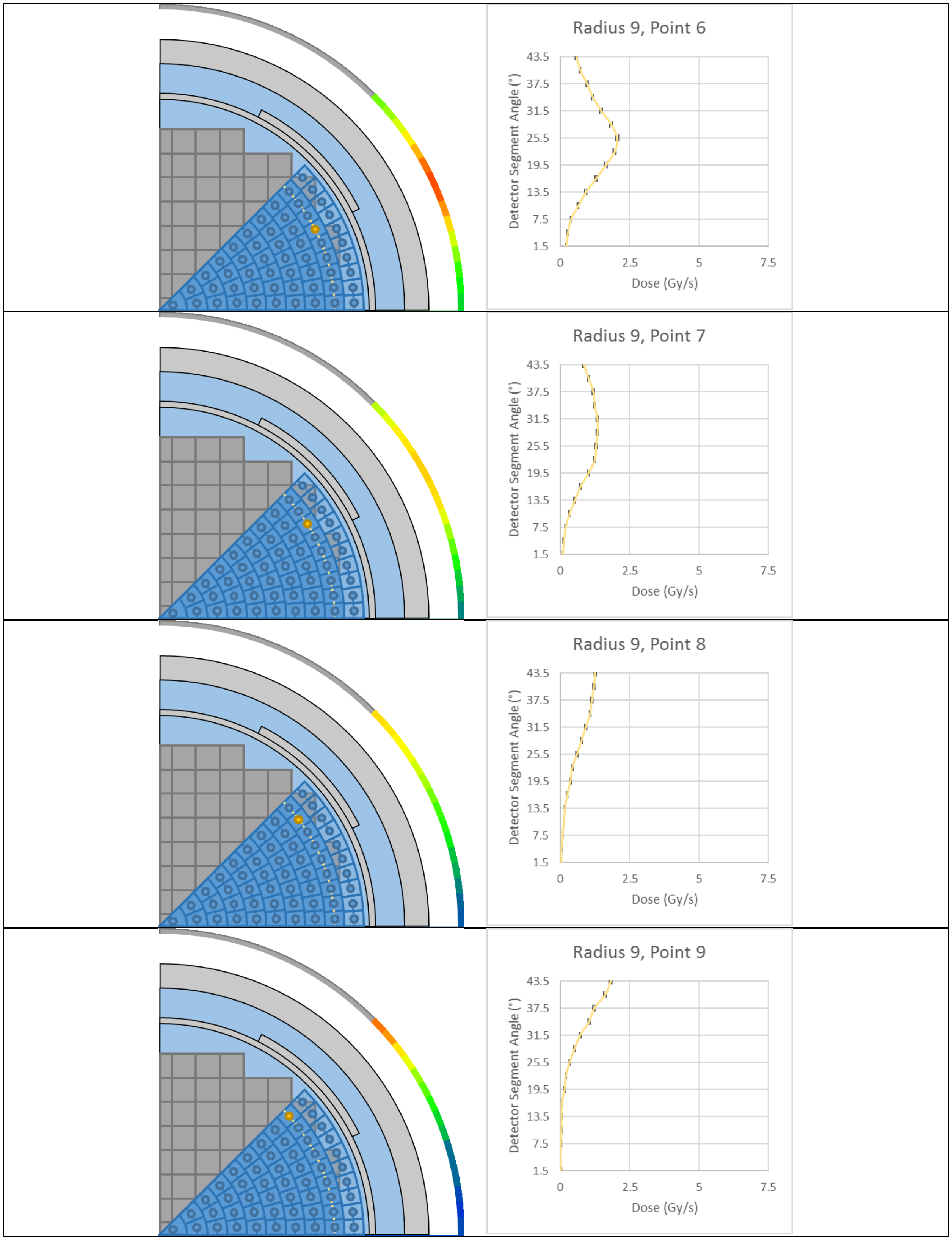

Figure A2.22: 55 Point Attenuation Factors Plotted, Radius 9 Continued

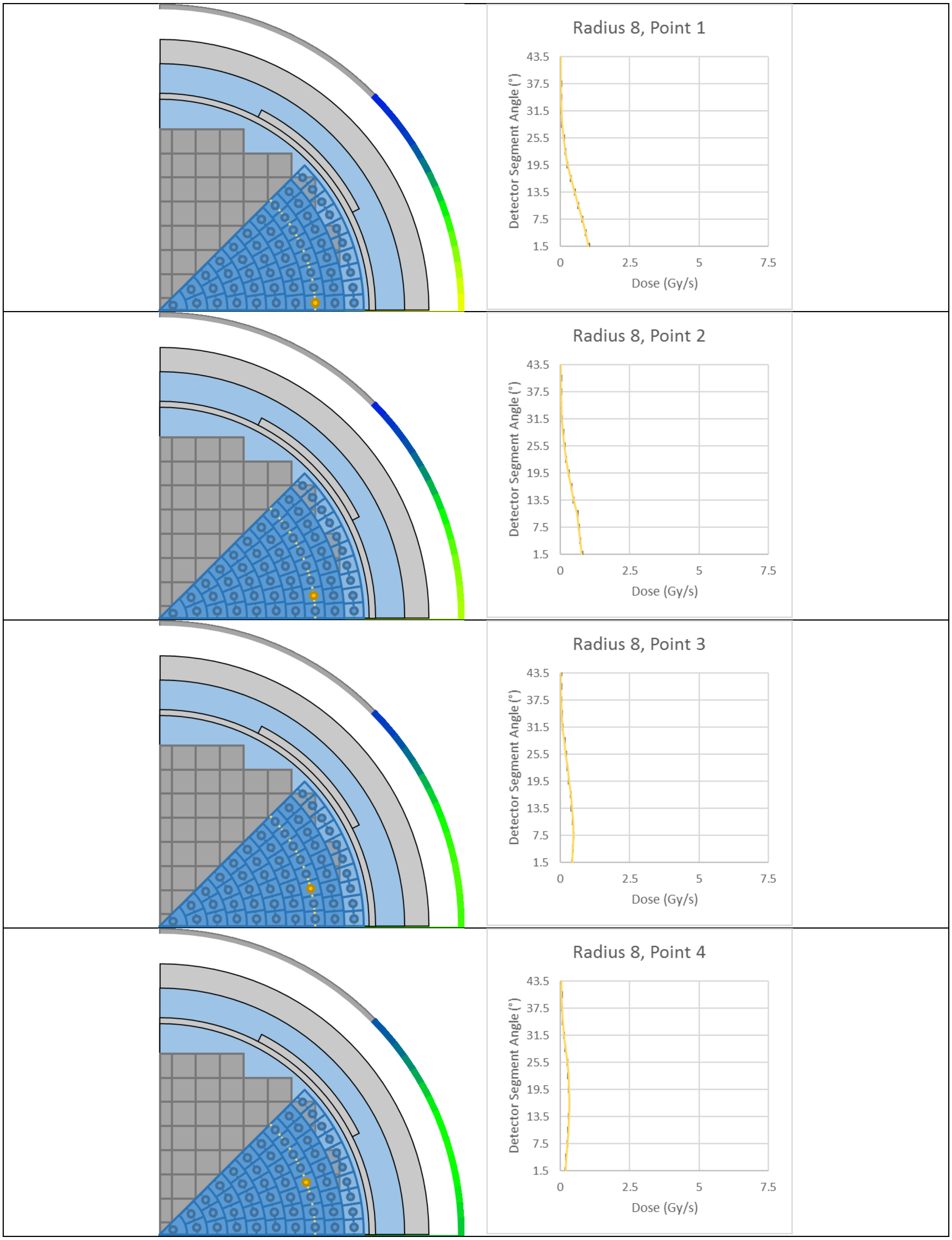

Figure A2.23: 55 Point Attenuation Factors Plotted, Radius 8

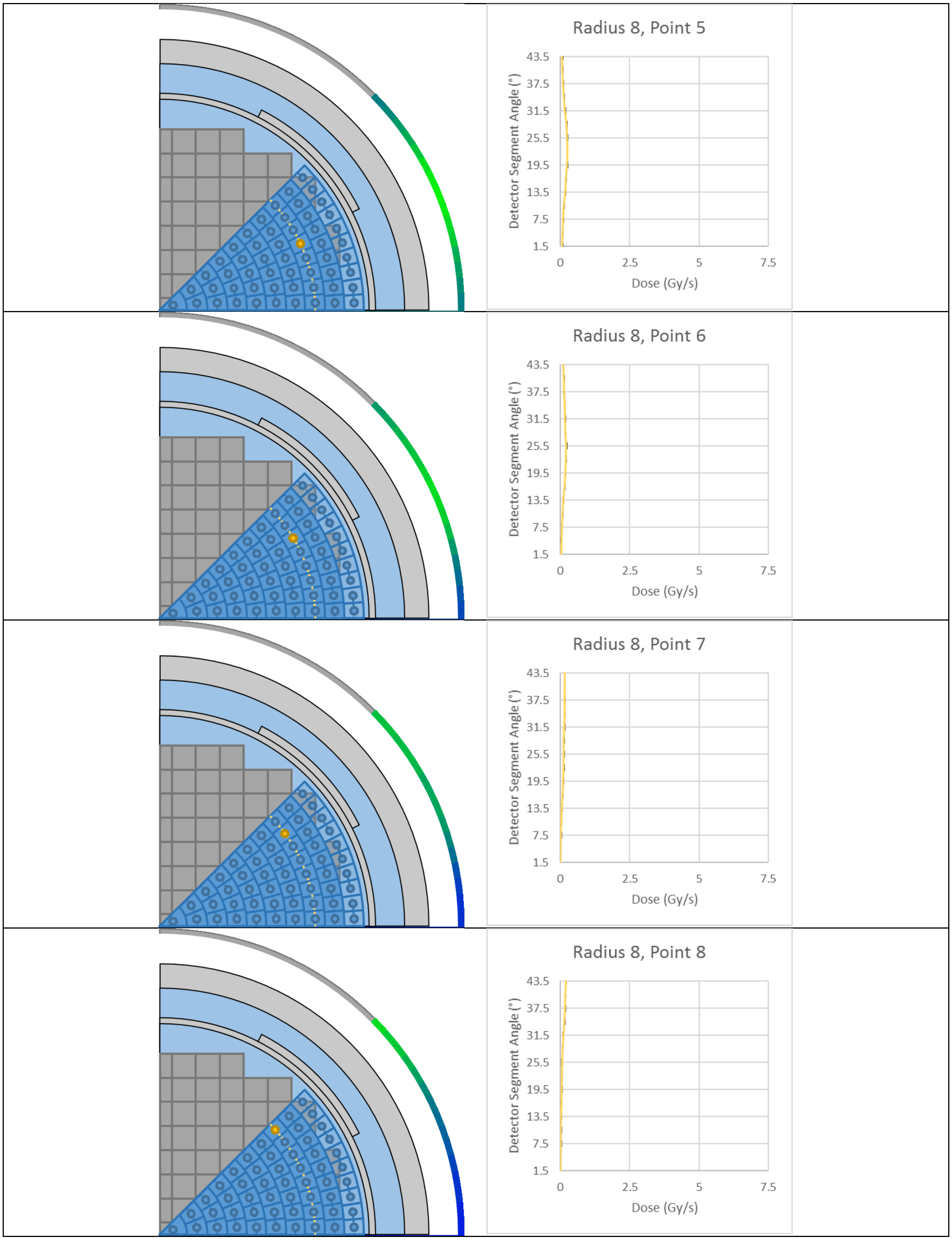

Figure A2.24: 55 Point Attenuation Factors Plotted, Radius 8 Continued

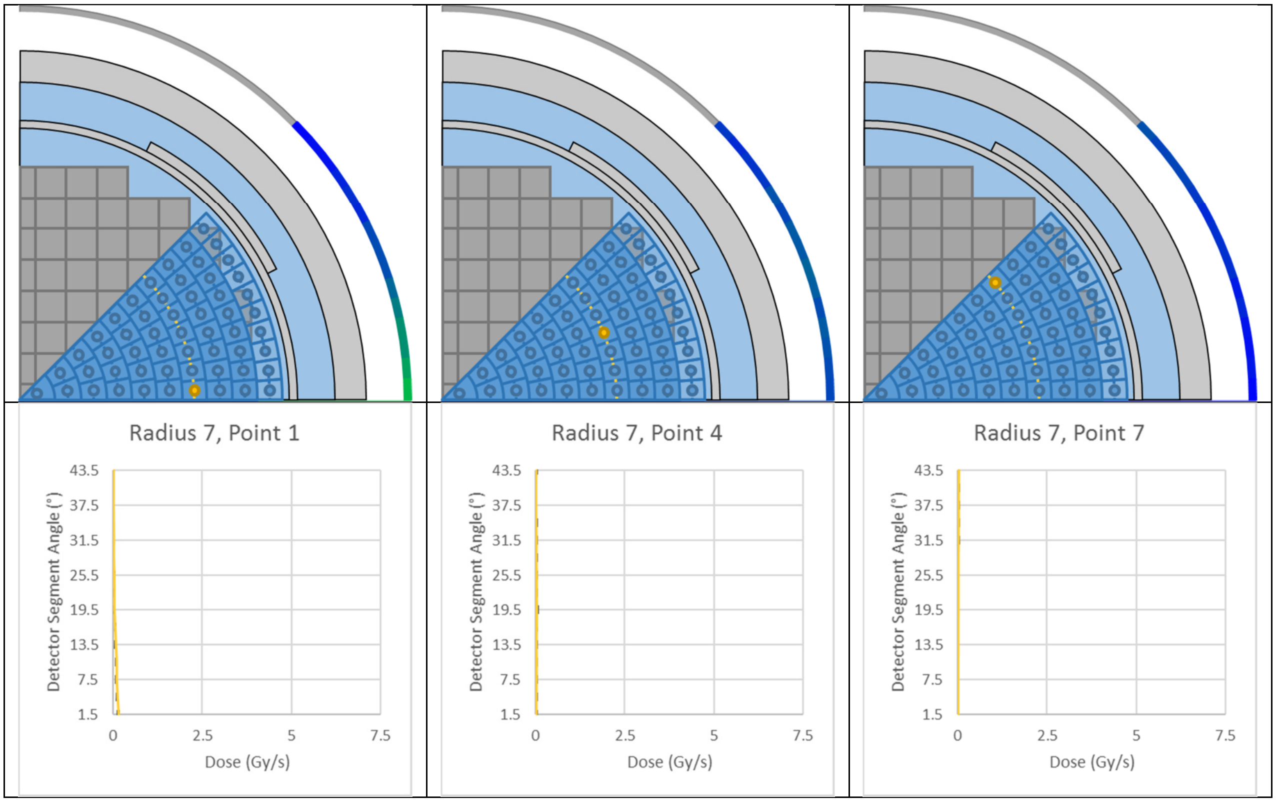

Figure A2.25: 55 Point Attenuation Factors Plotted, Radius 7 Select Points

A2.1.5 Conclusion on Attenuation Factors

Through the plotting of attenuation factors with a single scale per radius group and a consistent scale across groups helped to demonstrate the features of the source point characterization. For the single scale, it can be seen that even the most central points were able to obtain attenuation factors with good continuity. This required very long runs, high number of particles, and multiple iterations of the “weight window” variance reduction technique. For the scale across groups, it is better demonstrated the importance of correct factors for the outer radius groups while the inner radius groups affect is significantly diminished.

A2.2 Source Point Study 7x7 Array

A2.2.1 7x7 Array Description

A study to better understand the application of the source point reconstruction algorithm was conducted on a 7x7 array of points (7 rows by 7 columns). This was greatly simplified compared to the reconstruction evaluated with points distributed through a reactor model. Instead these points were in a uniform water medium. Without a criticality model, the comparison of reconstruction was in a way done against itself. The product formula of multiplying all the points by their known attenuation factors created the detector response, and the solution was then reconstructed to match this detector distribution. In this way, the solution could be reconstructed iteratively on acceptable solutions that varied by a certain percentage from the exact detector response.

This study provided for a benefit of evaluating the difference reconstruction techniques of either gamma dose evaluated or neutron dose or both together. The gamma and neutron provided unique sets of attenuation factors and therefore had unique solutions. The attenuation factors for select points from the 7x7 array are displayed in Figure A2.2a-1 and Figure A2.2a-2 for dose from gamma radiation and neutron radiation respectively.

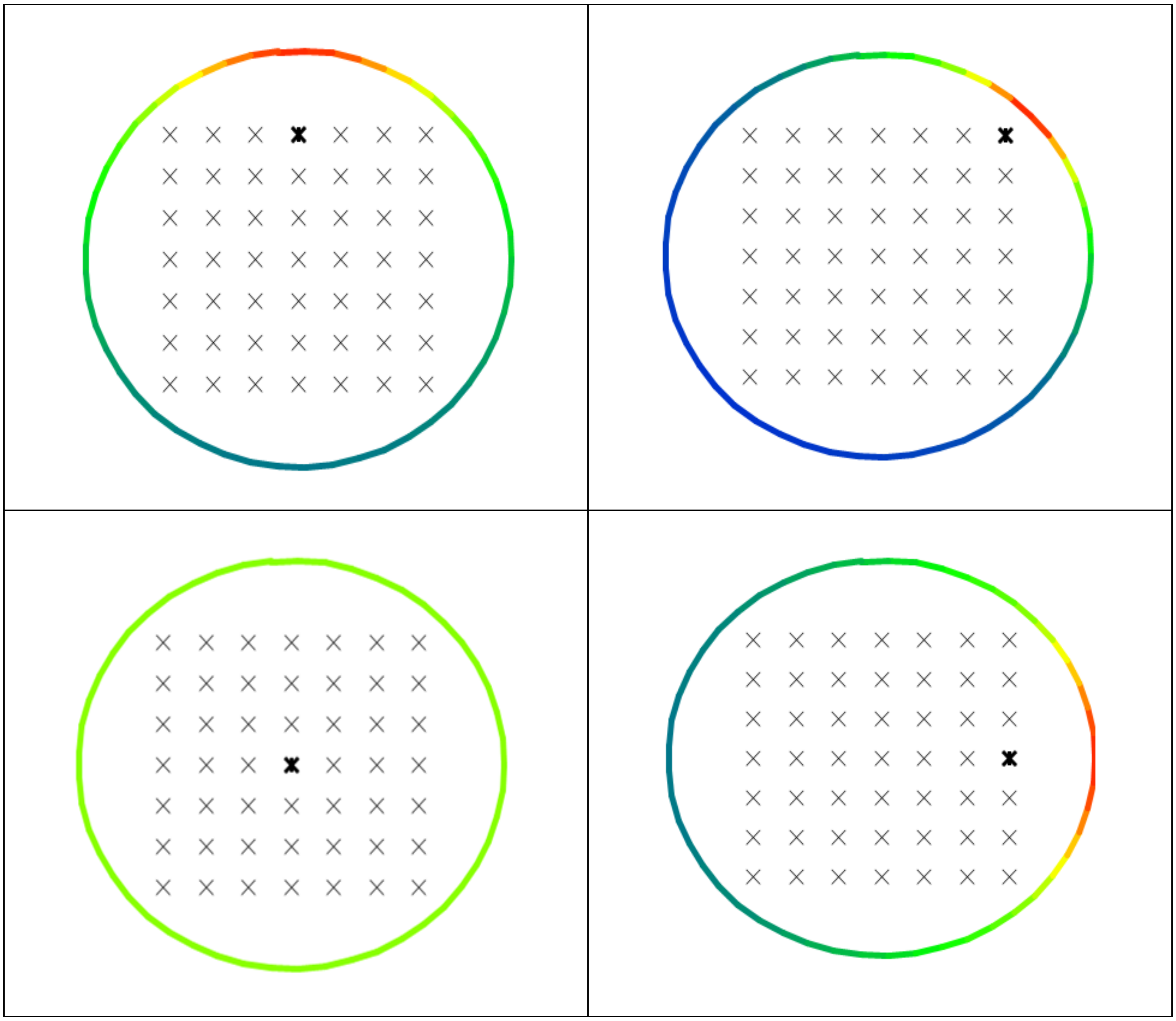

Figure A2.26: Attenuation Factors for Gamma Radiation from Select Points

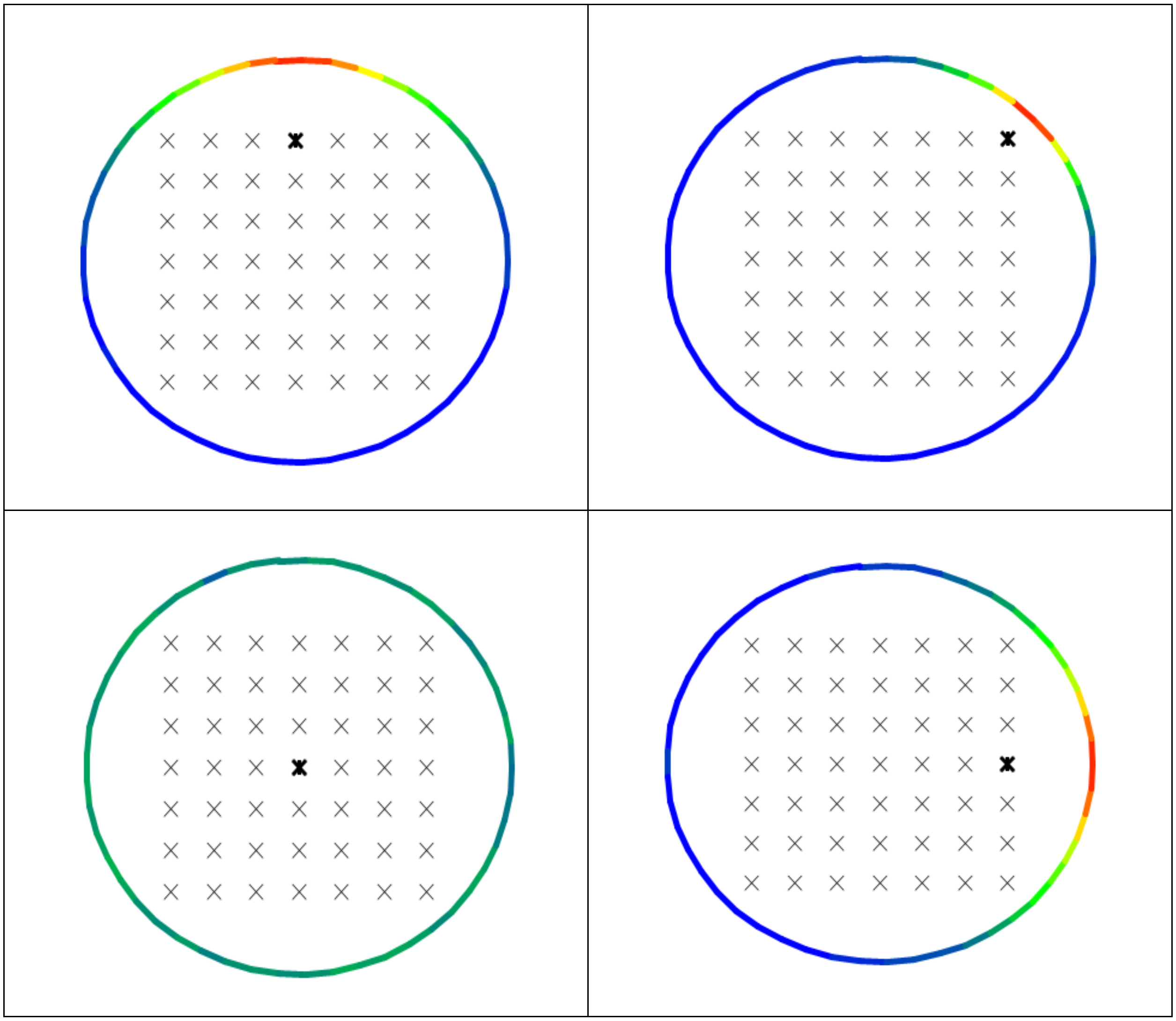

Figure A2.27: Attenuation Factors for Neutron Radiation from Select Points

What is noticeable about the different types of radiation is the penetration capability of the gamma radiation compared to the neutron radiation. This provides a more spread out dose distribution while the neutron dose is more acute. Using the product formula to sum all attenuation factors for all 7 x7 points (49 total) provides the detector dose distribution used in this study. The attenuation factors were therefore multiplied by predetermined source distribution. The selected source was a cosine shape in 2 dimensions which is plotted in Figure A2.28.

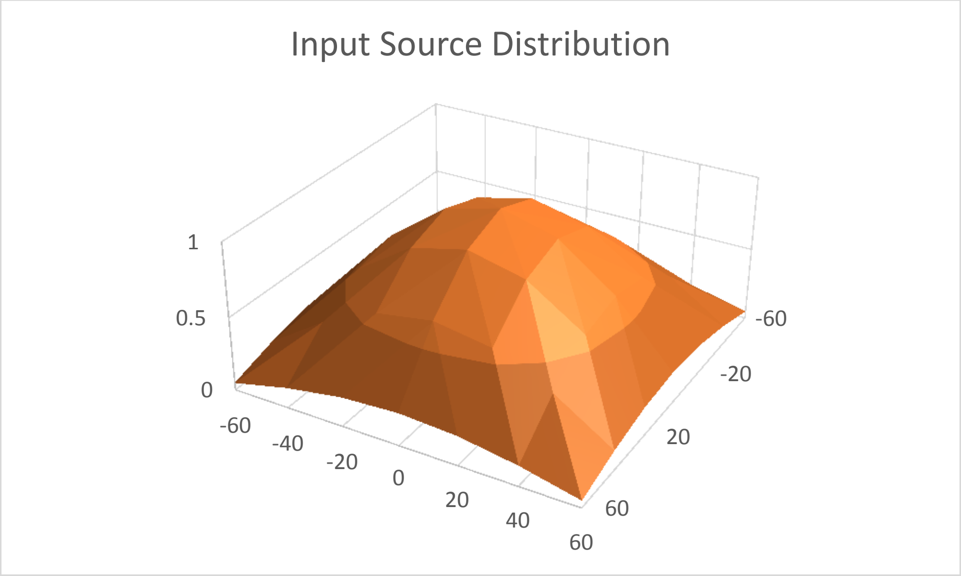

Figure A2.28: Plot of Input Source Distribution, 2 Directional Cosine

Multiplying this source by each attenuation factor of each point and totaling provided the detector dose distribution. The results for each radiation type is plotted in Figure A2.29 and Figure A2.30. Similar to the attenuation factors themselves, the gamma dose distribution is more spread out and the neutron dose distribution is more acute.

A2.29.

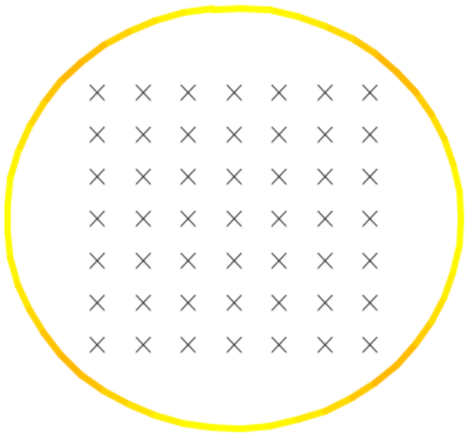

Figure A2.29: Gamma Dose Detector Distribution

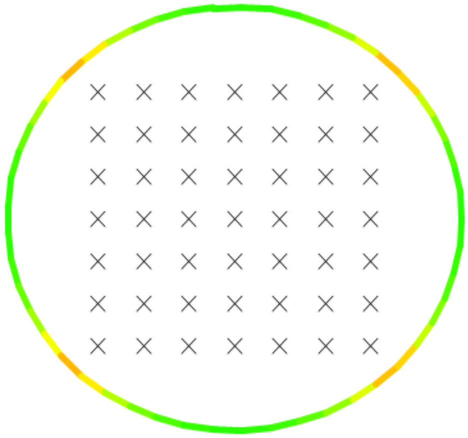

Figure A2.30: Neutron Dose Detector Distribution

A2.2.2 Results for 7x7 Study

The results for this study were found by iteratively solving for a reconstruction solution using a stopping criteria as a percentage match to the dose distribution. Each iteration was a solution converged on and increasing precise stopping criteria / percent match to the detector dose distribution. A comparison of the obtained solution using 10% match is displayed Figure A2.31.

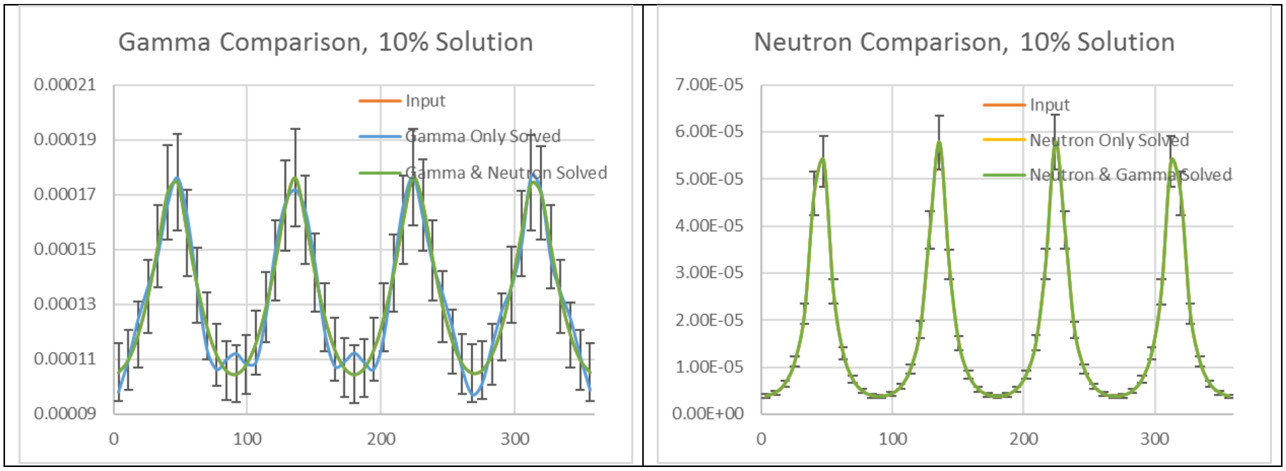

Figure A2.31: Comparison of Solutions for Gamma and Neutron Solutions, 10% Match

It is slightly difficult to see but the gamma solution is obtained with some solution points around 10% above or below the input dose distribution. For the neutron dose distribution, the solution is a close match. Comparison at 5% match stopping criteria is plotted in Figure A2.32.

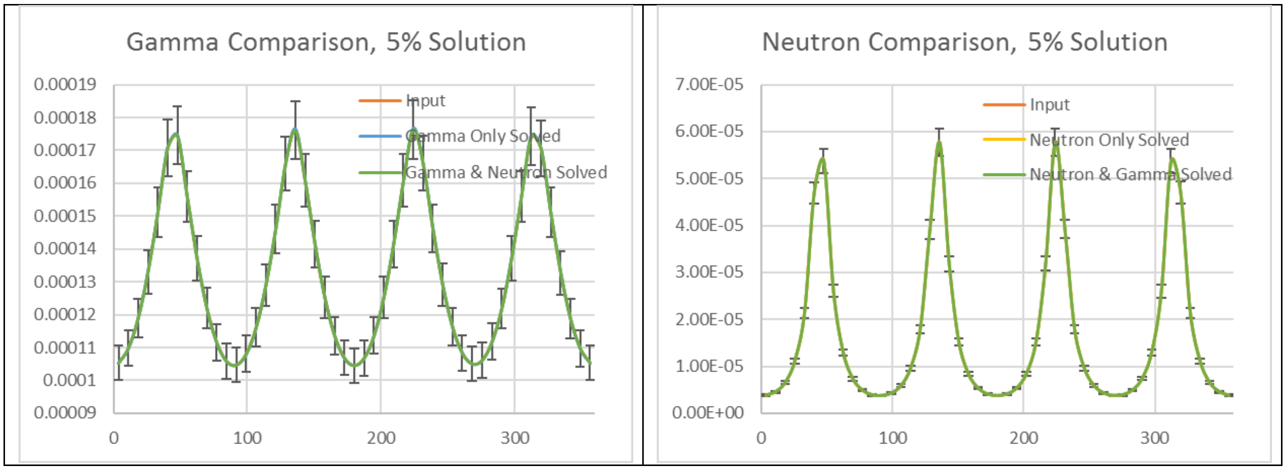

Figure A2.32: Comparison of Solutions for Gamma and Neutron Solutions, 5% Match

Within the comparison in Figure A2.31 and Figure A2.32, there is a second reconstruction solution that uses both the gamma and neutron radiation types. This is a significantly better reconstruction technique as can be seen it is a close match even for the gamma solution at 10%. It therefore is important to compare to each other, these different reconstruction solutions at the different stopping criteria. This is done in Figure A2.33 Figure A2.34.

The reconstructed solution with both gamma and neutron radiation types solved converges to the input solution at the last match percentage of 0.1%, which is within Figure A2.33. Figure A2.34 displays that the neutron only solution takes another order of magnitude to converge to the input solution while the very last row of the graphic shows the gamma only solution converging an additional 1 and ½ order of magnitude. These results show that it is very beneficial to have a reconstruction technique which uses both gamma and neutron radiation types. Looking back to the attenuation factors in the description (Figure A2.26 and Figure A2.27), these sets of information are unique to each other, therefore using both provides additional data to improve the solution. It is therefore understandable that both radiation types should be used.

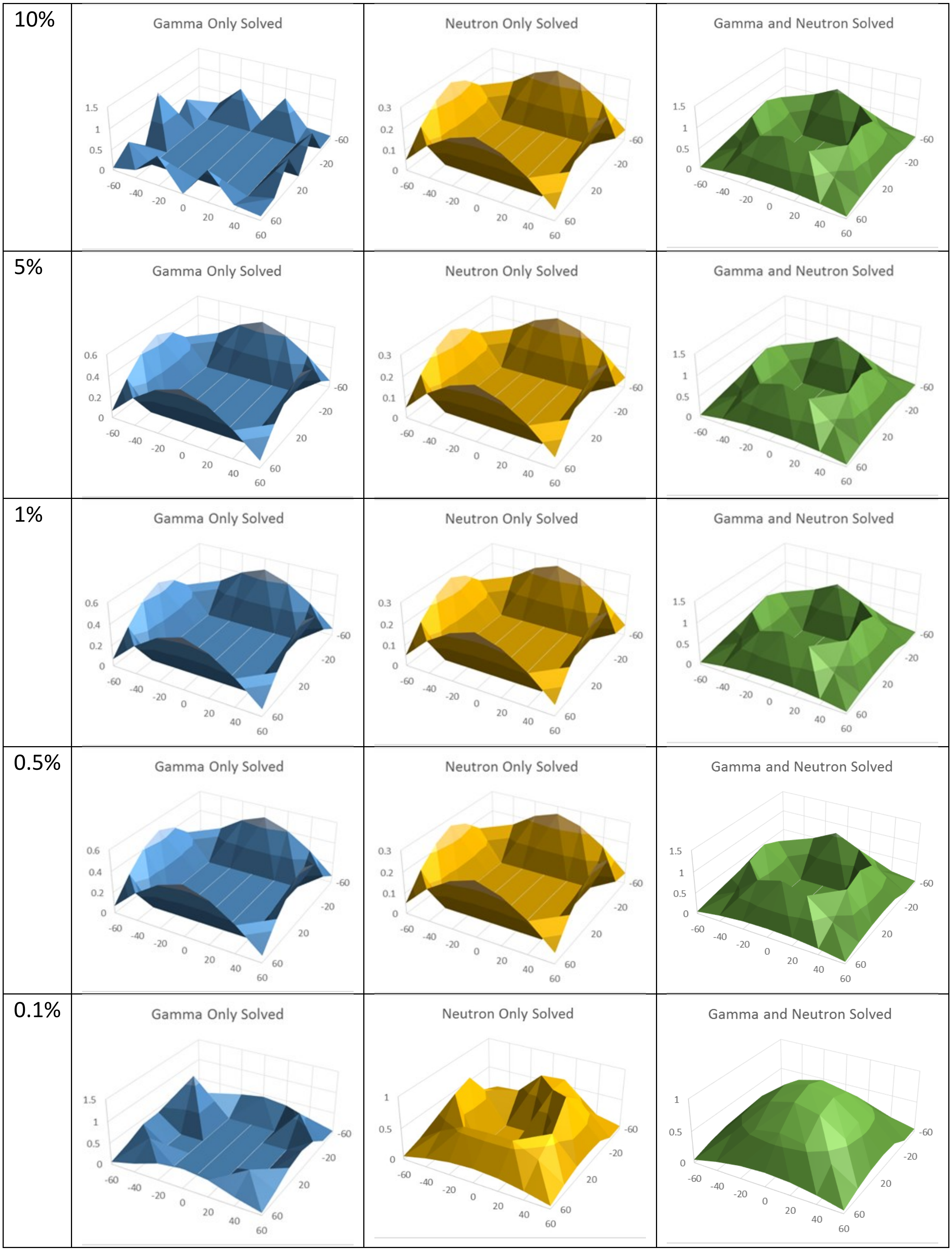

A2.33: Reconstruction Solution Comparison, 10% Match through 0.1%

0.05%	Gamma Only Solved 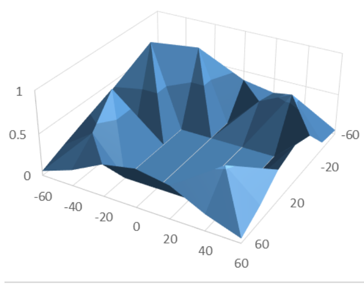	Neutron Only Solved 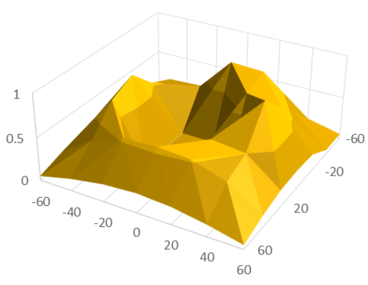	Gamma and Neutron Solved 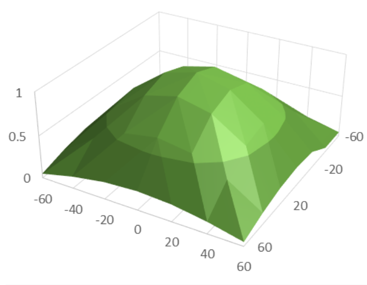
0.01%	Gamma Only Solved 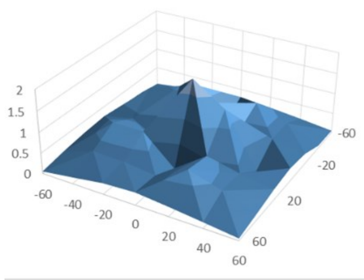	Neutron Only Solved 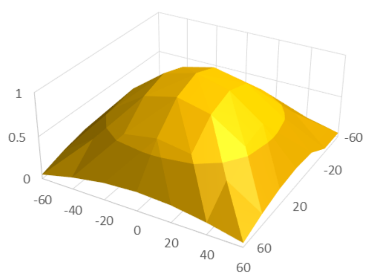	Gamma and Neutron Solved 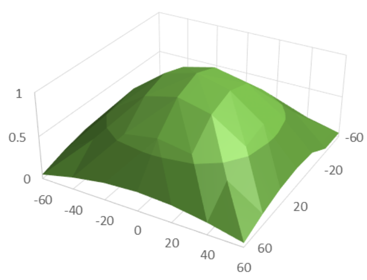
0.005%	Gamma Only Solved 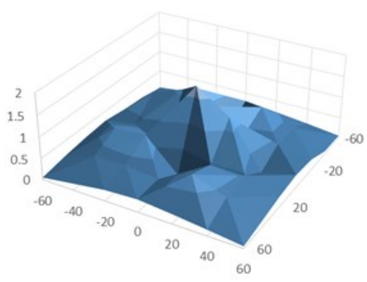	Neutron Only Solved 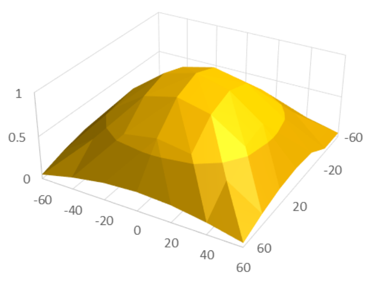	Gamma and Neutron Solved 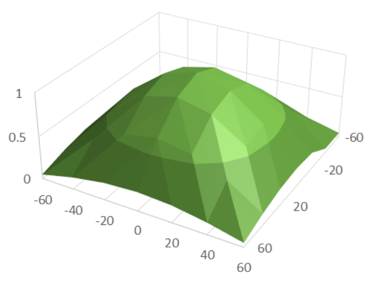
0.001%	Gamma Only Solved 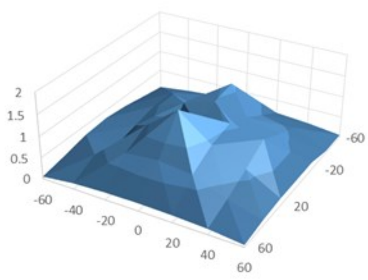	Neutron Only Solved 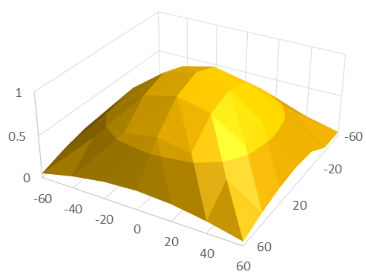	Gamma and Neutron Solved 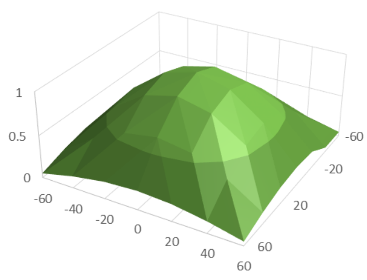
0.0005 %	Gamma Only Solved 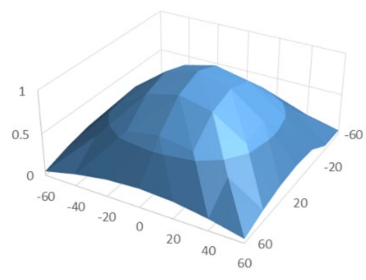	Neutron Only Solved 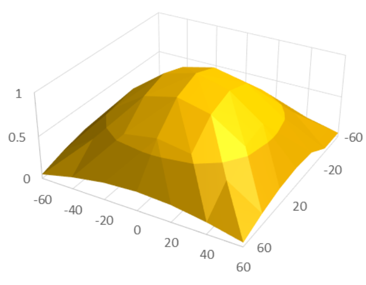	Gamma and Neutron Solved 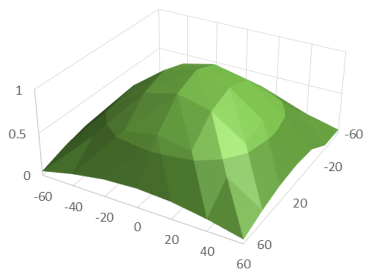

A2.34: Reconstruction Solution Comparison, 0.05% Match through 0.0005%

APPENDIX 3: HEAT SOURCE RECONSTRUCTION

A3.1 Heat Source Experiment Setup

A3.1.1 Appendix Introduction

This appendix chapter focuses on the materials and methods needed to build the heat source experiment setup. This includes pictures of the setup and diagrams detailing the construction.

A3.1.2 Heating Elements

The heating element in the heat source experiment setup were individual incandescent light bulbs. Each bulb had a maximum power output of 150 Watts which is for use typically as a light source but in this case the power was desired as heat source. The light was created as the effect on the filament getting hot, therefore the 150 Watts of light were also 150 Watts of thermal energy.

The light bulbs were arranged in a 3x3 array for a total of 9 bulbs. The bulbs were spaced evenly apart and were mounted on threaded rod rails. This enabled the axial height of the bulbs, therefore the heat source location, to be changed. The light bulb 3x3 array can be seen in the following figure:

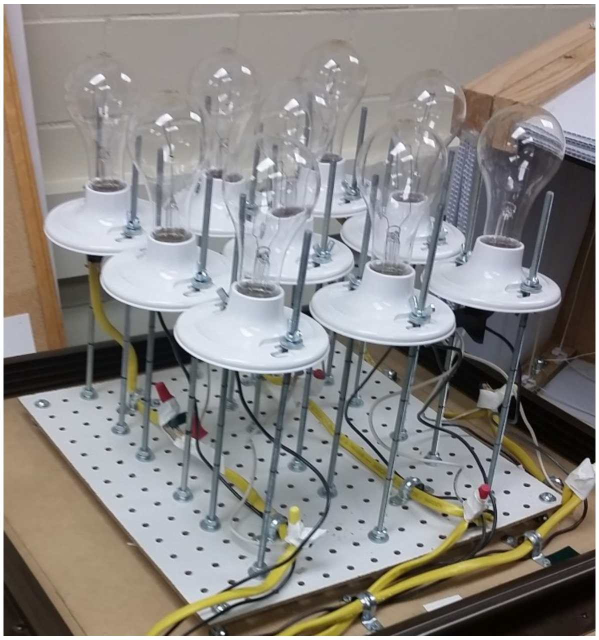

Figure A3.1: Light Bulb 3x3 Array

A3.1.3 Power Control

Each column of 3 bulbs was on its own circuit and each of the bulbs were wired in parallel. Each of these parallel circuits were terminated in a typical 3-prong plug as the power supply. The 3 columns' 3 plugs was connected to a power strip with a breaker at 15 amps just in case there was a malfunction like an electrical short. The maximum current expected by all 9 bulbs was 7 amps so it should have not tripped the breaker if wired correctly.

Within the circuit was a triple switch to provide the parallel circuit with 1 switch per bulb and a dimmer switch that operated on the entire circuit, or in other words, wired in series to the triple switch. A wire diagram of this arrangement can be as follows:

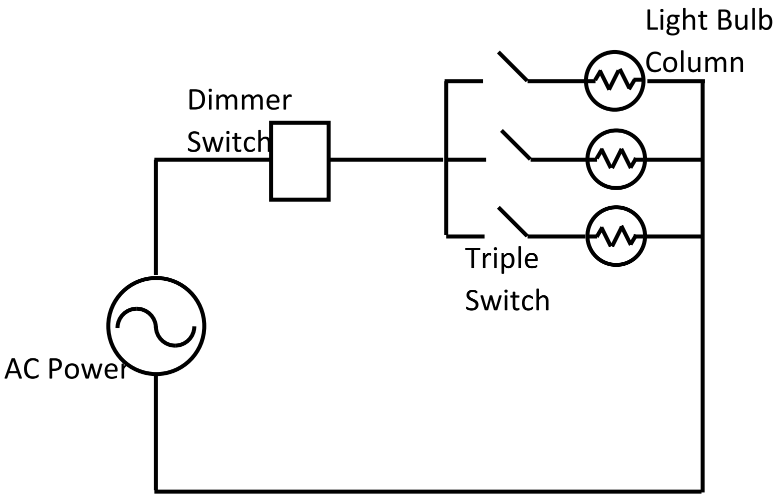

Figure A3.2: Wire diagram

A representation of this circuit pictorially to better demonstrate how it was implemented can be seen in the following figure:

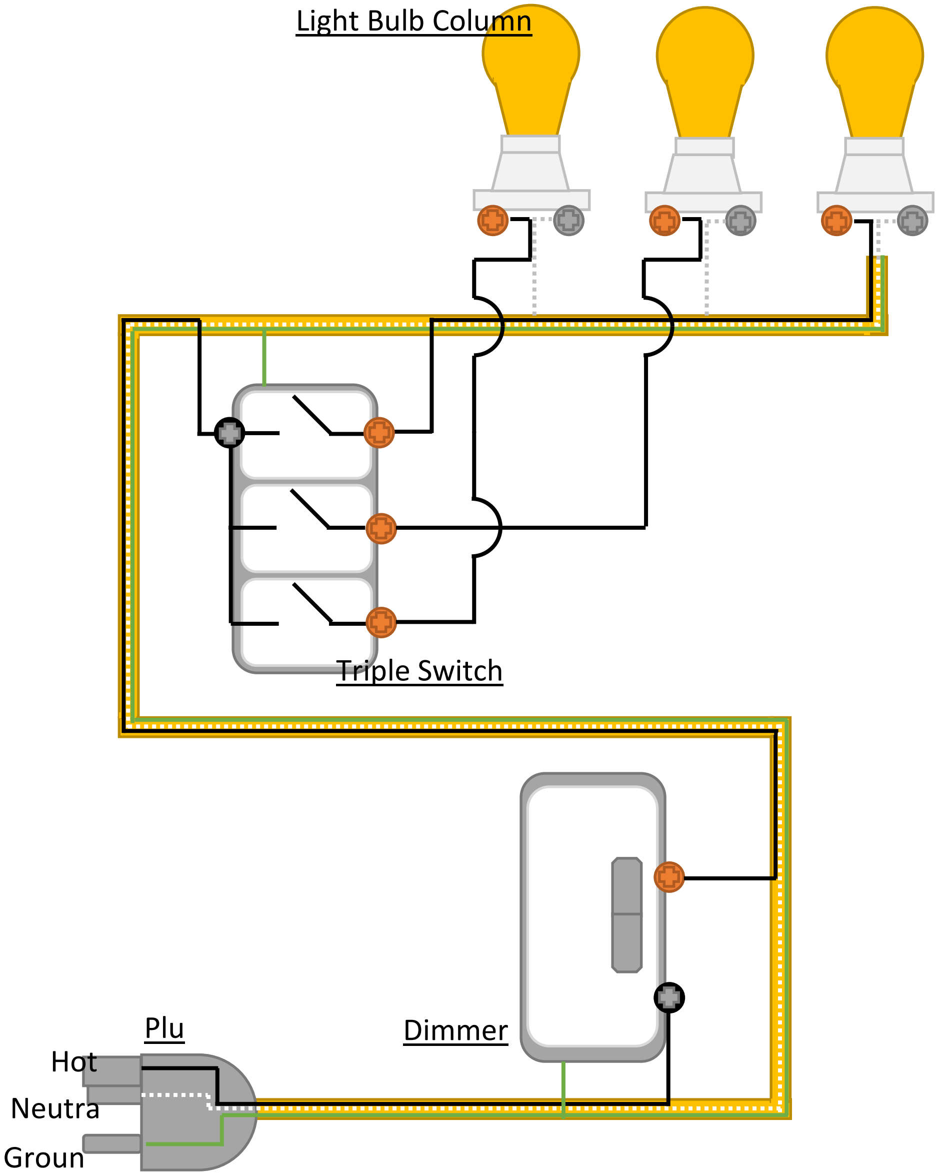

Figure A3.3: Pictorial Wire Diagram

This circuit as aforementioned was duplicated 3 times, once per light bulb column. Therefore each triple switch and dimmer switch was located as one of three and mounted in a three gang box. This mounting can be seen in the following figure:

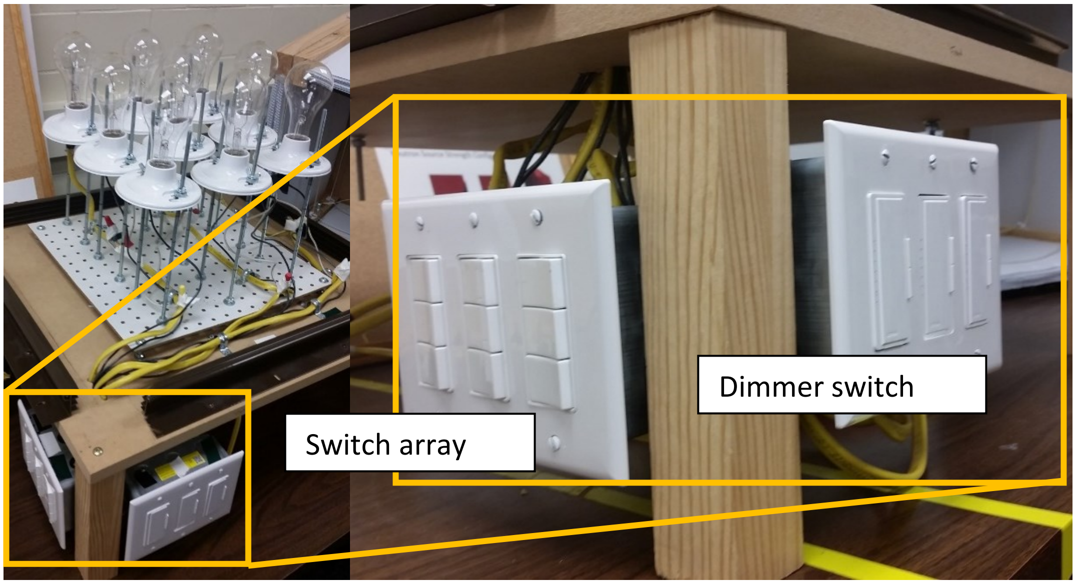

Figure A3.4: Mounting of Switches

Because each bulb had its own switch, the bulbs could be powered on or off one at a time. This was necessary to get the heating parameters of the bulbs individually, treating each bulb like a single point source of thermal radiation. The switches were mounted and wired such the leftmost column was the leftmost triple switch and the top of the triple switch was the bulb in the rear, the middle switch the middle bulb, and the bottom switch corresponding to the bulb in front. The correlation of 3x3 array of bulbs to the 3 triple switches as a 3x3 array can be seen in the following figures:

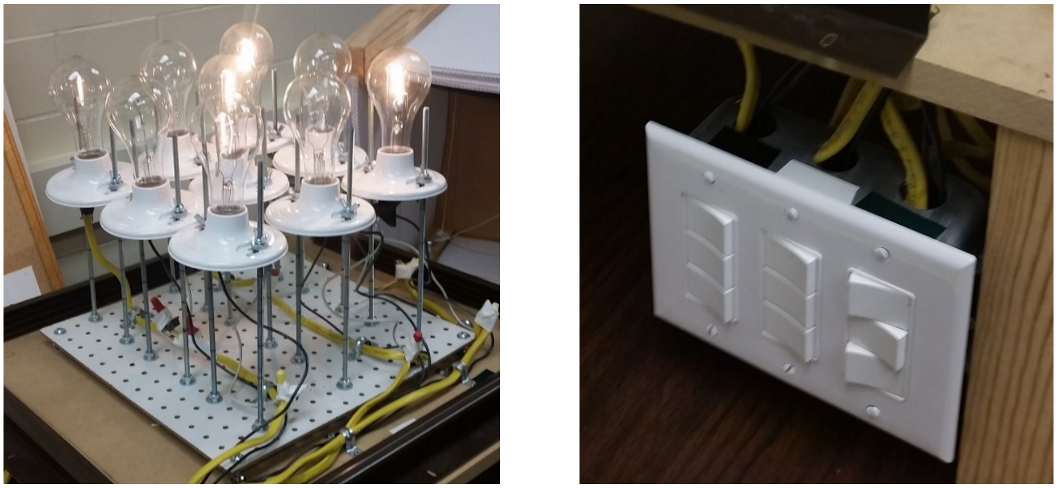

Figure A3.5: 3x3 Array of Bulbs and Switches

The dimmer switch provided the ability modulate the power (thermal radiance) of the bulbs. The dimmer switches were procured such that power could be incremented in even intervals with a corresponding LED indicator rather than using a simpler analog control. This was necessary for repeatability of experiments

There was a single dimmer switch per circuit, therefore the entire column would be at the same power level. Furthermore, the dimmer switch provided each column to be on its own power such that experiments could be conducted on power tilts and bulbs not at full power. Similar to the triple switches, the leftmost switch corresponded to the leftmost column of bulbs. This arrangement can be seen in the following figure:

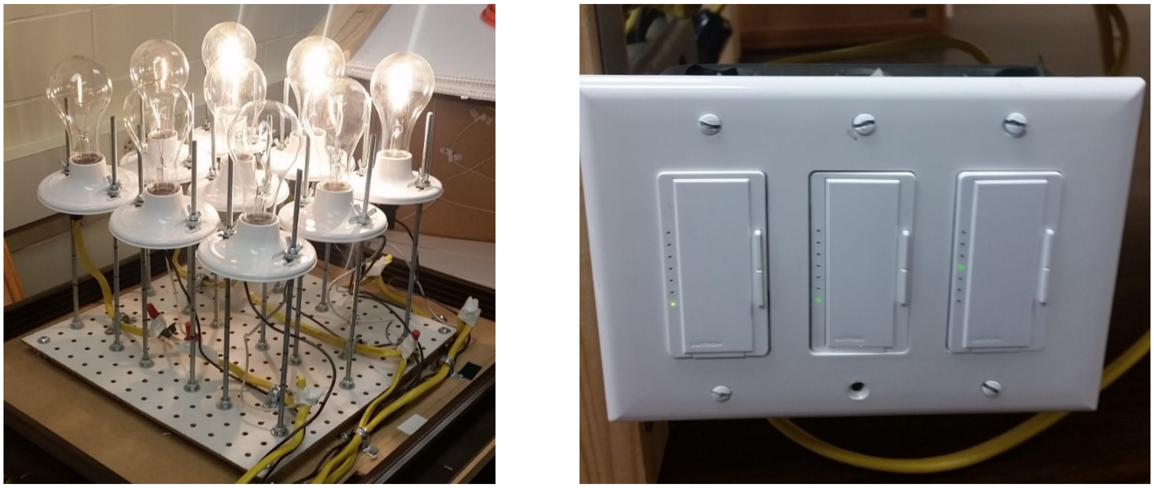

Figure A3.6: Arrangement of Dimmer Switches

A3.1.4 Fiber Optic Spiral

The heat source was monitored as a distributed temperature measurement using fiber optic technology. To capture spatial variation, the fiber optic traversed all sides of the box and spiraled upwards in height. This fiber optic (comprised of a yellow jacketing) completed two loops around the periphery and was connected externally to a 3 foot (90 centimeter) jumper cable which would connect into the measurement device. The fiber optic spiral and the connection to the jumper can be seen in the following figure:

Figure A3.7: Fiber Optic Spiral and Jumper Connection

Because of the box interface and the jumper cable, there were a total of three junctions. These are highlighted in the following figure.

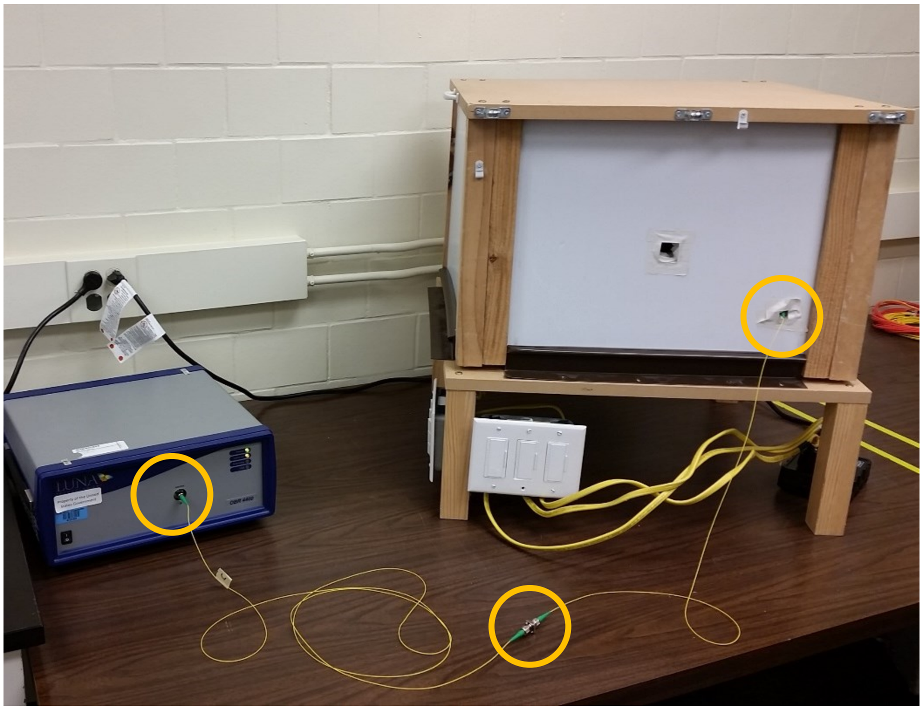

Figure A3.8: Fiber Optic Junctions

These junctions are easy to spot in a scan of the fiber because they case a large reflection due to the interface. This is shown in the following figure with the junctions highlighted.

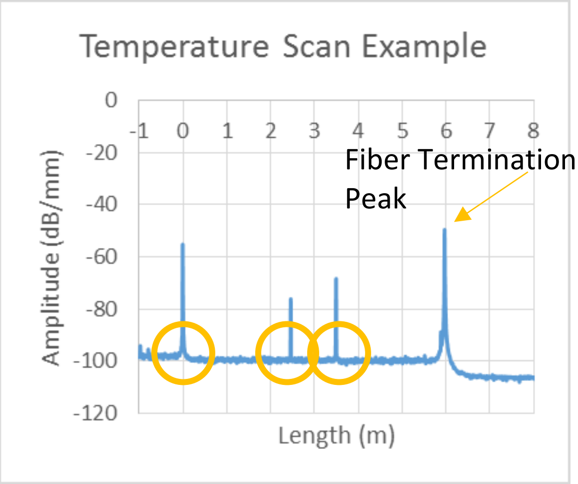

Figure 3.9: Temperature Scan Example with Junctions Highlighted

Although the reflection is large at each junction, nearly no signal loss occurs because there is a good connection. In addition to the scattering peaks at the junctions, there is always a large peak at the fiber termination because the signal encounters the interface of the fiber core's index of refraction meeting the index of refraction of air. Because of such a large reflection, the heat experiment data analysis used the first 2 meters of the fiber optic spiral rather than the full 2.5 meters.

A3.1.5 Box Construction

A box was designed to provide structure to the fiber optics and encapsulate the radiative heat in its entirety. This was necessary to mitigate heat transfer to the surroundings thus limiting conduction or convection affects. The sides of the box consisted of several layers of insulation board providing a near adiabatic surface. The structure of the box was with wood posts at the corners and a particle board top, both materials having good insulation properties. The box sat on top the light bulb array being surrounded by a rubber threshold material on all sides, effectively limiting air flow at these areas.

The box design had a single location of limited insulation. A cutout on the front panel of the box allowed for peering into the box to observe the light bulb array during the experiments. The backside of this front panel was a tinted Plexiglas (acrylic glass / plastic sheeting) permitting visual intrusion without air flow. This is also provided view of a digital thermometer which provided a bulk measurement of the temperature within the box. Although it was expected that the light bulb heat would not provide a safety risk, with a total of 1.35 kilowatts for all 9 bulbs at full power, it made sense to have a way to be able to easily observe the temperature level within the box. The cutout for internal viewing can be seen in the following figure of the experiment complete with the box encapsulating the light bulb array:

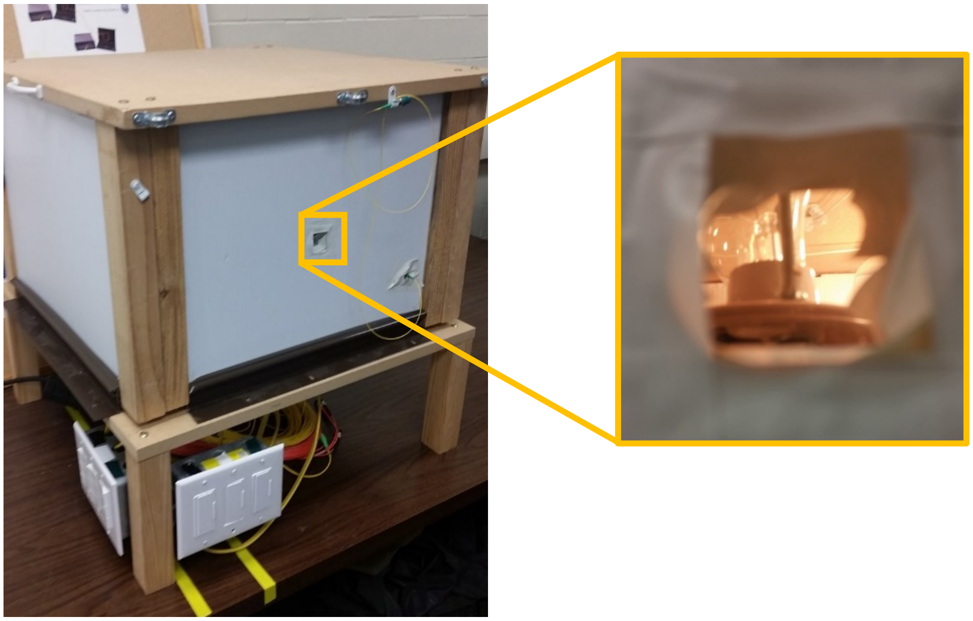

Figure A3.10: Experiment Complete with Box and Cutout on Front Panel

A3.1.6 Summary

This appendix section was written to provide an accurate documentation of the construction of the heat source experiment setup. It was herein demonstrated how the experiment setup was constructed such that it could be recreated using a similar design and materials. The primary goals of heat source monitoring at different power levels and configurations were deemed best achieved through such design and the materials were readily available for procurement.

A3.2 Experiment Results

A3.2.1 Appendix Introduction

This appendix chapter focuses on the results of the heat source reconstruction experiments. The graphing of the data and reconstruction algorithm complete results are contained within this chapter.

A3.2.2 3-D Graphing

To accurately represent the results from the heat source reconstruction experiments, a 3-D grapher was employed to show the temperature distribution over the length of the fiber. The 3-D grapher involved projecting the coordinates in 3 dimensions onto a 2 dimensional graph. The math involved in this projection was created as an open source tool constructed within the Microsoft program Excel (Doka, 2012). Measurements from the real setup helped to accurately locate the points on the graph. Therefore the graph overlayed correctly over top of an image of the experiment setup as seen in the following figures of the light bulb heat source:

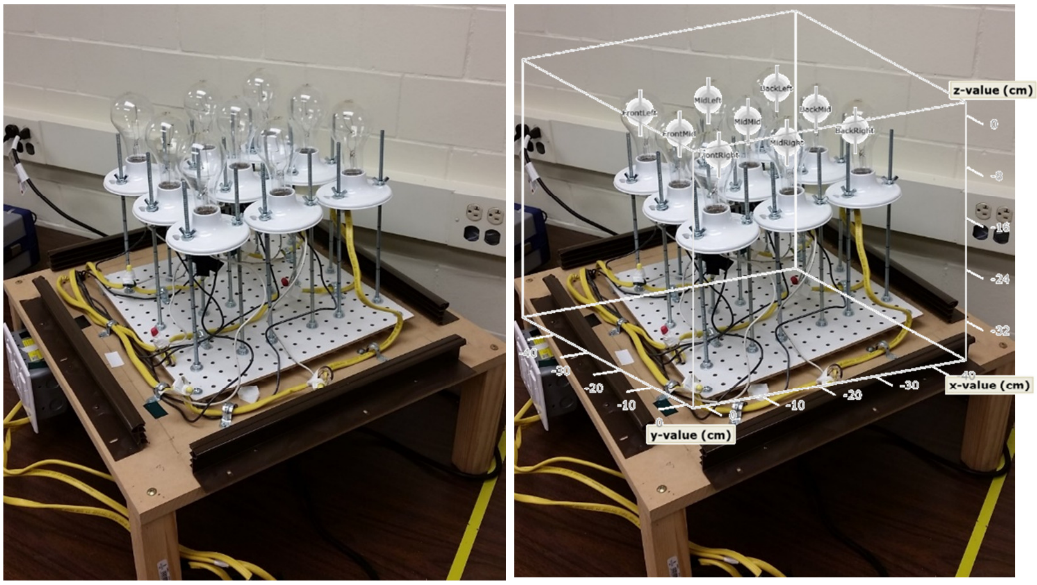

Figure A3.11: Graph Overlay of Light Bulb Heat Sources

Because the point sources could be located on the 3D graph, the different heat source distributions were represented. The graphed point sources were colored in accordance with their respective power levels. This is seen in the following figures:

<table>
<tr><td colspan="2">Single Light Bulb at Full Power</td></tr>
<tr><td>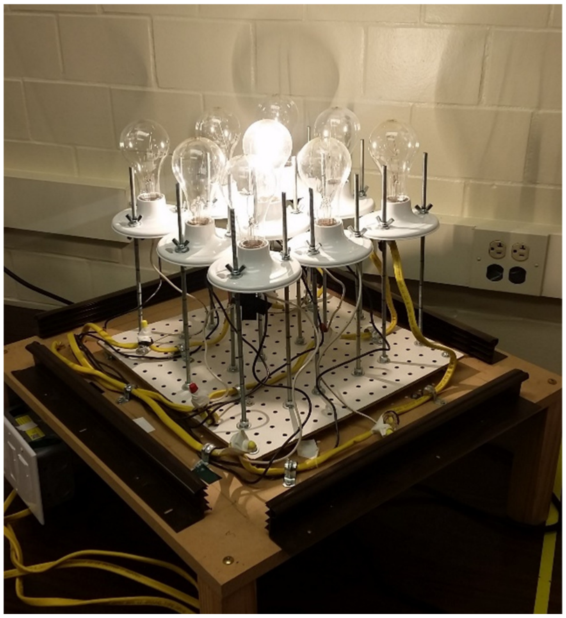</td><td>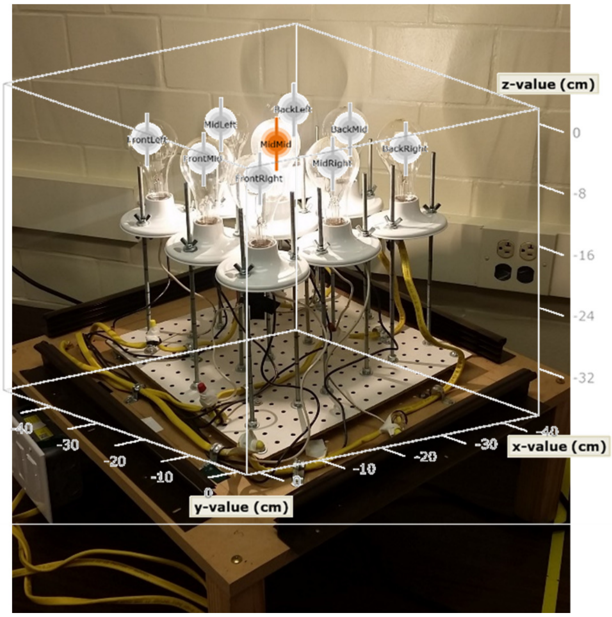
</td></tr>
<tr><td colspan="2">Single Light Bulb at Half Power</td></tr>
<tr><td>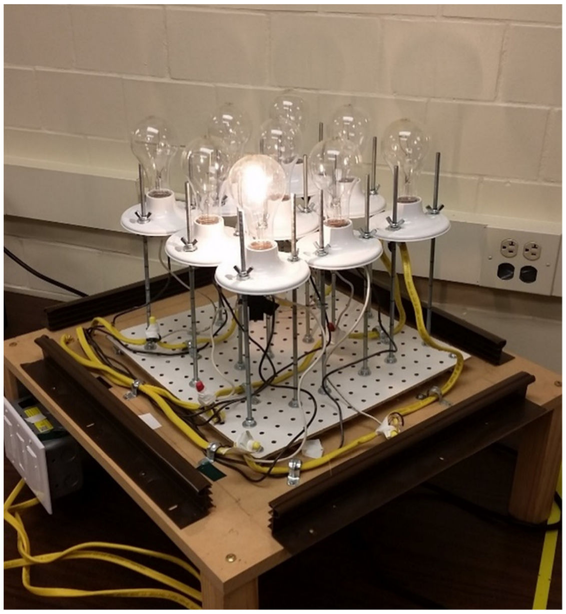</td><td>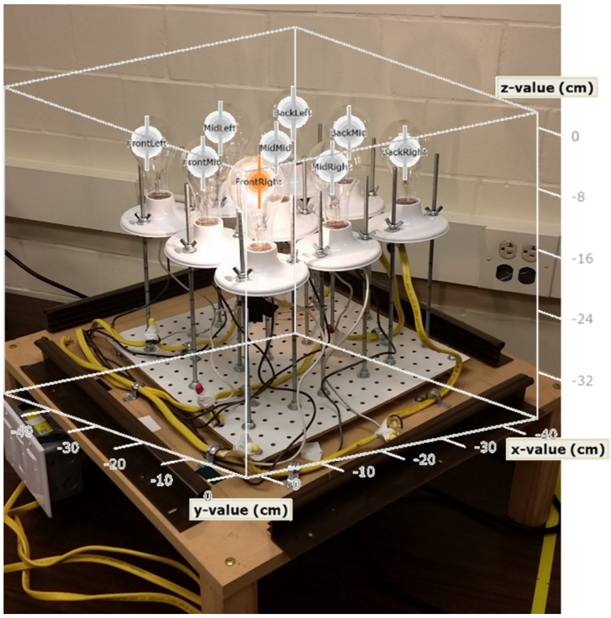
</td></tr>
</table>

Figure A3.12: Graph Overlay Showing Heat Source Power Levels

In addition to the graphing of the light bulb heat source array, the fiber optic measurement device was necessary to locate appropriately and plot. This fiber optic wrapped around the interior of the box structure which covered the heat source to create an adiabatic boundary and provided the structure to hold the fiber in place. This can be seen in the following figures:

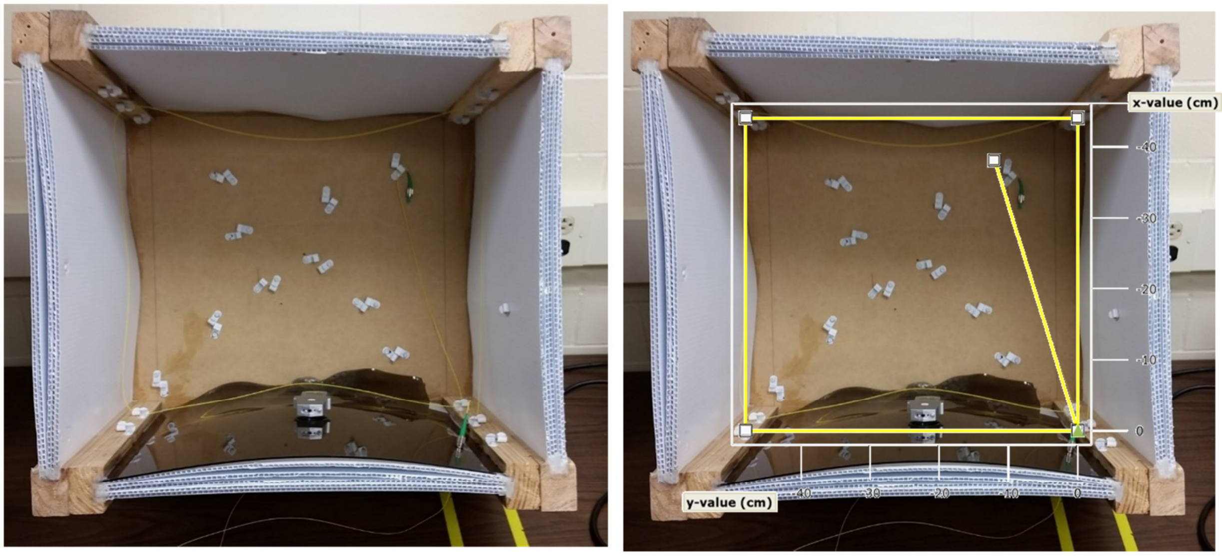

Figure A3.13: Graph of Fiber Optic Measurement Device within Box Structure

With the box covering the light bulb array, the plots of these point sources and the wrapped fiber optic could be combined in a single plot. This can be seen in the following figures:

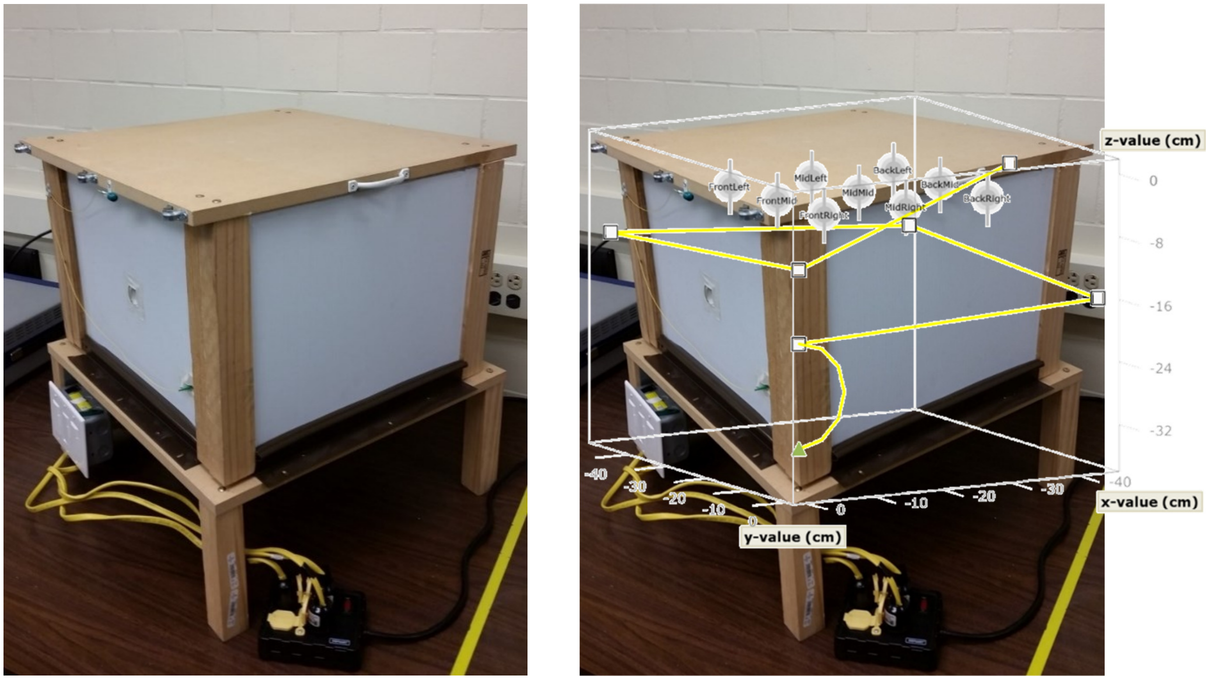

Figure A3.14: Combined Graph of Setup as 3D Overlay

This combined graph enabled the fiber optic to display the measurement of temperature recorded for each heat source with a color scale corresponding to temperature increase. This plot provided the full capability of the 3D graphing program as can be seen in the following full size figure:

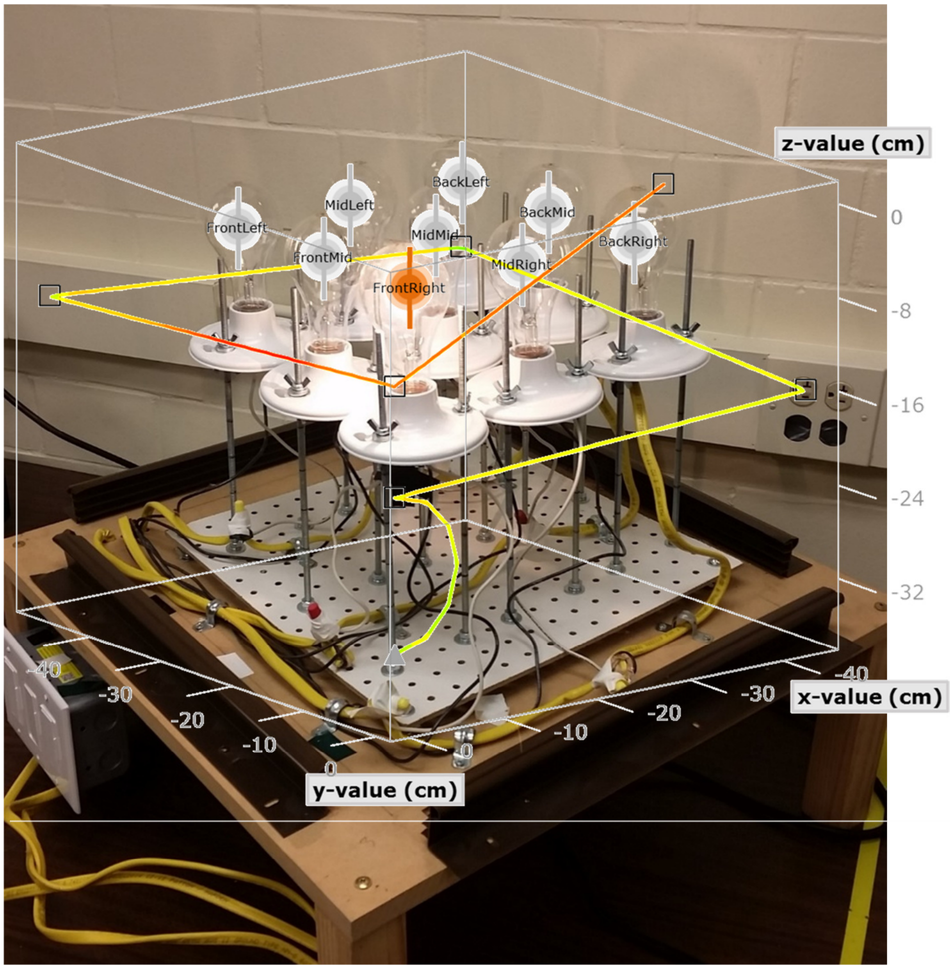

Figure A3.15: Full Size Temperature Distribution Graph

A3.2.3 Point Source Data

As part of the experiment objective, it was necessary to capture the data for how a temperature increase distributed incrementally all along the fiber can be attributed to a single point source. This relationship from the heat emitted by the source to the temperature change in a fiber increment is similar to what was referred to as an “attenuation factor” for the theoretical modeling objective. This can be seen in the following figure:

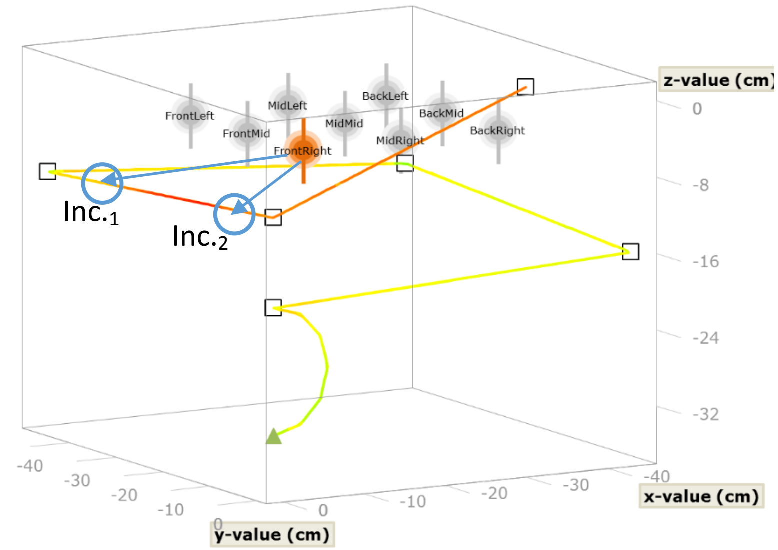

Figure A3.16: Representation of Attenuation Factors for Heat Experiment

Since the distance to Increment-1 is would be greater than the distance to Increment-2, it follows that the temperature increase should be greater for Increment-2 than Increment-1. Since the distances to each fiber increment were unique for each point source, therefore, each point source had its own unique set of attenuation factors. The experiments to capture these factors was done over a 10 minute time segment, with data taking at every 2.5 minutes. As the time progressed, the cumulative heat addition to the fiber optic resulted in an increasing fiber temperature. This can be seen in the following figures:

Single Bub Full Power Function of Time (Color Range 0° C to 50° C)

2.5 Minute

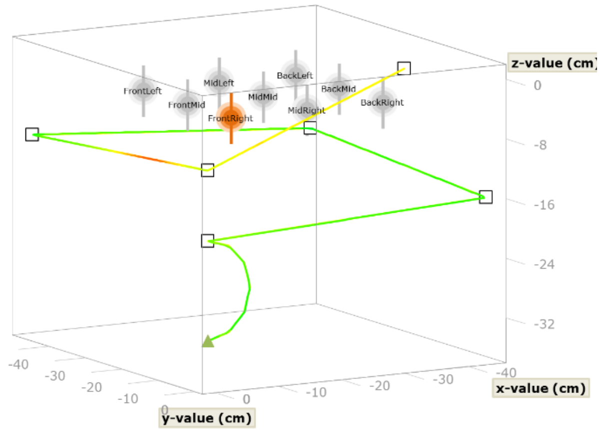

5 minute

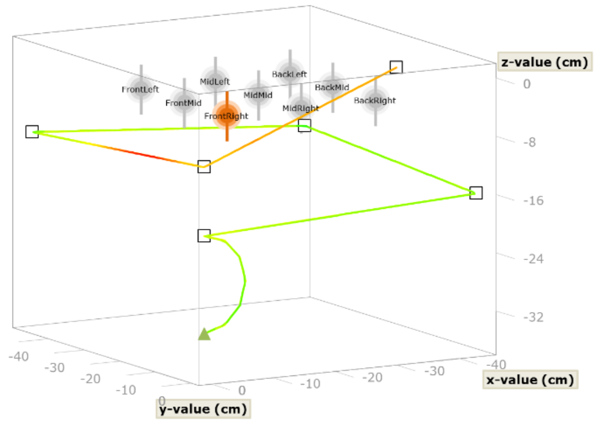

7.5 Minute

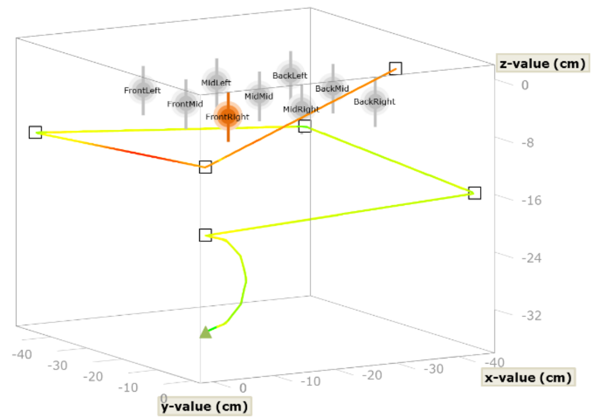

10 minute

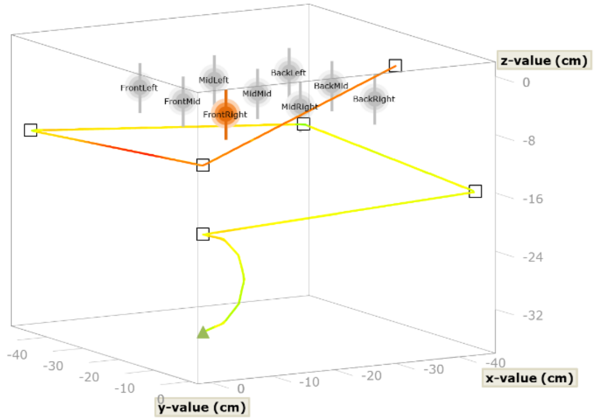

Figure A3.17: Time Progression for Heating of Fiber by Point Source

As an alternative to the pictorial representation of the fiber’s temperature increase, the raw data itself can also be plotted to display the progression of heat applied to the fiber by the point source. This is seen in the following figure.

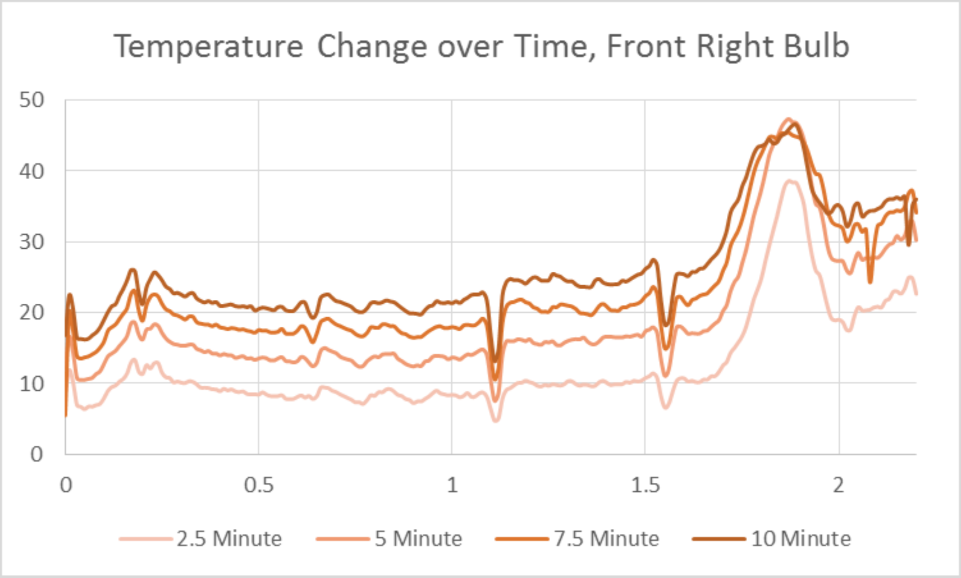

Figure A3.18: Time Progression as Raw Data

As mentioned before, the heating of the fiber was unique to each point source of heat. Therefore, 9 different point sources yielded 9 different sets of temperature distributions (sets of “attenuation factors”). This can be seen in the following series of figures (one per column):

Single Bub Full Power at 10 Minutes (Color Range 0° C to 50° C), Left Column

Back Left

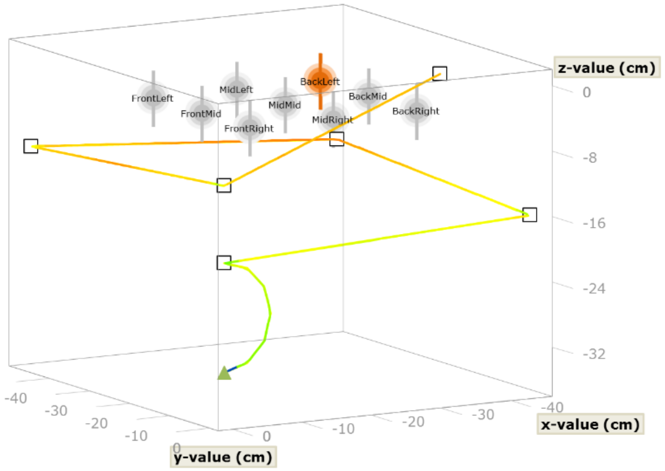

Middle Left

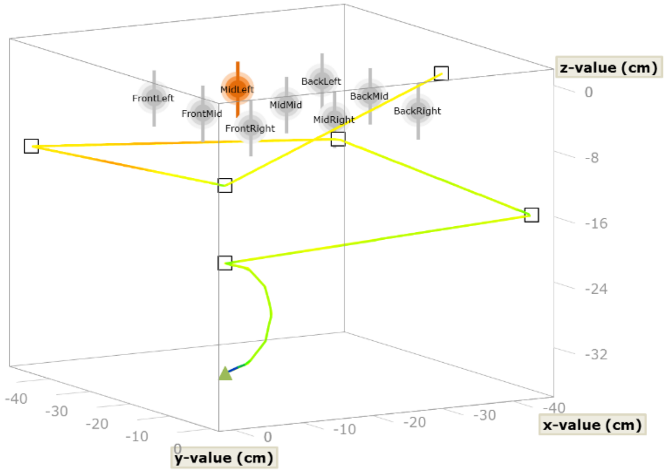

Front Left

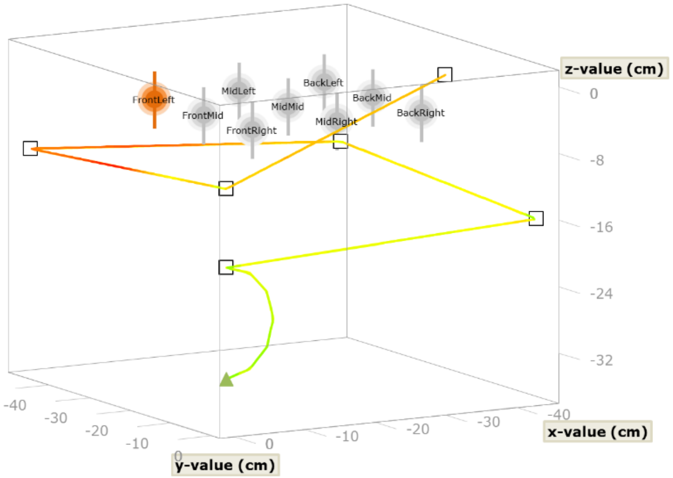

Figure A3.19: Display of Left Column

Single Bub Full Power at 10 Minutes (Color Range 0° C to 50° C), Middle Column

Back Middle

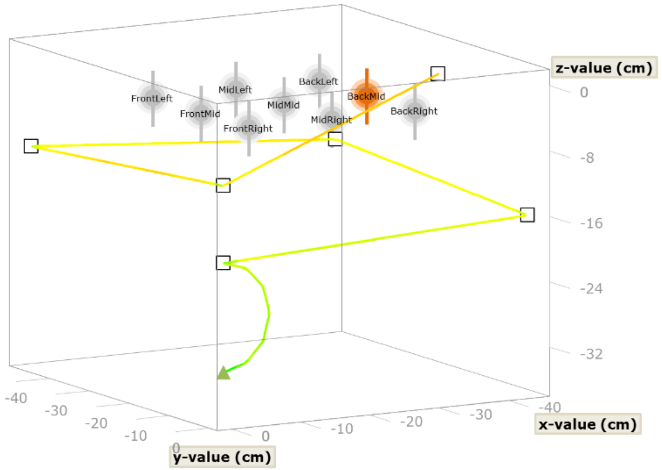

Middle Middle

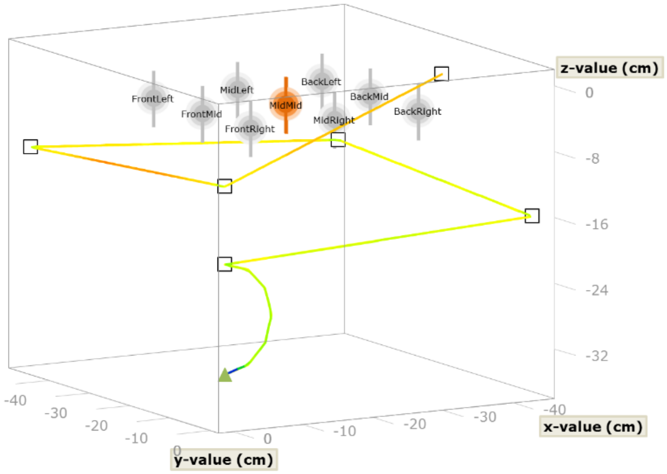

Front Middle

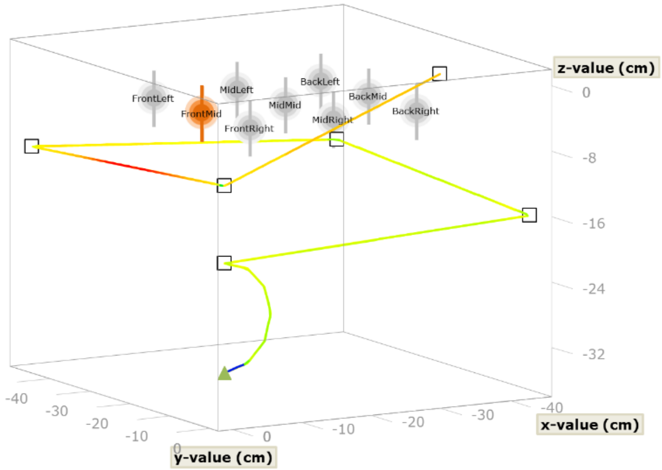

Figure A3.20: Display of Middle Column

Single Bub Full Power at 10 Minutes (Color Range 0° C to 50° C), Right Column

Back Right

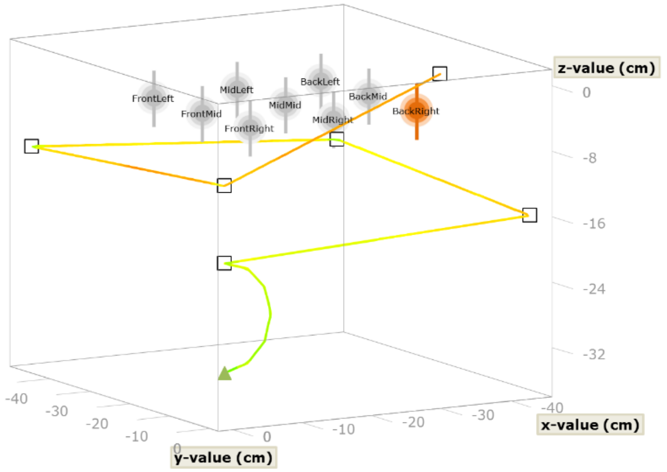

Middle Right

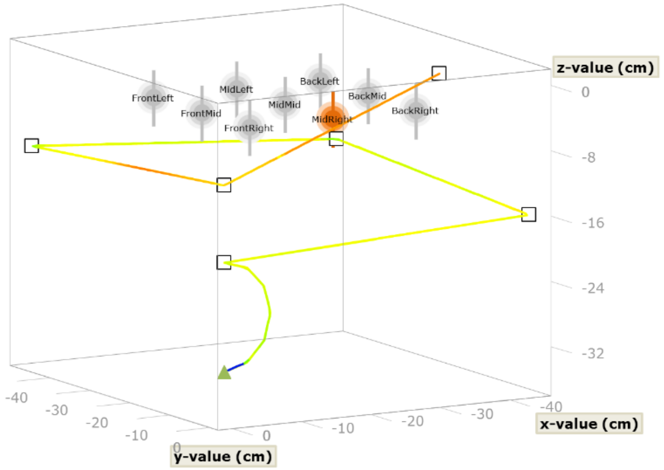

Front Right

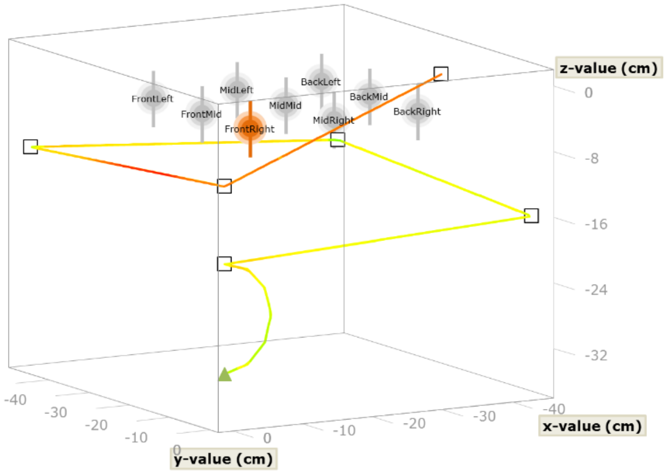

Figure A3.21: Display of Right Column

An alternative representation is all 9 bulbs displayed in a single figure, shown below.

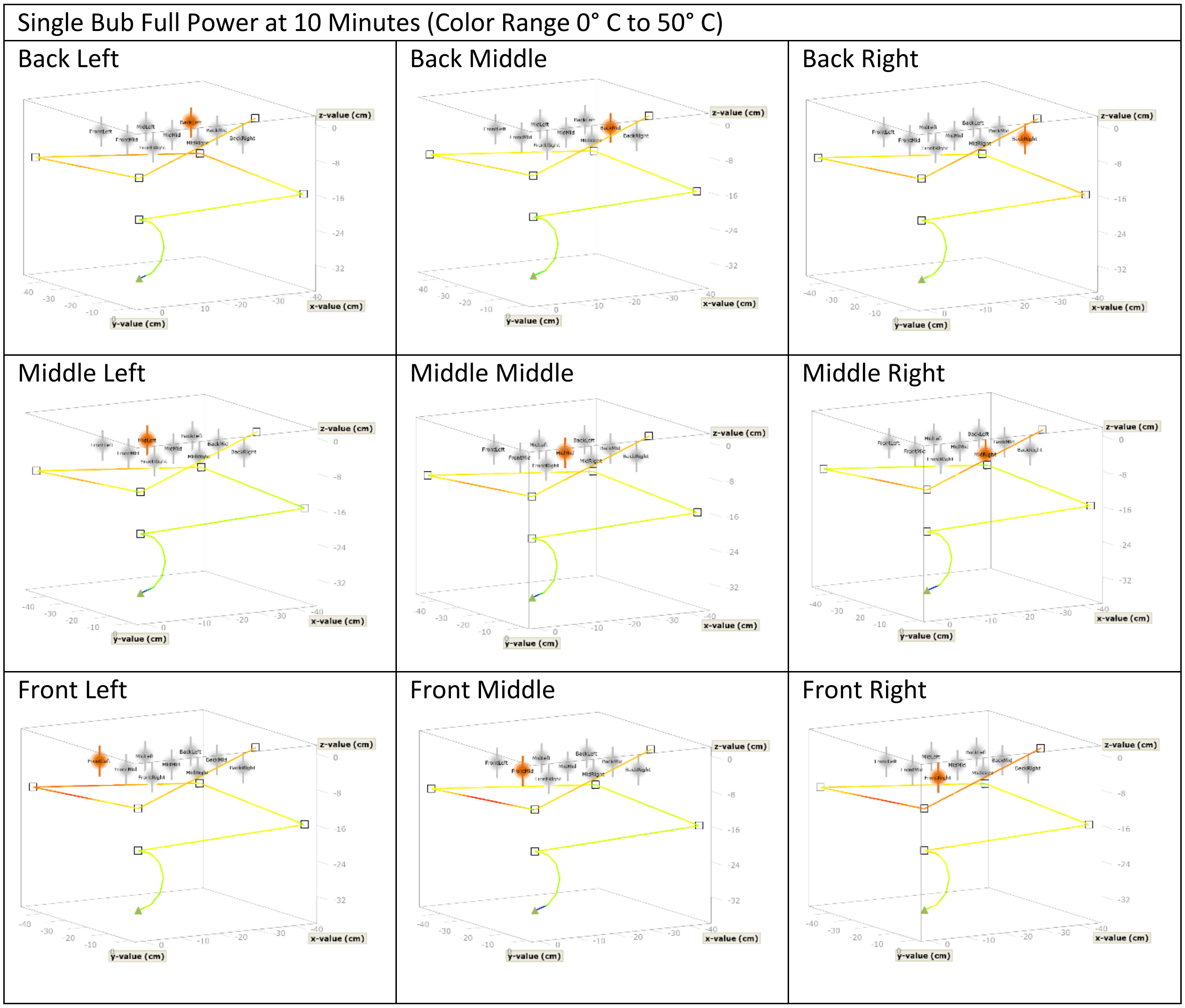
Single Bub Full Power at 10 Minutes (Color Range 0° C to 50° C)

Back Left

Back Middle

Back Right

Middle Left

Middle Middle

Middle Right

Front Left

Front Middle

Front Right

Figure A3.22: Display of All 9 Temperature Distributions

A3.2.4 Heat from Distributions of Power Level

Once the temperature changes due to each point source were captured, it was possible to apply this data to a heat source with multiple sources powered on. The data from these distributed heat sources were examined to see if the distribution could be predicted as a combination of the point source attenuation factors. One of the distributions was to have the left column at full power, the middle column at half power, and the right column at zero power. These distributions were possible because each column was on its own digital dimmer switch as detailed in the appendix chapter *Appendix 3.1 Heat Source Experiment Setup*. Therefore, heat distributions can be created with a power tilt to any of the columns. The distribution described here thus has a "power tilt left" as seen in the following figure:

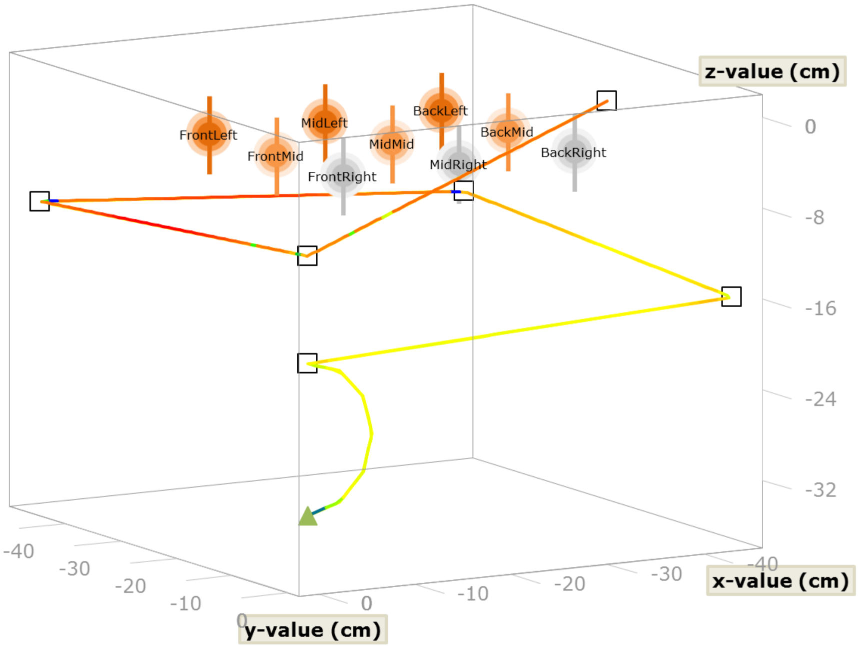

Figure A3.23: Display of Power Tilt Left

And all 6 tested power distributions can be seen in the following tables:

All Power Distributions, color scale 0 to 100 deg. C

Power Tilt Left

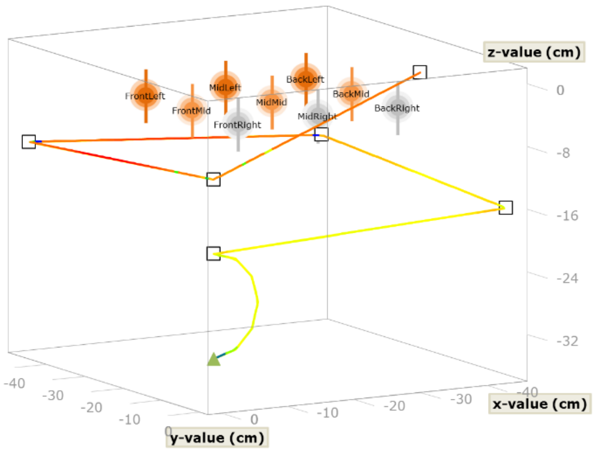

Power Tilt Right

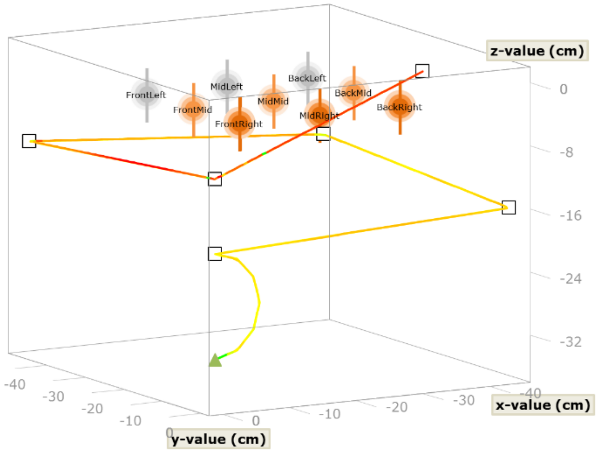

4 Corners Full Power

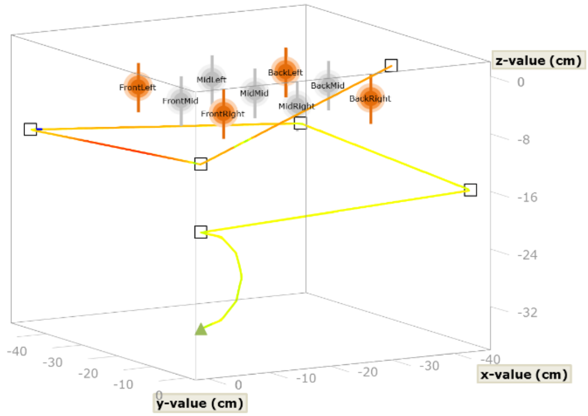

4 Corners Half Power

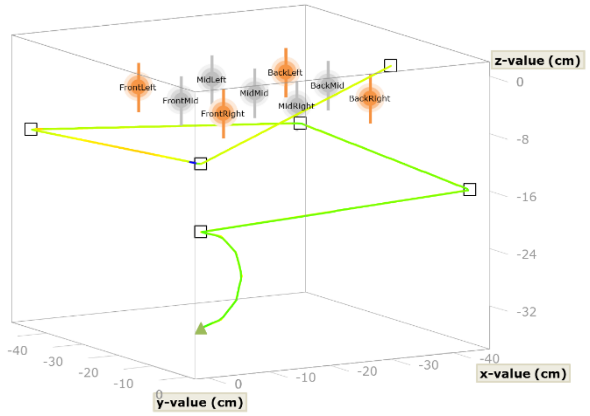

All Bulbs Full Power

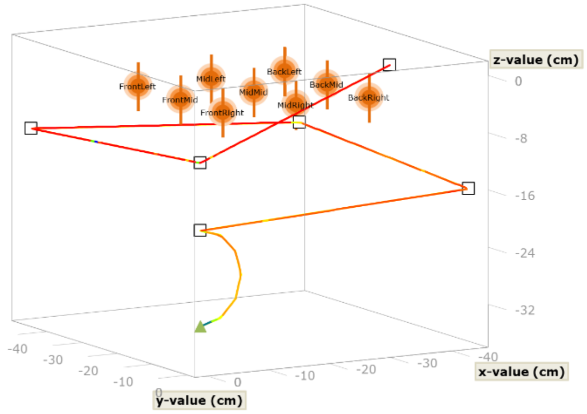

All Bulbs Half Power

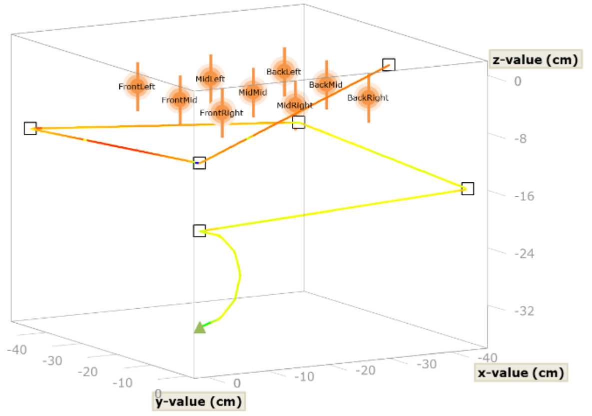

Figure A3.24: Display of All 6 Temperature Distributions

Graphing the data together on one plot can be seen in the following plot:

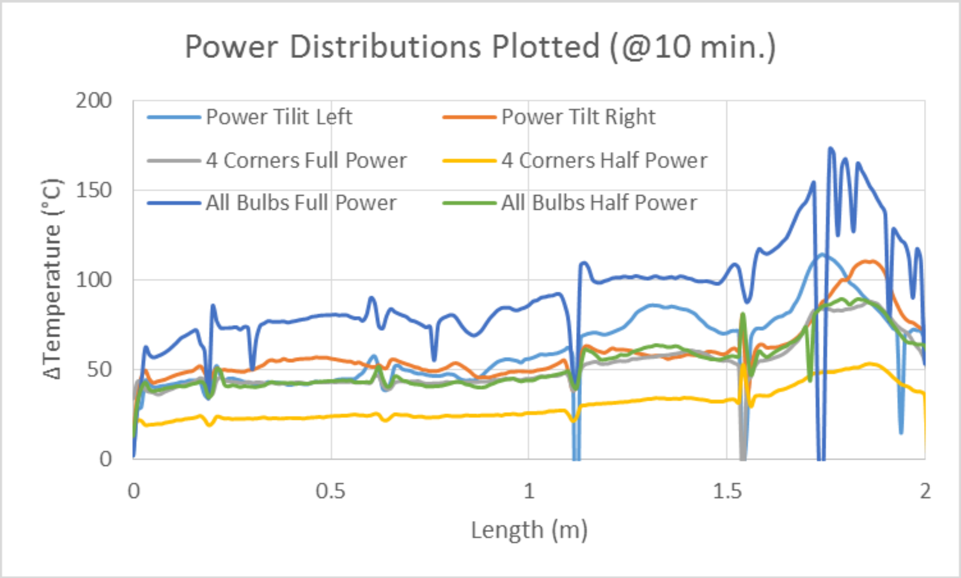

Figure A3.25: Data graphed of All 6 Temperature Distributions

In the above representation, it is quite difficult to compare one power distribution to the other. To offer a more easily seen comparison of two power distributions we can see the left and right power tilts as follows:

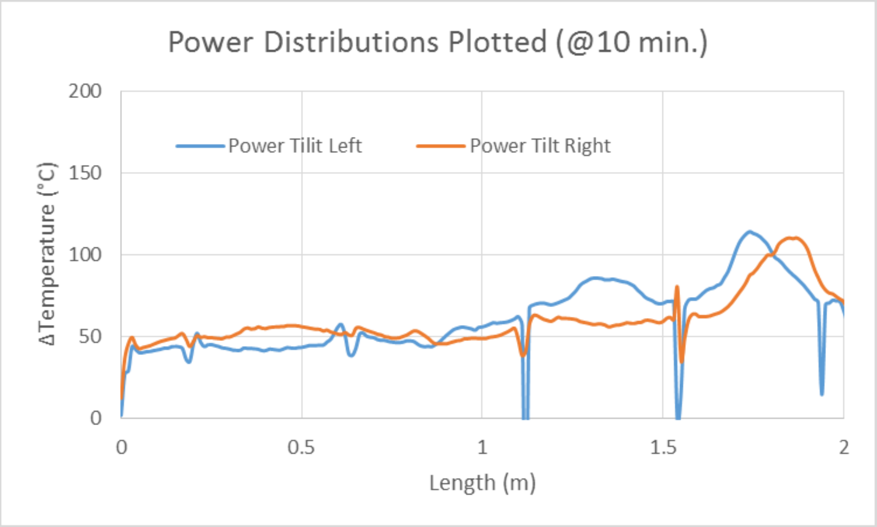

Figure A3.26: Graph of Left and Right Power Tilts

In this plot we can see there is a significant difference how the heat affects the fiber in each power distribution respectively. Because the data is unique, it presents the possibility that there is a unique solution to solve for calculating the power distribution for each of these data sets.

A3.2.5 Solve for Distribution using Non-negative Least Squares Method

The analysis of such distribution hinges on whether the temperature increase matches as if it was equal to the summing of the attenuation factors at the appropriate power level for each point sources. This comes from the mathematical assumption that the result should be the sum of the parts, or a sum of linear equations from the linear attenuation factors. This can be seen in the following equation where k is the attenuation factors from source term “i" to detector increment “j”, x is the source term, and y is the resulting temperature increase at increment “j”:

$$y_j = \sum_{i=1}^{i=9} k_{i,j}\, x_i$$

Because the set of data has 2 meters of measurement at 1 inch increments, there are a total of 200 increments yielding 200 of such equations. This hence creates a 200 position array for the temperature change from a matrix set of attenuation factors 200 rows down by 9 columns across to account for the summation of the 9 point source power levels. This is seen in the following equation:

$$\begin{bmatrix} y_{j=1} \\ \vdots \\ y_{j=200} \end{bmatrix} = \begin{bmatrix} k_{i=1,j=1} & \cdots & k_{i=9,j=1} \\ \vdots & \ddots & \vdots \\ k_{i=1,j=200} & \cdots & k_{i=9,j=200} \end{bmatrix} [x_{i=1} \quad \cdots \quad x_{i=9}]$$

Applying are known power distribution for as the input for the "x" array will yield a calculation of temperature increase ("y" array) based such an input. Yet, the research objective is such that the heat source is unknown rather than an input and can only be solved from the temperature change data using the previously recorded matrix of attenuation factors. Contrarily, the attenuation factors can be summed according to the input power level (referred to as "Calculated from Input"). This offers a comparison for how the temperature profile would have to appear to be reproduced identically from the numerical solver.

For the use of the numerical solver, if the columns and rows were equal, the solution could be calculated by inverting the matrix of attenuation factors ("k" matrix). This also has the potential to find solutions that yield negative values offset by large positive values for the solved power levels. Negative solutions for power are nonsensical, so the solver must not allow for such values.

These constraints provide for the use of a numerical solver using the technique of "Non-negative Least Squares," (hereafter abbreviated as NNLS). This technique can be solved in accordance with the "active set method" as published by Lawson and Hanson (Wikipedia, 2018). *Appendix 5 Programming Methods* details the implementation of this algorithm.

When the heat source distribution is solved for, it can be expected that it will not match identically to the actual heat source distribution providing such temperature measurement. This can be seen easily when we compare on a graph how the summation of point sources at that power level compare with the real data. This "Calculated from Input" line is well above the "Real Data" line in the following plot.

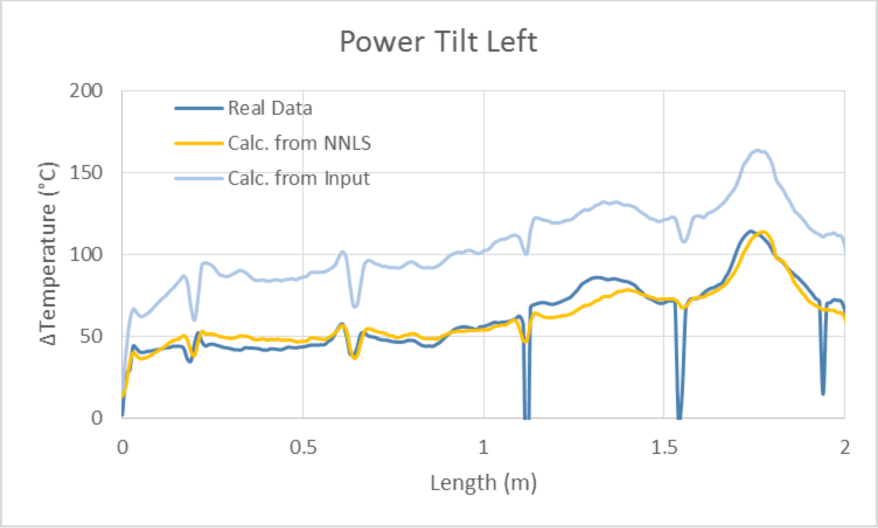

Figure A3.27: Graph of Power Tilt Left with Solution

As expected, the calculated from NNLS finds a solution that approximates the real data, but the solution does not match the real power distribution. What is still noteworthy, however, is that the shape of the curve is unique and "Calculated from Input" has a similar shape but is on a different magnitude. When compared to the “Power Tilt Right” we see that the power shape is unique. The “Power Tilt Right” graph can be seen below:

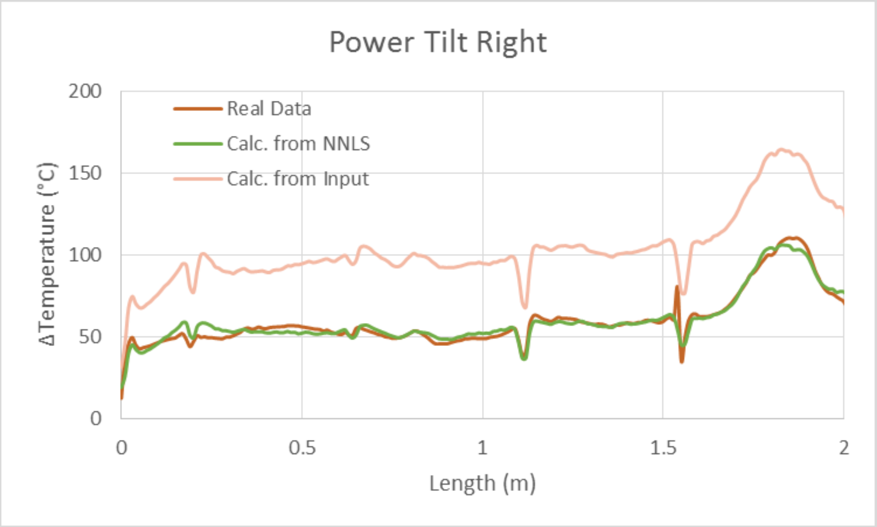

Figure A3.28: Graph of Power Tilt Left Right with Solution

It is apparent in the above figure that the peaked region of the last segment (~1.5m to ~2m) is significantly more round than in the “Power Tilt Right” temperature profile. We can quantify this as what is known as the “Full Width, Half Max” (FWHM) measurement. As the name suggests, the measurement quantifies a peak by the width it has at half its maximum value. The calculation of this value can be seen in the following graph of the “Power Tilt Right” with the points necessary to calculate FWHM called out.

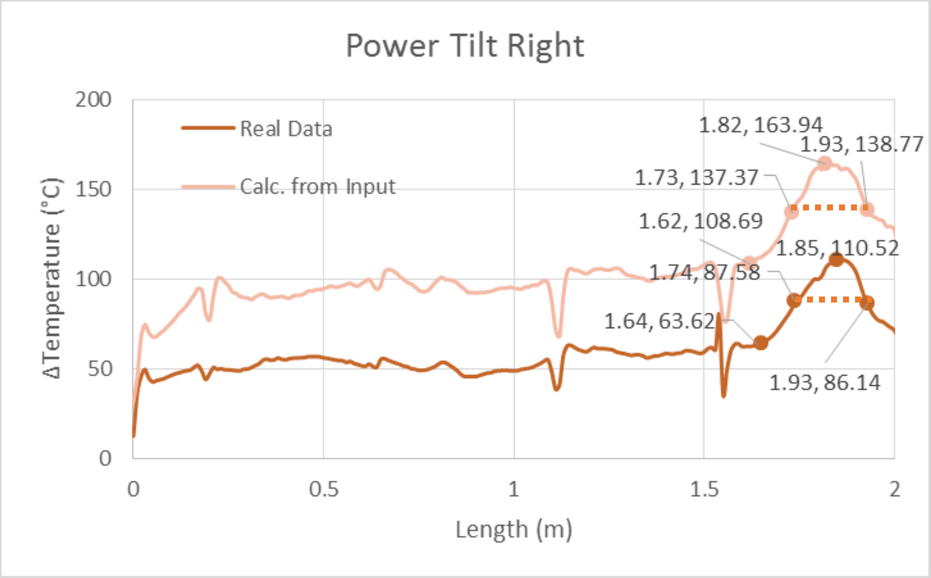

Figure A3.29: Graph of Power Tilt Left Right for Full Width Half Max

For comparison, the points of interest for calculating FWHM for the “Power Tilt Left” can be seen as follows:

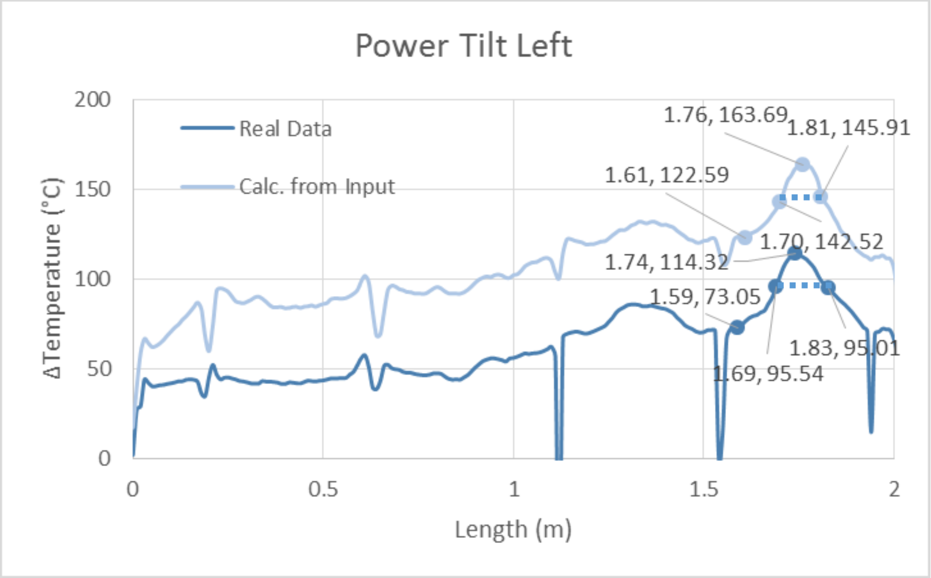

Figure A3.30: Graph of Power Tilt Left Right for Full Width Half Max

It's easily distinguished that the "Power Tilt Right" has a larger FWHM value in both its real data and the temperature calculated from the multiplication of the individual attenuation factors ("Calculated from Input"). A plot of this comparison is shown below:

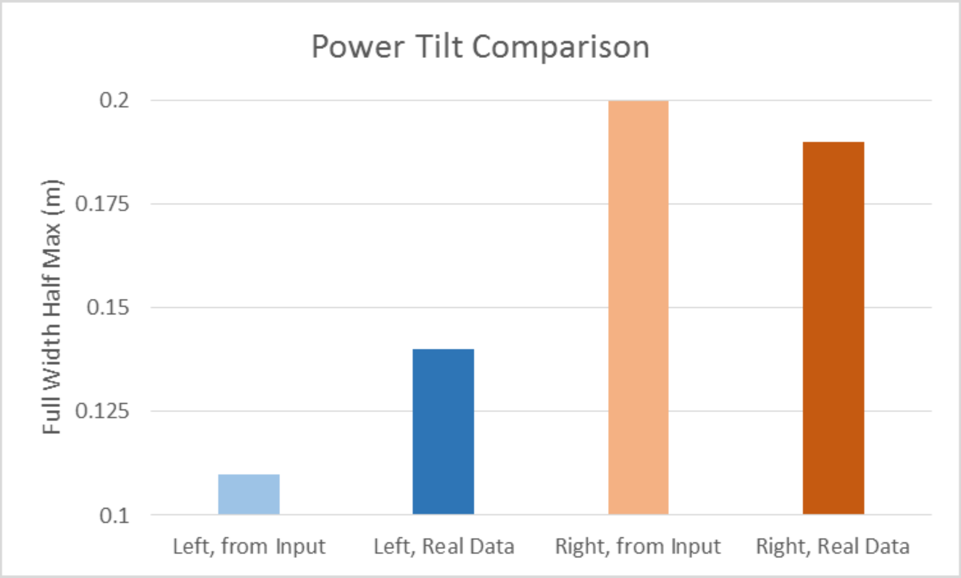

Figure A3.31: Graph of Full Width Half Max Comparison

Another feature in the plots besides the FWHM which is apparent in both the real data and the calculated from input projection, is the presence of a peak (local maximum) in the second to last segment in both "Power Tilt Left" profiles, while the second to last segment in "Power Tilt Right" has a trough (local minimum). What is important to note about these features is addition to them being prevalent in both the "Calculated from Input" and "Real Data" for the right and left power tilts respectively, these local maxima / minima appear in nearly the same position (within 1 cm of each other). This can be seen in the following figures where the maxima / minima are called out:

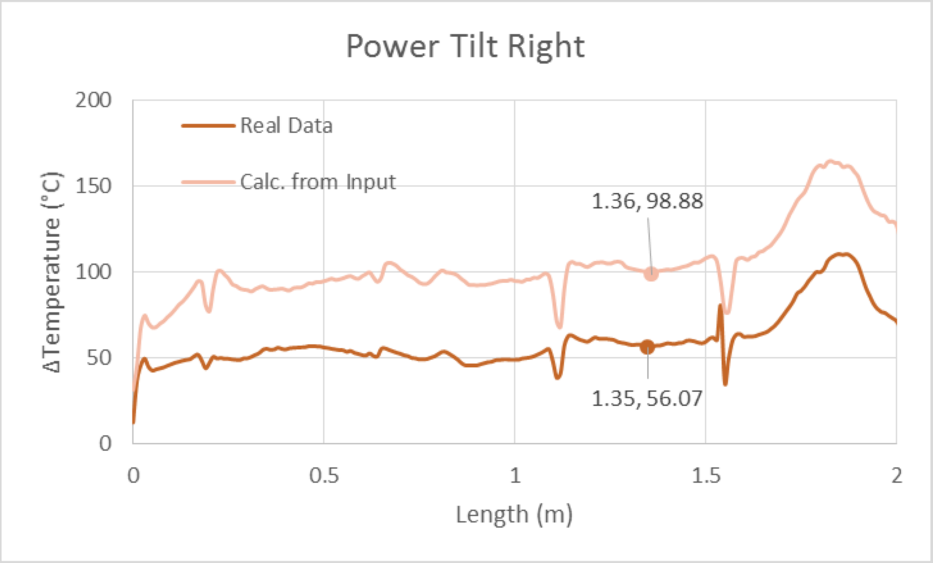

Figure A3.32: Power Tilt Right with Local Minimum

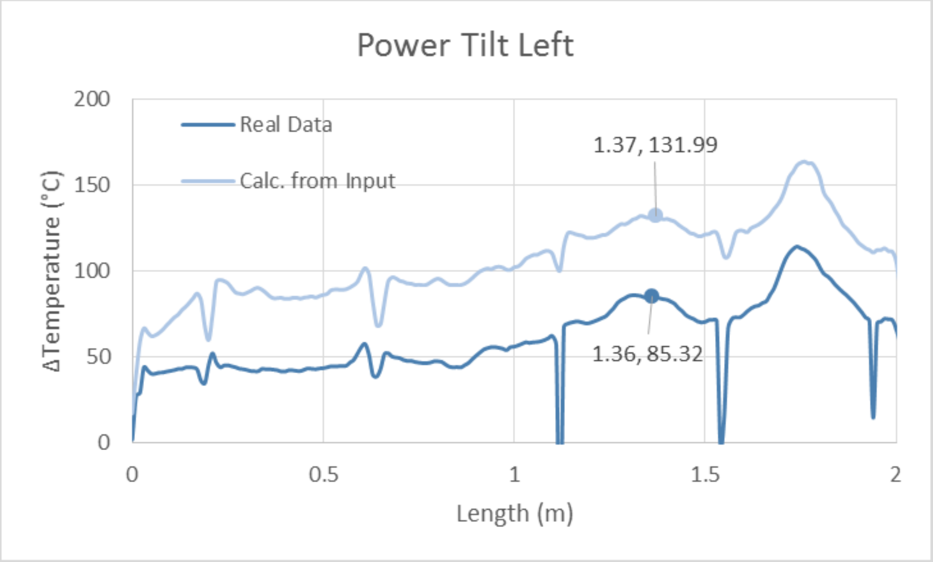

Figure A3.33: Power Tilt Left with Local Maximum

These similarities demonstrate that the “Calculated from Input” projection has some value or by demonstrating similar features when used in modeling the heat transfer physics even if there are some non-linarites that prevent the projection from capturing the correct values. The uniqueness for each power configurations heat distribution provides for the solver method to come up with unique solutions for each case. Although there are significant differences in input to output, we see that the solution technique finds unique solutions in the prediction of a power tilt left versus is a power tilt right.

Figure A3.34: Comparison of Solutions for Left and Right Power Tilts

Another set of power distributions were the use of the bulbs in the 4 corners. These bulbs were powered to full power and to half power. The difference in the temperature distribution can be seen as follows:

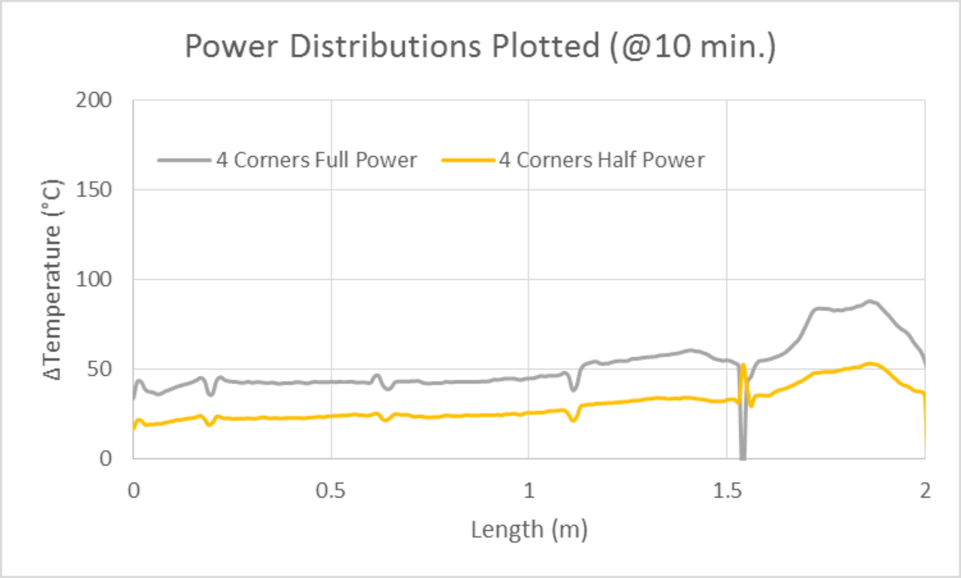

Figure A3.35: Graph of 4 Corner Power Distributions

The projection using the attenuation factors (Calculated from Input) does not project an accurate distribution for the full power. The final segment is somewhat round rather than peaked as shown in the projection and also in the previous power distributions. This is not detected by the projection. This can be seen as follows:

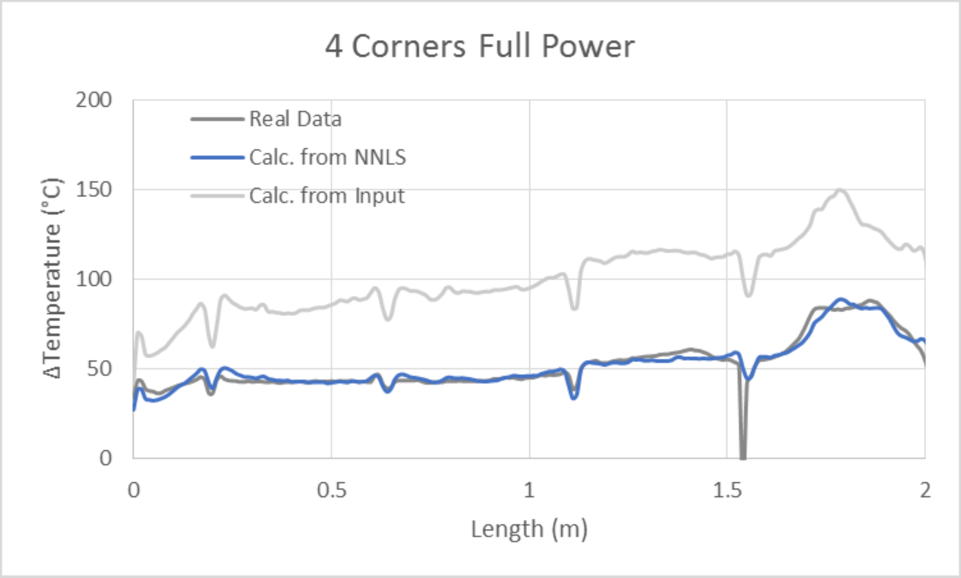

Figure A3.36: Graph of 4 Corner Full Power with Solution

The half power projection is quite close in magnitude and shape. This can be seen as follows:

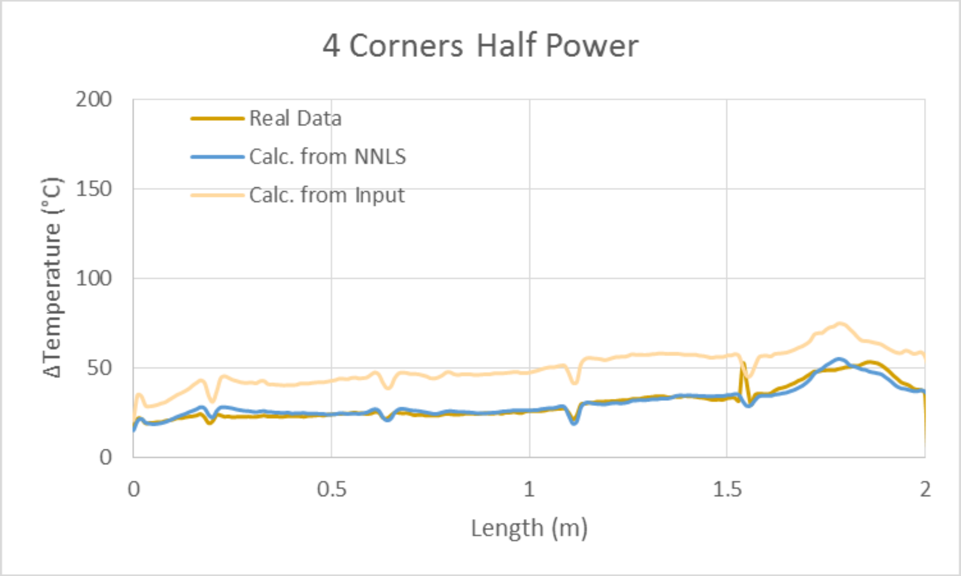

Figure A3.37: Graph of 4 Corner Half Power with Solution

To compare and contrast these power distributions, we can evaluate the ability of the algorithm to predict a full power distribution compared to a half power. Similarly to the power tilt solutions, the algorithm does not predict all bulbs' power levels correctly but does detect that there is a significant uniqueness to the solution. We see that at the full power measurement, the solver's solution is significantly higher than the half power solution.

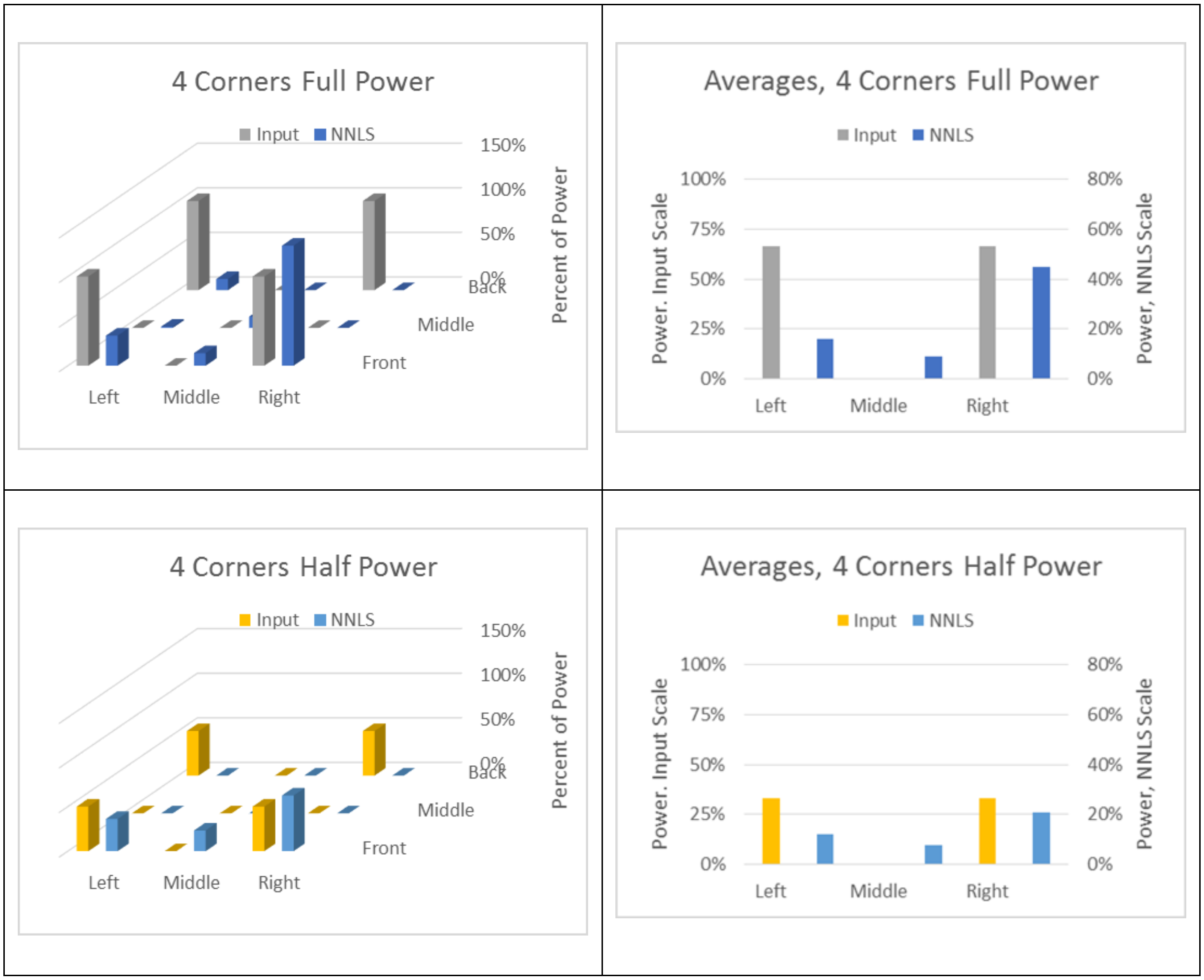

Figure A3.38: Comparison of Solutions for 4 Corners, Half and Full Power

Once again, for a comparison of full to half power distributions, the solution set for all bulbs being powered on shows a similar ability of the solution algorithm to attribute a diminished power level in its solution. As the first measured data set with significant calculation problems, the all bulbs full power has unrealistic temperature swings near the end of the fiber's measurement. This demonstrates that there is a possible problem in the temperature measurement algorithm. Since the algorithm is comparing individual segments to each other and finding the stretching effect of thermal expansion, when the temperature change is too great, it can be seen that the algorithm has trouble matching the appropriate segments and calculating the appropriate temperature change. It is obvious that the temperature change should not oscillate from a positive 100 to negative 100 degrees Celsius from one inch increment to the next. This is a limitation in the temperature calculating algorithm. This can be seen in the Figure A3.39 of the full power temperature change compared to the half power.

The full power distribution demonstrates the extent at which the combination of the individual attenuation factors is the most nonlinear. The calculated from input source distribution is much larger than the actual data. This can be seen in the Figure A3.40.

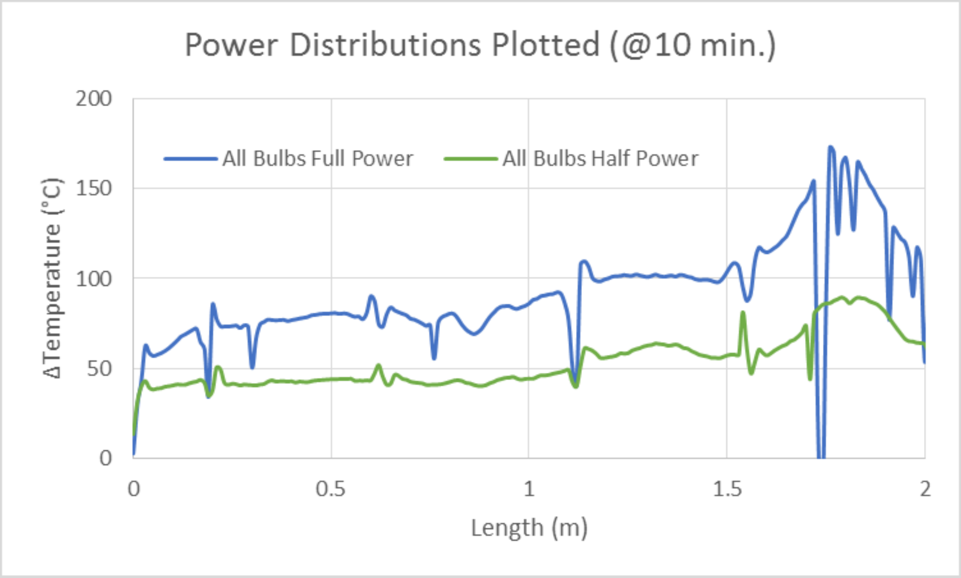

Figure A3.39: Comparison of All Bulbs at Half and Full Power

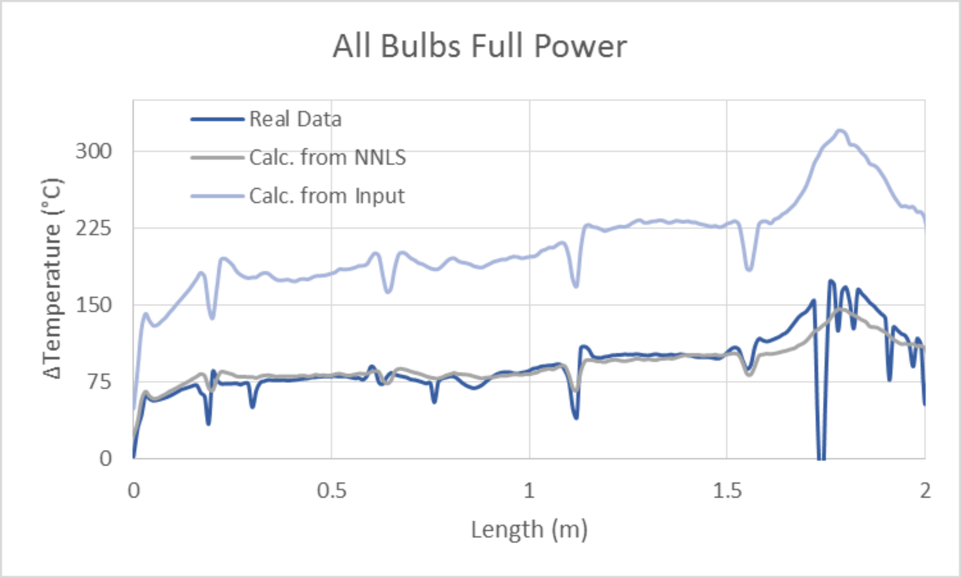

Figure A3.40: Comparison of All Bulbs at Full Power

The NNLS solver in this case has difficulty matching the real data because of the discontinuities in the last segment caused by the temperature calculating algorithm errors. For this reason, the NNLS has to solve for many highly negative data points leading it to underestimate a temperature profile which is true to form.

The general shape of the last segment is has a sharp peak when ignoring the errors. This is matched by the “calculation from input” even if the magnitude is too high. Conversely, this prediction method demonstrates a more rounded peak in the last segment for the half power temperature distribution, which is matched in the real data. This is shown in the following graph:

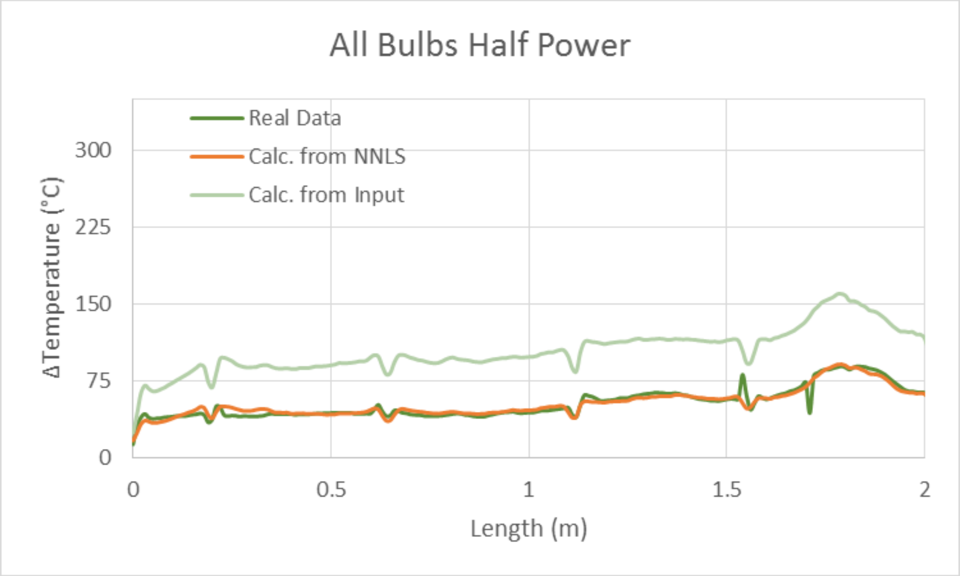

Figure A3.41: Comparison of All Bulbs at Half Power

Since the calculated from input does not match in magnitude for either power profile, although in shape but not magnitude, the NNLS calculation is not able to match the input. What is demonstrated quite clearly, however, is that the power profile for all bulbs should be twice as higher for full power than half power. The NNLS is successful in this comparison. The solver results can be seen in the following figures.

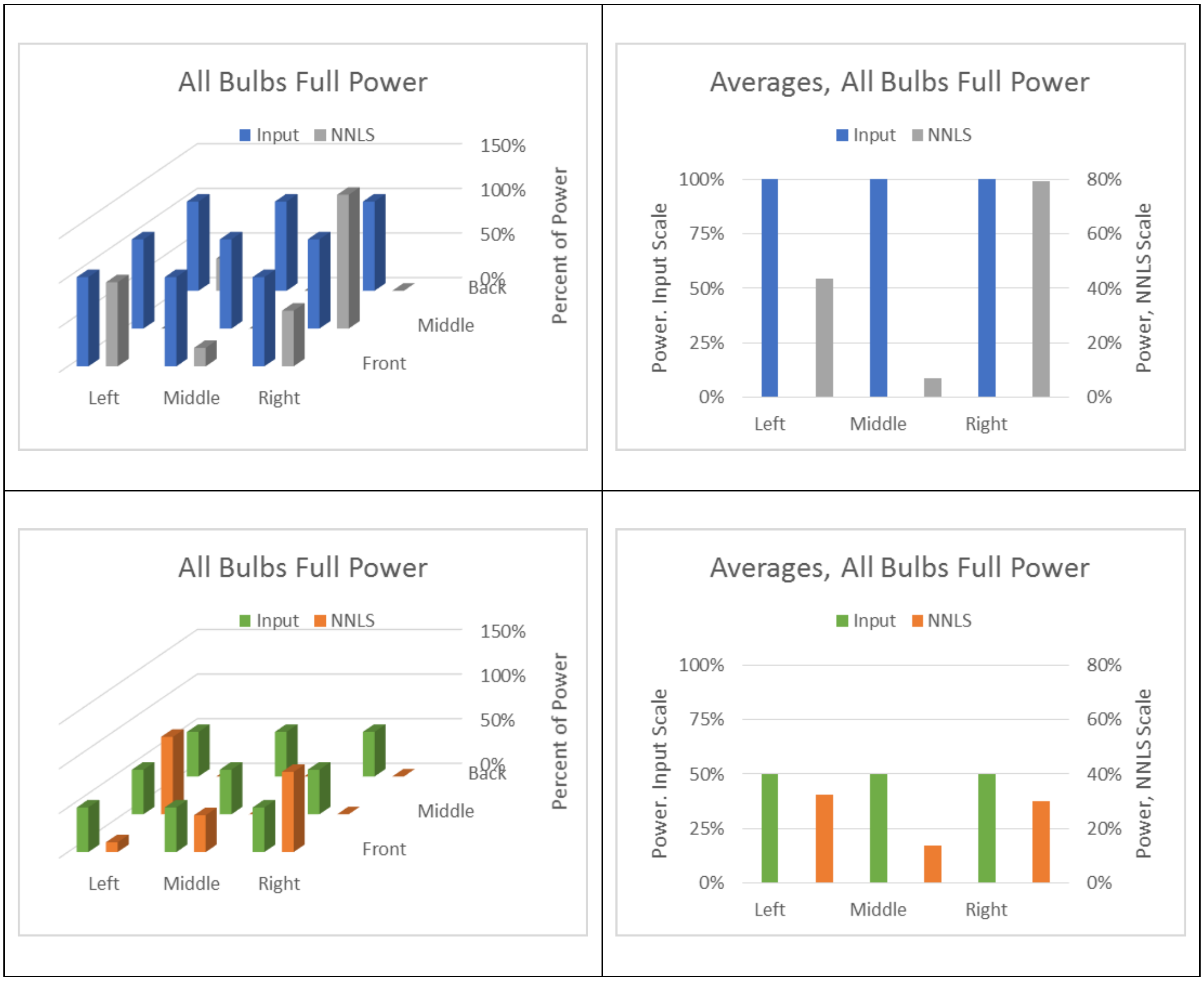

Figure A3.42: Comparison of NNLS Solver for All Bulbs at Full and Half Power

A3.2.6 Summary

When calculating the temperature change using the attenuation coefficients multiplied by the input source power distribution, it can demonstrated that there are significant non-linearities which prevent this calculation from matching the real data. This was present in all temperature tests. However, this “Calculation from Input” method displayed similar trends and shapes in its temperature profile to the real data even if the magnitude was inaccurate. This uniqueness in the profiles provided the opportunity and ability for the NNLS solver to calculate power distributions that were similar to the actual input source distribution and able to capture the differences from contrasting power profiles.

APPENDIX 4: CORRELATION OF RADIATION DOSE (RESPONSE FUNCTION)

A4.1 Construction of Test Rig

A4.1.2 Introduction

It an effort to make repeatable the experimentally derived results of Chapter 4, *Correlation of Radiation Dose (Response Function)*, it was deemed necessary and important to carefully document the construction of the test rig. This appendix section is complete with text and figures such that it be known the methods and materials in the rigs' construction, in addition to the performed experiments and the results that were obtained.

A4.1.2 Equipment

Various equipment and devices were needed to construct the test rigs for the purpose of irradiation. The most difficult construction item was the fibers themselves. It was necessary to terminate the fibers with a connector so that they could be interrogated by the measurement device. A design decision was made that the best method for adding the connector would be splicing the fibers to a short fiber segment which already had a connector (known as a "pigtail"). The overall setup of equipment to perform this construction can be seen in the following figure:

Figure A4.1: Overall Equipment Setup

The splicing operation took several tools to prepare the fibers for a successful splice. A layout of these fiber tools can be seen as follows:

Figure A4.2: Layout of Fiber Splicing Tools

After stripping the outer coating of the fibers, they had to be cut with a special tool known as a fiber “cleaver.” This cleaving procedure would produce a very clean, 90° edge as the fiber tip. It would then be possible to use the fusion splicer to align the two tips (pigtail fiber and experiment fiber) to be perfectly matched and then melted together with an electric arc. These operations can be seen in the following figures:

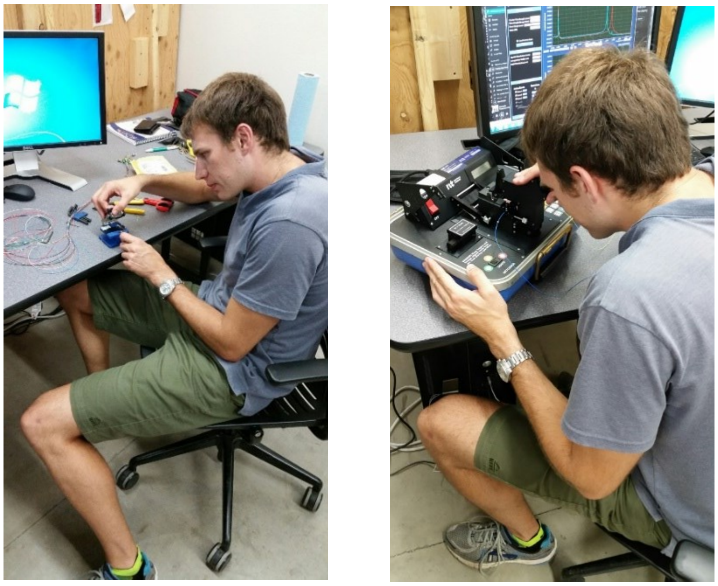

Figure A4.3: Fiber Cleaver and Fusion Splicer in Operation

The measurement device was an important component in the construction of the fibers. This device, known as an Optical Backscatter Reflectometer (OBR), is the same device used throughout this dissertation for interrogating the fibers for temperature and radiation response testing. Its function during the construction was to connect with a jumper into a prepared fiber to see if a splice was successfully performed. If the splice was successful, the scan of the fiber would show a large reflection at the end of the entire fiber length instead of a large reflection at the splice and no data afterwards. A photo of the OBR device and associated computer software to review the scans can be seen as follows:

Figure A4.4: OBR Measurement Device and Operating Software

A4.1.3 Materials

The experimental fiber comes from fibers leftover from the collaboration with Luna Technologies for studying the effects of high temperature and high radiation on fibers using the TRIGA reactor at Texas A&M University. The OBR measurement device was also procured during this study.

Luna Technologies characterized their fibers as “Temperature,” “Gamma,” and “Neutron.” In actuality, as single mode fibers, all three fibers have the ability to measure temperature with the OBR technology. Furthermore, the three fibers used in the study were pure silicon, germanium-doped, and boron-doped and it is thought that they characterize the “Temperature,” “Gamma,” and “Neutron” fibers respectively. Prior to this dissertation’s effort, it was not demonstrated whether any of the three fibers was better for establishing a correlation to radiation dose.

Having substantial leftover fibers of all types, it was decided that every test rig should have each fiber. Because of the conjecture that the germanium-doped fiber was more sensitive to gamma radiation, this fiber was duplicated in the test rig while the other types were one fiber each for a total of four fibers per test rig. The fibers were shipped from Luna on several spools, one each for the germanium-doped and pure silica fiber, and the rest were all boron-doped. The boron-doped were clearly in over-abundance so this was the fiber of choice for experimenting with construction techniques and an extra test rig was made of only boron-doped fibers. The abundance of the experimental fiber can be seen in the figure of the shipped fibers below:

Figure A4.5: Shipment of Fibers from Luna Technologies

Being spools of bare fibers, it was necessary to add connectors to provide the ability for measurement by the OBR device. The device required connectors of the type FC/APC or Ferrule Connector / Angled Physical Contact. As an alternative to attaching individual FC/APC connectors to each bare fiber with an adhesive, a short fiber segment with a built-in connector (known as a “pigtail”) was spliced to each bare, experimental fiber. These “pigtails” could be procured very cheaply in packs of 12, each having its own color of fiber jacketing. The connector color became important for distinguishing which of the bare fiber types was spliced to each pigtail. The pack of 12 pigtails as purchased can be seen in the following figure:

Figure A4.6: Procured Pack of Fiber Optic “Pigtails”

The other materials used in the construction of the test rigs were purely structural. It was necessary to use conduit to secure the fiber optic as a coil around a central tube since the bare fiber was very difficult to coil. An outer tube then protected the coil and kept it in its place. Unique colors of electrical tape distinguished which test rig was with which irradiation scheme since the test rigs were otherwise identical. Pipe hanger straps made of plastic secured the fiber optic connectors in place. Metal wire provided a handle for use to manipulate in and out of the irradiation containers. A figure of all these structural materials can be seen as follows:

Figure A4.7: Structural Materials

A4.1.4 Assembly

Constructing the rig involved first taking the bare experimental fiber and cutting to a length of approximately 5.5 meters (18 feet). Subsequently, splicing this fiber to the pigtail of approximately 1.5 meters (5 feet) produced a fiber of 7 meters (23 feet) in its entirety. Because the bare fiber was difficult to bend at a fixed radius, it was required to be placed in split tubing as a conduit for coiling with the test rig. Therefore, this tubing was cut also to a length of 7 meters (23 feet). Preparing these measurements was done on a long experiment table as can be seen in the following figure:

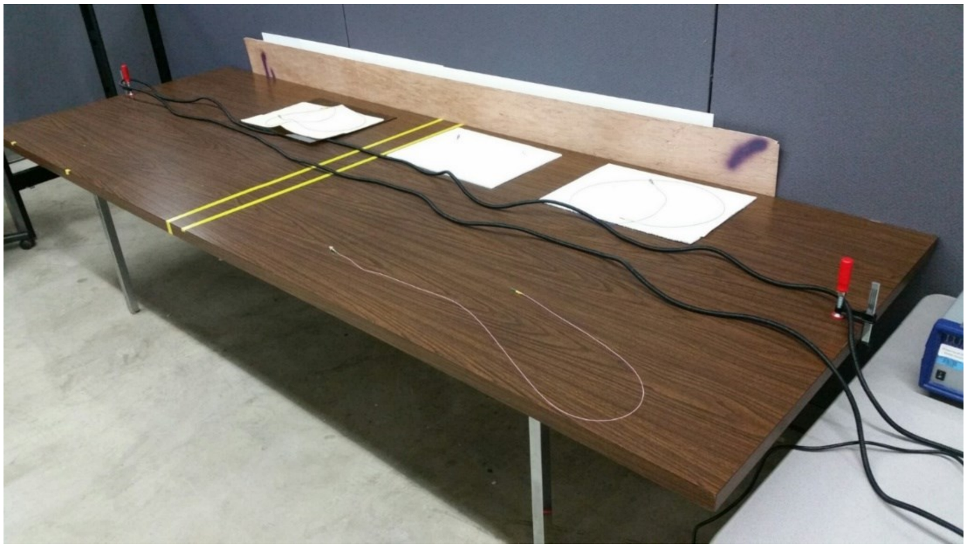

Figure A4.8: Preparations for Cutting Conduit and Fibers on Experimental Table

Once the fibers and tubing were prepared, there was the difficult process of getting the fibers within the tubing. The tubing had a split down the middle, but because the fibers as bare material were very fragile and difficult to maintain a fixed radius, it was difficult to push the fibers into the tubing. Instead, the most successful method proved to be pulling the fibers through the tubing. The ends of the fiber with the connecter were taped together so the four fibers could be pulled together at once. The ends were pulled along the split in the tubing, after which the split would be taped to prevent the fibers from exiting the tubing through the split. This process can be seen in the following figure:

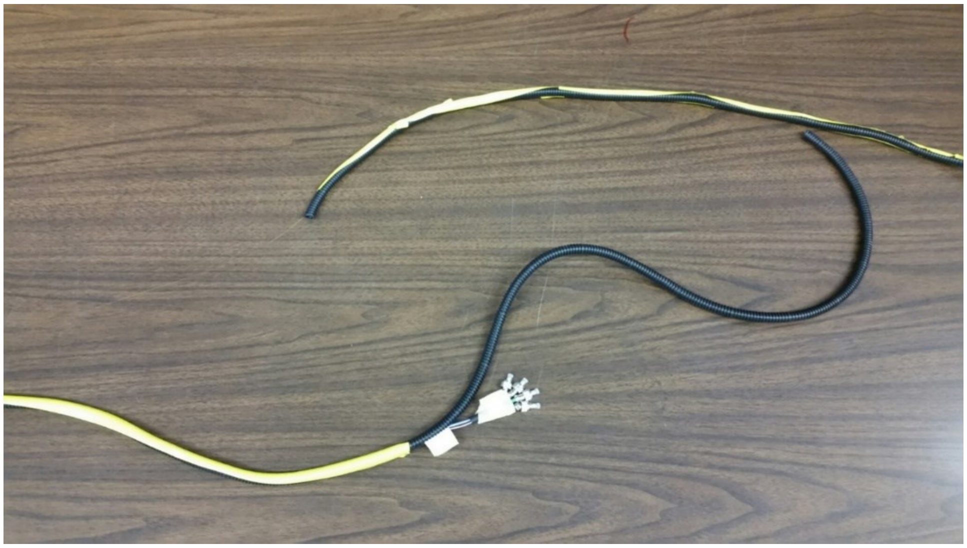

Figure A4.9: Process of Pulling Fibers Through Split Tubing

Pulling the fibers through the tubing proved tedious and difficult since it put stress on the splice within the fibers. Occasionally the fiber would break at the splice location if the fiber was pulled with too much tensile strength. This would necessitate the fibers to be taken out of the tubing at the splice location and repeat the fusion process. For several fibers, the breaks were not discovered until after assembly. In these cases, the test rigs were irradiated with these fiber breaks, having the ability to take the rig apart and re-splice post-irradiation if necessary.

Once the fibers were pulled completely through the tubing and the tubing split was completely taped. The tubing containing the fibers was wrapped around a small diameter, 1 ½ inch PVC pipe creating a coil. This pipe was cut to length and had a slot cut on one end and pipe hanger straps attached on that end. The slot was cut so the fibers could exit the tubing within the center pipe while the hanger strap was used such that the holes within the strap could hold the fiber connectors in place. On the opposite end, a hole was drilled through the pipe so the fiber coil could be held in place on that end by attaching the tubing within that hole. This complete assembly of the fiber optic coil can be seen in the following figure:

Figure A4.10: Assembly of Fiber optic Coil on Central PVC Pipe

A second pipe was used which had a larger diameter (3 inch) and made of metal. This type of pipe was of the type typically used for household ductwork. The pipe was thin metal making it possible to cut to a length slightly longer than the central PVC pipe. A hole drilled in one end corresponded to a hole drilled in the PVC pipe so that they could be attached with a bolt and nut arrangement. Two holes on the opposite end provide for the bolts on the hanger straps to attach to the outer metal pipe. A comparison of the construction of the central pipe and outer pipe can be seen in the following figure:

Figure A4.11: Comparison of Construction of Test Rig Pipes

The driver for the design was for use at the Oak Ridge Nation Lab (ORNL) Gamma Irradiation Facility (GIF). As such, the dimensions of the test rig were determined by the irradiation canister and a wire was fastened to the outer pipe for handling at the facility. The goal was then to maximize the length of fiber contained within those dimensions which lent itself to the coil design. The figures below show the final dimensions of the test rig, a 3 inch (7 ½ centimeters) diameter and a length of 20 inches (50 centimeters):

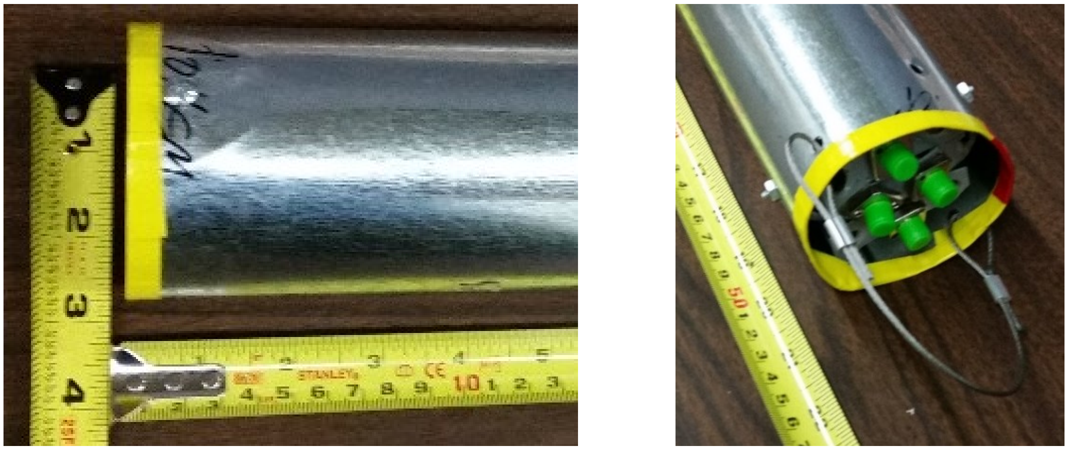

Figure A4.12: Final dimensions of Test Rig

A4.1.5 Irradiation

The main plan for the test rigs was to irradiate in the ORNL GIF. However, and opportunity presented itself to irradiate at the University of Cincinnati Cobalt-60 irradiation facility. This was for two very lose doses, 100 Gy and 1 kGy. The irradiation canister was exactly big enough for the test rig even though its design had not taken into account this facility's irradiation canister. Pictures of preparing the irradiation canister and lowering it into the pool at the University of Cincinnati facility can be seen in the following figure:

Figure A4.13: Irradiation at University of Cincinnati Cobalt Facility

The other test rigs were irradiated at ORNL GIF. As a scoping study with little information to suggest which irradiation duration would be optimal, it was decided to irradiate each rig differently by an order of magnitude. A redundant irradiation was done at 10 kGy because an extra rig was prepared with only boron doped fiber as all four coiled fiber optics. The rigs were color coded by different color electrical tape which was used to cover the edge on the metal pipes. The color-coded rigs with their corresponding doses can be seen in the figure as follows:

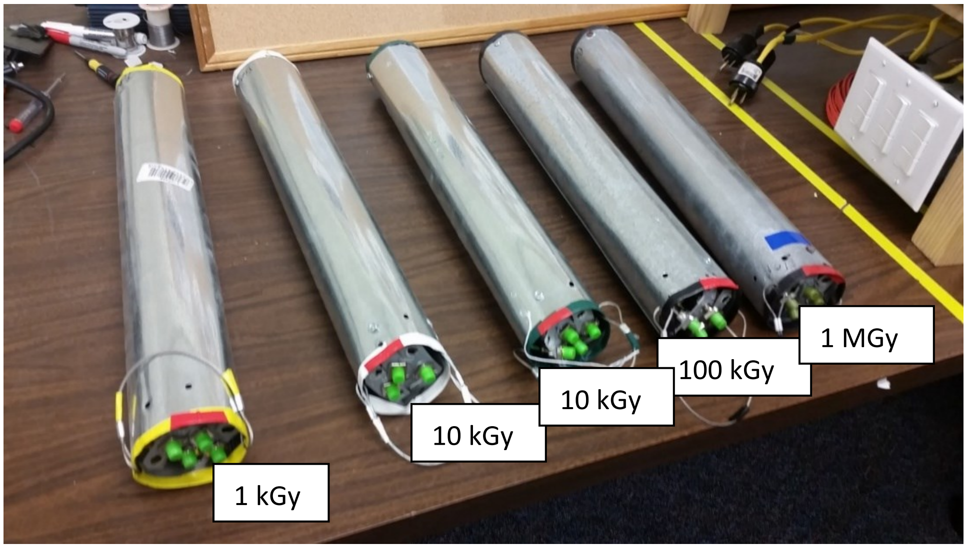

Figure A4.14: Color Coded Test Rigs and Corresponding Doses

It was noticeable that the last rig appeared to be a redundant color code as both appeared taped with black electrical tape. However, this was because the test rig was originally taped in blue but as the highest irradiation test rig at 1 MGy, the blue tape had turned black. The harshness of such a high irradiation made notable color changes on other materials as well. The PVC was originally white, and even at some of the lower irradiations of 100 kGy and 10 kGy the color developed a dark tint corresponding to the dose received. Furthermore, at the 1 MGy level, the white PVC turned completely black. Additionally, at this high dose, the metal bolts and nuts experienced corrosion. These changes in the structural materials can be seen in the following figure:

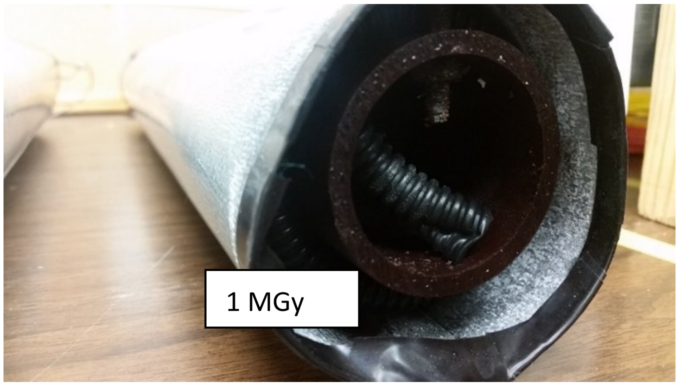

Figure 4.15: Color Change and Corrosion as a Result of 1 MGy Irradiation

A4.2 Measurement Data

A4.2.1 Introduction

This appendix chapter details the collection of data used towards the research objective of *Chapter 4: Correlation of Radiation Dose (Response Function)*. There were a total 5 individual test rigs built for this experiment. Each of the sections in this appendix details the results obtained from each test rig.

A4.2.2 Blue Test Rig (1 MGy)

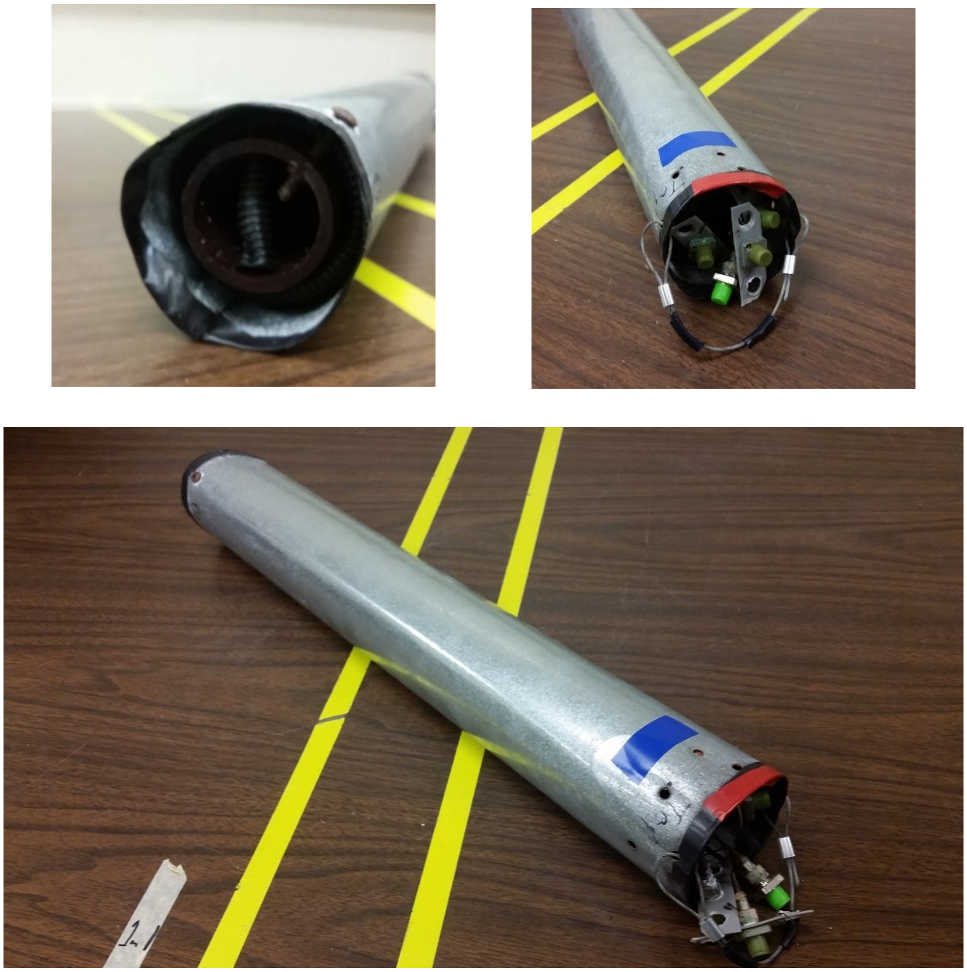

Figure A4.16: Blue Test Rig Assembled

The following graphs are scans after the splice connection was made:

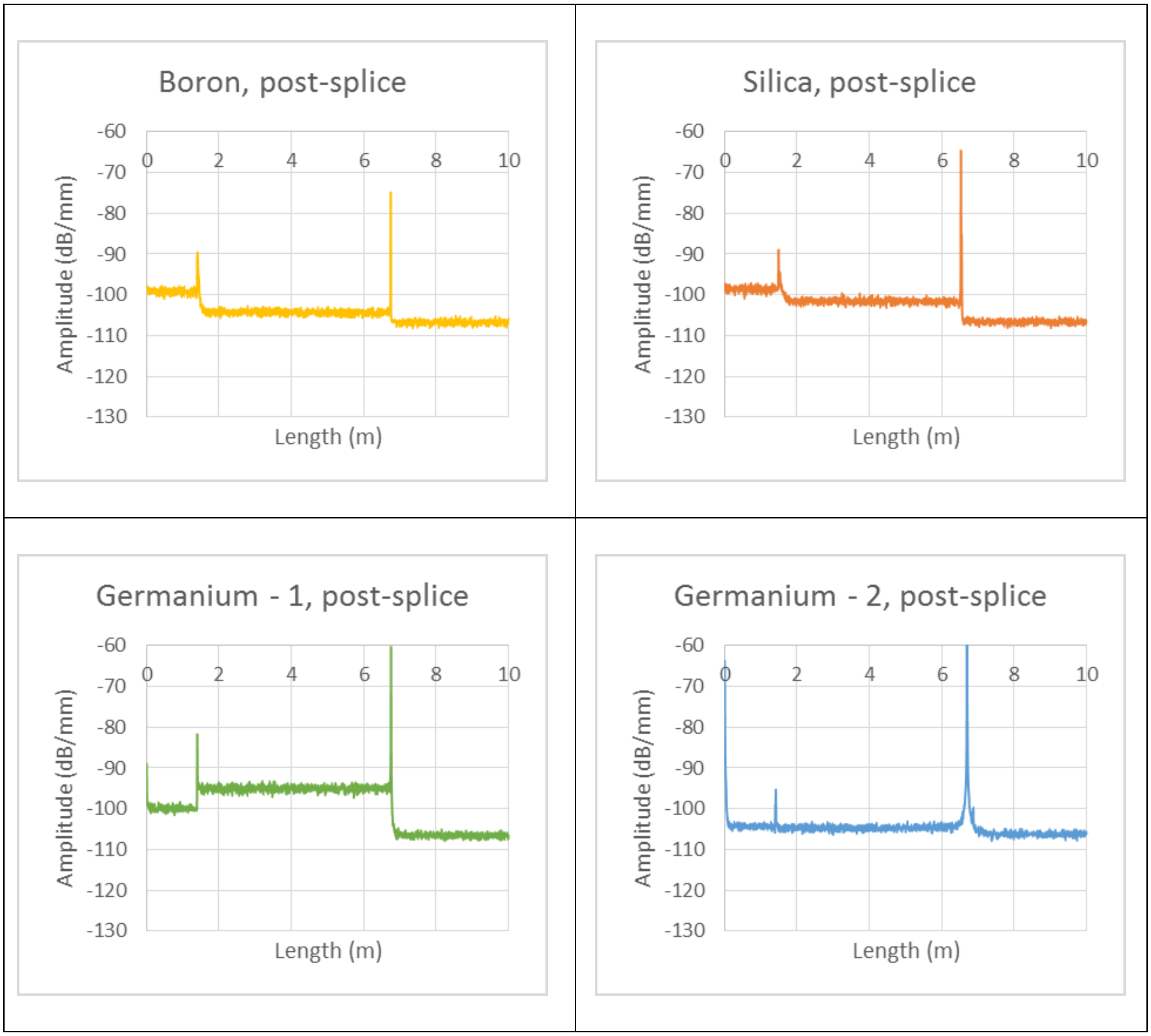

Figure A4.17: Graphs Post Splice

During the assembly, several splices broke. It was decided not to disassemble and resplice. These splice breaks can be seen for the pre-irradiation (0 Gy dose) graphs as follows:

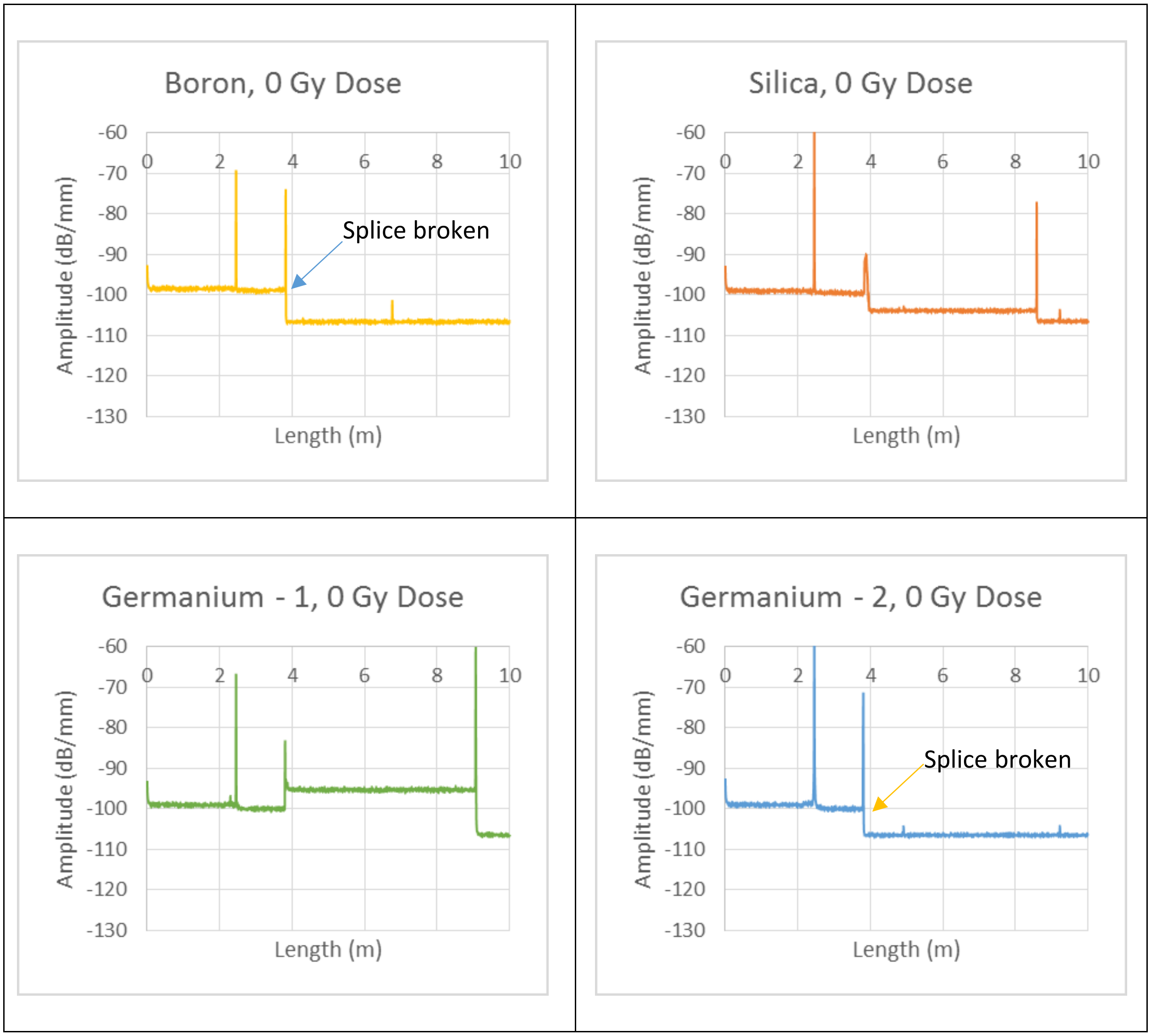

Figure A4.18: Graphs Pre Irradiation (0 Gy Dose)

In the process of transporting the rig, an additional fiber optic (pure silica) had its splice break. The remaining germanium-doped fiber was available for analysis. This is seen in the following graphs:

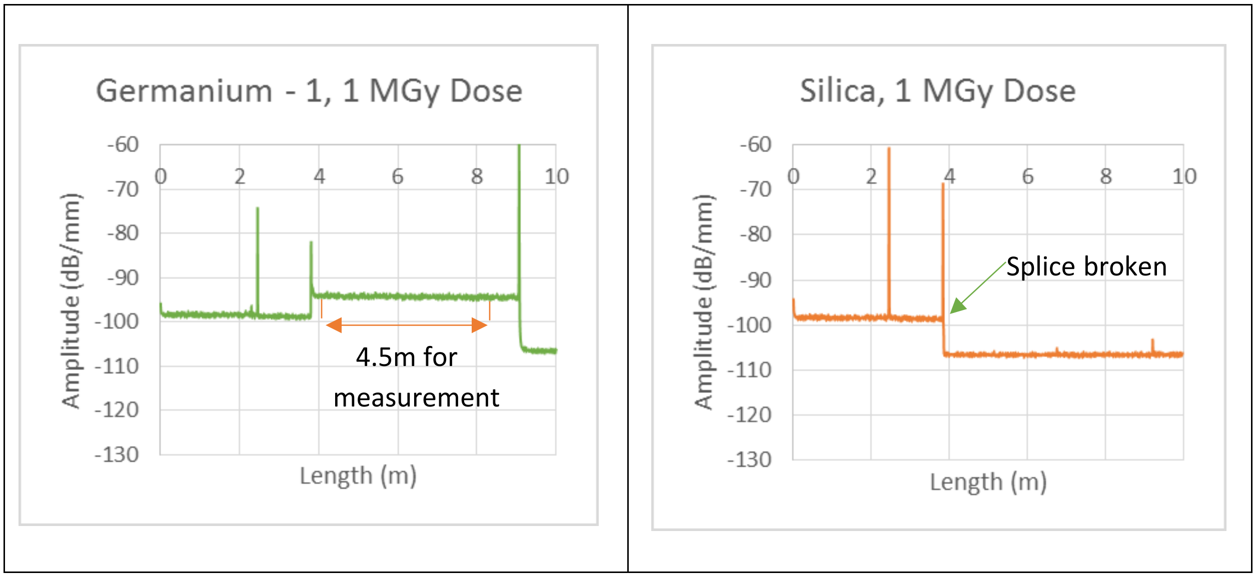

Figure A4.19: Graphs Post Irradiation

Although the 4.5 meters available for measurement appears to be without much variation, when graphed on a different scale for the axis, the high frequency fluctuations are more obvious. This is true in both the long scan version of the data (43 nm frequency range) and the short scan version (5nm frequency range). These graphs can be seen as follows:

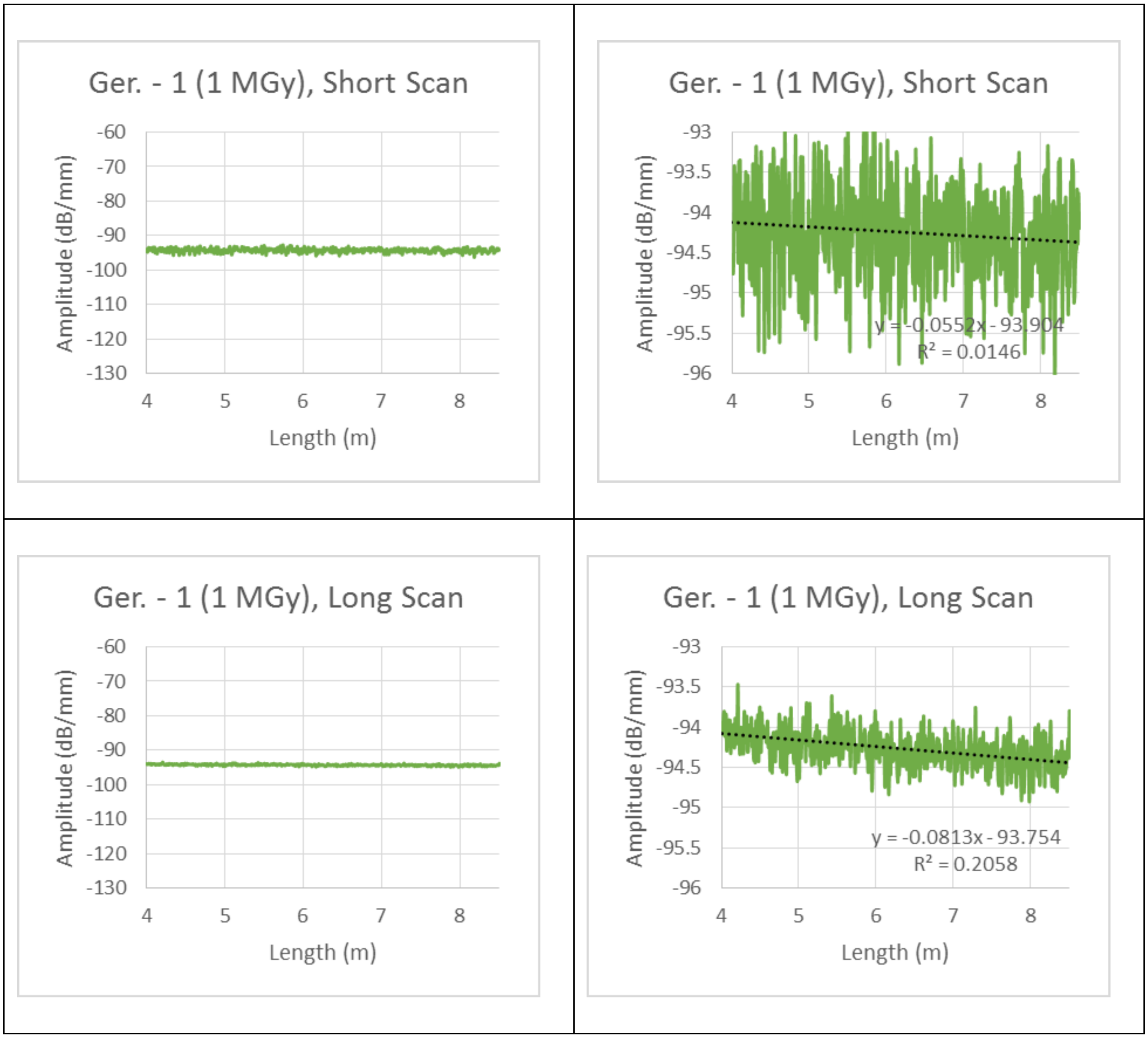

Figure A4.20: Graphs of Long Scan Compared to Short Scan

It is clear by examining the Coefficient of Determination (R^2) that the long scan is preferable for analysis since it provides for a better trend line established by linear regression techniques. The analysis was dependent on correlating the effect of radiation dose on the increase in the negativity of the slope corresponding as presented by the declining signal within the fiber. To provide for a smoother response, averaging techniques were used to better demonstrate the negative slope property. The equations for averaging for 2 fiber scans (before and after irradiation) look as follows:

$$Average_1 = \frac{\sum_{n=1}^{n=N} X_{1_n}}{N}$$

$$Average_2 = \frac{\sum_{n=1}^{n=N} X_{2_n}}{N}$$

$$\Delta Average\ (Method\ 1) = Average_1 - Average_2 = \frac{\sum_{n=1}^{n=N} X_{1_n}}{N} - \frac{\sum_{n=1}^{n=N} X_{2_n}}{N}$$

$$\Delta Average\ (Method\ 2) = \frac{\sum_{n=1}^{n=N} X_{1_n} - X_{2_n}}{N} = \frac{\sum_{n=1}^{n=N} X_{1_n}}{N} - \frac{\sum_{n=1}^{n=N} X_{2_n}}{N}$$

From these equations it can be seen that either averaging formula provides for the same results. Taking the average from a set of points provides for modifiable parameters of what's known as "gage length" which determines how many points are used to calculate the average, and "gage gap" which is the spacing from one average to the next. Comparing two averaging techniques, one with a gage length of 10 points (8.4 cm) and gage gap of 5 points (4.2 cm) and the other with 20 points length (16.8 cm) and 10 point gap (8.4 cm). Plots of this comparison for both the short scan and long scan can be seen as follows:

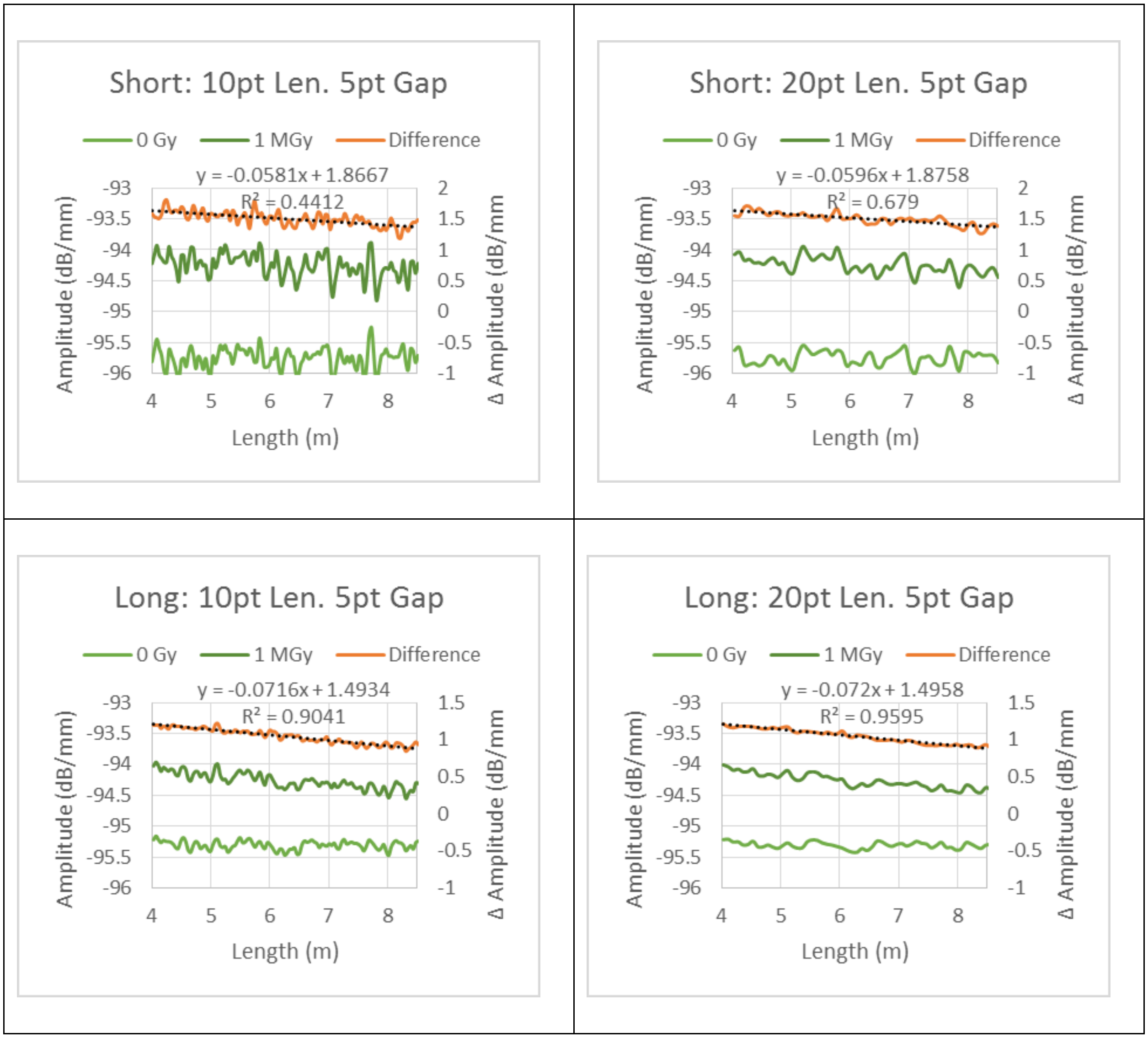

Figure A4.21: Graphs of Different Averaging Techniques

Since the slope of the trendline is related to a material property change induced by the radiation dose, it is a possible to use as a metric to make a distributed measurement of radiation dose magnitude. Therefore, dividing the measurement into shorter segments for individual trendlines should present a correlation to the distributed nature of the radiation dose. This was done in 1.5 meter sections (38 averages for the 5 point gage gap, 19 for the 10 point gage gap). These results can be seen as follows for the short scan:

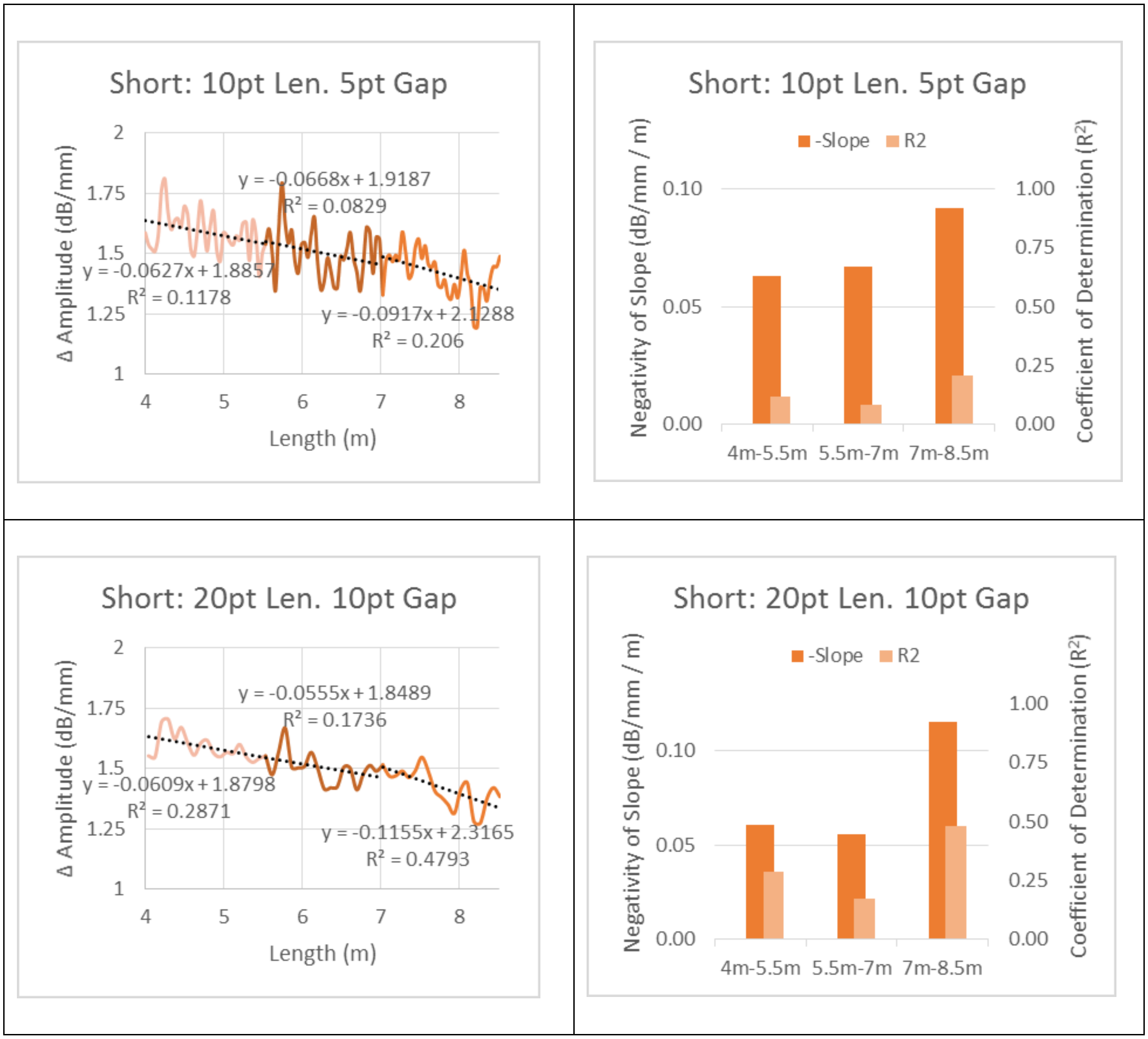

Figure A4.22: Graphs of Segmented Trendlines for short scans

It is apparent in these graphs that the trendlines are a poor representation of the data for the short scans as demonstrated by the low values for the coefficient of determination (R^2).

All R^2 values were less than 0.5 and for the 10 point length / 5 point gap averaging technique specifically, all R^2 values were below 0.25. Contrarily, representing the long scan data by trendlines was more successful. This is seen in the following graphs:

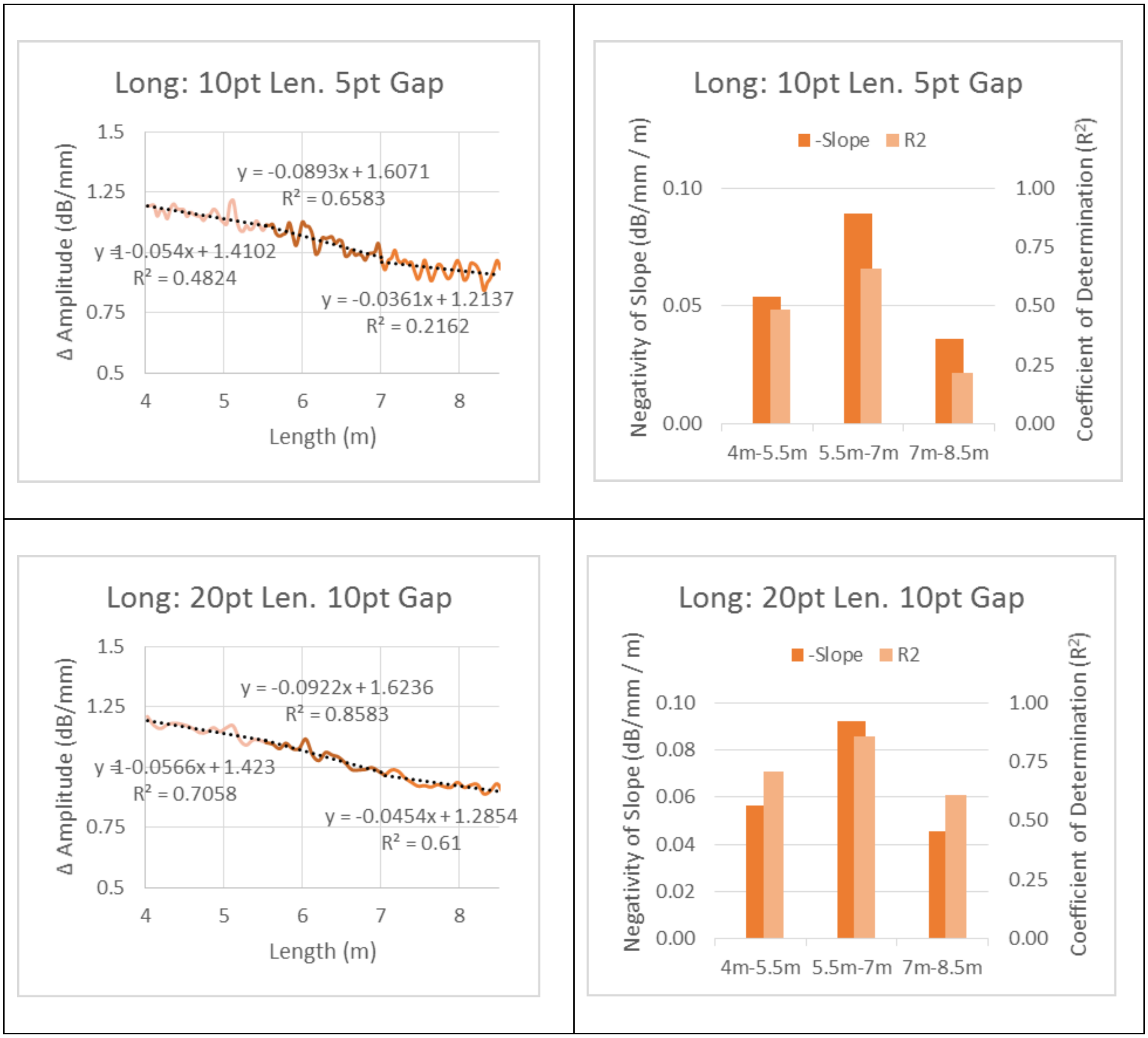

Figure A4.23: Graphs of Segmented Trendlines for Long Scans

The long scans demonstrated significant improvement in R^2 values compared to the short scans. Because of the breaks in the other fibers, even after disassembly of the irradiation rigs and resplicing the connections, the only data available would be short scans for comparison. However, working with the single fiber that had long scans available for comparison, it was clear that this dataset provided a useable method for a radiation response function analysis. The 20 point length / 10 point gap averaging technique had the superior R^2 values of the two averaging techniques, demonstrating that analyzing the data in this way provided the best representations of trendlines in the data set.

A second analysis could be then conducted on the length of segments for constructing the trendlines. Adjusting the segment length to provide for 5 separate trendlines then used segments comprised of 11 points of averaged data. The data represented in this way can be seen in the following graphs:

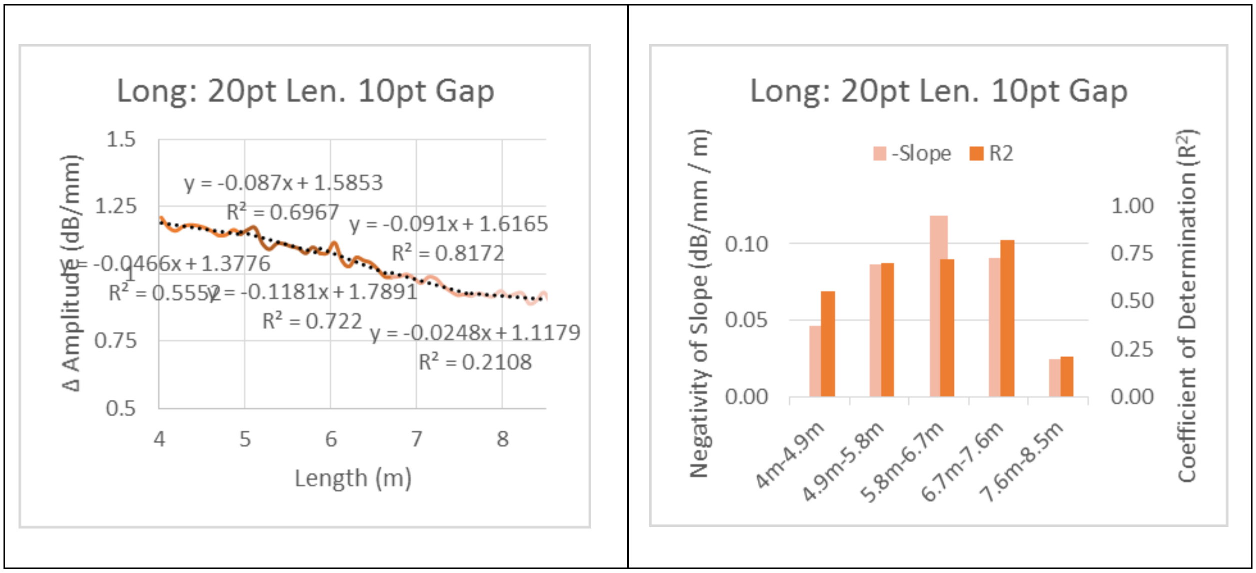

Figure A4.24: Graphs of 5 Separate Segmented Trendlines

These trendlines all had R^2 values of 0.5 or higher except for the last segment which was quite low in comparison (0.21). It should therefore be noted that this segment was closest to the fiber tip which may cause some distortion in the data. However, what is clear in the data for both segment lengths is the slope of the trendlines for each segment increases towards the center and decreases towards either end. This is similar to the way fuel burns in a reactor such that the centerline is the most active (and most radioactive) region of the fuel. Hence, an irradiation facility constructed of used fuel such as the Oak Ridge facility should follow a similar radiation distribution.

Dosimetry from the conducted irradiations provided 3 data points, one at center and one for top and bottom respectively. Comparing the trendline representation of the fiber optic data to those dose points (or extrapolated dose to create 5 data points) can be seen in the following plots:

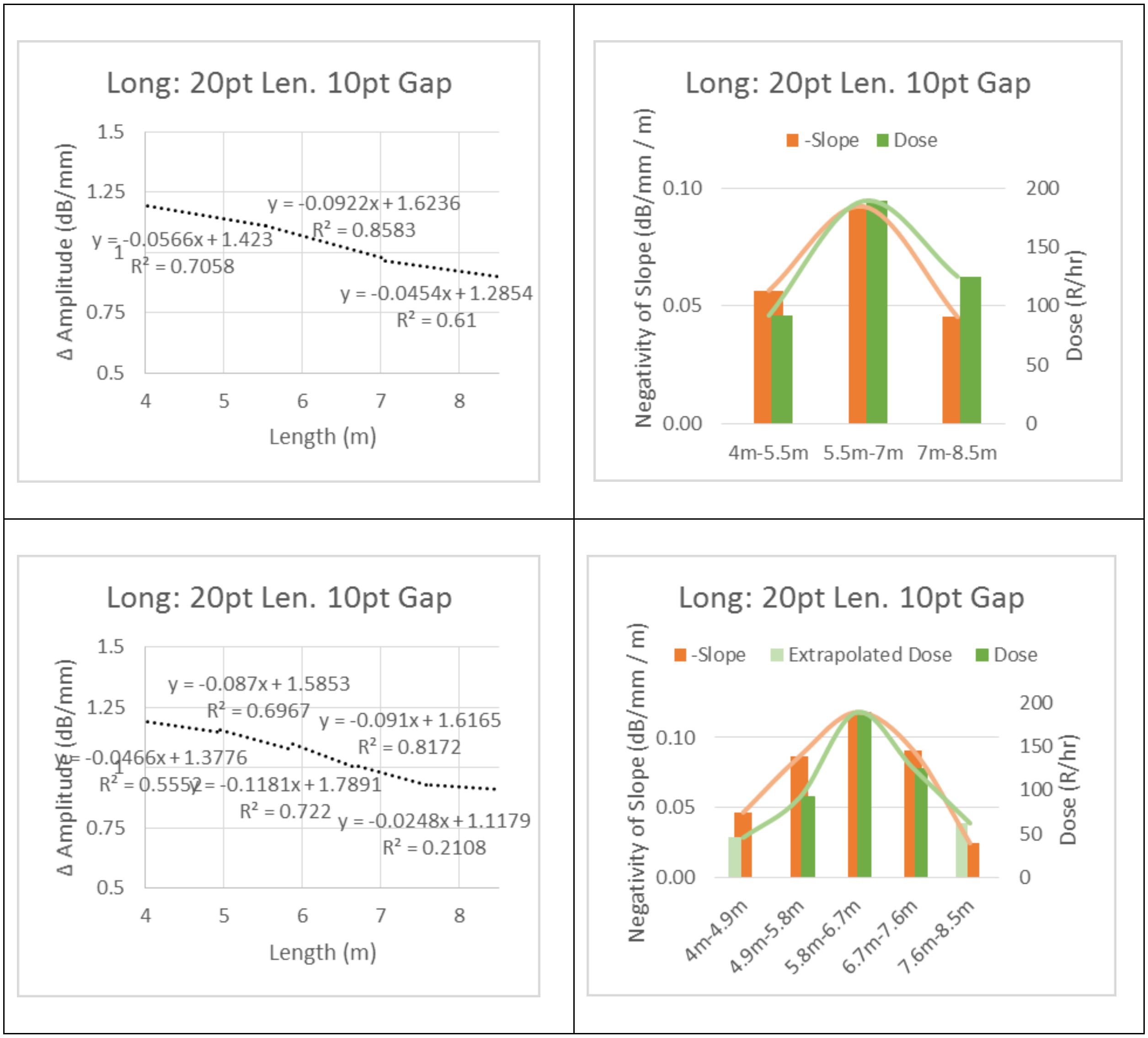

Figure A4.25: Trendline Data Compared to Radiation Dosimetry

This data provides for a significant new finding: the trendline data (either as 3 or 5 data points) appears to follow the radiation dose distribution. Although it is not a perfect match, it is difficult to dictate exactly where the dosimetry data was taken so the fact that it matches as well as it does is a significant finding.

A4.2.3 Black Test Rig (100 kGy)

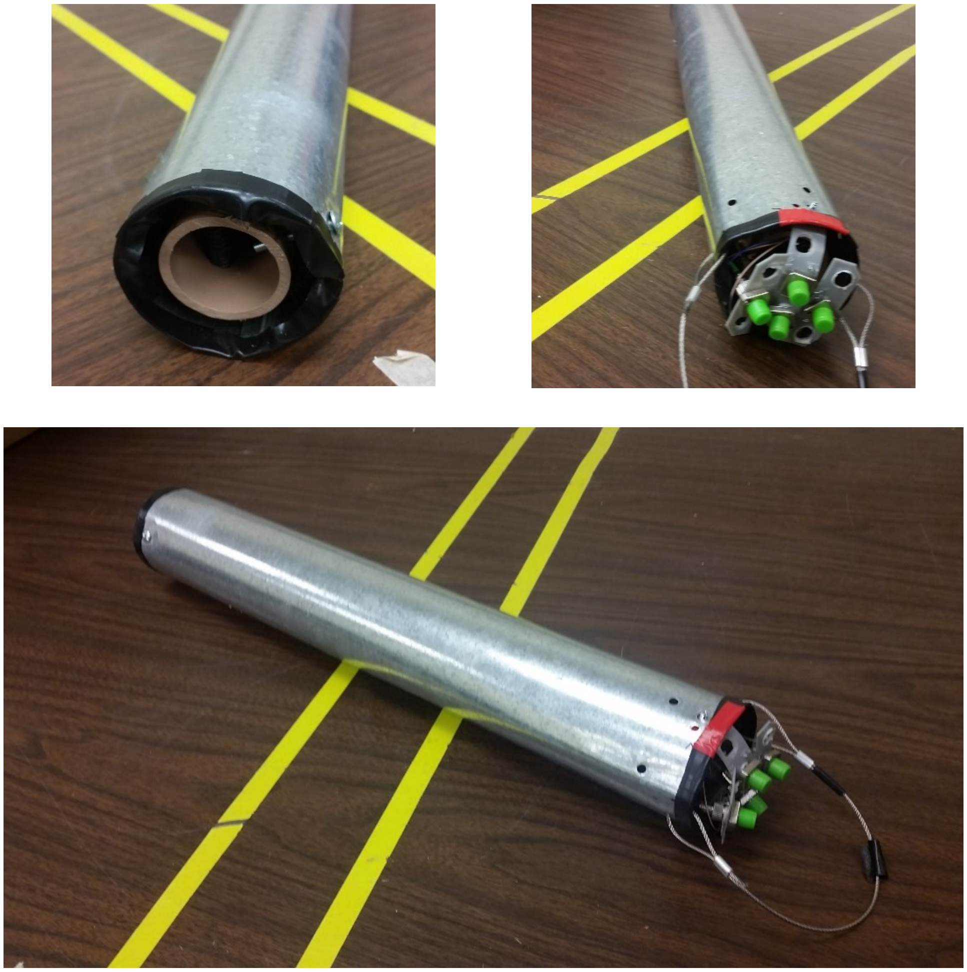

Figure A4.26: Black Test Rig Assembled

The following graphs are scans after the splice connection was made:

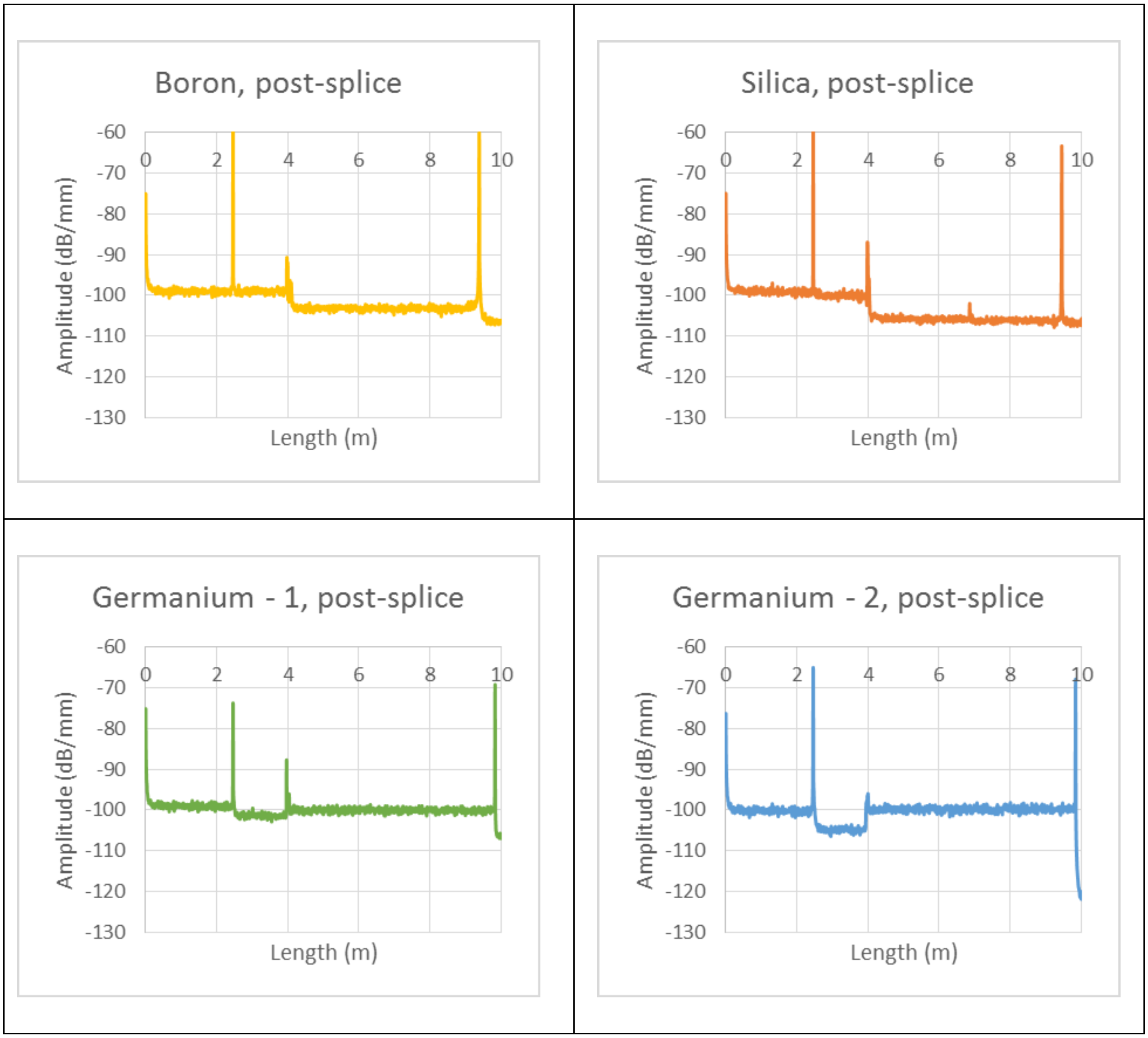

Figure A4.27: Graphs Post-Splice

During the assembly, all splices broke. It was decided not to disassemble and resplice.

These splice breaks can be seen for the pre-irradiation (0 Gy dose) graphs as follows:

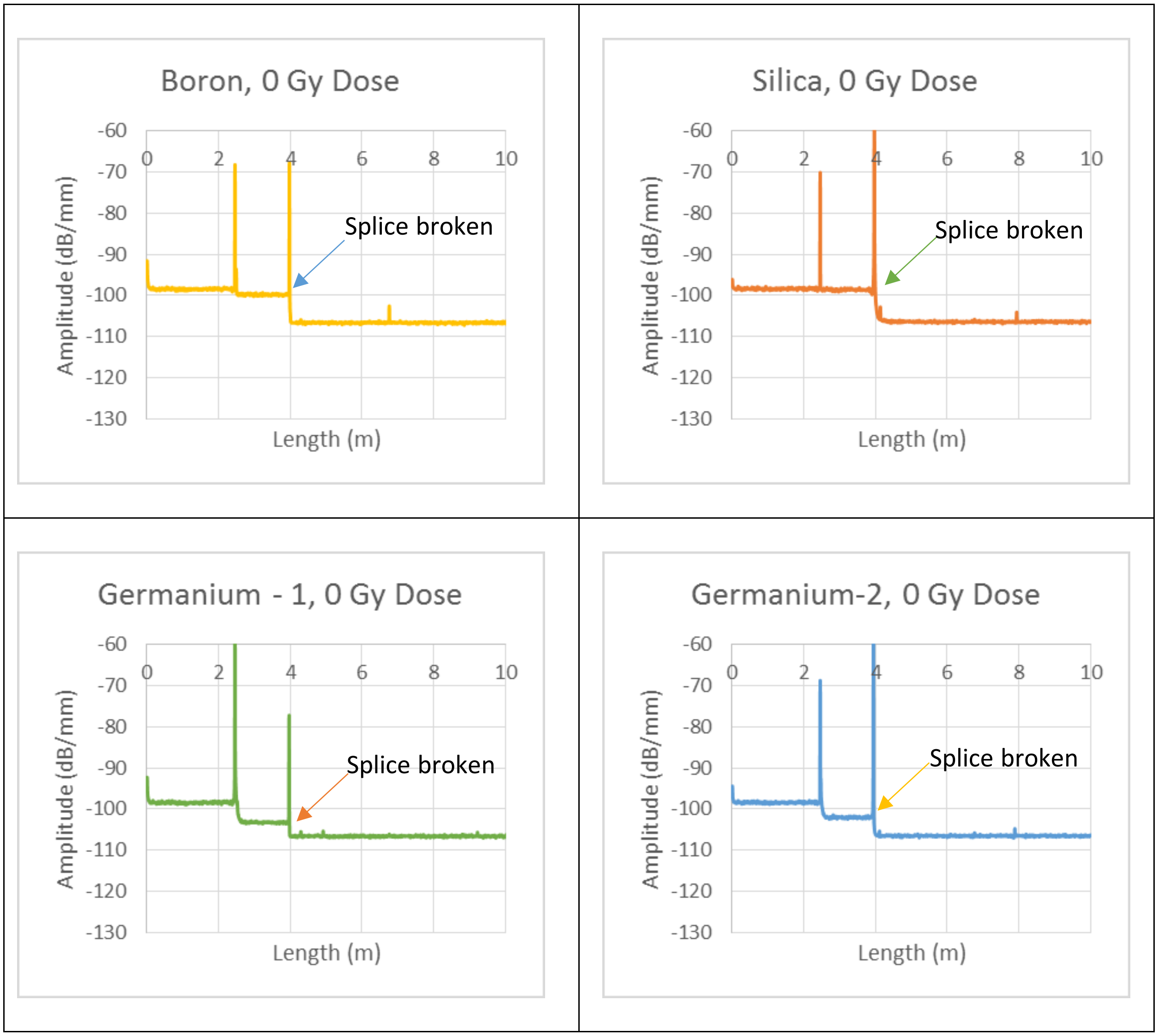

Figure A4.27: Graphs Pre-Irradiation (0 Gy Dose)

Since all scans before irradiation had already broken at the splice, there is no data to be analyzed post-irradiation until the rig is taken apart and the connections re-spliced.

A4.2.4 Green Test Rig (10 kGy)

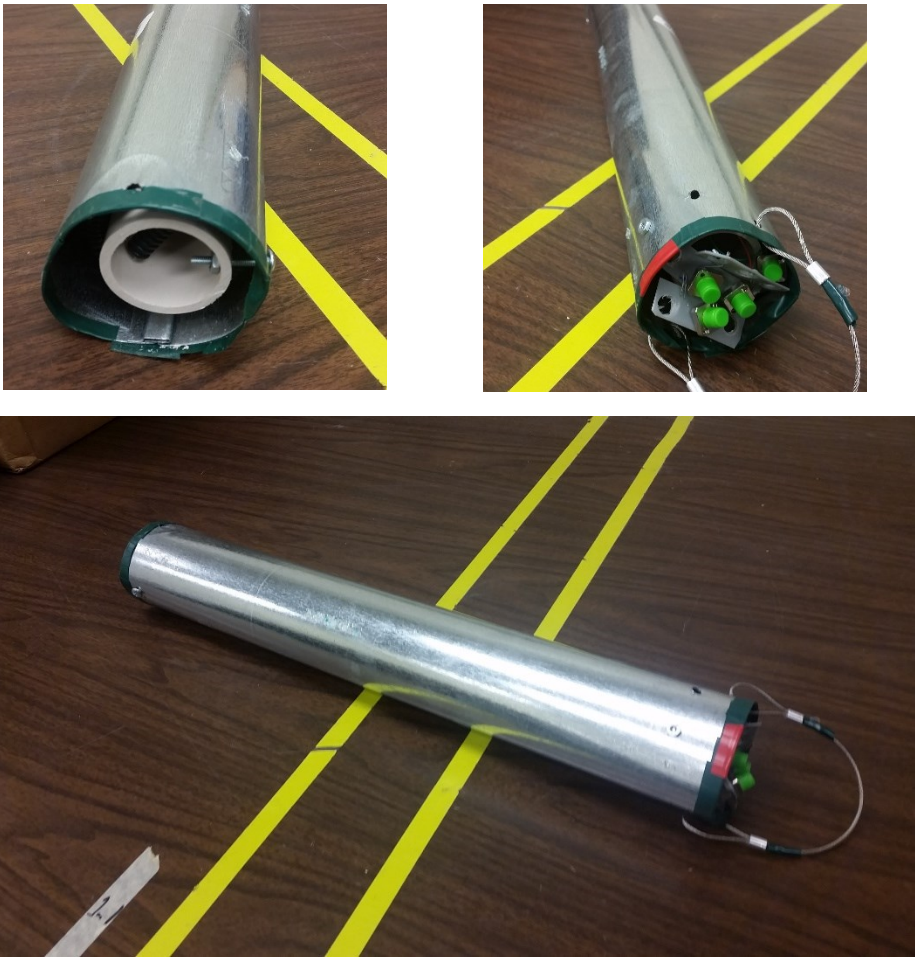

Figure A4.28: Green Test Rig Assembled

The following graphs are scans after the splice connection was made:

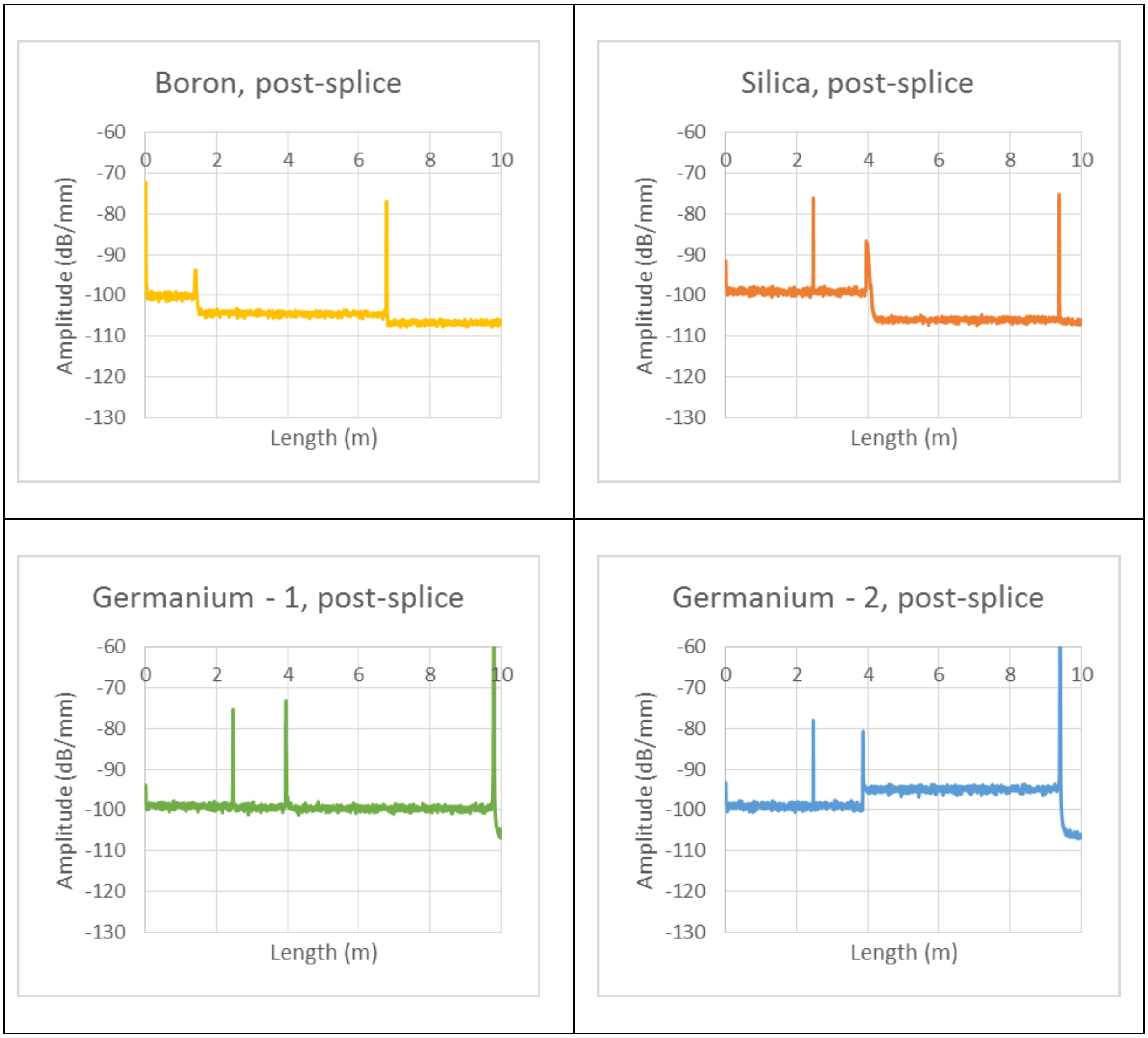

Figure A4.29: Graphs Post-Splice

During the assembly, all splices broke. It was decided not to disassemble and resplice.

These splice breaks can be seen for the pre-irradiation (0 Gy dose) graphs as follows:

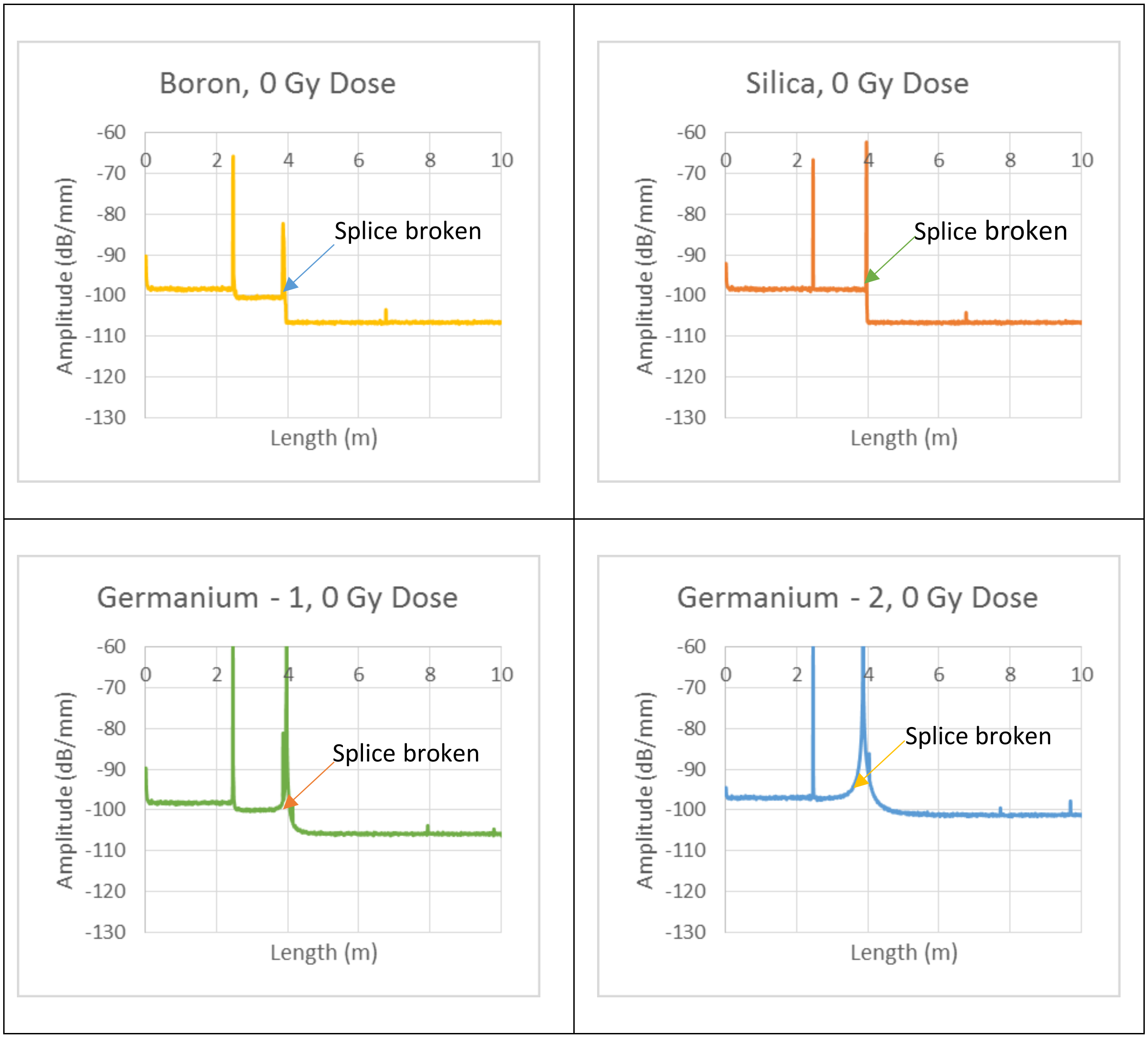

Figure A4.30: Graphs Pre-Irradiation (0 Gy Dose)

Since all scans before irradiation had already broken at the splice, there is no data to be analyzed post-irradiation until the rig is taken apart and the connections re-spliced.

A4.2.5 White Test Rig (10 kGy)

Figure A4.31: White Test Rig Assembled

The white test rig used fiber optic technicians from Oak Ridge National Laboratory to make the splice connections. This rig was considered redundant since the Green Test Rig was also irradiated at 10 kGy. Therefore, rather than having each fiber type represented, the white test rig was boron fiber only. The boron fiber was the most plentiful so it was decided there was plenty to spare for an extra test rig. Since the measurement equipment was at the Texas A&M university laboratory, there were no scans of the fiber optic immediately after the splice connection was made. Instead, the test rig was irradiated in the University of Cincinnati Cobalt-60 lab facility to a dose of 100 Gy before the first data scans could be taken. These scans are seen in the following graphs:

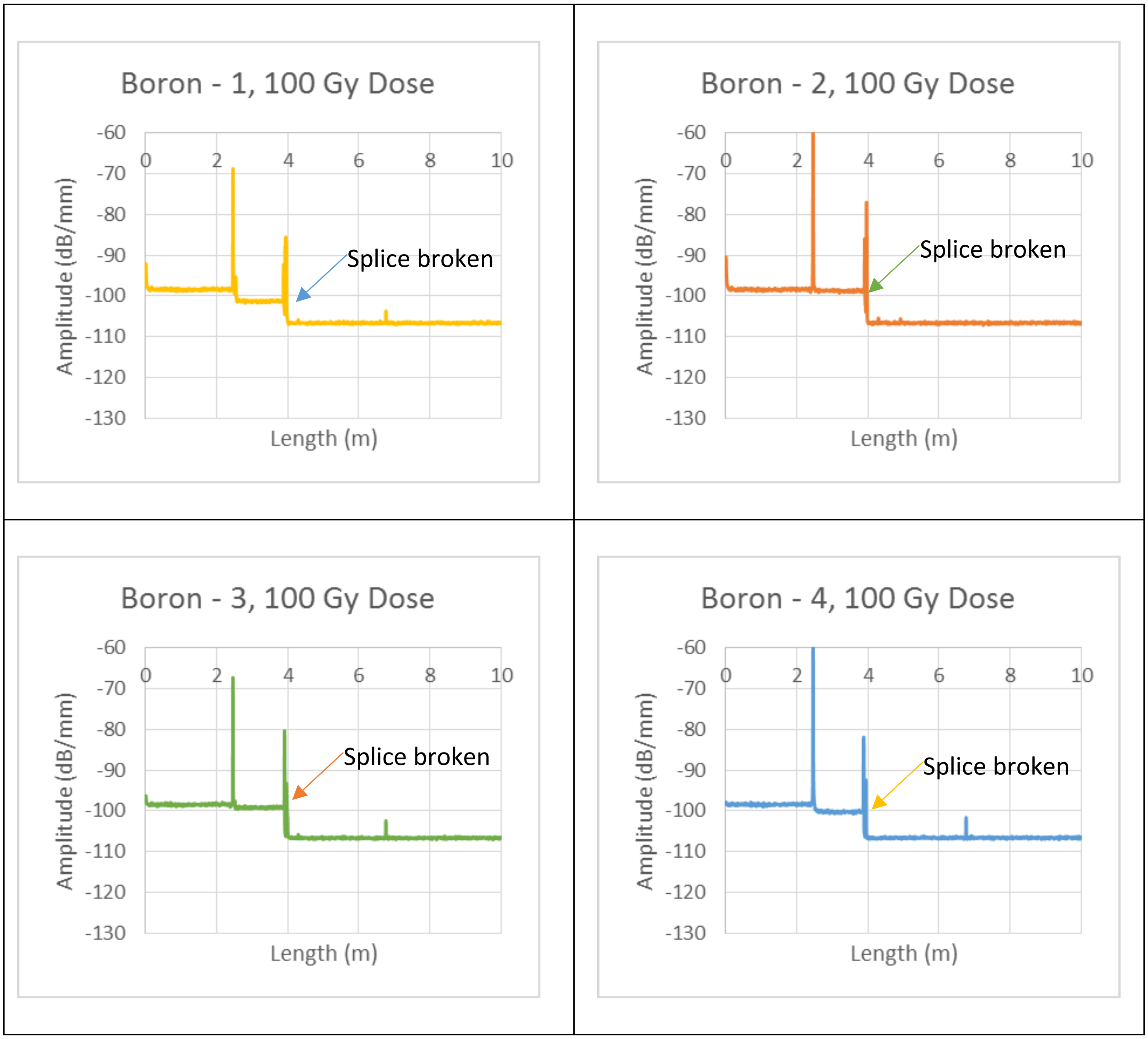

Figure A4.32: Graphs Post Low Irradiation (100 Gy)

As apparent in these data scans due to assembly and / or transport, all splices became broken.   It was decided not to disassemble and re-splice. Since all scans before irradiation had already broken at the splice, there is no data to be analyzed post-irradiation until the rig is taken apart and the connections re-spliced.

A4.2.6 Yellow Test Rig (1 kGy)

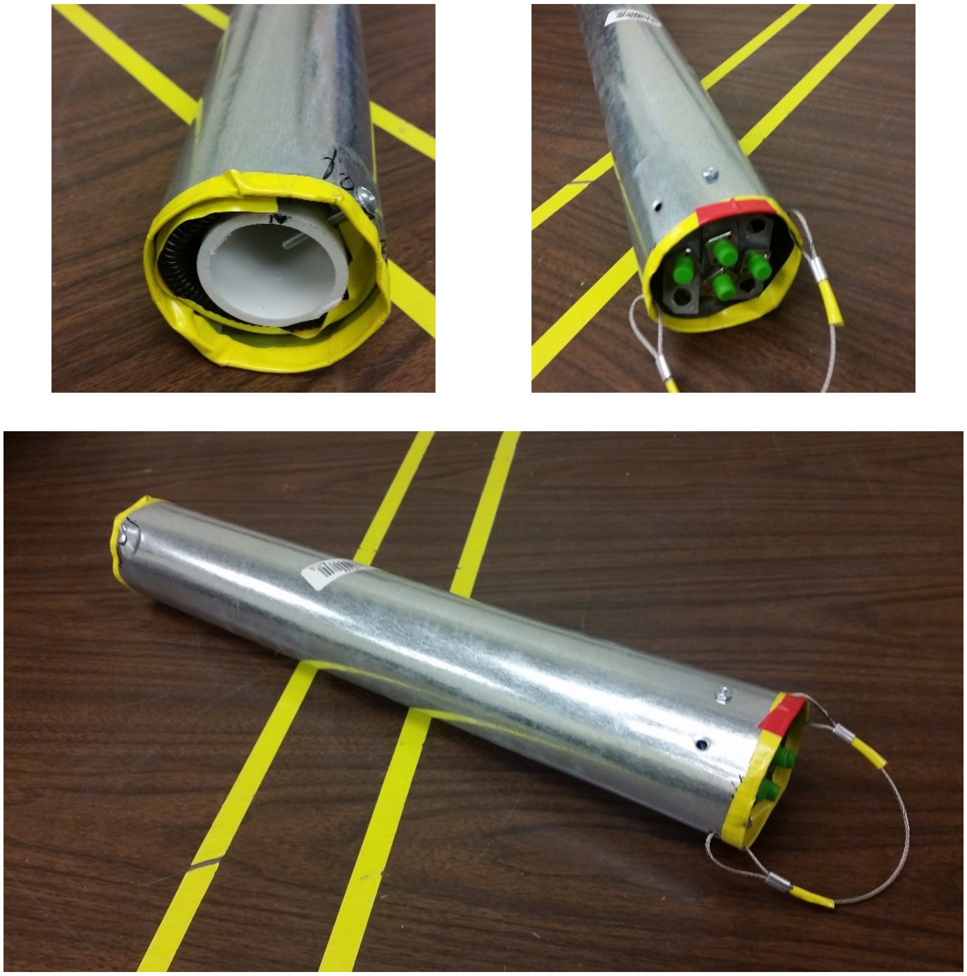

Figure A4.33: Yellow Test Rig Assembled

The yellow test rig was the first constructed and was used for the lowest level irradiations. It was also the most successfully spliced. The graphs post splice and then pre-irradiation can be seen as follows:

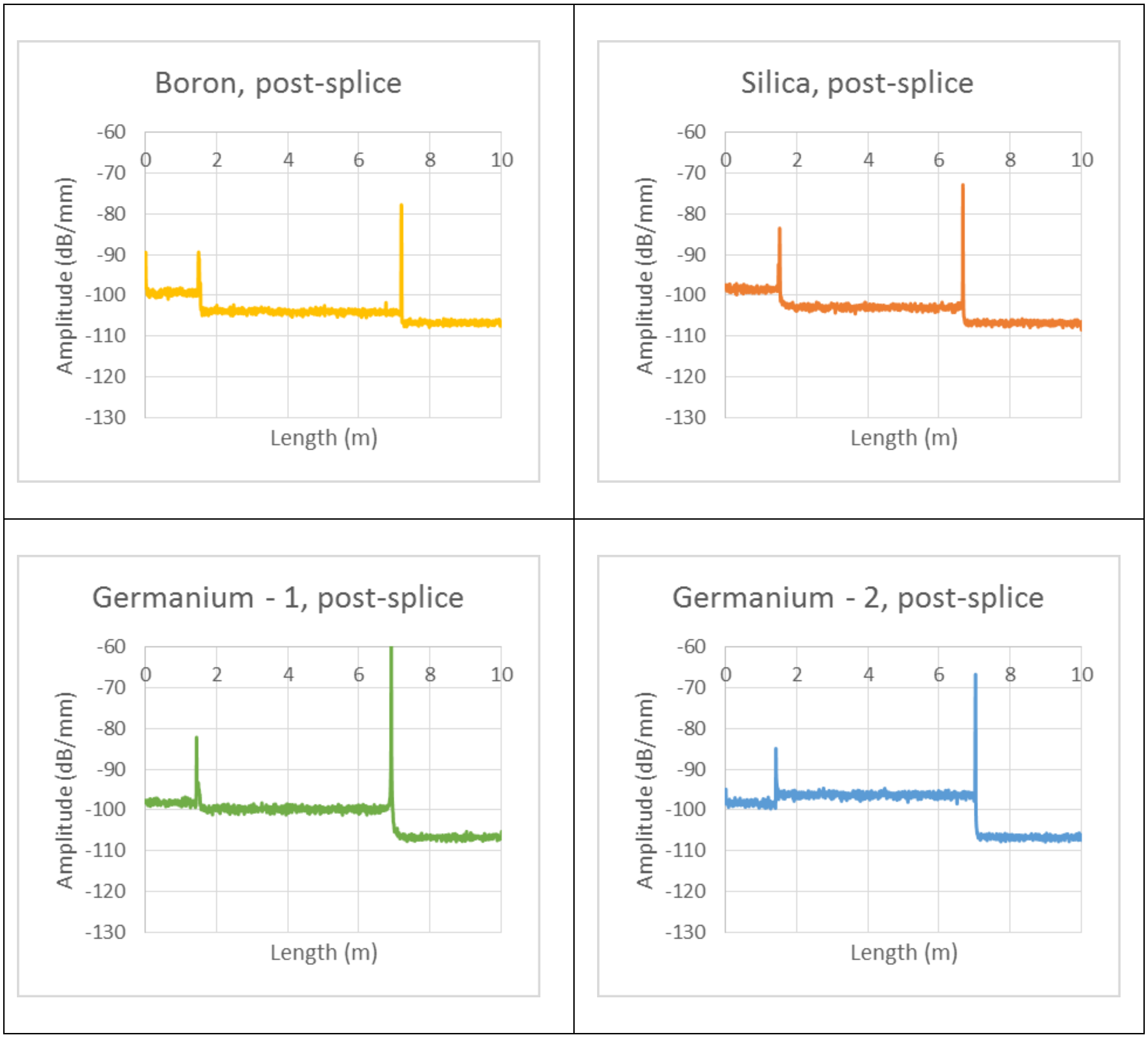
Boron, post-splice

Silica, post-splice

Germanium - 1, post-splice

Germanium - 2, post-splice

Figure A4.34: Graphs Post-Splice

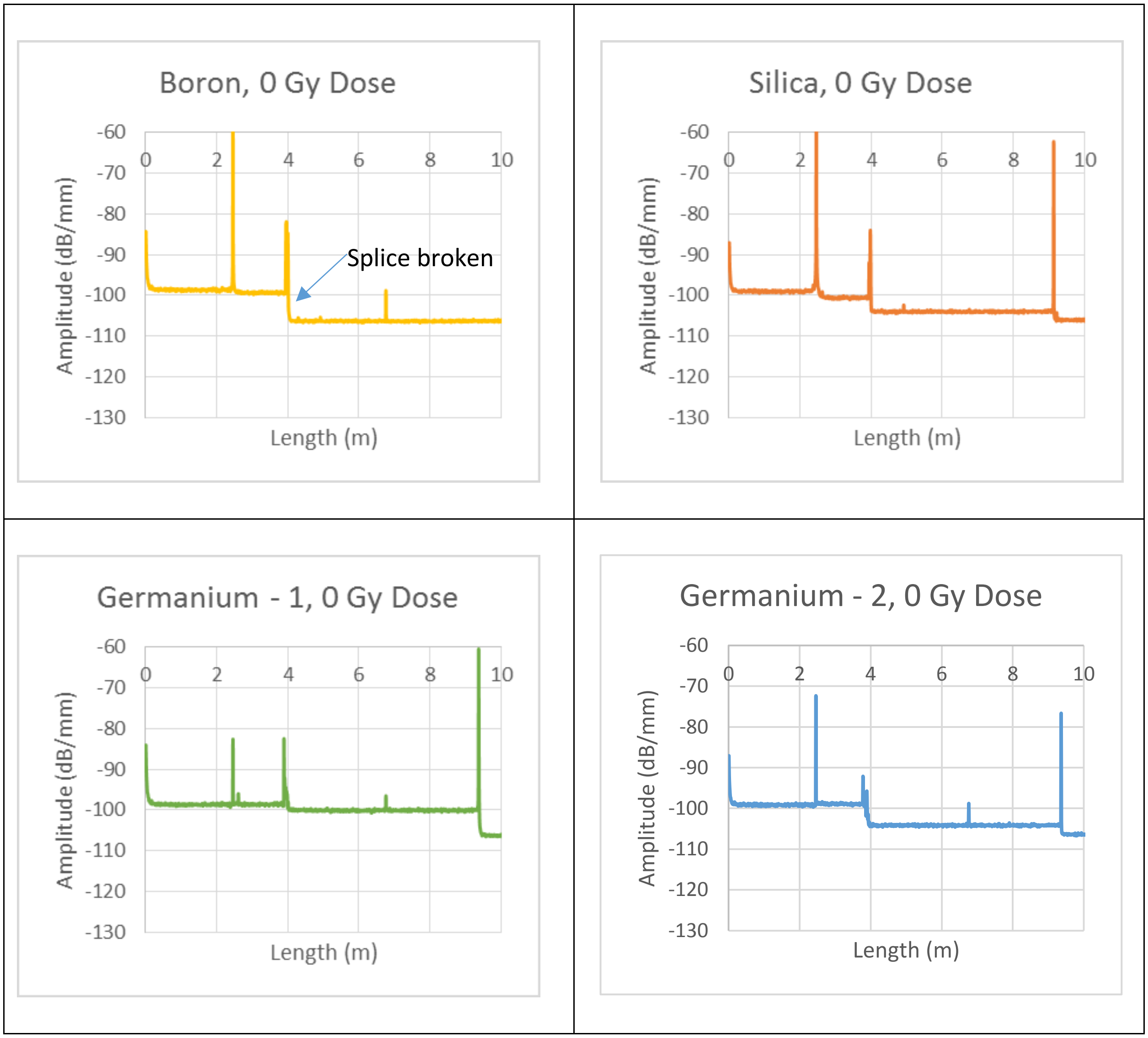

Figure A4.35: Graphs Pre-Irradiation (0 Gy Dose)

Since these were successfully assembled without breaking 3 of the splices, the scans could be analyzed for a response function as was done with the 1 MGy dose range. Since this test rig was dosed at several orders of magnitude lower, even employing the most successful averaging technique for the 1 MGy rig (20 point gage length, 10 point gage gap), it is understandable that the response function is not discernable. This can be seen for each fiber from the yellow test rig with an intact splice connection.

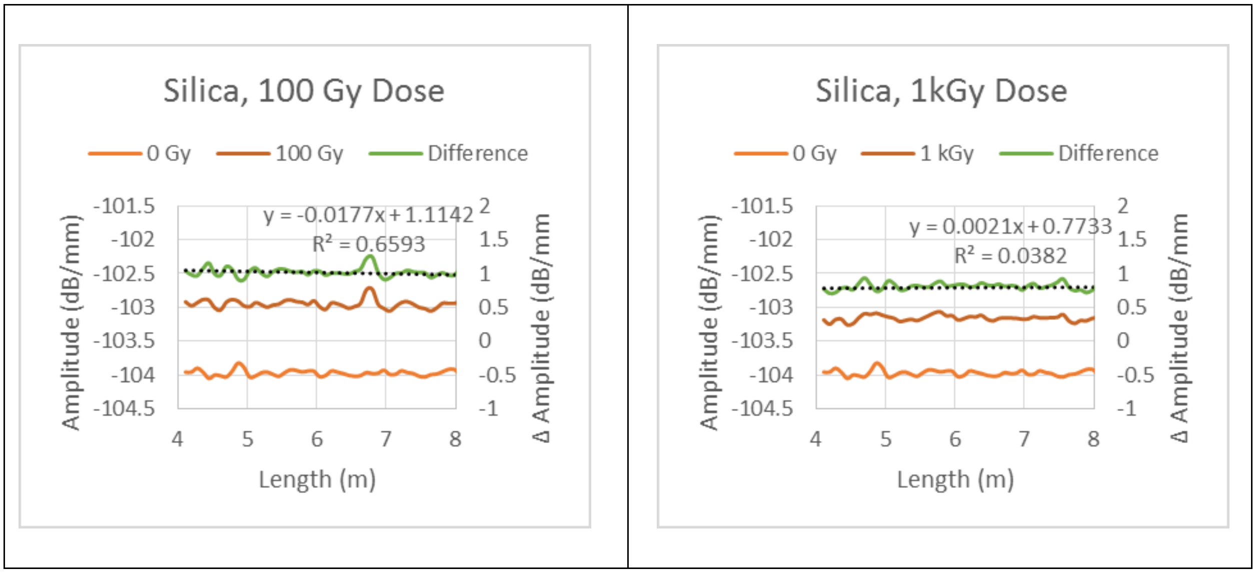

Figure A4.36: Response Function Analysis for Silica Fiber at Low Dose Ranges (100 Gy and 1 kGy)

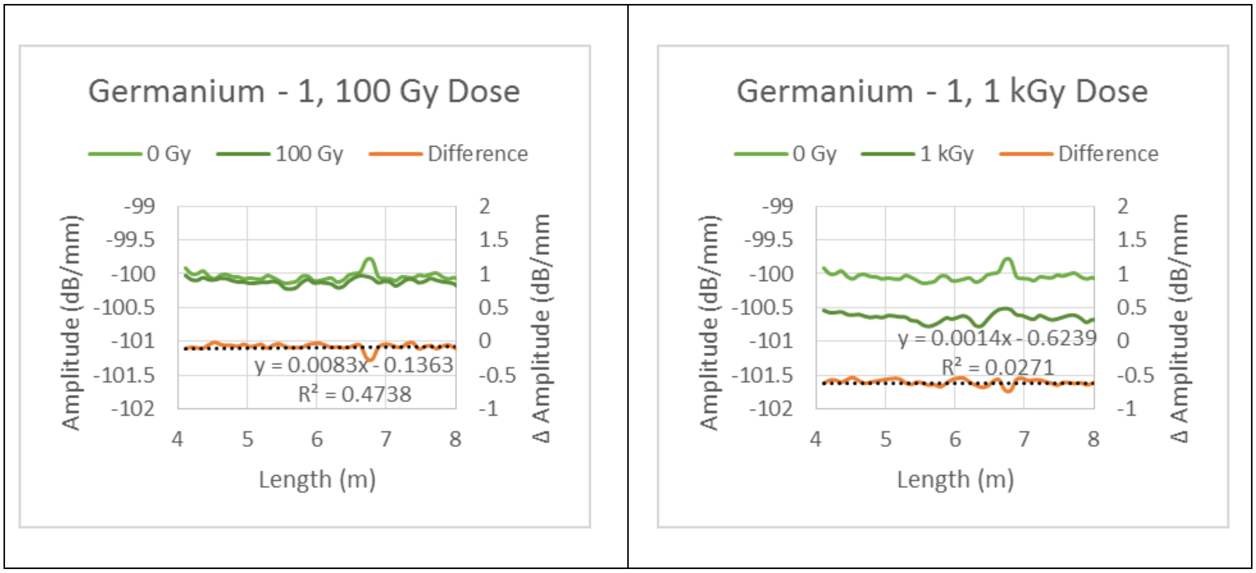

Figure A4.37: Response Analysis for Germanium (1) Fiber at Low Dose Ranges (100 Gy and 1 kGy)

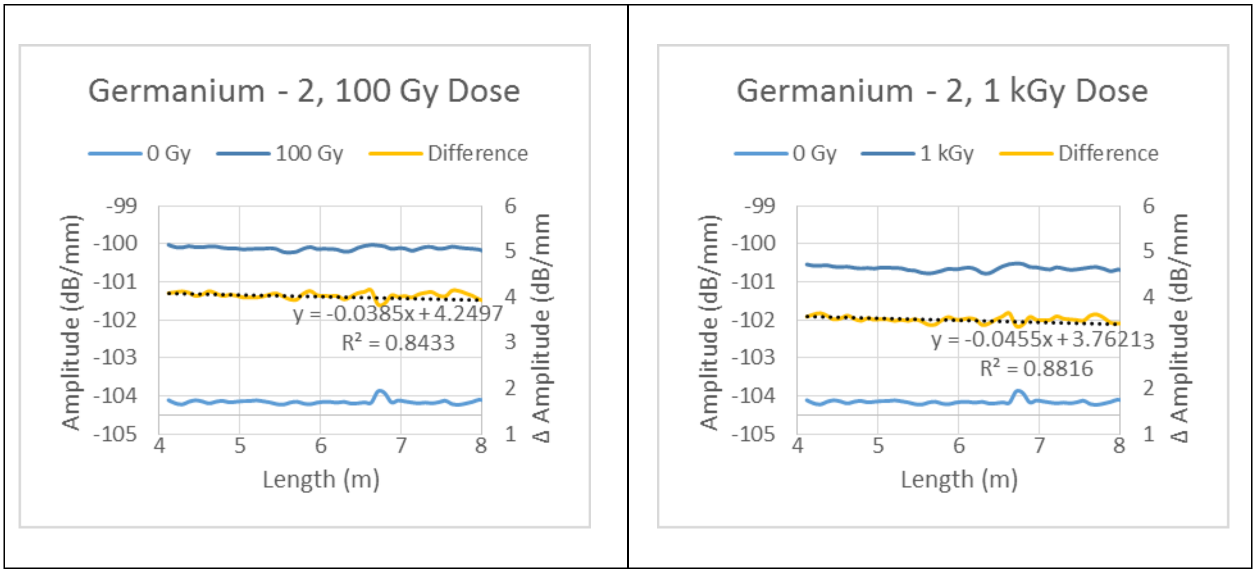

Figure A4.2f-6: Response Analysis for Germanium (2) Fiber at Low Dose Ranges (100 Gy and 1 kGy)

APPENDIX 5: PROGRAMMING METHODS

A5.1 Introduction

A5.1.1 Point Source Characterization

This section details the programming work that was needed to conduct the research. Both research objectives of theoretical models and the heat experiments needed a numerical solver for determining the power distribution of either radiation or heat. The effect of the source (heat and radiation) on its measurement system can be seen in the following diagrams:

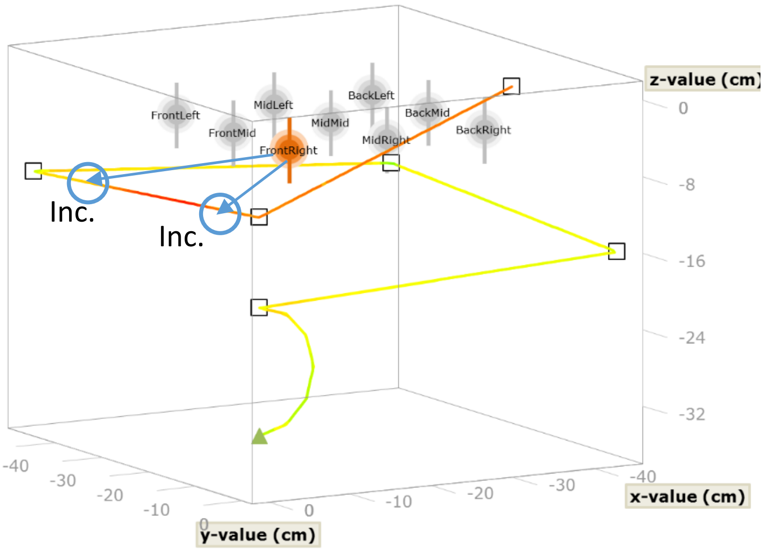

Figure A5.1: Light Bulb Source To Detector Increment

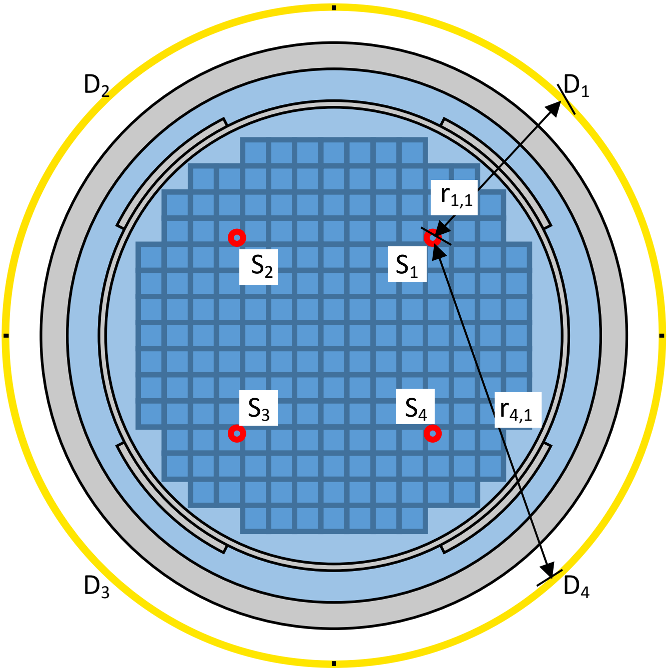

Figure A5.2: Radiation Source To Detector Increment

These diagrams both show that the detector segments have unique attribution from the source to the detector. It can be thought of that the source (either heat or radiation) follows a pathway to the detector. Since the pathways are unique, so is the attribution. The reduction caused by the pathway can be thought of as an “attenuation factor.” From here it follows that there is a unique attenuation factor from each source to each detector. The response therefore for each detector increment is a summation of each source times its attenuation factor. For the simple reactor diagram with 4 sources and 4 detector increments, the mathematical formulas appear as follows:

$$D1 = K1{,}1 * S1 + K1{,}2 * S2 + K1{,}3 * S3 + K1{,}4 * S4$$

$$D2 = K2{,}1 * S1 + K2{,}2 * S2 + K2{,}3 * S3 + K2{,}4 * S4$$

$$D3 = K3{,}1 * S1 + K3{,}2 * S2 + K3{,}3 * S3 + K3{,}4 * S4$$

$$D4 = K4{,}1 * S1 + K4{,}2 * S2 + K4{,}3 * S3 + K4{,}4 * S4$$

This can be put in a matrix form as follows:

$$\begin{bmatrix} D1 \\ D2 \\ D3 \\ D4 \end{bmatrix} = \begin{bmatrix} K1{,}1 & K1{,}2 & K1{,}3 & K1{,}4 \\ K1{,}1 & K2{,}2 & K2{,}3 & K2{,}4 \\ K3{,}1 & K3{,}2 & K3{,}3 & K3{,}4 \\ K4{,}1 & K4{,}2 & K4{,}3 & K4{,}4 \end{bmatrix} * \begin{bmatrix} S1 \\ S2 \\ S3 \\ S4 \end{bmatrix}$$

A solution technique for then solving for the source term is to invert the matrix of attenuation factors (k terms) and multiply the inverted matrix by the detector response values. However, although this inversion method is possible for this example, where there are 4 equations and 4 unknowns, this is not necessarily true in the method application. The heat source experiments, for example, had over 200 data points for detector responses, while only 9 unique source positions.

A second problem with the inversion matrix methods is it allows for negative values. This could happen in such case that a very large positive value is offset by a very large negative value. The negative value does not make physical sense and the positive value could never be so large if not offset by a negative value.

These reasons dictated that the solution method should be a regression technique (to provide for non-equal solution values and solution equations) and a solver within non-negative solutions only. The resultant solver method was then chosen a non-negative least squares regression. The reference behind this method and its implementation can be seen thru reading the rest of this appendix section.

A5.1.2 Non-Negative Least Squares (NNLS) Pseudocode and Code Diagram

A widely used algorithm for NNLS analysis comes from a book by Lawson and Hanson, “Solving Least Squares Problems” (Wikipedia, 2018). Pseudocode for this algorithm appears as follows:

```
• Inputs:
    o a real-valued matrix $A$ of dimension $m \times n$
    o a real-valued vector $\mathbf{y}$ of dimension $m$
    o a real value $\varepsilon$, the tolerance for the stopping criterion
• Initialize:
    o Set $P = \emptyset$
    o Set $R = \{1, ..., n\}$
    o Set $\mathbf{x}$ to an all-zero vector of dimension $n$
    o Set $\mathbf{w} = A^{\mathrm{T}}(\mathbf{y} - A\mathbf{x})$
• Main loop: while $R \neq \emptyset$ and $\max(\mathbf{w}) > \varepsilon$,
    o Let $j$ in $R$ be the index of $\max(\mathbf{w})$ in $\mathbf{w}$
    o Add $j$ to $P$
    o Remove $j$ from $R$
    o Let $A^P$ be $A$ restricted to the variables included in $P$
    o Let $s$ be vector of same length as $\mathbf{x}$. Let $s^P$ denote the sub-vector with
      indexes from $P$, and let $s^R$ denote the sub-vector with indexes from $R$.
    o Set $s^P = ((A^P)^{\mathrm{T}} A^P)^{-1} (A^P)^{\mathrm{T}}\mathbf{y}$
    o Set $s^R$ to zero
    o While $\min(s^P) \leq 0$:
        ▪ Let $\alpha = \min(x_i/(x_i - s_i))$ for $i$ in $P$ where $s_i \leq 0$
        ▪ Set $\mathbf{x}$ to $\mathbf{x} + \alpha(s - x)$
        ▪ Move to $R$ all indices $j$ in $P$ such that $x_j = 0$
        ▪ Set $s^P = ((A^P)^{\mathrm{T}} A^P)^{-1} (A^P)^{\mathrm{T}}\mathbf{y}$
        ▪ Set $s^R$ to zero
    o Set $\mathbf{x}$ to $s$
    o Set $\mathbf{w}$ to $A^{\mathrm{T}}(\mathbf{y} - A\mathbf{x})$
```

The implementation of this pseudo code also relied on the MATLAB NNLS function for debugging assistance (The MathWorks, Inc., 2012). This function referred to the work of Lawson and Hanson as did the Wikipedia article. To explain the method in a different format, a diagram of the code can be seen as follows:

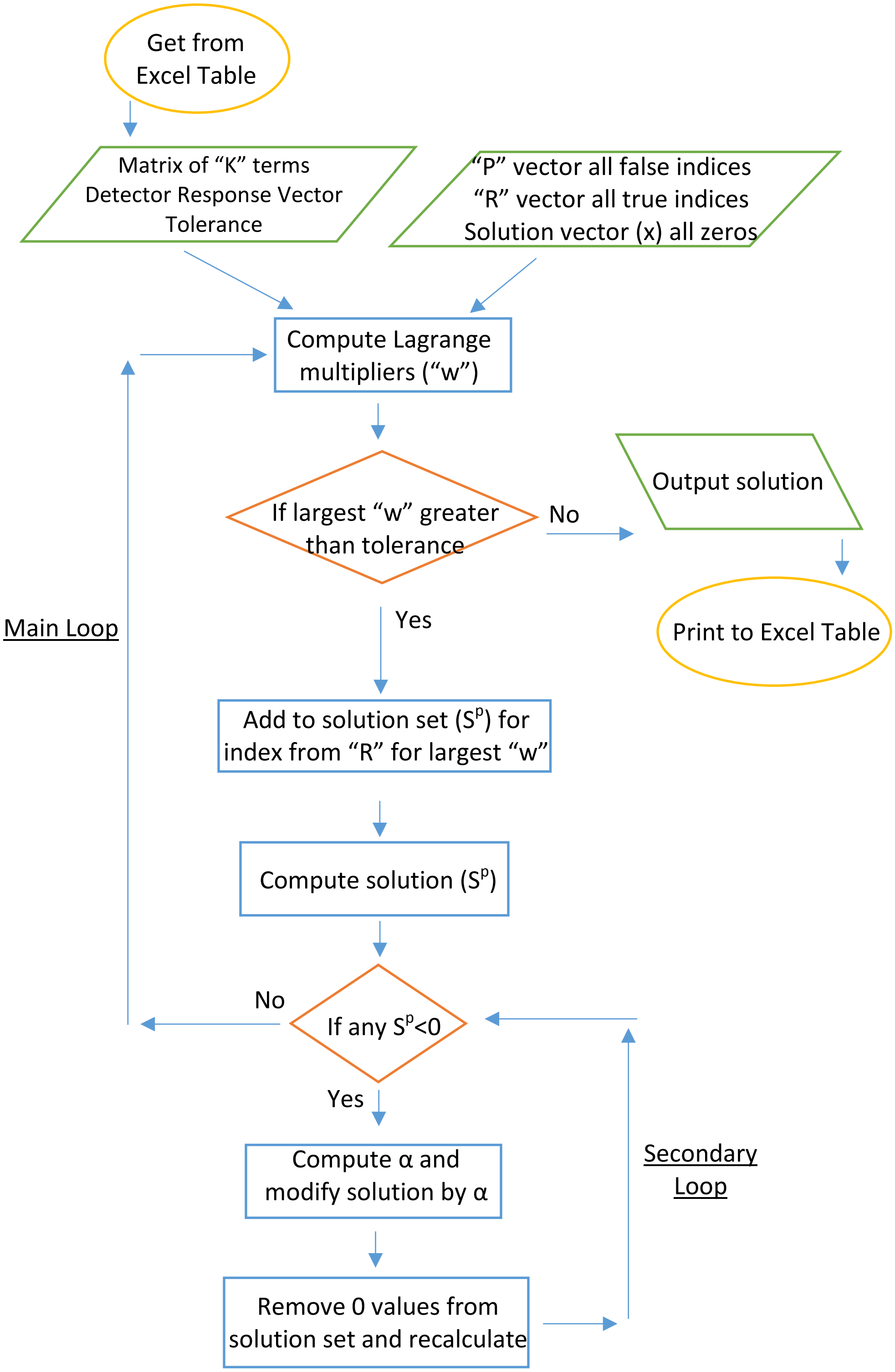

Figure A5.3: NNLS Code Diagram

A5.2 Implementation

A5.2.1 Program Construction / “Set-up Method”

The programming for this method was written in Visual Basic for Applications contained within Microsoft Excel. This provided for a suitable user interface such that the data could be displayed in tabular format and easily graphed. There was however the requirement for the construction of the program to have a main method which loads in the data referring to specific cells within a table.

The inputs for the method that are variable appear within in the first block of the code. These are as follows:

- SizeColumns (number of columns in “K” matrix)
- SizeRows (number of rows in “K” matrix / number of rows in solution and detector response vector)
- Worksheet name (dependent on Excel sheet)

From the definition of these variables, the algorithm preforming the NNLS method can be called and executed with the output being the solution vector. The complete “set-up” method code can be seen as follows:

```
Sub SetUpNNLS()

   'Set up calculation

   Dim sizeColumns As Integer
   Dim sizeRows As Integer
   Dim II, JJ, KK As Integer 'counting indices

   Set mydoc = Worksheets("NNLS") 'worksheet where macro is run from
   sizeColumns = 9 'set size for solution
   sizeRows = Int(mydoc.Cells(3, 8) * 100)

   'Load in Values
   Dim matrixA() As Double
   Dim vectorY() As Double
```

```
    ReDim matrixA(sizeRows - 1, sizeColumns - 1)
    ReDim vectorY(sizeRows - 1)

    'Load matrix of factors
    II = 0
    Do While II < sizeRows
       JJ = 0
       Do While JJ < sizeColumns
          matrixA(II, JJ) = mydoc.Cells(21 + II, 3 + JJ)
          JJ = JJ + 1
       Loop
       II = II + 1
    Loop

    'Load product vector
    II = 0
    Do While II < sizeRows
       vectorY(II) = mydoc.Cells(21 + II, 13)
       II = II + 1
    Loop

    'Run NNLS script
    Dim tolerance As Double
    Dim vectorX() As Double
    tolerance = CalculateTolerance(matrixA)
    vectorX = RunNNLS(matrixA, vectorY, tolerance)

    'Output solution
    II = 0
    Do While II < sizeColumns
       mydoc.Cells(6 + II, 8) = vectorX(II)
       II = II + 1
    Loop

 End Sub
```

The coding above was used for the heat source experiment, but a nearly identical block of code was necessary for the theoretical radiation transport models. The only difference being the location of the data to be loaded in as dictated by the array sizes and placement within the excel sheet. Programming for this method was written in Visual Basic for Applications (VBA) contained within Microsoft Excel and displaying the script syntax in VBA style relied on a subsequent VBA script with Microsoft Word (Newman, 2015).

A5.2.2 NNLS Main Looping Method

The looping method executing the NNLS mathematical methods outlined by the aforementioned pseudo code is then run from the main “set-up method.” Although the “set-up method” is unique to each application because it is dependent on the location of the data within the Excel spreadsheet, the looping method is designed to pair with any configuration once the “set-up method” is constructed. From the “set-up method” the main looping method takes the following inputs:

- MatrixA (the “K” term matrix)
- vectorY (the detector response vector)
- tolerance (stopping criteria)

Output:

- vectorX (solution vector)

The following is the code as written in the solver:

```
Function RunNNLS(matrixA() As Double, vectorY() As Double, tolerance As
   Double) As Double()

   'Initiate solution sets
   Dim II, JJ, KK As Integer 'counting indices
   Dim vectorR() As Boolean
   Dim vectorP() As Boolean 'initially all false
   Dim vectorX() As Double
   Dim vectorS() As Double

   ReDim vectorP(UBound(matrixA, 2))
   ReDim vectorR(UBound(matrixA, 2))
   ReDim vectorX(UBound(matrixA, 2))
   ReDim vectorS(UBound(matrixA, 2))

   'Initial vector values
   II = 0
   Do While II < UBound(matrixA, 2) + 1
      vectorR(II) = True 'initially all true
```

```
   vectorP(II) = False 'initially all false
   vectorX(II) = 0 'Start with zeros for X
   vectorS(II) = 0 'Start with zeros for s
   II = II + 1
Loop

'Initial "w" vector
Dim vectorW() As Double
Dim matrixAt() As Double 'matrix A transposed
Dim vectorAx() As Double 'matrix A times vector X
Dim residual() As Double 'difference of vector y and A
                         times X
Dim maximumW As Double

ReDim vectorW(UBound(matrixA, 2))
ReDim matrixAt(UBound(matrixA, 2), UBound(matrixA, 1))
ReDim vectorAx(UBound(matrixA, 1)) As Double
ReDim residual(UBound(matrixA, 1)) As Double

matrixAt = TransposeMatrix(matrixA)
vectorAx = MultiplyMatrixByVector(matrixA, vectorX)
residual = SubtractVector(vectorY, vectorAx)
vectorW = MultiplyMatrixByVector(matrixAt, residual)


'Initial Loop Values
Dim matrixAp() As Double 'matrix A with only value
                          according to vector P
Dim matrixApt() As Double 'transpose of matrix A,p
Dim matrixAptAp() As Double 'transpose of matrix Ap
                             multiplied by matrix A,p
Dim vectorAptY() As Double 'transpose of matrix Ap
                            multiplied by vector Y
Dim vectorSp() As Double

ReDim matrixAp(UBound(matrixA, 1), 0)

maximumW = FindMaximum(vectorW)
JJ = FindMaximumIndex(vectorW)

'Main loop
Do While UBound(matrixAp, 2) < UBound(matrixA, 2) + 1 And
   maximumW > tolerance 'tolcheck

   'take away J and shift R 'Not sure if really need R-vector
   vectorR(JJ) = False

   'add J to p
   vectorP(JJ) = True

   'Operation functions
   matrixAp = CreateAp(matrixA, vectorP)
   matrixApt = TransposeMatrix(matrixAp)
   matrixAptAp = MultiplyMatrixByMatrix(matrixApt, matrixAp)
   vectorAptY = MultiplyMatrixByVector(matrixApt, vectorY)
   vectorSp = LUdecomposition(matrixAptAp, vectorAptY)
```

```
            'Loop for any Sp less than 0
            vectorSp = MimSpLoop(vectorSp, matrixA, vectorX, vectorY,
               vectorP, vectorR, tolerance)

            vectorS = VectorSfromSp(vectorSp, vectorP)
            II = 0
            Do While II < UBound(matrixA, 2) + 1
               vectorX(II) = vectorS(II)
               II = II + 1
            Loop

            vectorAx = MultiplyMatrixByVector(matrixA, vectorX)
            residual = SubtractVector(vectorY, vectorAx)
            vectorW = MultiplyMatrixByVector(matrixAt, residual)

            maximumW = FindMaximum(vectorW)
            JJ = FindMaximumIndex(vectorW)
         Loop

         RunNNLS = vector

      End Function
```

A5.2.3 NNLS Secondary Looping Method

Within the NNLS main looping method is a second loop which ensures the solution is indeed non-negative. Therefore, a second function was written to be applied within the main loop. It is worth noting that the writing of a function within Visual Basic permits the passing of arguments by reference ("ByRef") or by value ("ByVal"). The default is by reference which means that any change to the arguments within the function will be as such for the use of these arguments upon the exiting of the function. This is important because the secondary loop modifies the vectors that dictate which indices of the solution vector is to be solved for ("P" vector and "R" vector") in addition to the solution vector ("S" vector). The inputs for the code are as follows:

- vectorSp (the solution vector for only variables declared in vector)
- matrixA (the complete matrix of "K" terms)
- vectorX (the complete solution vector)
- vectorY (the detector response vector)
- vectorP (part of the solution vector to be solved for)
- vectorR (part of the solution vector to be skipped)
- tolerance (stopping criteria)

Because of the use of all these variables as arguments of type "ByRef," all of the input arguments are tied to the function as an output. However the primary function output is as follows:

- vectorSp (the solution vector for only variables declared in "P" vector)

The complete method as code can be seen as follows:

```
Function MimSpLoop(vectorSp() As Double, matrixA() As Double, vectorX()
   As Double, vectorY() As Double, vectorP() As Boolean, vectorR() As
   Boolean, tolerance As Double) As Double()

   Dim minimumSp As Double
   Dim minimumAlpha As Double
   Dim II, JJ As Integer 'Counting variable

   Dim vectorAlpha() As Double
   ReDim vectorAlpha(UBound(matrixA, 2))

   Dim matrixAp() As Double 'matrix A with only values according to
                             vector P
   Dim matrixApt() As Double 'transpose of matrix A,p
   Dim matrixAptAp() As Double 'transpose of matrix Ap multiplied by
                                matrix A,p
   Dim vectorAptY() As Double 'transpose of matrix Ap multiplied by
                               vector Y

   minimumSp = FindMinimum(vectorSp)

   Do While minimumSp <= 0

      vectorS = VectorSfromSp(vectorSp, vectorP)
      II = 0
      JJ = 0
      Do While II < UBound(matrixA, 2) + 1
         If vectorP(II) = True And vectorS(II) <= 0 Then
```

```
                ReDim Preserve vectorAlpha(JJ)
                vectorAlpha(JJ) = vectorX(II) / (vectorX(II) - vectorS(II))
                JJ = JJ + 1
            End If
            II = II + 1
        Loop
        minimumAlpha = FindMinimum(vectorAlpha)

        II = 0
        Do While II < UBound(matrixA, 2) + 1
            vectorX(II) = vectorX(II) + minimumAlpha * (vectorS(II) -
                vectorX(II))
            II = II + 1
        Loop

        II = 0
        Do While II < UBound(matrixA, 2) + 1
            If Abs(vectorX(II)) < tolerance And vectorP(II) = True Then

                'Line 175 MATLAB, removes values close
                 to zero (+/- tolerance) from solution vector "P"
                vectorR(II) = True
                vectorP(II) = False
            End If
            II = II + 1
        Loop

        matrixAp = CreateAp(matrixA, vectorP)
        matrixApt = TransposeMatrix(matrixAp)
        matrixAptAp = MultiplyMatrixByMatrix(matrixApt,   matrixAp)
        vectorAptY = MultiplyMatrixByVector(matrixApt, vectorY)
        vectorSp = LUdecomposition(matrixAptAp, vectorAptY)
        minimumSp = FindMinimum(vectorSp)

    Loop 'Loop on minimum "S"

    MimSpLoop = vectorSp

End Function
```

A5.2.4 Matrix Methods / LU Decomposition

As seen in the looping methods, the mathematical operations of matrices (such as matrix multiplication / matrix subtraction) require individual methods to be written for each. These methods are straight forward so will not be documented here.

One operation which is more complicated however is the requirement to perform the matrix inversion. This is apparent within the pseudo code as the following line which is repeated twice:

- $s^P = ((A^P)^\mathrm{T} A^P)^{-1} (A^P)^\mathrm{T}\mathbf{y}$

Although there are several different numerical methods that can perform a matrix inversion, the one implemented here was the "LU decomposition." This method relies on solving for the inverse by factoring the matrix into two triangular matrices: one lower and one upper (Chapra, 2008). Computing the inverse in such way is a fairly common numerical method so its implementation is not documented here.

A5.2.5 Stopping Criteria ("Tolerance")

The looping NNLS method must have a stopping criteria to exit the loop at some point. One criteria must be such that when the entire solution vector is solved for, yielding a value greater than zero for the entire vector, then the regression analysis is complete. An additional stopping criteria is such that if all calculated Lagrange multipliers (the "w" value in the pseudo code) are less than a certain value, the solution is satisfactory and the method should exit its loop. This value can be considered a "tolerance" and is ambiguous in the referenced pseudo code, however the MATLAB reference choses a default value to be calculated according to the following formula:

$$Tolerance = 10 * Max\big(Size(C)\big) * Norm(C, 1) * EPS$$

In this formula, the variable “C” is the matrix of attenuation factors (“K”), the size function is either the number of rows or number of columns of this matrix, the maximum function takes whichever is greater, the norm function (of type 1) is the largest sum of any column, and “EPS” is the value for the distance from 1.0 to the next largest double-precision number (computed to be 2^-52). The calculation of tolerance in this manner as a stopping criteria proved satisfactory.